Development of methods to decrease aneuploidy in mammalian oocytes

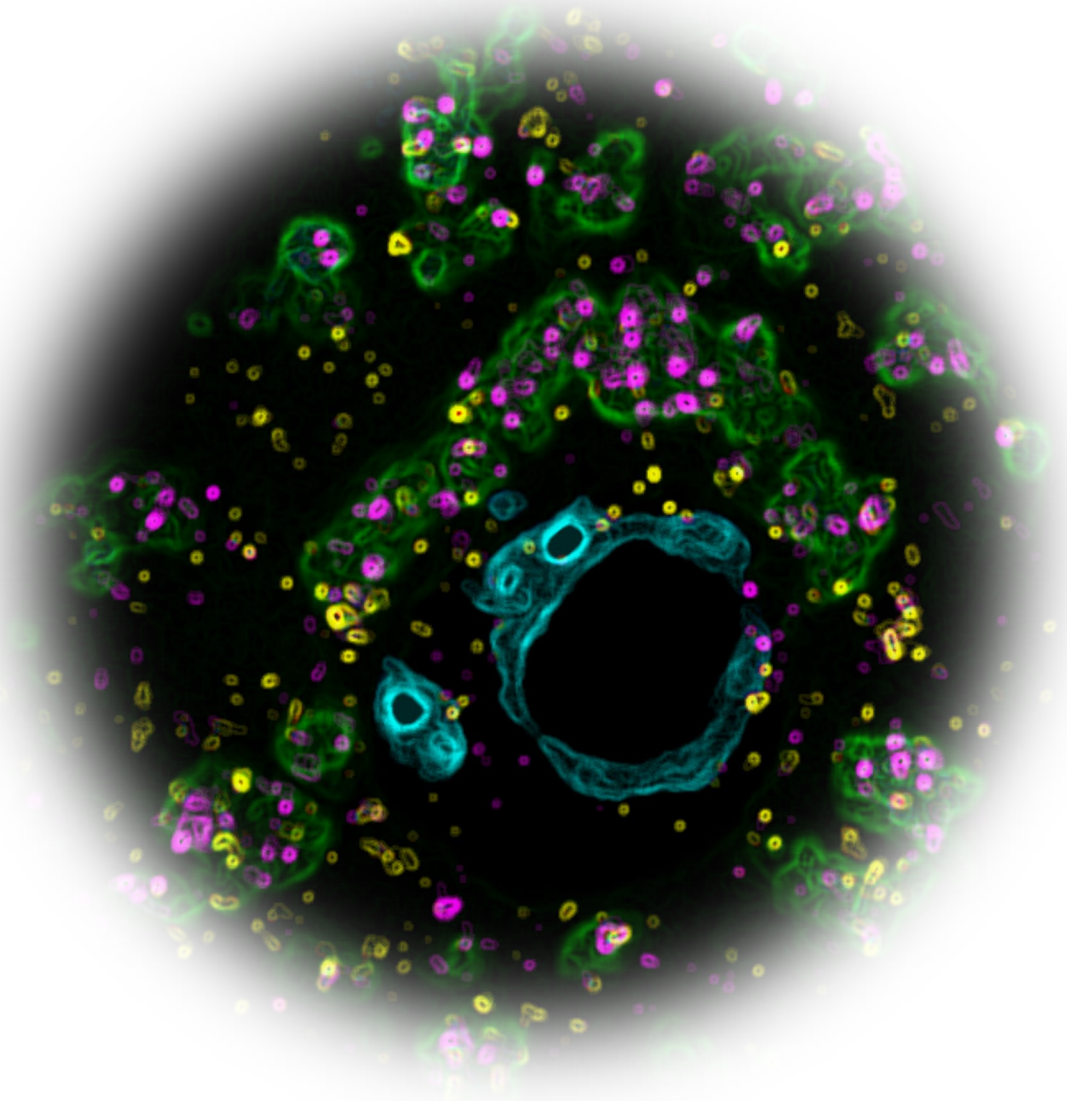

Development of methods to decrease aneuploidy in mammalian oocytes

Dissertation
for the award of the degree
"Doctor rerum naturalium"
of the Georg-August-Universität Göttingen

within the doctoral program
International Max Planck Research School Molecular Biology
of the
Georg-August University School of Science (GAUSS)

submitted by
Gerrit Altmeppen
from Lingen (Ems), Germany

Max Planck Institute for Multidisciplinary Sciences

Göttingen 2022

Thesis Committee

Dr. Melina Schuh
Department of Meiosis
Max Planck Institute for Multidisciplinary Sciences

Dr. Ufuk Günesdogan
Department of Developmental Biology
Göttingen Center for Molecular Biosciences

Prof. Sarah Köster
Institute for X-Ray Physics
Georg-August-University Göttingen

Members of the Examination Board

1st Referee
Dr. Melina Schuh
Department of Meiosis
Max Planck Institute for Multidisciplinary Sciences

2nd Referee
Prof. Ernst Wimmer
Department of Developmental Biology
Johann-Friedrich-Blumenbach-Institute of Zoology and Anthropology

Further members of the Examination Board

Dr. Peter Lenart
Department of Cytoskeletal Dynamics in Oocytes
Max Planck Institute for Multidisciplinary Sciences

Dr. Jochen Rink
Department for Tissue Dynamics and Regeneration
Max Planck Institute for Multidisciplinary Sciences

Dr. Ufuk Günesdogan
Department of Developmental Biology
Göttingen Center for Molecular Biosciences

Prof. Timo Betz
Third Institute of Physics - Biophysics
Georg August University Göttingen

Prof. Michael Meinecke
Biochemistry Center (BZH)
Heidelberg University

Date of oral examination: March 31st, 2022

Table of contents

Abstract of the PhD thesis

Maternal mRNAs accompany and control all processes from the onset of meiosis until the blastocyst stage when the maternal pool of mRNAs is fully replaced by the emryonic mRNA set. The successful development of blastocysts relies on the stability of maternal mRNAs before and during meiosis. Numerous maternal mRNA controlling proteins have been identified in the oocytes of *Drosophila melanogaster*, *Xenopus laevis* and *Mus musculus*. Although the function of many mRNA binding proteins is known, the exact mechanisms that regulate translation and mRNA stability remain unclear. A better understanding of this topic would be very important both from a fundamental research as well as from a medical perspective, because the orchestrated translation and decay of maternal mRNAs is crucial for the successful development of early embryo. In addition, alterations in the sequence of translation and decay affect the process of meiosis and impair the developmental capacity of oocytes. Delayed maturation and aneuploidy are consequences of imbalanced maternal mRNA pools. Aneuploidy in eggs is the main cause of infertility and miscarriages in women. The aim of my thesis was to identify new mRNA regulatory pathways that support the healthy development of oocytes and early embryos, and to develop methods that can be used to decrease aneuploidy.

In the first part of my thesis, I investigated a maternal mRNA controlling protein that we termed maternal mRNA-Sequestering Protein (MMSP). We found that MMSP organizes a novel mRNA storage domain in oocytes, and characterized the dynamics, composition and physical properties of this domain. In addition, I studied how depletion of MMSP in a knockout mouse model affects the functionality of the oocyte and progression through meiosis.

In the second part of my thesis, I used specific dyes and single molecule RNA-FISH (smRNA-FISH) to study a specific gene whose mRNA is sequestered by MMSP. We showed that the pre-mature loss of the mRNA in MMSP knockout oocytes causes severe defects in the lipid metabolism and mitochondrial activity in immature oocytes. We further provide evidence that altered lipid metabolism and mitochondrial activity cause oxidative stress. Oxidative stress is known to contribute to age-related damage in oocytes that eventually can lead to aneuploidy.

In the third part of my thesis, I aimed to develop tools to correct chromosome segregation errors by artificially moving chromosomes inside living oocytes. I used different types of magnetic tweezers and glass needles to reposition chromosomes within oocytes, or to remove chromosomes from oocytes. This work provides a proof-of-concept that chromosomes can be modified inside oocytes, and also be removed from oocytes without affecting oocyte viability. However, substantial further development will be required to apply related methods to the reduction of aneuploidy in fertility treatments.

“The whole universe was in a hot dense state, then nearly 14 billion years ago, expansion started – wait!”

History of everything by the Barenaked Ladies

General introduction

Phase separation

Phase separation in biological cells

Phase separation is the spontaneous demixing of a mixture of molecules and a solvent. During phase separation, condensates form that contain high concentrations of one or multiple molecules. The molecule(s) in the surrounding solvent are therefore diluted[1]. In cells, phase separated structures have been thought to form so-called "membraneless organelles" by Liquid-Liquid Phase Separation (LLPS) because they are distinct from the cytosol. These membraneless organelles have been implicated in energy exchange within the cell[2]. Some are as complex as "classical" membranous organelles but are able to react to different states of the cell more quickly than the canonical membrane-surrounded organelles. Centrosomes, the structures that nucleate microtubules in somatic cells and sperm, are phase-separated structures that contain the centrioles as an inner core and multiple cytosolic factors that do not bind stably to any of the centrosomic structures. The most obvious phase-separated structure in an oocyte is the nucleolus, a part of the nucleus that was first discovered in 1845 in spider oocytes and 1864 in mammalian oocytes[3–5]. The nucleolus is the place within a cell where the rDNA is located and it controls both the synthesis of rRNA and its assembly into ribosomes[3,6]. It was found in 1971 that the nucleolus compacts and rDNA transcription is decreased as a point of silencing in oocytes during growth and maturation[7]. In oocytes, the recently described Liquid-like meiotic spindle domain (LISD) structure was shown to be a liquid-like condensate which is involved in spindle formation of mouse oocytes (Fig. 1)[8].

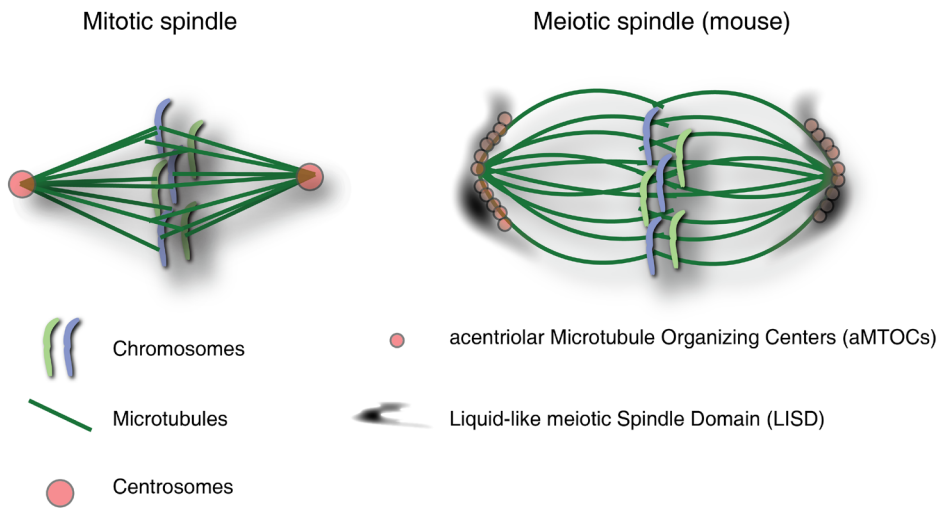

Fig. 1 The missing centrosomes cause the meiotic spindle to have a distinct shape from the mitotic spindle. In somatic cells, the spindle is organized by large phase-separated structures, the centrosomes. The core of centrosomes consists of centrioles that are inherited to the daughter cells. Oocytes lack centrosomes and centrioles. Mouse oocytes express centrosomal proteins that form various small clusters, so-called acentriolar Microtubule Organizing Centers (aMTOCs). Together with the phase-separated Liquid-like meiotic Spindle Domain (LISD), the spindle is stabilized. The figure is based on Bennabi *et al.* and So *et al.*[8,9].

Maternal mRNAs

Cells have strategies to cope with translational stress and can stably form an equilibrium of mRNA synthesis and decay. Germ cells however, have a very delicate task: They need to be highly functionalized until they undergo fertilization, which requires them to switch into a totipotent cell. During prophase I arrest, the transcription rate is reduced in mammalian oocytes. Transcription is fully suppressed when the oocyte resumes meiosis[10]. Therefore, the mRNA pool within an oocyte needs to be tightly orchestrated in a spatiotemporal manner. Translation and decay of subpopulations require complex regulation pathways and in that sense, membraneless RNA compartments, which can be specialized for storage, repression and decay of mRNAs, seem to be ideal candidates to fulfill this job.

A significant fraction of the total mRNA pool in an oocyte is transcribed during the growth and maturation phase and remains in the oocyte until fertilization initiates the so-called maternal-to-zygotic transition (MZT), during which most of the mRNA is degraded and transcription of new mRNA is initiated (Fig. 2C). The transcripts that are responsible for the initiation of the final step of sexual reproduction are called maternal mRNAs[10,11].

Early experiments showed that the cytoplasmic mRNA pool is much more important to the immediate developmental process of oocytes than the nuclear content, which is only important for later developmental steps[10]. This requires special solutions since mRNAs usually have high turnover rates in the order of magnitude of hours to a few days[12]. The mechanisms usually involve RNA-binding proteins (RBPs), for example YBX1 which has been shown to bind the 3` UTR of a specific mRNA in *Danio rerio* called squint and thereby protects it from degradation[13]. Translational activity, however, is encoded within the mRNA itself. The poly(A) tail varies in length depending on the need for the specific mRNA to be translated. Specific sequences in the 3` UTR can shift the equilibrium to rather long or short poly(A) tails. The cytoplasmic polyadenylation element (CPE) induces synthesis of more adenosines whereas AU-rich elements (AREs) promote deadenylation. This is done by recruiting a diverse set of cytoplasmic factors that regulate the activity of enzymes, such as the Poly(A)-Polymerase (PAP) or PAN2 or PAN3 deadenlyases. The Poly(A)-binding proteins (PABPs) usually stabilize the tail and recruit the translation initiation factor eIF4G, which leads subsequent translation[14].

RNA binding proteins in phase separated structures

As shown in the examples above, RNA and some membrane-bound organelles such as mitochondria are often the key component of RNA particles (RNPs) and membraneless structures, but it is usually a single or couple of specialized proteins that are responsible for the formation of a LLPS organelle. What do all of these proteins have in common? It is he low complexity and the disordered regions that cause condensation and lead to the moderate clustering and dynamic behavior observed in LLPS organelles.

Popular examples of phase-separated RNPs are usually those in *Xenopus laevis* and *Drosophila melanogaster* eggs, where asymmetrical concentration gradients of mRNAs determine the fate of the daughter cells during the first mitotic cell devisions[15].

Biological examples of membraneless organelles in germ cells

1. Balbiani body

The key protein of the Balbiani body in *Xenopus laevis* is Xvelo1 (Bucky ball in zebrafish)[16]. Xvelo1 binds to mitochondria and acts as a scaffold for the Balbiani body (Fig. 2B). This is why Xvelo1 is considered to undergo so-called "self-assembly". It was discovered that Xvelo1 contains a prion-like domain, which in theory allows Xvelo1 to undergo dynamics and the thermodynamical behavior that is considered as "liquid-solid phase separation" (Fig. 2A)[17].

The Balbiani body was found in most vertebrate oocytes. In fish and frogs, it is known that it serves as germplasm, accumulating and protecting maternal mRNAs and mitochondria during maturation of oocytes. It is also involved in the polarization of oocytes and subsequently the fertilized egg in these species[17].

Notably, it was found that the mitochondria in Balbiani bodies show reduced activity of cytochrome c oxidase, indicating that another function of this membraneless compartment could be to keep mitochondria in a dormant state, reducing the amount of ROS and the chance of mutations of mtDNA. Since the germ plasm determines which embryonic cells enter the germ line, this mechanism seems to ensure that only healthy mitochondria are transferred to the next generation, preventing an accumulation of mutations in mtDNA[18]. It has been shown that not only invertebrates, amphibians and fish have Balbiani bodies, but mice as well. However, this structure disappears once the follicle starts to grow[19]. Thus, a function for the Balbiani body in mammals is yet to be discovered.

2. P granules

Another structure that oocytes of species like *Caenorhabditis elegans* and *Drosophila melanogaster* show, is the P granule. The P granules are transferred through the P lineage and, similarly to the Balbiani body, cause the cells to stay in the germ line. Their integrity and LLPS behavior is mainly determined by a specific class of proteins, called PGL proteins[20]. Other factors were also found to be enriched in P granules that protect mRNAs from degradation[21]. Remarkably, P granules were the first RNP structure for which LLPS dynamics like fusion and fission were shown[22].

3. P bodies

P bodies got their name from their processing function. Other than Balbiani bodies or P granules, mRNAs are not simply stored or protected in P bodies but actively modified. P bodies are involved in the repression and decay of mRNA[23]. Moreover, P bodies were shown to undergo LLPS, too[23].

From the perspective of mammalian oocytes, P bodies are much more interesting than the two structured described above, since P bodies were found in all kinds of animals.

Even though mRNA and mRNA decay proteins such as DCP1A, DCP2, EDC3 and EDC4 localize to P bodies, which led to the assumption that P bodies are involved in mRNA decay, there are indications that not only the mRNA is repressed within P bodies but so are their decay proteins. In addition to this, it was shown that mRNAs can leave P bodies again and that mRNA decay does not rely on P bodies[24,25]. It thus might rather be that P bodies have similar functions to stress granules[24].

The usual degradation pathway of mRNAs happens via deadenylation by the CCR4-NOT complex and decapping by DCP1 and DCP2, followed by decay in either direction by the exosome or specialized exonucleases[26]. Notably, not all mRNAs enter the decay pathway in the same way. Some mRNAs contain an AU-rich element (ARE) in their untranslated 3' region (UTR), which recruits decapping complexes[25].

For P bodies, LLPS has been shown as well. There are several methods used for this, especially the analysis of dynamic behavior such as fusion and fission *in vitro* and *in vivo* as well as fluorescence recovery after photobleaching (FRAP) experiments, in which fluorescently labeled proteins of interest are bleached within a structure and diffusion of non-bleached fluorescently-labelled proteins into the structure is measured[23,27]. In addition to this, the appearance as round droplets indicates high surface tension characteristic for phase-separated structures[23]. P bodies are an example for the fact that many LLPS structures consist of RNAs and RNA binding proteins. Furthermore, P bodies were not only shown to be LLPS-driven granules that rely on certain factors but also on RNA itself[25,28,29].

4. Stress granules

Stress granules share many similarities with P bodies. They do not only share some of the same proteins but they can also interact with each other[25,30]. When under stress, a cell stops translation and thus accumulates mRNAs. These mRNAs become stored in so-called stress granules[30]. In contrast to P bodies, stress granules additionally accumulate several factors for the induction of translation[23]. Notably, RNA degradation seems to be reduced during translational stress, indicating that it is favorable to buffer the stress situation rather than enhancing mRNA decay[31,32]. Like stress granules, P bodies were shown to dissolve when synthesis of new mRNAs is inhibited[24]. Furthermore, stress granules are now thought of as a sorting compartment that exports certain mRNAs to P bodies when they need to be degraded while other mRNAs are released into the cytoplasm for translation[30].

5. Microtubule Organizing Centers (MTOCs)

Not all cytoplasmic phase-separated structures are RNPs. The spindle in mitotic and meiotic cells is instable during formation[33]. Structures have evolved by evolution that stabilize the spindle apparatus: MicroTubule Organizing Centers (MTOCs), a class of structures that nucleate microtubules. MTOCs are essential for the formation of a bipolar spindle. Most MTOC structures undergo phase-separation. Previous studies suggest that phase-separation is an important feature of MTOCS to concentrate microtubule-nucleation factors, which prevents the generation of more poles[34]. In somatic cells, the centrosomes maintain spindle stability, whereas in mouse oocytes, acentriolar MTOCs (aMTOCs) were discovered on the spindle poles[35,36]. The recently discovered Liquid-Like meiotic Spindle Domain (LISD) domain stabilizes the meiotic spindle in mouse oocytes and contributes to the functional segregation of chromosomes[8].

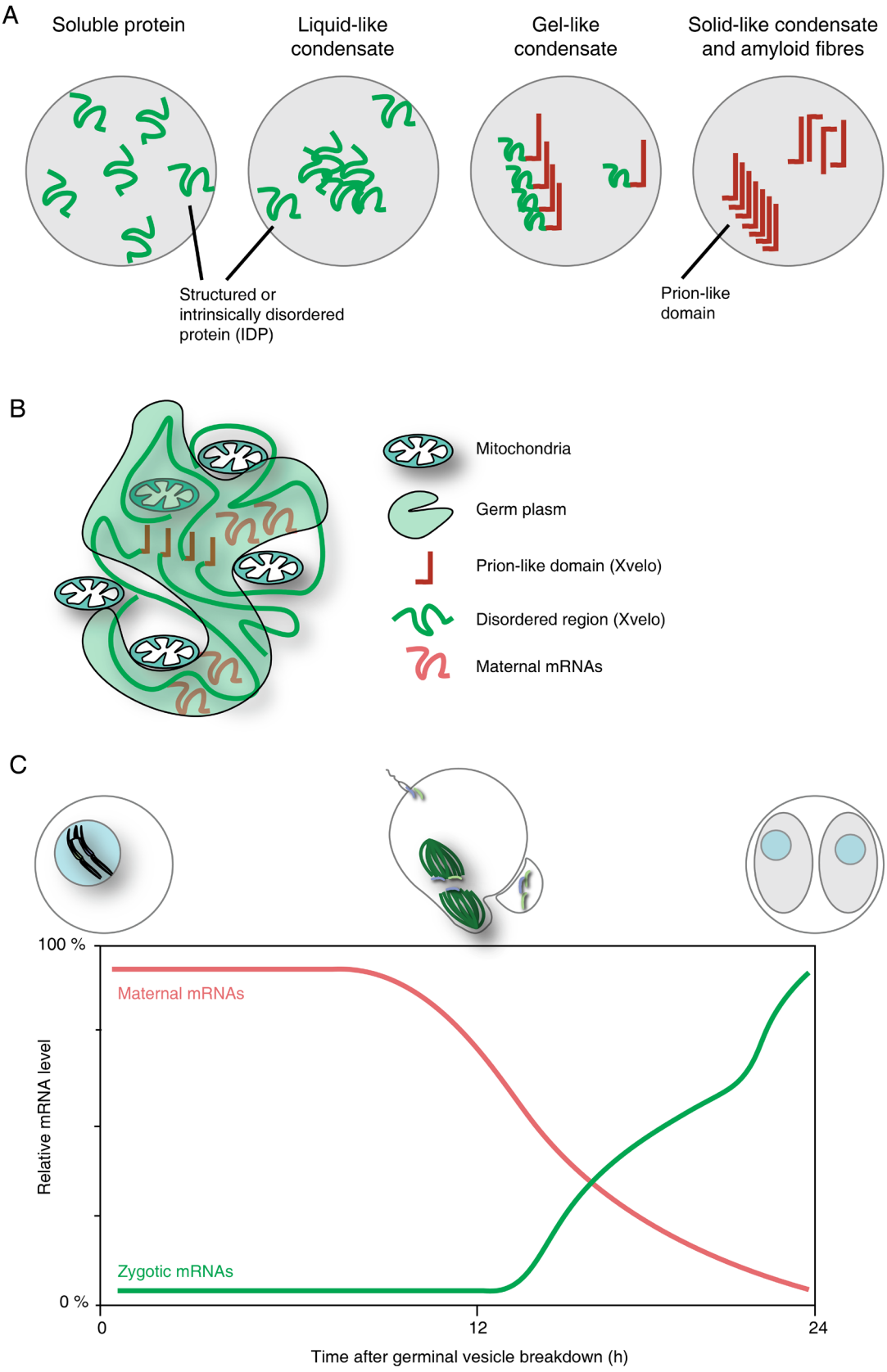

Fig. 2 Liquid-liquid phase separation drives the formation of RNA condensates like the Balbiani body and might control the decay of maternal mRNAs. (A) Proteins (green) can be soluble in the cytosol (grey). Most proteins are either structured or intrinsically disordered (IDP). IDPs tend to condensate like oil droplets in water. Nevertheless, proteins are in an equilibrium and show steady state dynamics between the condensate and the cytosol. Proteins can have dedicated amino acid sequences or domains that tend to cluster with each other. Examples are the FG

domain in proteins of the nuclear pores or prion-like domains like in Xvelo, a protein that forms the Balbiani body. Proteins with dedicated regions show reduced diffusion or exchange dynamics with the cytosol and act more as a gel. The equilibrium is shifted towards condensation. If a protein has no or just a small soluble region, the dynamics are greatly shifted towards the condensate and nearly no exchange of proteins with the cytosol is observed. In extreme cases, the proteins form amyloid aggregates. Amyloid aggregates cannot be degraded by the cell machinery and accumulate. The resulting functional impairment of affected cells causes diseases such as Alzheimer's Disease and Creutzfeld Jakob Disease[37]. (B) A schematic model of the Balbiani body, based on the figures of So *et al.*[1]. The Balbiani body sequesters certain maternal mRNAs (orange) in *Xenopus laevis* oocytes to the vegetal pole. The driving protein is Xvelo that consists of disordered regions (green) and prion-like domains (red). The Balbiani body additionally contains mitochondria. The exact reason is still unknown. Yet, it is has been hypothesized that the Balbiani body sequesters "healthy" mitochondria for passage to the next lineage of germ cells. Further, partly unknown factors are sequestered into the condensates. In the literature, the structure of factors is referred to as germ plasm (pale green)[16,38,39]. (C) Maternal-to-zygotic transition (MZT) in mouse oocytes. After the onset of meiosis, marked by GVBD, maternal mRNAs (orange) are translated and mRNA degradation pathways are activated. Upon fertilization, the entire pool of maternal mRNAs is diminished within 12 h. Simultaneously, the DNA and histones are modified and transcription of the zygotic mRNAs (green) starts. At the 2-cell stage of the embryo, a second wave of transcription is observed and the final levels of zygotic mRNAs are reached at the blastocyst stage (not shown). Figure inspired by Eckersley-Maslin *et al.* [40].

Meiosis

Separation of chromosomes

Every eukaryotic cell contains a certain number of chromosomes. In sexually reproducing eukaryotes, half of these chromosomes were given by the mother's oocyte, the other half by the father's sperm. In humans, there are a total of 46 chromosomes, 44 so-called autosomes and two sex chromosomes which define the sex of the individual. Cells need to divide without losing genetic information. Since the amount of genetic material remains the same between offspring and parents, an equal number of chromosomes must be inherited to the offspring. As the simple combination of all chromosomes from both parents would lead to accumulation of genetic material over time, the number of chromosomes in the oocyte as well as in the spermatogonial stem cell (the progenitor of sperm cells) must be divided in half before fertilization takes place. The reduction of chromosomes is an ultimate requirement for successful sexual reproduction. Meiosis is the process dedicated to halving the set of chromosomes. To accomplish this, chromosomes are organized as bivalents which pairs of homologous chromosomes. Homologous chromosomes are chromosomes that share the same structural features and have the same genes in the same loci. Each chromosome is a pair of two sister chromatids – exact copies that are generated during the S phase of the cell cycle. In meiosis I, the bivalents are separated, in meiosis II, the sister chromatids are separated. After the oocyte and the sperm fuse, the cell is called zygote. The zygote develops into an embryo and consists of the full set of chromosomes. When cells divide, e.g. during growth of an organism, a process called mitosis takes place to separate these sister chromatids from each other.

Stages of meiosis

Meiosis can be divided into several steps, starting with the pairing of chromosomes. The initial maturation during prophase is divided into 5 stages (Fig. 3A). Firstly, the leptotene stage marks the start of prophase during which the homologs pair. The leptotene stage is followed by the zygotene stage, the phase when the synaptomenal complex is formed. Afterwards, the pachytene stage takes place, marked by the full synapsis of homologs. After the end of the pachytene stage, the diplotene stage is the phase in which the chiasmata, physical links between the homologous chromosomes at the site of the recombination, are visible[41]. The final stage of prophase in which the chromosomes further condense is called the diakinesis stage.

In more detail, axial elements are loaded onto the chromosomes and double strand breaks are introduced. This is the stage of leptotene, which is followed by zygotene, in which the lateral element binds to the axial element, forming the synaptonymal complex, a structure which aligns the homologous chromosomes and brings them in close contact over their full length. After this step, homologous chromosomes are observed under a light microscope as dense objects[42]. In the period of pachytene, double strand breaks are repaired and crossing-over sites are generated. This happens multiple times and in the end, a few crossovers remain[43]. When the synaptomenal complex is removed during the diplotene stages, these crossover sites, called chiasmata become visible. In case of an oocyte, the cell remains at that stage during this so-called prophase I arrest or dictyate for decades, until they are reactivated by hormonal changes that happen during menstrual cyclc eas a female enters puberty[44]. In the menstrual cycle, the luteinizing hormone (LH) is secreted. LH causes the cAMP levels in oocytes to decrease and initiates the resumption of meiosis[45]. Upon resumption of meiosis, the last prophase stage called diakinesis starts. Diakinesis results in maximal condensation of the chromosomes. Simultaneously, nuclear envelope breakdown (NEBD), also called germinal vesicle breakdown (GVBD) happens and, in certain species like humans or pigs, an actin mesh is pulled around the chromosomes (Harasimov *et al.*; data not published). At the same time as the GVBD takes place, the spindle starts to form (Fig. 3B). During prometaphase, proteins are loaded onto the centromeres, forming kinetochores and microtubules bind to them. In this phase, the spindle is established and is highly instable in humans until a stable bipolar spindle is formed in metaphase[46]. Now, the chromosomes line up on the metaphase plate. Only when the spindle assembly checkpoint (SAC) is activated by the anaphase promoting complex (APC), the cell enters anaphase. Upon entry into anaphase, separase cleaves Rec8, a part of cohesin, and the meiosis-specific homolog of Rad21, leading to the separation of the homologous chromosomes in anaphase. The chromosomes are pulled towards the two ends of the spindle by combined actions of kinesins and dyneines[47,48]. As the chromosomes separate, a subcortical actin ring is formed: the contractile ring, which divides the cytoplasm and the separated chromosomes into two individual cells[49]. The corresponding process is termed cytokinesis. In meiosis, metaphase II starts immediately. In case of oocytes, cytokinesis does not divide the cell symmetrically but extrudes a minimal fraction of the cytoplasm as so-called polar body and an egg which retains most of its volume. The reason for this is that the oocyte must provide all the nutrients, energy and developmental factors until its implantation into the uterus. Sperm cells are tiny compared to oocytes and during fertilization, they lose their membrane and almost their entire cytoplasm, providing only their own genetic material. The polar body of an oocyte lacks important factors and thus does not contribute to meiosis II, in contrast to

spermatocytes, which induce entry into anaphase II when they fuse with the egg. In the beginning of metaphase II, the spindle rearranges and the microtubules again bind to the kinetochores and arrange the chromosomes on the metaphase II plate. In anaphase II, the sister chromatids are pulled into opposite directions. For the transition between metaphase II and anaphase II, the remaining cohesin must be cleaved. This fraction is protected by shugoshin during anaphase I. Shugoshin, the Japanese term for "guardian spirit", binds to REC8 and recruits the phosphatase PP2A, which keeps Rec8 unphosphorylated and thereby prevents cleavage by separase. Separase is recruited by the anaphase promoting complex (APC) and cleaves Rec8. Thus, cohesin is released from the chrmosomes[50]. During telophase II and the second cytokinesis, a second polar body is generated. It is important to mention that anaphase II in mammalian oocytes only takes place after fertilization. This means, meiosis in oocytes is only finished when the egg is fertilized.

Meiosis and mitosis

Meiosis and mitosis are processes designed to separate chromosomes[51]. Mitosis segregates sister chromatids equally into daughter cells and preserves their genetic content. Meiosis additionally segregates homologous chromosomes and thereby reduces the genetic information. Mammalian meiosis is therefore a two-step process. Together with fertilization, meiosis enables sexual reproduction[52,53].

The separation of chromosomes is no simple task. Meiosis might have evolved from mitosis as the structural and molecular similarities suggest. Mitosis is the process of the separation of sister chromatids in somatic cells[54].

Meiosis and mitosis both rely on the spindle. The spindle is a structured assembly of microtubules. During meiosis and mitosis, the spindle forms a bipolar shape. Some microtubules bind to the chromosomes and align them. At a certain point of both meiosis and mitosis, all chromosomes are aligned in the center of the spindle. In meiosis I, the spindle separates homologous chromosomes. In meiosis II and mitosis, the spindle separates sister chromatids. The attachment of microtubules to chromosomes is mediated by the kinetochores. Kinetochores are protein complexes that assemble on centromeres. Centromeres are regions on the chromosomes that are dedicated to the assembly of kinetochores.

Oocytes and eggs

Eggs are produced by females. Mammals contain eggs with a haploid set of chromosomes and the purpose of eggs is to form a new organism upon fertilization by its male counterpart, the sperm cell[55,56]. Eggs develop from progenitor cells, the oocytes, and mature into an embryo upon fertilization. Oocytes are located in the ovarian tissue of female mammals and develop during the embryonal phase. Once the female is born, the oocytes remain in the ovarian tissue until maturation is initiated. When an oocyte has matured into an egg, the egg is released into the fallopian tube during ovulation. Upon fusion of a sperm cell with an egg, fertilization is completed and the fertilized egg, which is now called a zygote, is transported further down the fallopian tube while the embryo expands by cell divison[57]. After about 6 rounds of cell divisions, the embryo reaches the blastocyst stage (60 – 250 cells) and implantation into the uterine epithelium takes place[58,59]. After implantation, further cell divisions drive the development and

growth of the embryo. At the point of fertilization, the zygote bears the genetic material from both parents.

Maternal age effect

In meiosis, homologous chromosomes and sister chromatids are separated and equally distributed among the daughter cells. In each daughter cell, precisely one copy of each chromosome remains. However, oocytes cope with further requirements compared to the male counterpart: While spermatozoa are continuously generated from stem cells, the pool of oocytes in a female is created only once during embryogenesis[60]. Thereafter, the number of oocytes decreases continuously over the lifetime of the individual[61]. Human females are fertile until an average age of 47 years, marked by the onset of the menopause. Until then, oocytes have to sustain integrity and the ability to undergo meiosis for a very long time[27,62,63]. While women age, the women's fertility declines. Moreover, the prevalence of genetic disorders increases with the age of the respective woman. Especially trisomies (three copies of one chromosome) and monosomies (one copy of one chromosome) are found in children of women that are at an advanced age during the conception (Fig. 4A)[64]. Oocytes also lack centrosomes which makes them different from sperm and somatic cells in humans. Without centrosomes, the spindle is more instable during its formation and allows the loss of chromosomes[46,65]. The term "maternal age effect" was first mentioned by Penrose in 1933. Thereafter the existence of the maternal age effect was underlined as a correlation between increasing age of women and births of children with genetic disorders was found[66,67]. Later on, the chances of aneuploidies in the oocytes were shown to increase with increased maternal age. Aneuploidy is defined as the state in which a cell contains an aberrant number of chromosomes that is not a multiple of the normal set[68–70].

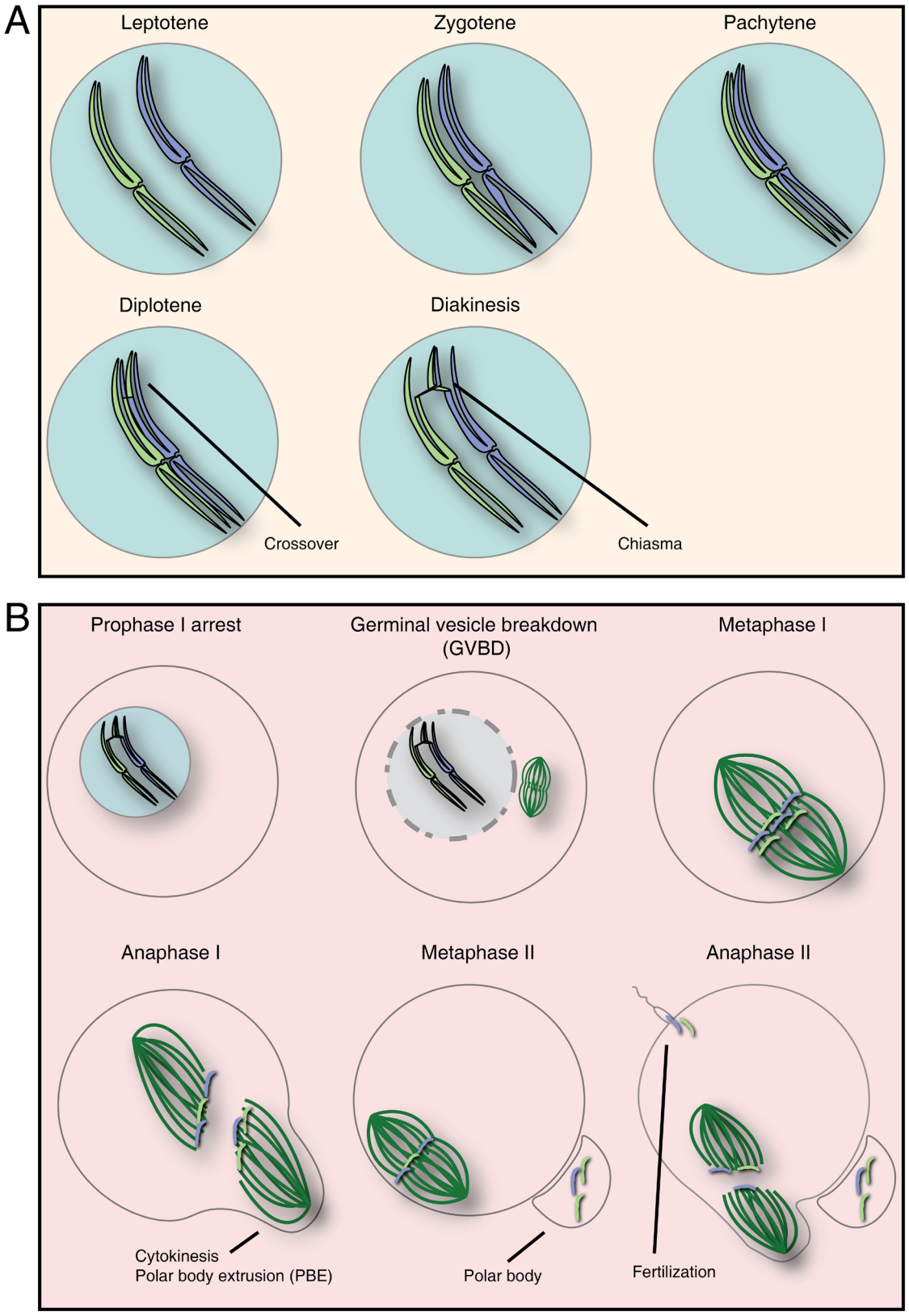

Fig. 3 Oocyte maturation transforms germ cells with 2N into eggs with 1N and genetic diversity. (A) Early maturation of germ cells. In leptotene, the chromosomes condense. In zygotene, the synaptomenal complex (SC) is formed between the homologous chromosomes. The SC acts as a zipper and brings the homologous chromosomes in vicinity of each other. In pachytene, the SC formation is finished and the homologous chromosomes touch on their full length. In diplotene, crossover events are introduced by double strand breaks (DSBs) of the DNA. During the

repair of the DSBs, some genetic regions are swapped between the chromosomes. In diakinesis, the SC disassembles and the final crossover sites are visible as so-called chiasmata. The oocytes are now on Prophase I arrest. (B) Upon hormonal induction, oocytes re-enter meiosis. After the final compaction of the chromosomes, the nuclear envelope disassembles, a process called germinal vesicle breakdown (GVBD). The spindle is formed simultaneously. The chromosomes are captured by the spindle and re-arranged into a plate. The corresponding stage is called metaphase I and it is followed by the anaphase I, the moment in which the chromosomes separate. In anaphase I, homologous chromosomes are separated. One half of the chromosomes is extruded into a polar body by cytokinesis. The polar body is later degraded. The chromosomes that remain in the oocyte are rearranged in the metaphase II spindle. The oocyte enters the metaphase II arrest from which it is released upon fertilization by a sperm cell. In anaphase II, the sister chromatids are separated similarly to a mitotic segregation.

Aneuploidy

Phenotypical observations

There are several types of aneuploidy that have different causes and mechanistic pathways (Fig. 4C)[71,72]. The different types are:

1. Nondisjunction

Nondisjunction is characterized by the failure of two homologous chromosomes or two sister chromatids to separate[73]. Nondisjunction can happen in anaphase I and II. It was found to happen with higher chances when the recombination sites (chiasmata) are either located close to the centromeres or at a distal position on the chromosome arms or when recombination has not occured[69]. It is speculated that chiasmata participate in the discrimination between tension forces of bipolar attachments (one kinetochore attached to both spindle poles) and monopolar (correct) attachments[74]. During a nondisjunction event in anaphase I, both homologous chromosomes are pulled to one spindle pole together. Even if the correct separation of sister chromatids is error-free in MII, the oocyte remains with either an n + 1 or n – 1 karyotype in respect to this chromosome. Alternatively, MI correctly separates both homologous chromosomes but the pair of sister chromatids is not separated during MII, resulting again in either an n + 1 or n – 1 karyotype[27]. Nondisjunction is the major cause of Trisomy 21[75].

2. PSSC

While for nondisjunction, homologous chromosomes or the sister chromatids do not separate, pre-mature separation of sister chromatid (PSSC) happens when sister chromatids separate before the onset of meiosis I, pulling them in opposite directions of the spindle. In case of the so-called reverse segregation, the homologous chromosomes are turned 90° compared to the other chromosome pairs along the metaphase plate axis and opposite microtubules attach to the kinetochores of the sister chromatids instead of those of the homologous chromosomes[71,76]. Microtubules do not discriminate between kinetochores of sister chromatids and can bind to any kinetochore structure. However, the arrangement of chromosomes on the metaphase plate is highly optimized to avoid erroneous microtubule-kinetochore-attachments. When the chromosomes are fully condensed in pro-metaphase, cohesin keeps both homologous chromosomes and sister chromatids together. The kinetochores of sister chromatids are in close proximity of each other and act as a single kinetochore whereas these "kinetochore pairs" of both homologous chromosomes face into opposite directions. When the chromosomes are aligned on the metaphase plate, the spindle pulls the two kinetochore pairs away from one another. The net force between the sister chromatids is very low. The second mechanism is the well-orchestrated activity of separase and cohesin. Shugoshin protects a fraction of cohesin from being cleaved during meiosis I. The subfraction holds sister chromatids together. It is mainly loaded around the kinetochores of the sister chromatids and cause the sister kinetochores to act as a single kinetochore[77].

3. Reverse segregation

In case of reverse segregation, the kinetochore pairs split and rotate around the metaphase plate axis. The rotation causes the kinetochores of single sister chromatids to be attached to microtubules from opposite spindle poles and the subsequent missegregation of the erroneously[76].

While these phenotypical errors of meiosis are easily identifiable with modern microscopy techniques, the reasons for their occurrence are less easy to investigate. Taken together, aneuploidies seem to be caused by time-dependent mechanisms, as infertility and miscarriage rates increase with age in humans and mice.

Causes of aneuploidy

1. Cohesin loss

The most important findings can so far explain the maternal age effect at least regarding the decline of the quality of oocytes while humans age. Kinetochore splitting is one reason for impaired chromosome segregation. Strongly correlated with this is the pre-mature loss of cohesion. Before the separation in anaphase, the chromosomes are held together by cohesin. Cohesin is a ring-like protein which acts like a belt that holds the chromosomes together. When the chromosomes are separated, cohesin is cleaved. In the leptotene stage in meiosis I, an early stage of the oocyte development, the chromosomes are partly condensed and individualized[78]. At the same time, cohesin is loaded onto the chromosomes. There is no turnover or replacement of cohesin. Therefore, cohesin loaded onto the chromosomes stays there for decades in humans[79,80]. It consists of SMC1β, SMC3, RAD21/Rec8 and SA1/SA2 or SA3. SMC1β and SMC3 form two clamps, binding each other on one side and forming a closed circle with Rad21/Rec8 on the other side[80].

Any kind of damage is irreversible and leads to either dysfunction or disintegration of that structure[81]. Because an oocyte is a dynamic containment which harbors a multitude of chemical reactions, there is a certain stress on the integrity of proteins. Especially the mitochondrial reactions produce highly reactive side products, called reactive oxygen species. This causes oxidative stress, which accumulates over time.

2. Recombination failure

In pachytene, recombination takes place and chiasmata are formed. Not only do the crossovers serve to increase genetic diversity but these physical bonds also link homologous chromosomes together until anaphase I. However, specific patterns might lead to events of nondisjunction. For example, when crossover sites are close to the telomere ends of chromosomes and there is not sufficient force generated by distal arm cohesin, these chiasmata are lost[75]. It can also happen that no chiasmata are formed during pachytene[72]. It was found that 1 out of 10 chromosome pairs in oocytes show no chiasmata. While in sperm, there is a strict checkpoint that induces apoptosis, if there are one or several chromosomes without chiasmata, the corresponding checkpoint in oocytes is leaky[82].

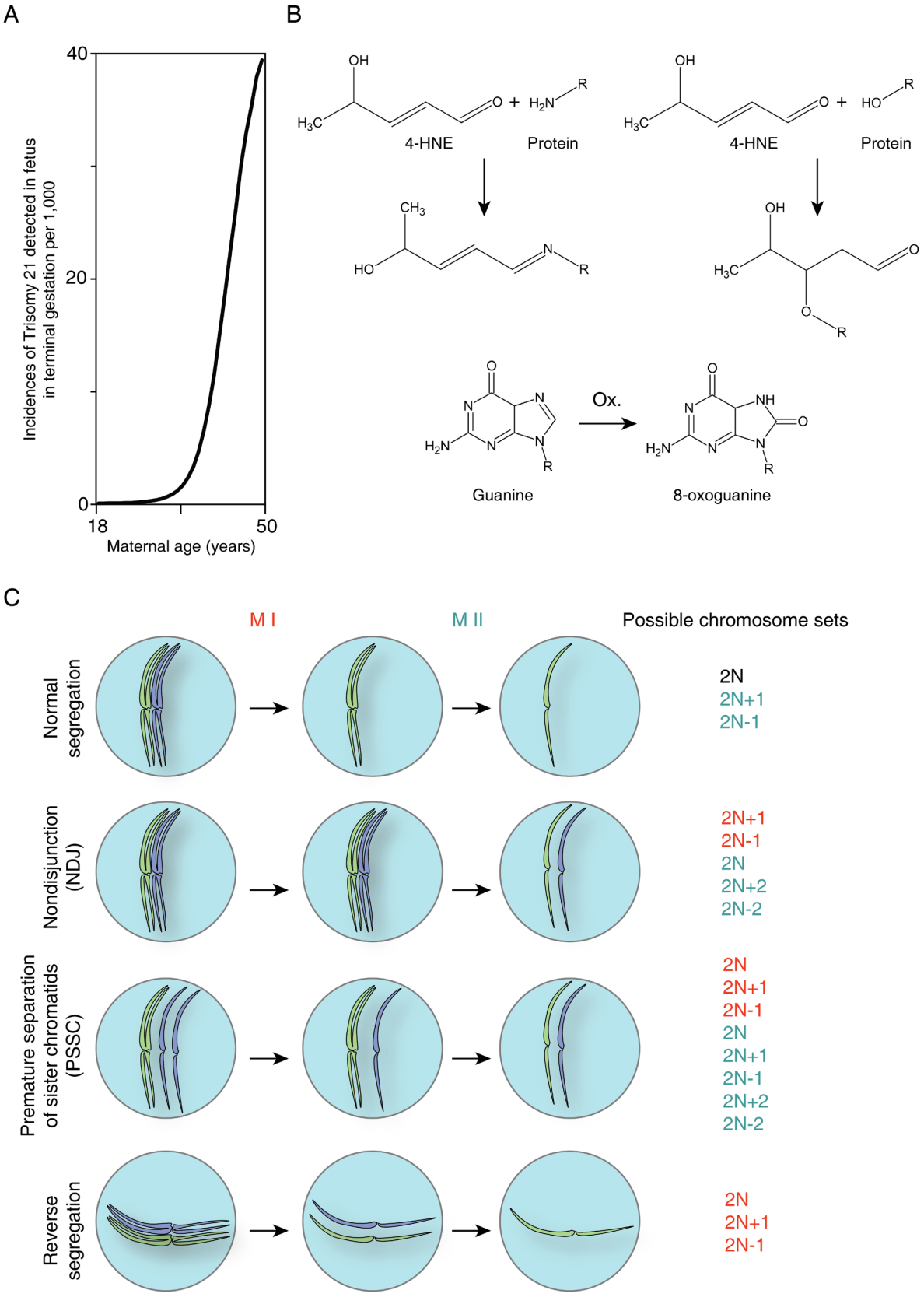

Fig. 4 The maternal age effect is caused partly by oxidative stress and leads to increased chanced of aneuploidy in oocytes from aged female mammals. (A) A plot that shows the correlation between the age of a human female at the point of impregnation (x axis) and the number of incidences in which the fetus was identified as trisomic for chromosome 21 (Down Syndrome) during the terminal gestation period per 1,000 (y axis). Data was used from multiple studies[83–87]. (B) Reactions enhanced by reactive oxygen species (ROS). Lipid can be oxidized by ROS into

lipid peroxides and lipid aldehydes. 4-hydroxynonenal (4-HNE) is the aldehyde of nonenal. Its reacts with free amine and hydroxyl groups that are primarily found in proteins. By a Schiff's base formation (left reaction) or Michael addition (right reaction), it forms an adduct with the protein and alters its function and stability[88]. ROS also modify nucleic acid molecules. Guanine is oxidized into 8-oxoguanine (8-oxoG). 8-oxoG has altered interactions with the other bases and leads to mutations. 8-oxoG and 4-HNE can be used as markers for oxidative stress. (C) When female mammals age, (oxidative) damage accumulates and the cohesion forces between the chromosomes decline. As a result, chromosome segregation becomes more prone to errors. The major events are nondisjunction (NDJ), premature separation of sister chromatids (PSSC) and reverse segregation[71]. Error can occur in both meiotic steps (M I and M II)[89]. In case of a normal segregation, the resulting oocyte has a chromosome set of 2N. Errors in M I (red) can lead to one excessive or missing chromosome (e.g. chromosome 21). M II errors (blue) can additionally cause the loss or gain of two chromosomes. Notably, errors can cancel each other out and result in oocytes with a normal karyotype. Yet, it is also possible that the errors involve different chromosomes, for example the loss of one X chromosome and the gain of an additional chromosome 21.

3. Leaking Spindle Assembly Checkpoint (SAC)

Anaphase is the process during which cohesin is degraded and chromosomes are separated: the homologous chromosomes in meiosis I and the sister chromatids in mitosis and meiosis II. Anaphase is controlled by the so-called spindle assembly checkpoint (SAC). The SAC is a checkpoint which collects information about the binding of kinetochores to microtubules and controls the output by suppressing the anaphase promoting complex/cyclosome (APC/C), an E3 ubiquitin ligase. The APC/C, once activated, initiates the degradation of cyclin B and securin. Securin is the inhibitor of separase[27,90].

When the spindle is formed, the microtubule ends are nucleated and stabilized in the proximity of chromosomes[91]. This is achieved by a RanGTP gradient, generated by RCC1, which is located on the chromosomes. Most of the microtubules of the meiotic spindle do not bind kinetochores but will eventually align with fibers from the other pole[9]. Microtubules that bind kinetochores, are very stable as shown in a method called the cold-stable assay, where cells are placed on ice for a few minutes. At cold temperatures, the balance of growth and decay of the (+)-ends of microtubules is shifted towards depolymerization. Microtubules that are still visible after this treatment are called kinetochore fibres (k-fibres)[92]. Only if all kinetochores are "saturated" with k-fibres, certain SAC factors, which otherwise bind unbound kinetochores, are released and contribute to the signal for the APC/C. However, this mechanism shows low fidelity in meiotic cells, allowing meiosis to continue even with one or few kinetochores unattached[93,94]. Since the checkpoint are rather weak in oocytes, there are chances that cytokinesis and telophase take place with the entire chromosome pair either inside the cell or the polar body[71]. Moreover, as a consequence of growing oxidative stress, the expression of SAC components seems to decrease with a females' age, increasing the chances of promoting anaphase prematurely[72].

4. Mitochondrial dysfunction

Mitochondria produce reactive oxygen species (ROS). ROS diffuse freely through the cytoplasm and are capable of oxidizing a wide range of biochemical compounds. Most importantly, the reaction of ROS with DNA has a high potential to cause damage. This characteristic is of special interest for cancer research, because cancer cells show a high metabolism, consuming extraordinarily amounts of glucose and oxygen. Therefore, ROS levels are high in cancer cells and it was previously shown that high ROS levels contribute to a positive feedback loop of

DNA damage and further mutations, which eventually also turns a benign tumor into a malign tumor.

Oocytes consume high amounts of energy. High energy is required as the size of oocytes correlates with the total amount of proteins and metabolites, which require a steady, energy intensive turnover as well as for the process of meiosis. To cover the necessary amount of ATP, oocytes are equipped with a proportionally high amount of mitochondria. The highest concentration of mitochondria can be observed around the spindle during both phases of meiosis[95–97]. Oocytes show DNA damage, too. As mammalian females age, oxidative stress and DNA damage in the oocytes increase[98].

Furthermore, it was shown that the expression of DNA repair genes decreases while females age[99]. This is in line with the decreased expression of SAC proteins and highlights again that not only the probability and severity of damage increases over time but that simultaneously, the cell's ability to counteract and repair DNA damage decreases.

Another factor is the DNA damage inside the mitochondria itself. It is commonly accepted that mitochondria are exclusively inherited by the mother since most of the sperm mitochondria do not enter the ooplasm. Those sperm mitochondria that are released into the ooplasm upon fertilization, are degraded upon entry[100–102]. It was shown that when oocytes age, the copy number as well as the mtDNA integrity decrease[103]. There are several mitochondria-associated diseases, which are caused by mutations in mitochondrially encoded genes, e.g. gastrointestinal pseudo-obstruction, coenzyme Q10 deficiency or ophthalmologic diseases such as retinal dystrophy, Leigh syndrome or myopathy[104]. Most of these cannot be treated by medication. Moreover, genetic analysis of the mitochondrial genetic integrity is no common practice in IVF clinics yet. The only currently available solution in most countries for humans harboring genetic disorders related to mitochondria is to adopt in case they want to have a child. Two techniques allow to replace the mitochondrial pool of an oocyte: spindle transfer and pronuclear transfer. For spindle transfer, the metaphase II spindle is removed from the patient's egg and transferred into a donor egg. The donor egg is donated by a healthy person and its metaphase II spindle is discarded before the injection of the patient's spindle. The egg with chromosomes from the patient and mtDNA from the donor is then fertilized. Alternatively, the patient's egg is first fertilized. After fertilization, the female and the male chromosomes form respective pronuclei. Both pronuclei are transferred into a donor zygote. Before the pronuclei of the patient's zygote are transferred, the pronuclei of the donor's zygote are removed. Both techniques allow the transfer of nuclear genetic material into a cell that contains mitochondria without disorder-associated mutations[105]. Spindle transfer and pronuclear transfer can be used as mitochondria replacement therapies (MRT) and are legalized in a few countries, e.g. in the UK[106]. First successful live births are reported upon spindle transfer in human oocytes[107]. The offspring indeed does not show signs of associated genetic disorders despite the heteroplasmy[105]. Therefore, MRTs seem to be the most promising technique for the treatment of mitochondrial diseases, but so far, there are still problems that have yet to be overcome, for example an encompassing removal of all mitochondria associated to the patient's spindle.

Unfortunately, "bad" mitochondria harboring mutations that cause diseases are thought to also have better propagation chances (i.e. genetic drift within a few generations due to the extensive splitting of the mitochondrial pool during early embryogenesis)[108]. Unequal propagation chances imply that very few mutated mitochondria in an oocyte (e.g.

after spindle transfer from a female having mitochondrial associated diseases to a donor oocyte from a healthy person) are able to cause diseases in the child[102,109–111].

Not only do high ROS levels affect DNA (and RNA) integrity but ROS are also capable of oxidizing proteins and lipids (Fig. 4B). Lipid aldehydes, side products of fatty acid β oxidation (FAO), are able to form adducts with any kind of protein. It was shown that certain lipid aldehydes, such as 4-HNE, accumulate in aged oocytes. Lipid aldehydes were shown to react with free amine and hydroxyl groups of proteins and to form adducts. The upper reactions in Fig. 4B illustrate the adduct formation. As one of the consequences, polar body extrusion rates decrease[112]. Even more delicate is the direct oxidation of cohesin by ROS, which also increases the chance of chromosome missegregation, although the impact is moderate[113].

Apart from the implications of ROS on oocytes and meiosis, there is evidence for the correlation between increasing ROS levels and several diseases of the female reproduction system, e.g. endometriosis, as well as implications during pregnancy[114].

5. Missing MTOCs

Centrosomes consist of a pair of centrioles. After each somatic cell division, one centriole ends up in each of the daughter cells and duplicates during interphase. For the next mitotic division, the two centrioles act, together with other factors, as microtubule-organizing center (MTOC) since it nucleates microtubules and binds to the (-)-end. Upon nuclear envelope breakdown, the centrosome splits, creating the typical shape of a mitotic spindle as shown in Fig. 1.

However, for mouse oocytes, which do not contain centrosomes, aMTOCs were shown to form during meiosis, causing a highly dynamic rearrangement of the spindle until it becomes stabilized in its bipolar form[115]. Human oocytes lack both centrosomes and aMTOCs. The absence of MTOCs causes the round shape of human meiotic spindles[9]. For humans, the spindle is highly unstable and loses bipolarity multiple times before it forms a stable spindle[116]. For a long time, the reason for this spindle instability remained unknown. It was shown recently that it is caused by the lack of the motor protein KIFC1 in human oocytes. It has been shown that in KIFC1-depleted systems that normally contain the protein, spindle instability increases significantly, mimicking the spindle instability observed in humans. In humans, this spindle instability frequently leads to the formation of tripolar spindles and subsequent tripolar segregation. Tripolar segregation of chromosomes causes aneuploidy (So *et al.*, accepted manuscript). Therefore, there is a certain probability that chromosomes become lost or attached to microtubules in an incorrect manner, which leads to the inability to segregate during anaphase.

Implications of aneuploidy

While the worldwide mean age of women at childbearing lowered from 29 years in the 1950s to 27.5 years in the 2010s, the opposite trend is observed in the global north. For North America, the mean age increases from 26 years to 28.75 in the same period of time[117]. This trend is very strong and it can be expected that the mean age of childbearing will exceed 30 years for the northern hemisphere in less than 10 years. As explained in detail above, maternal age has a tremendous effect on the health of the newborn child but also on the success of pregnancy overall. While assisted reproductive technology (ART) is debated in regard to overpopulation and its consequences, fertility clinics allow a high degree of self-determination[118,119]. By doing research on the causes of aneuploidy, we are gaining a better understanding of one of the most complex mechanisms in mammalian cells. Many genetic disorders and even cancer are linked to aneuploidy[69,120]. 0.3% of all newborn children have detectable aneuploidies, one third of all spontaneous abortions in humans are related to a pathological karyotype and up to 70% of all analyzed oocytes and preimplantation embryos show chromosomal defects[82]. Thereby, almost half of all women that were pregnant experience spontaneous abortion at least once in their life according to a study in Israel[121]. Therefore, both more research and higher awareness are required to better understand the reasons and the consequences of aneuploidy.

Summary of the thesis

In this thesis, a novel membraneless structure is described that accumulates mitochondria and maternal mRNAs, making it similar to the Balbiani body. Yet, it contains other RNA binding proteins. It is stable until the onset of meiosis, when the structure dissolves. In contrast to the Balbiani body, it is assembled during the growth of oocytes. Overall, it might be that in mammalian oocytes this specific structure, called MARDO, replaces the Balbiani body after the initial stage, acting as a storage compartment for maternal mRNAs and mitochondria. In contrast to the Balbiani body, this structure could be adapted for the prolonged time of dormancy, which – in contrast to other species – can last for decades in mammals.

Second, I will present how this structure is important for the regulation of mitochondrial activity and ROS levels by indirectly controlling the export of fatty acids from lipid droplets, showing the implication of this structure in the overall metabolism of mammalian oocytes and acting as an example for the regulation of maternal mRNAs.
Oxidative stress is one of the factors that lead to aneuploidy. As the respective oxidative damage accumulates in oocytes, I wanted to develop a method that can correct aneuploidies.

Therefore, I will present a method that allows precise manipulation of chromosomes within oocytes in the third part. To enable artificial manipulation, I developed the base for a replacement of the biological spindle, which enables both the detailed study of generation of aneuploidies and the cells reactions as well as further research to build a tool that one day might be used in assisted reproductive medicine in order to ensure successful fertilization of healthy eggs.

References

1. So, C., Cheng, S. & Schuh, M. Phase Separation during Germline Development. *Trends Cell Biol.* **31**, 254–268 (2021).
2. Frey-Wyssling, A. Concerning the concept 'organelle'. *Experientia* **34**, 547–547 (1978).
3. FLEMING, W. N. & SAACKE, R. G. FINE STRUCTURE OF THE BOVINE OOCYTE FROM THE MATURE GRAAFIAN FOLLICLE. *Reproduction* **29**, 203–213 (1972).
4. Anderson, E. & Beams, H. W. Cytological observations on the fine structure of the guinea pig ovary with special reference to the oogonium, primary oocyte and associated follicle cells. *J. Ultrastruct. Res.* **3**, 432–446 (1960).
5. Pederson, T. The Nucleolus. *Cold Spring Harb. Perspect. Biol.* **3**, a000638–a000638 (2011).
6. Lafontaine, D. L. J. Birth of Nucleolar Compartments: Phase Separation-Driven Ribosomal RNA Sorting and Processing. *Molecular Cell* vol. 76 694–696 (2019).
7. CHOUINARD, L. A. A Light- And Electron-Microscope Study of the Nucleolus During Growth of the Oocyte in the Prepubertal Mouse. *J. Cell Sci.* **9**, 637–663 (1971).
8. So, C. *et al.* A liquid-like spindle domain promotes acentrosomal spindle assembly in mammalian oocytes. *Science (80-.).* **364**, (2019).
9. Bennabi, I., Terret, M.-E. & Verlhac, M.-H. Meiotic spindle assembly and chromosome segregation in oocytes. *J. Cell Biol.* **215**, 611–619 (2016).
10. Winata, C. L. & Korzh, V. The translational regulation of maternal <scp>mRNA</scp> s in time and space. *FEBS Lett.* **592**, 3007–3023 (2018).
11. Flemr, M., Ma, J., Schultz, R. M. & Svoboda, P. P-Body Loss Is Concomitant with Formation of a Messenger RNA Storage Domain in Mouse Oocytes1. *Biol. Reprod.* **82**, 1008–1017 (2010).
12. Yang, E. *et al.* Decay Rates of Human mRNAs: Correlation With Functional Characteristics and Sequence Attributes. *Genome Res.* **13**, 1863–1872 (2003).
13. Kumari, P. *et al.* An essential role for maternal control of Nodal signaling. *Elife* **2**, (2013).
14. Jalkanen, A. L., Coleman, S. J. & Wilusz, J. Determinants and implications of mRNA poly(A) tail size – Does this protein make my tail look big? *Semin. Cell Dev. Biol.* **34**, 24–32 (2014).
15. Cabral, S. E. & Mowry, K. L. Organizing the oocyte: RNA localization meets phase separation. in 87–118 (2020). doi:10.1016/bs.ctdb.2020.02.007.
16. Boke, E. & Mitchison, T. J. The balbiani body and the concept of physiological amyloids. *Cell Cycle* **16**, 153–154 (2017).

17. Comert, F. & Dubin, P. L. Liquid-liquid and liquid-solid phase separation in protein-polyelectrolyte systems. *Adv. Colloid Interface Sci.* **239**, 213–217 (2017).

18. Kogo, N. *et al.* Germ-line mitochondria exhibit suppressed respiratory activity to support their accurate transmission to the next generation. *Dev. Biol.* **349**, 462–469 (2011).

19. Pepling, M. E., Wilhelm, J. E., O'Hara, A. L., Gephardt, G. W. & Spradling, A. C. Mouse oocytes within germ cell cysts and primordial follicles contain a Balbiani body. *Proc. Natl. Acad. Sci.* **104**, 187–192 (2007).

20. Kawasaki, I. *et al.* The PGL Family Proteins Associate With Germ Granules and Function Redundantly in Caenorhabditis elegans Germline Development. *Genetics* **167**, 645–661 (2004).

21. Wang, J. T. & Seydoux, G. P granules. *Curr. Biol.* **24**, R637–R638 (2014).

22. Brangwynne, C. P. *et al.* Germline P Granules Are Liquid Droplets That Localize by Controlled Dissolution/Condensation. *Science (80-.).* **324**, 1729–1732 (2009).

23. Luo, Y., Na, Z. & Slavoff, S. A. P-Bodies: Composition, Properties, and Functions. *Biochemistry* **57**, 2424–2431 (2018).

24. Brengues, M., Teixeira, D. & Parker, R. Movement of Eukaryotic mRNAs Between Polysomes and Cytoplasmic Processing Bodies. *Science (80-.).* **310**, 486–489 (2005).

25. Franks, T. M. & Lykke-Andersen, J. The Control of mRNA Decapping and P-Body Formation. *Mol. Cell* **32**, 605–615 (2008).

26. Parker, R. & Sheth, U. P Bodies and the Control of mRNA Translation and Degradation. *Mol. Cell* **25**, 635–646 (2007).

27. Alberts, B. *et al. Molecular Biology of the Cell*. (W.W. Norton & Company, 2017). doi:10.1201/9781315735368.

28. Eulalio, A., Behm-Ansmant, I., Schweizer, D. & Izaurralde, E. P-Body Formation Is a Consequence, Not the Cause, of RNA-Mediated Gene Silencing. *Mol. Cell. Biol.* **27**, 3970–3981 (2007).

29. TEIXEIRA, D., SHETH, U., VALENCIA-SANCHEZ, M. A., BRENGUES, M. & PARKER, R. Processing bodies require RNA for assembly and contain nontranslating mRNAs. *RNA* **11**, 371–382 (2005).

30. Kedersha, N. *et al.* Stress granules and processing bodies are dynamically linked sites of mRNP remodeling. *J. Cell Biol.* **169**, 871–884 (2005).

31. Bollig, F. *et al.* Evidence for general stabilization of mRNAs in response to UV light. *Eur. J. Biochem.* **269**, 5830–5839 (2002).

32. Kawai, T., Fan, J., Mazan-Mamczarz, K. & Gorospe, M. Global mRNA Stabilization Preferentially Linked to Translational Repression during the Endoplasmic Reticulum Stress Response. *Mol. Cell. Biol.* **24**, 6773–6787 (2004).

33. Oriola, D., Jülicher, F. & Brugués, J. Active forces shape the metaphase spindle through a mechanical instability. *Proc. Natl. Acad. Sci. U. S. A.* **117**, 16154–16159 (2020).

34. Ong, J. Y. & Torres, J. Z. Phase Separation in Cell Division. *Mol. Cell* **80**, 9–20 (2020).

35. Wang, X., Baumann, C., De La Fuente, R. & Viveiros, M. M. CEP215 and AURKA regulate spindle pole focusing and aMTOC organization in mouse oocytes. *Reproduction* **159**, 261–274 (2020).

36. Hinchcliffe, E. H. Centrosomes and the Art of Mitotic Spindle Maintenance. in *International Review of Cell and Molecular Biology* vol. 313 179–217 (Elsevier Inc., 2014).

37. Sprunger, M. L. & Jackrel, M. E. Prion-Like Proteins in Phase Separation and Their Link to Disease. *Biomolecules* **11**, 1014 (2021).

38. Boke, E. *et al.* Amyloid-like Self-Assembly of a Cellular Compartment. *Cell* **166**, 637–650 (2016).

39. Kloc, M., Jedrzejowska, I., Tworzydlo, W. & Bilinski, S. M. Balbiani body, nuage and sponge bodies – The germ plasm pathway players. *Arthropod Struct. Dev.* **43**, 341–348 (2014).

40. Eckersley-Maslin, M. A., Alda-Catalinas, C. & Reik, W. Dynamics of the epigenetic landscape during the maternal-to-zygotic transition. *Nat. Rev. Mol. Cell Biol.* **19**, 436–450 (2018).

41. Hirose, Y. *et al.* Chiasmata Promote Monopolar Attachment of Sister Chromatids and Their Co-Segregation toward the Proper Pole during Meiosis I. *PLoS Genet.* **7**, e1001329 (2011).

42. Fletcher, J. M. Light microscope analysis of meiotic prophase chromosomes by silver staining. *Chromosoma* **72**, 241–248 (1979).

43. Crismani, W. & Mercier, R. What limits meiotic crossovers? *Cell Cycle* **11**, 3527–3528 (2012).

44. Pan, B. & Li, J. The art of oocyte meiotic arrest regulation. *Reprod. Biol. Endocrinol.* **17**, 8 (2019).

45. Jaffe, L. A., Norris, R. P., Freudzon, M., Ratzan, W. J. & Mehlmann, L. M. Microinjection of Follicle-Enclosed Mouse Oocytes. in 157–173 (2009). doi:10.1007/978-1-59745-202-1_12.

46. Thomas, C., Cavazza, T. & Schuh, M. Aneuploidy in human eggs: contributions of the meiotic spindle. *Biochem. Soc. Trans.* **49**, 107–118 (2021).

47. Houghtaling, B. R., Yang, G., Matov, A., Danuser, G. & Kapoor, T. M. Op18 reveals the contribution of nonkinetochore microtubules to the dynamic organization of the vertebrate meiotic spindle. *Proc. Natl. Acad. Sci.* **106**,

15338–15343 (2009).

48. Gatlin, J. C. *et al.* Spindle Fusion Requires Dynein-Mediated Sliding of Oppositely Oriented Microtubules. *Curr. Biol.* **19**, 287–296 (2009).
49. Miller, A. L. The contractile ring. *Curr. Biol.* **21**, R976–R978 (2011).
50. Hellmuth, S., Böttger, F., Pan, C., Mann, M. & Stemmann, O. PP2A delays APC/C-dependent degradation of separase-associated but not free securin. *EMBO J.* **33**, 1134–1147 (2014).
51. Murray, A. W. & Szostak, J. W. Chromosome Segregation in Mitosis and Meiosis. *Annu. Rev. Cell Biol.* **1**, 289–315 (1985).
52. Ohkura, H. Meiosis: An Overview of Key Differences from Mitosis. *Cold Spring Harb. Perspect. Biol.* **7**, a015859 (2015).
53. Prosée, R. F., Wenda, J. M. & Steiner, F. A. Adaptations for centromere function in meiosis. *Essays Biochem.* **64**, 193–203 (2020).
54. Wilkins, A. S. & Holliday, R. The Evolution of Meiosis From Mitosis. *Genetics* **181**, 3–12 (2009).
55. Duncan, F. E. *et al.* Unscrambling the oocyte and the egg: clarifying terminology of the female gamete in mammals. *Mol. Hum. Reprod.* **26**, 797–800 (2020).
56. Boden, J., Hunt, J. & Williams, D. I. When (and what) is an egg? *Hum. Fertil.* **5**, 47–50 (2002).
57. Croxatto, H. B. Physiology of gamete and embryo transport through the Fallopian tube. *Reprod. Biomed. Online* **4**, 160–169 (2002).
58. Johnson, M. H. The Significance of Cell Polarity in Early Mammalian Development. in *Reference Module in Biomedical Sciences* (Elsevier, 2019). doi:10.1016/B978-0-12-801238-3.99504-7.
59. Ochota, M., Wojtasik, B. & Niżański, W. Total Cell Number and its Allocation to Trophectoderm and Inner Cell Mass in *In Vitro* Obtained Cats' Blastocysts. *Reprod. Domest. Anim.* **51**, 339–345 (2016).
60. Baker T G. A quantitative and cytological study of germ cells in human ovaries. *Proc. R. Soc. London. Ser. B. Biol. Sci.* **158**, 417–433 (1963).
61. MANDL, A. M. & ZUCKERMAN, S. THE RELATION OF AGE TO NUMBERS OF OOCYTES. *J. Endocrinol.* **7**, 190–193 (1951).
62. Yamamoto, T. *et al.* Effect of maternal age on the developmental competence and progression of nuclear maturation in bovine oocytes. *Mol. Reprod. Dev.* **77**, 595–604 (2010).
63. Herbert, M., Kalleas, D., Cooney, D., Lamb, M. & Lister, L. Meiosis and Maternal Aging: Insights from Aneuploid Oocytes and Trisomy Births. *Cold Spring Harb. Perspect. Biol.* **7**, a017970 (2015).

64. HASSOLD, T., JACOBS, P., KLINE, J., STEIN, Z. & WARBURTON, D. Effect of maternal age on autosomal trisomies. *Ann. Hum. Genet.* **44**, 29–36 (1980).

65. Namgoong, S. & Kim, N.-H. Meiotic spindle formation in mammalian oocytes: implications for human infertility. *Biol. Reprod.* **98**, 153–161 (2018).

66. Penrose, L. S. The relative effects of paternal and maternal age in mongolism. *J. Genet.* **88**, 9–14 (2009).

67. Gaulden, M. E. Maternal age effect: The enigma of Down syndrome and other trisomic conditions. *Mutat. Res. Genet. Toxicol.* **296**, 69–88 (1992).

68. Hassold, T. & Chiu, D. Maternal age-specific rates of numerical chromosome abnormalities with special reference to trisomy. *Hum. Genet.* **70**, 11–17 (1985).

69. Hassold, T. & Hunt, P. To err (meiotically) is human: the genesis of human aneuploidy. *Nat. Rev. Genet.* **2**, 280–291 (2001).

70. Holland, A. J. & Cleveland, D. W. Losing balance: the origin and impact of aneuploidy in cancer. *EMBO Rep.* **13**, 501–514 (2012).

71. Webster, A. & Schuh, M. Mechanisms of Aneuploidy in Human Eggs. *Trends in Cell Biology* vol. 27 55–68 (2017).

72. Mikwar, M., MacFarlane, A. J. & Marchetti, F. Mechanisms of oocyte aneuploidy associated with advanced maternal age. *Mutat. Res. Mutat. Res.* **785**, 108320 (2020).

73. Bridges, C. B. NON-DISJUNCTION AS PROOF OF THE CHROMOSOME THEORY OF HEREDITY. *Genetics* **1**, 1–52 (1916).

74. Moffatt, B. A. & Ashihara, H. Purine and Pyrimidine Nucleotide Synthesis and Metabolism. *Arab. B.* **1**, e0018 (2002).

75. MacLennan, M., Crichton, J. H., Playfoot, C. J. & Adams, I. R. Oocyte development, meiosis and aneuploidy. *Semin. Cell Dev. Biol.* **45**, 68–76 (2015).

76. Zielinska, A. P., Holubcova, Z., Blayney, M., Elder, K. & Schuh, M. Sister kinetochore splitting and precocious disintegration of bivalents could explain the maternal age effect. *Elife* **4**, (2015).

77. Clift, D. & Marston, A. L. The Role of Shugoshin in Meiotic Chromosome Segregation. *Cytogenet. Genome Res.* **133**, 234–242 (2011).

78. Zickler, D. & Kleckner, N. THE LEPTOTENE-ZYGOTENE TRANSITION OF MEIOSIS. *Annu. Rev. Genet.* **32**, 619–697 (1998).

79. Burkhardt, S. *et al.* Chromosome Cohesion Established by Rec8-Cohesin in Fetal Oocytes Is Maintained without Detectable Turnover in Oocytes Arrested for Months in Mice. *Curr. Biol.* **26**, 678–685 (2016).

80. Ishiguro, K. The cohesin complex in mammalian meiosis. *Genes to Cells* **24**, 6–30 (2019).

81. Krisko, A. & Radman, M. Protein damage, ageing and age-related diseases. *Open Biol.* **9**, 180249 (2019).

82. Nagaoka, S. I., Hassold, T. J. & Hunt, P. A. Human aneuploidy: mechanisms and new insights into an age-old problem. *Nat. Rev. Genet.* **13**, 493–504 (2012).

83. Maternal age-related risk common fetal trisomy across pregnancy - UpToDate. https://www.uptodate.com/contents/image?imageKey=OBGYN%2F75423&topicKey=OBGYN%2F5439&source=see_link.

84. Morris, J. K., Mutton, D. E. & Alberman, E. Revised estimates of the maternal age specific live birth prevalence of Down's syndrome. *J. Med. Screen.* **9**, 2–6 (2002).

85. Morris, J. K. & Savva, G. M. The risk of fetal loss following a prenatal diagnosis of trisomy 13 or trisomy 18. *Am. J. Med. Genet. Part A* **146A**, 827–832 (2008).

86. Savva, G. M., Morris, J. K., Mutton, D. E. & Alberman, E. Maternal age-specific fetal loss rates in Down syndrome pregnancies. *Prenat. Diagn.* **26**, 499–504 (2006).

87. Savva, G. M., Walker, K. & Morris, J. K. The maternal age-specific live birth prevalence of trisomies 13 and 18 compared to trisomy 21 (Down syndrome). *Prenat. Diagn.* **30**, 57–64 (2010).

88. Castro, J. P., Jung, T., Grune, T. & Siems, W. 4-Hydroxynonenal (HNE) modified proteins in metabolic diseases. *Free Radic. Biol. Med.* **111**, 309–315 (2017).

89. Tyc, K. M., McCoy, R. C., Schindler, K. & Xing, J. Mathematical modeling of human oocyte aneuploidy. *Proc. Natl. Acad. Sci.* **117**, 10455–10464 (2020).

90. Thomas, C. *et al.* A prometaphase mechanism of securin destruction is essential for meiotic progression in mouse oocytes. *Nat. Commun.* **12**, 4322 (2021).

91. Caudron, M., Bunt, G., Bastiaens, P. & Karsenti, E. Spatial Coordination of Spindle Assembly by Chromosome-Mediated Signaling Gradients. *Science (80-.).* **309**, 1373–1376 (2005).

92. Lane, S. I. R., Yun, Y. & Jones, K. T. Timing of anaphase-promoting complex activation in mouse oocytes is predicted by microtubule-kinetochore attachment but not by bivalent alignment or tension. *Development* **139**, 1947–1955 (2012).

93. Chiang, T., Schultz, R. M. & Lampson, M. A. Meiotic Origins of Maternal Age-Related Aneuploidy1. *Biol. Reprod.* **86**, (2012).

94. Lane, S. & Kauppi, L. Meiotic spindle assembly checkpoint and aneuploidy in males versus females. *Cell. Mol. Life Sci.* **76**, 1135–1150 (2019).

95. Bertram, R., Gram Pedersen, M., Luciani, D. S. & Sherman, A. A simplified model for mitochondrial ATP production. *J. Theor. Biol.* **243**, 575–586 (2006).

96. Yu, Y., Dumollard, R., Rossbach, A., Lai, F. A. & Swann, K. Redistribution of mitochondria leads to bursts of ATP production during spontaneous mouse

oocyte maturation. *J. Cell. Physiol.* **224**, 672–680 (2010).

97. Srinivas, U. S., Tan, B. W. Q., Vellayappan, B. A. & Jeyasekharan, A. D. ROS and the DNA damage response in cancer. *Redox Biol.* **25**, 101084 (2019).

98. Titus, S., Stobezki, R. & Oktay, K. Impaired DNA Repair as a Mechanism for Oocyte Aging: Is It Epigenetically Determined? *Semin. Reprod. Med.* **33**, 384–388 (2015).

99. Horta, F., Catt, S., Ramachandran, P., Vollenhoven, B. & Temple-Smith, P. Female ageing affects the DNA repair capacity of oocytes in IVF using a controlled model of sperm DNA damage in mice. *Hum. Reprod.* **35**, 529–544 (2020).

100. Giles, R. E., Blanc, H., Cann, H. M. & Wallace, D. C. Maternal inheritance of human mitochondrial DNA. *Proc. Natl. Acad. Sci.* **77**, 6715–6719 (1980).

101. Babayev, E. & Seli, E. Oocyte mitochondrial function and reproduction. *Curr. Opin. Obstet. Gynecol.* **27**, 175–181 (2015).

102. Yamada, M. *et al.* Mitochondrial replacement by genome transfer in human oocytes: Efficacy, concerns, and legality. *Reprod. Med. Biol.* **20**, 53–61 (2021).

103. Zhang, D., Keilty, D., Zhang, Z. F. & Chian, R. C. Mitochondria in oocyte aging: current understanding. *Facts, views Vis. ObGyn* **9**, 29–38 (2017).

104. Falk, M. J. & Sondheimer, N. Mitochondrial genetic diseases. *Curr. Opin. Pediatr.* **22**, 711–716 (2010).

105. Sharma, H. *et al.* Development of mitochondrial replacement therapy: A review. *Heliyon* vol. 6 (2020).

106. Castro, R. J. Mitochondrial replacement therapy: the UK and US regulatory landscapes. *J. Law Biosci.* **3**, 726–735 (2016).

107. Ishii, T. & Hibino, Y. Mitochondrial manipulation in fertility clinics: Regulation and responsibility. *Reprod. Biomed. Soc. Online* **5**, 93–109 (2018).

108. Klopstock, T., Klopstock, B. & Prokisch, H. Mitochondrial replacement approaches: challenges for clinical implementation. *Genome Med.* **8**, 126 (2016).

109. Gorman, G. S. *et al.* Prevalence of nuclear and mitochondrial <scp>DNA</scp> mutations related to adult mitochondrial disease. *Ann. Neurol.* **77**, 753–759 (2015).

110. Reznichenko, A., Huyser, C. & Pepper, M. Mitochondrial transfer: Implications for assisted reproductive technologies. *Appl. Transl. Genomics* **11**, 40–47 (2016).

111. Yamada, M., Akashi, K., Ooka, R., Miyado, K. & Akutsu, H. Mitochondrial Genetic Drift after Nuclear Transfer in Oocytes. *Int. J. Mol. Sci.* **21**, 5880 (2020).

112. Mihalas, B. P., De Iuliis, G. N., Redgrove, K. A., McLaughlin, E. A. & Nixon, B. The lipid peroxidation product 4-hydroxynonenal contributes to oxidative stress-

mediated deterioration of the ageing oocyte. *Sci. Rep.* **7**, 6247 (2017).

113. Perkins, A. T., Das, T. M., Panzera, L. C. & Bickel, S. E. Oxidative stress in oocytes during midprophase induces premature loss of cohesion and chromosome segregation errors. *Proc. Natl. Acad. Sci.* **113**, E6823–E6830 (2016).

114. Agarwal, A., Aponte-Mellado, A., Premkumar, B. J., Shaman, A. & Gupta, S. The effects of oxidative stress on female reproduction: a review. *Reprod. Biol. Endocrinol.* **10**, 49 (2012).

115. Schuh, M. & Ellenberg, J. Self-Organization of MTOCs Replaces Centrosome Function during Acentrosomal Spindle Assembly in Live Mouse Oocytes. *Cell* **130**, 484–498 (2007).

116. Holubcová, Z., Blayney, M., Elder, K. & Schuh, M. Error-prone chromosome-mediated spindle assembly favors chromosome segregation defects in human oocytes. *Science (80-.).* **348**, 1143–1147 (2015).

117. *World Fertility Report 2015*. moz-extension://07e9ca27-ef25-4fcb-8891-e6d42d543c8a/enhanced-reader.html?openApp&pdf=https%3A%2F%2Fwww.un.org%2Fen%2Fdevelopment%2Fdesa%2Fpopulation%2Fpublications%2Fpdf%2Ffertility%2Fwfr2015%2FworldFertilityReport2015.pdf.

118. Trevors, J. T. Total Abuse of the Earth: Human Overpopulation and Climate Change. *Water. Air. Soil Pollut.* **205**, 113–114 (2010).

119. Gupta, J. A. & Richters, A. Embodied Subjects and Fragmented Objects: Women's Bodies, Assisted Reproduction Technologies and the Right to Self-Determination. *J. Bioeth. Inq.* **5**, 239–249 (2008).

120. Salmina, K. *et al.* The Cancer Aneuploidy Paradox: In the Light of Evolution. *Genes (Basel).* **10**, 83 (2019).

121. Cohain, J. S., Buxbaum, R. E. & Mankuta, D. Spontaneous first trimester miscarriage rates per woman among parous women with 1 or more pregnancies of 24 weeks or more. *BMC Pregnancy Childbirth* **17**, 437 (2017).

A mitochondria-associated membraneless compartment governs the fate of maternal mRNAs in mammalian oocytes

Authors

Shiya Cheng[1]*, Gerrit Altmeppen[1]*, Chun So[1], Luisa Welp[2], Sarah M Penir[1], Torben Ruhwedel[3], Katerina Menelaou[1], Katarina Harasimov[1], Henning Urlaub[2], Wiebke Möbius[3,4], Melina Schuh[1,4†]

*These authors contributed equally to this work.

†Corresponding author. Email: melina.schuh@mpinat.mpg.de

Affiliations:

[1]Department of Meiosis, Max Planck Institute of Multidisciplinary Sciences, Göttingen, Germany

[2]Bioanalytical Mass Spectrometry group, Max Planck Institute of Multidisciplinary Sciences, Göttingen, Germany

[3]Eletron Microscopy Core Unit, Department of Neurogenetics, Max Planck Institute of Multidisciplinary Sciences, Göttingen, Germany

[4]Cluster of Excellence "Multiscale Bioimaging: from Molecular Machines to Networks of Excitable Cells" (MBExC), University of Göttingen, Göttingen, Germany

Abstract

Proper storage, translation and decay of maternal mRNAs are critically important for oocyte maturation and early embryonic development. Despite extensive studies of mRNA storage compartments in non-mammals, little is known about where and how maternal mRNAs are stored in mammalian oocytes. In this study, we find that mRNAs are deposited at a mitochondria-associated RNP (ribonucleoprotein particle) domain in oocyte (MARDO). The RNA-binding protein ZAR1 promotes MARDO assembly around mitochondria, which is dependent on the increase of mitochondrial membrane potential during oocyte growth. MARDOs coalesce and form hydrogel-like matrixes that sequester mitochondria in clusters. Maternal mRNAs, including those required for meiosis and embryogensis, are stored in MARDO in a translationally silenced form. Loss of ZAR1 disrupts MARDO, disperses mitochondria, and causes premature translation and degradation of mRNAs that are normally stored in MARDO. When oocytes resume

meiosis, ZAR1 is phosphorylated by CDK1, which partially relieves translational repression. MARDOs disperse during metaphase I (MI) to metaphase II (MII) transition due to proteasomal degradation of ZAR1, thus allowing the release, translation and decay of stored mRNAs. Our data identify a mitochondria-associated membraneless compartment that controls mitochondrial dynamics and coordinates maternal mRNA storage, translation and decay in mammalian oocyte.

Introduction

The female gamete (oocyte) is responsible for transmitting the maternal genome and many other maternal factors, including organelles, mRNAs and proteins, all of which are important for restarting a life[1-3]. To accomplish this mission, the oocyte grows into a giant cell and accumulates large amounts of mRNAs and membrane-bound organelles. In mammals, such as the mouse, transcription is globally silenced during the final phases of oocyte growth and is not significantly restored until the 2-cell embryonic stage[4,5]. During this period, the oocyte can only use stored mRNAs to encode proteins. Thus, proper storage of maternal mRNAs is critical for meiotic maturation of oocyte and early embryonic development.

Maternal mRNAs are usually stored with RNA-binding proteins. RNA-binding proteins and mRNAs can assemble into higher-order membraneless compartments through phase separation [6-8]. RNA storage compartments have been well characterized in non-mammalian oocytes, such as the P granules in *C. elegans*[9], the polar granules in *Drosophila*[10], and the Balbiani body in *Xenopus* and zebrafish[11]. P granules are liquid-like condensates appearing at all phases of germline development[12,13]. Polar granules display both liquid-like and hydrogel-like properties[14]. They are formed during oocyte growth, and are later segregated into primordial germ cells during early embryonic development[10]. The Balbiani body is a "super-organelle" composed of membrane-bound organelles (mitochondria, ER and Golgi) and germ plasm[11,15]. It is formed via amyloid-like self-assembly of prion-like proteins in the early-stage dormant oocyte[16,17], and is fragmented when oocyte starts to grow[18]. Human primary oocytes contain the Balbiani body[19,20]. Whether mouse primary oocytes contain a Balbiani body is controversial[21-23]. No Balbiani bodies were seen in late-stage oocytes of either humans or mice. Therefore, it is still unknown where and how maternal mRNAs are stored in human and mouse oocytes during oocyte growth, especially when oocytes enter the stage of transcriptional silencing. Previous study suggests that mRNAs are enriched at a subcortical domain in mouse oocytes [24]. However, the exact localization of maternal mRNAs in mammalian oocytes remains unclear.

Maternal mRNAs are progressively degraded during maternal to zygote transition (MZT)[25]. Clearance of the maternal messengers from oocyte at the appropriate time points may facilitate the transition of differentiated gametes to a

totipotent embryo[26,27]. This however requires precise coordination of mRNA storage and degradation. The translational activation of factors involved in mRNA decay during oocyte maturation is a known mechanism[28-33]. It is unclear whether other mechanisms participate in the coordination of maternal mRNA storage and decay.

Oocyte also accumulates a large number of membrane-bound organelles during growth. For example, the number of mitochondria reaches 100,000 in a fully-grown human oocyte[34]. Mitochondria have their own genetic information that is maternally transmitted to the next generation[35-37]. Maternal mitochondria energize oocyte maturation and early embryonic development[38]. However, mitochondria also generate reactive oxygen species (ROS) that threaten the integrity of genetic materials to be transmitted to the next generation[39]. Therefore, proper control of mitochondrial activity is critically important for oocyte/embryo development. Interactions between membrane-bound and membraneless compartments are an emerging field. Accumulating evidence has revealed that their interactions play fundamental roles in cellular organization and function[40]. For instance, TIS granules enable translation of specific mRNAs at an ER subdomain[41]; RNA granules hitchhike on lysosomes for long-distance transport in neuronal cells[42]; intermitochondrial cement (IMC) is formed between mitochondria, and is implicated in piRNA biogenesis[43-45]. Overall, membrane-bound compartments provide platforms for the assembly of membraneless compartments and regulate their biogenesis[46,47], dynamics[48], or transport[42]. In return, the membraneless compartments modulate the formation[49], clustering[50,51], or storage[16] of membrane-bound compartments[40,52]. Oocyte accumulates both maternal mRNAs and membrane-bound organelles. An intriguing question is whether there are physical and functional interactions between them.

The main objective of this study was to identify the RNA storage compartment in mammalian oocytes, and also investigate its interaction with membrane-bound organelles. To this end, we started from identification of highly expressed RNA-binding proteins in oocytes, and then stained them together with different membrane-bound organelles in oocytes collected from several mammalian species. We identified a previously unknown mitochondria-associated RNA storage compartment in mammalian oocytes. We further found that it plays a key role in controlling mitochondrial dynamics and coordinating maternal mRNA storage, translation, and decay.

Results

Identification of a mitochondria-associated RNA storage compartment in mammalian oocytes (MARDO)

To investigate where mRNAs are stored, we analyzed the localization of highly expressed RNA-binding proteins in mouse oocytes by staining them together with different kinds of membrane-bound organelles (Fig. S1M). We found that several RNA-binding proteins, including ZAR [53-56], YBX2[57-60], LSM14B[61], DDX6[62], and 4E-T[63], co-localized well with mitochondria labeled by cytochrome c antibody (Fig. 1, A and B, and fig. S1, A to H). RNA-binding proteins and mitochondria formed clusters that were distributed throughout the cytoplasm (Fig. 1A). High resolution images revealed that ZAR1 accumulated around mitochondria (Fig. 1, C and D). We then used fluorophore-conjugated oligo dT to label mRNAs by FISH (fluorescence in situ hybridization), and found that ZAR1 co-localized with oligo dT (Fig. 1, E and F, and fig. S1, I and J). Consistent with this, ZAR1 co-localized with the poly(A)-binding protein PABPC1L[64,65] as well as the other four RNA-binding proteins YBX2, LSM14B, DDX6 and 4E-T (Fig. 1, G to N, and fig. S1, K and L). Collectively, these results indicate that mRNAs and RNA-binding proteins both accumulate around mitochondria in mouse oocytes. In addition, we discovered that ZAR1 didn't associate with other organelles, such as the endoplasmic reticulum (ER), Golgi apparatus, recycling endosomes and lysosomes, labeled by KDEL, GM130, RAB11A and LAMP1 antibodies, respectively (Fig. 1, O to V). Proximity ligation assay (PLA) further confirmed ZAR1's specific association with mitochondria. Much more PLA spots were observed when ZAR1 was ligated to TOMM20 than RAB11A (Fig. 1, W and X). Accumulation of ZAR1 or other RNA-binding proteins around mitochondria was also observed in human, porcine and bovine oocytes (Fig. 1Y and fig. S2). As in mice, in these mammals, RNA-binding proteins and mitochondria formed clusters distributed throughout the cytoplasm. Together, these data show that RNA-binding proteins and mRNAs are deposited exclusively around mitochondria of various mammalian oocytes. This structure is distinct from any known RNA-containing compartment. We thus name the RNA storage compartment "mitochondria-associated RNP (ribonucleoprotein particle) domain in oocyte" or MARDO in short.

An intriguing question is why MARDO forms only around mitochondria. By examining oocytes at different growing stages, we found that MARDO gradually appeared during oocyte growth, and became most prominent in the fully-grown SN oocytes (Fig. 2, A to H). TMRM, but not MitoTracker Green (MTG) is sensitive to mitochondrial membrane potential[66,67]. Thus, the signal ratio of TMRM to MTG can monitor the change of mitochondrial membrane potential. Coincidentally, mitochondrial membrane potential also increased during oocyte growth, and reached a maximum in the SN oocytes (Fig. 2, I and J). The correlation of MARDO formation and mitochondrial membrane potential increase promoted us to investigate whether

MARDO formation requires mitochondrial polarization. We used different mitochondrial inhibitors to treat oocytes[68]. Treatment with Antimycin A or FCCP almost completely depolarized the mitochondria (Fig. S3, C to E). Treatment with Oligomycin A partially depolarized the mitochondria (Fig. S3, C to E). Notably, MARDO was disrupted when the oocytes were treated with any of these chemicals, implying that the mitochondrial polarization acquired during oocyte growth is essential for MARDO formation (Fig. 2, K and L). This explains why MARDO only forms around mitochondria.

ZAR1 promotes MARDO formation and mitochondrial clustering via organizing a hydrogel-like matrix

RNA-binding proteins, ZAR1, YBX2, LSM14B, DDX6, and 4E-T, all accumulate in MARDO. To find out which one is critical for MARDO formation, we co-expressed Mito-EGFP with these RNA-binding proteins in mouse oocytes. By comparing the ratio of signals on mitochondria to in cytosol, we found that ZAR1 showed the best localization on mitochondria (Fig. 3, A to D, and fig. S4, A to D). Remarkably, ZAR1 and mitochondria coalesced into huge clusters when ZAR1 was overexpressed (Fig. 3, A to C, and E). Thus, ZAR1 can promote MARDO coalescence and mitochondrial clustering. By contrast, LSM14B only slightly promoted mitochondrial clustering, while YBX2, DDX6 and 4E-T had no significant effect on mitochondrial clustering (Fig. 3E and fig. S4, A to D). We then confirmed the effect of ZAR1 on mitochondrial clustering by MitoTracker Green staining (Fig. S5A). We also observed prominent mitochondrial clusters by electron microscopy (EM) when ZAR1 was overexpressed (Fig. S6A). High resolution images revealed that ZAR1 intermingled with mitochondria (Fig. 3B). It formed a meshwork that sequestered the mitochondria inside. Immunoelectron microscopy on ZAR1-mClover3 also indicated that ZAR1 was localized in the interspace of mitochondrial cluster (Fig. S6B).

Overexpression of ZAR1 promotes the coalescence of MARDO, which provides a more intuitive way to examine its localization with other organelles. We did immunostaining in the context of ZAR1 overexpression. In contrast to the RNA-binding protein YBX2, which was enriched in MARDO, other organelles, including the ER, Golgi apparatus, recycling endosomes, lysosomes and ribosomes, were largely excluded from MARDO (Fig. S5, B to G). A small fraction of the ER was localized in MARDO (Fig. S5C). This is probably due to the direct interaction between the ER and mitochondria[69]. These results further validate that MARDO is exclusively associated with mitochondria.

The ability of MARDO to coalesce slowly suggests that it may be phase-separated compartment (Fig. 3F). When ZAR1 was partially photobleached in MARDO, ZAR1 diffused from the non-bleached region to the bleached region, which indicated the presence of internal rearrangement in MARDO (Fig. 3G). The signal recovery of ZAR1 was slow. Only about half of the signal was recovered within four minutes (Fig. 3, H and I). The slow fusion and slow recovery after photobleaching suggest that MARDO

is a hydrogel-like matrix in which the mitochondria are sequestered. 1,6-hexanediol treatment destroyed MARDO (Fig. S7A). Thus, hydrophobic interactions are required for MARDO formation. RNA buffers the phase separation behavior of prion-like RNA-binding proteins, and RNase treatment enhances the phase separation of these RNA-binding proteins[70]. We found that RNase injection promoted MARDO coalescence and mitochondrial clustering (Fig. S7B). Mitochondrial clustering occurred within four minutes after RNase injection, which excluded the possibility that RNase acted by affecting translation and the amounts of intracellular proteins (Fig. S7C). This result further indicates that MARDO is a phase-separated compartment whose formation is buffered by RNA levels. DDX6, LSM14B and 4E-T form complex and play a role in translational repression and mRNA decapping[71]. After RNase treatment, DDX6, LSM14B and 4E-T were still bound to MARDO probably through direct or indirect interaction with ZAR1[72], whereas YBX2 was dissociated (Fig. S7D). Thus, the association of YBX2 with MARDO is dependent on RNA-binding.

ZAR1 played a major role in promoting MARDO coalescence and mitochondrial clustering. We hypothesized that formation and coalescence of this phase-separated compartment is achieved through ZAR1 phase separation. ZAR1 has an unstructured N-terminal domain and a structured C-terminal RNA-binding domain (Fig. 3J). By expressing truncations of ZAR1 in the mouse oocytes, we found that the unstructured N-terminal domain of ZAR1 was required and sufficient for promoting MARDO coalescence and mitochondrial clustering (Fig. 3, K to N, and fig. S7E). We then purified the N-terminal domain of ZAR1, ZAR1(1-263), and found that it can phase-separate on its own in vitro (Fig. 3, O and P). In the presence of a SUMO tag that increases protein solubility, the N-terminal domain of ZAR1 formed liquid-like condensates with rapid signal recovery after photobleaching (Fig. 3, Q to S). When the SUMO tag was removed, it formed hydrogel-like condensates with slow recovery after photobleaching, which resembled the behavior of MARDO in vivo (Fig. 3, Q to S). Together, our data suggest that MARDO is hydrogel-like condensate formed by ZAR1 phase separation.

Loss of ZAR1 disrupts MARDO formation and mitochondrial clustering

ZAR1 is an oocyte-specific RNA-binding protein that is critical for oocyte maturation and early embryonic development[55,73,74]. To confirm that ZAR1 is essential for MARDO assembly and mitochondrial clustering, we made *Zar1* knockout mice (Fig. S8A). Immunostaining showed that knocking out *Zar1* caused disruption of MARDO that was labeled by another MARDO-localized protein YBX2 (Fig. 4, A and B). Concomitantly, mitochondria dispersed due to the elimination of MARDO (Fig. 4, A and C). These phenotypes were more pronounced in MI oocytes. MARDO and mitochondria normally clustered around spindle in MI oocytes, however they dispersed completely in the absence of ZAR1 (Fig. 4, D to F). Similar results were observed when *Zar1* was knocked down by RNAi (Fig. S8, B to D). LSM14B-mScarlet showed nice colocalization with

ZAR1-mClover3 (Fig. S8E). When used Mito-EGFP to label mitochondria and used LSM14B-mScarlet to label MARDO, we also observed MARDO disruption and mitochondrial dispersion in *Zar1* knockout oocytes (Fig. S8, F to H). The Oligo dT-labeled mRNAs normally deposited in MARDO dispersed in *Zar1* knockout oocytes, indicating that mRNAs no longer accumulated around mitochondria due to the disruption of MARDO (Fig. 4, G and H).

Proximity ligation assay can detect the association between MARDO and mitochondria (Fig. 1, W and X). The association of MARDO-localized DDX6 with mitochondrial outer membrane protein TOMM20 was significantly diminished in *Zar1* knockout oocytes (Fig. 4, I and J). RNase treatment promoted mitochondrial clustering through enhancing MARDO coalescence in wild-type oocytes, but not in *Zar1* knockout oocytes (Fig. S7B, and fig. S8, I to L). Using Trim-Away[75] to deplete ZAR1 acutely, we observed obvious mitochondrial dispersion, although ZAR1 proteins were only partially degraded due to the limited amount of antibody injected (Fig. S8, M to O). These results further indicate that ZAR1 is essential for MARDO formation and mitochondrial clustering.

We then performed rescue experiments in *Zar1* knockout oocytes. Both the unstructured N-terminal domain of ZAR1 and the full-length ZAR1 promoted mitochondrial clustering (Fig. 4, K and M). This is consistent with previous observations that the N-terminal domain of ZAR1 mediates MARDO coalescence and mitochondrial clustering (Fig. 3, K to S). In comparison to the N-terminus of ZAR1, the full-length ZAR1 not only promoted mitochondrial clustering, but also concentrated YBX2 on MARDO (Fig. 4, K to M). The recruitment of YBX2 to MARDO is RNA-dependent (Fig. S7D). Thus, the unstructured N-terminal domain of ZAR1 forms the scaffold of MARDO around mitochondria, while the C-terminal RNA-binding domain of ZAR1 mediates the recruitment of mRNAs to MARDO.

MARDO regulates mRNA storage and buffers mRNA translation

RNA-binding proteins and mRNAs accumulate in MARDO. We thus investigated whether disruption of MARDO impairs mRNA stability. RNA sequencing of *Zar1* knockout oocytes, in which MARDOs were disrupted, revealed that more than one thousand mRNAs were down-regulated by at least half (Fig. 5A and Table S1). We selected several mRNAs that were moderately changed, and confirmed their reductions in *Zar1* knockout oocytes by RT-qPCR (Fig. 5, A and B). Taking *Tcstv1*, *Wdr37* and *Elovl7* as examples, we performed single molecule RNA FISH (smFISH)[76], and found that these mRNAs were relatively enriched in MARDO compared to other mRNAs such as *Actin* (Fig. 5, C to F). These results suggest that numerous mRNAs are stored in MARDO, and the integrity of MARDO is essential for maintaining their stability.

Gene set enrichment analysis (GSEA) of the RNA-seq results revealed that MARDO disruption induced significant upregulation of translation-related pathways

(Fig. S9). This implies that MARDO is a domain that represses mRNA translation. Proximity ligation of RPL24 and phospho-RPS6 can label ribosomes assembled on mRNAs[77]. The reliability of this assay was verified by using cycloheximide (CHX) treatment to stabilize ribosomes and EDTA treatment to disassemble ribosomes (Fig. S10A). Proximity ligation of RPL24 and phospho-RPS6 showed that the assembled ribosomes were mostly excluded from MARDO (Fig. 5G). Consistent with the result of PLA assay, electron microscopy showed that polysomes appearing as clustered beads were readily visible throughout the cytoplasm but were excluded from MARDO (Fig. 5H). To further demonstrate that mRNAs in MARDO are translationally silenced, we performed a tethering assay to artificially tether ZAR1 to a reporter mRNA and recruit it to MARDO by employing the interaction between PP7 hairpin and PP7 coat protein (PCP)[78]. Reporter mRNA *mClove3-2xPP7* and control mRNA *mScarlet* were co-injected with either *tdPCP* (tandem dimer of PCP)[79] or *tdPCP-ZAR1*, and the expression of reporter mRNA was assessed by the signal ratio of mClover3 to mScarlet (Fig. 5I). We found that tdPCP-ZAR1 reduced the translation of reporter mRNA to less than half compared to tdPCP alone in GV oocytes (Fig. 5, J and K). It is noteworthy that the translational repression effect of ZAR1 was largely lost in the oocytes that had undergone GVBD (germinal vesicle breakdown) (Fig. 5L). Translation of MARDO-stored mRNAs, such as *Wdr37* and *Elovl7*, was increased in *Zar1* knockout oocytes (Fig. S10, B to D). Collectively, these results indicate that MARDO buffers mRNA translation by sequestering mRNAs and repressing mRNA translation.

Many mRNAs are stored in a dormant state during oocyte growth and are translationally activated when the oocyte resumes meiosis[80]. We found that many of these mRNAs, such as *Tex19.1* and *Epsti1*, were also under the control of ZAR1 (Fig. S10E and Table S2). TEX19.1 and EPSTI1 proteins were normally kept at low levels in GV oocytes and started to accumulate after GVBD (Fig. S10, F to I). However, despite the reduced mRNA levels, their protein levels were remarkably increased in *Zar1* knockout GV oocytes (Fig. S10, E and J). This indicated that these mRNAs were prematurely translated and degraded when MARDO was disrupted. Moreover, a lot of mRNAs involved in embryonic development were down-regulated in *Zar1* knockout oocytes, which may be responsible for defective embryonic development (Table S3).

CDK1-mediated ZAR1 phosphorylation partially relieves translational repression during meiosis

We discovered that ZAR1-mediated translational repression was largely alleviated after GVBD (Fig. 5L). This may be caused by post-translational modifications of ZAR1 and other RNA-binding proteins in MARDO[81,82]. Western blot analysis showed that there was a slight upshift of the ZAR1 band when the oocytes resumed meiosis (Fig. 6A). The upshift disappeared when treated the samples with lambda protein phosphatase (PP) before loading, suggesting that ZAR1 is phosphorylated during resumption of meiosis

(Fig. 6A). CDK1 is a master regulator of meiosis[83]. When treated the oocytes with the CDK1 inhibitor RO-3306 just after GVBD, the upshift of the overexpressed ZAR1(1-263) also disappeared (Fig. 6B). Thus, ZAR1 is phosphorylated by CDK1 during meiosis.

To find out which amino acids of ZAR1 are phosphorylated, we performed in vitro phosphorylation of ZAR1(1-263) by CDK1-CyclinB1 and mass spectrometry analysis. Among all the identified phosphorylated amino acids, five of them (S105, S124, T154, S161 and S244) matched the minimal consensus motif Ser/Thr-Pro (S/T-P)[84] phosphorylatable by CDK1 (Fig. 6C). To further identify which of them are phosphorylated in vivo, we collected approximately 1500 GV oocytes treated with RO-3306 and approximately 1500 MI oocytes treated with DMSO for enrichment of phosphorylated peptides and mass spectrometry analysis. We found that T154 and S161 were specifically phosphorylated in MI oocytes, while S105 was phosphorylated in both GV and MI oocytes (Fig. 6D). Phsophorylation of S124 and S244 was not detected in either of these samples. Consistent with the results of mass spectrometry analysis, ZAR1(T154A, S161A), but not ZAR1(S124A, S161A) or ZAR1(S161A, S244A) fully blocked the upshift of the ZAR1(1-263) band during resumption of meiosis (Fig. S11, A to C).

We then raised an antibody with ZAR1(152-168), a peptide covering both T154 and S161 (Fig. 6A). Immunostaining and western blot analysis demonstrated that this antibody only recognized the non-phosphorylated ZAR1 in GV oocytes, but didn't recognize the phosphorylated ZAR1 in oocytes that had resumed meiosis (Fig. 6A, and E to H). The antibody was thus named anti-ZAR1-NP (non-phosphorylated) antibody. Treatment with Lambda protein phosphatase or RO-3306 enabled ZAR1 to be re-recognized by anti-ZAR1-NP antibody, whereas treatment with the proteasome inhibitor MG-132 or the MEK1/2 inhibitor U0126 had no effect on antibody recognition (Fig. 6, I to L, and fig. S11D). These results further confirmed that ZAR1 was phosphorylated by CDK1 during meiosis. There are two phosphorylation sites, T154 and S161, in the antigen (Fig. 6D). In order to find out which of them is crucial for antibody recognition, we expressed the phosphomimetic variants of ZAR1 in *Zar1* knockout oocytes. We found that the S161D but not the T154D mutation blocked the recognition of ZAR1 by anti-ZAR1-NP antibody. However, this doesn't mean T154 is not phosphorylated during meiosis. It is possible that T154 is not on the antibody-binding epitope, so its phosphorylation does not affect antibody binding. The ZAR1(T154D, S161D) phosphomimetic variant was still localized in MARDO as wild-type ZAR1 (Fig. S11, G and H). Nevertheless, ZAR1(T154D, S161D) had weaker repression effect on mRNA translation than wild-type ZAR1, indicating that ZAR1 phosphorylation partially relieved translational repression (Fig. 6M). Notably, the mass spectrometry data showed that LSM14B, DDX6, 4E-T and YBX2 were all phosphorylated upon resumption of meiosis (Table S4). It is possible that their phosphorylation plays a synergistic role in relieving translational repression during meiosis.

Proteasomal degradation of ZAR1 promotes MARDO dissolution and mRNA decay during MI-MII transition

Immunostaining of ZAR1 at different stages of meiosis showed that MARDO was progressively disassembled (Fig. 7, A and B). Dissolution of MARDO was accompanied by a decrease in ZAR1 protein levels (Fig. 7, C and D). Live imaging analysis indicated that MARDO dissolution occurred during the transition from MI to MII, and was delayed when ZAR1 was overexpressed (Fig. 7E). The overexpressed ZAR1 proteins were still fully phosphorylated in MII oocytes (Fig. S12A). We hypothesized that MARDO dissolution requires proteasome-mediated degradation of ZAR1. Consistent with this hypothesis, MG-132 treatment blocked both ZAR1 degradation and MARDO dissolution (Fig. 7, D, F and G). MG-132 treatment also arrested oocyte maturation at MI stage[85]. To exclude the possibility that impaired MARDO dissolution was due to impaired meiotic progression upon MG-132 treatment, we further treated oocytes with nocodazole, an agent that disrupts microtubules and impairs spindle assembly, and found that nocodazole treatment had no effect on MARDO dissolution (Fig. 7G). ZAR1 overexpression delayed MARDO dissolution, which provided us an approach to skip MI stage and directly investigate ZAR1 degradation and MARDO dissolution in MII oocytes (Fig. 7E). In contrast to LSM14B, which almost ceased to change after reaching its maximum, the overexpressed ZAR1 was still degraded gradually in MII oocytes (Fig. S12, B and C). In this context, MG-132 treatment also blocked the degradation of ZAR1 and the dissolution of MARDO (Fig. S12, D and E). Together, these results indicate that proteasomal degradation of ZAR1 promotes MARDO dissolution during MI-MII transition.

The time point of MARDO dissolution coincided with the time point of maternal mRNA decay[31]. We performed mRNA FISH with oligo dT, and found that overexpression of ZAR1 affected both MARDO dissolution and mRNA decay (Fig. 7, H and I). Consistent with the FISH assay, RT-qPCR analyses indicated that the degradation of individual mRNAs stored in MARDO was also affected when ZAR1 was overexpressed (Fig. S12G). By contrast, those mRNAs that are not down-regulated in *Zar1* knockout oocytes and potentially not stored in MARDO, were not affected by ZAR1 overexpression (Fig. S12, F and H). Thus, proteasomal degradation of ZAR1 is required for MARDO dissolution and timely mRNA decay.

Discussion

In non-mammals, oocyte-specific RNA storage compartments have been extensively studied[9-11]. However, little is known about where and how maternal mRNAs are stored in mammalian oocytes. We identified MARDO, a membraneless compartment associated with mitochondria, in mouse, bovine, porcine and human oocytes. MARDO is assembled by ZAR1 phase separation, which is dependent on the increase of mitochondrial membrane potential during oocyte growth. MARDOs coalesce and form hydrogel-like matrixes that sequester mitochondria in clusters. Translationally silenced mRNAs are stored in MARDO. CDK1-mediated ZAR1 phosphorylation, together with phosphorylation of other RNA-binding proteins in MARDO, may relieve translational repression upon resumption of meiosis. Proteasomal degradation of ZAR1 promotes MARDO dissolution and mRNA decay during MI-MII transition. Our data reveal a previously unknown mechanism that couples maternal mRNA storage, translation and decay to meiotic progression (Fig. 7J).

Emerging evidence reveals extensive interactions between membrane-bound and membraneless compartments[40]. However, MARDO only forms around mitochondria. During the long growth phase of oocytes, mitochondria maintain a relatively low activity. Low mitochondrial activity results in less ROS production and less DNA damage. This is beneficial for maintaining the stability of genetic materials in oocytes. The complete polarization of mitochondria occurs in the fully-grown SN oocytes, which ensures the energy supply for meiosis and subsequent embryogenesis. MARDO forms during oocyte growth by sensing the gradual increase of mitochondrial membrane potential, and becomes most prominent in SN oocytes. Another characteristic of SN oocytes is that they are transcriptionally silenced[86]. Therefore, proper storage of the existing mRNAs becomes extremely important when oocytes enter the SN phase. The formation of MARDO coincides perfectly with the requirement for proper mRNA storage. What are the benefits of storing mRNAs around mitochondria? Mitochondria are the main source of ATP. RNA helicases use ATP to bind or remodel RNA or RNP[87]. DEAD-box RNA helicases can regulate the assembly and turnover of membranless compartments through ATP binding and ATP hydrolysis, respectively[88]. ATP may also compete with Mg^{2+}-dependent deadenylase for Mg^{2+}, thus maintaining the stability of stored mRNAs[89-91].

Mitochondria serve as a platform for MARDO assembly. In return, MARDO acts like a glue that holds the mitochondria together. In mouse, bovine, porcine and human oocytes, mitochondria are all present as clusters with different sizes. The exact function of the clustered mitochondria is not clear yet. During meiosis, mitochondria tend to cluster around the MI spindle[92,93]. Moreover, the mitochondria around the spindle have a higher membrane potential[67]. Concentrating active mitochondria in areas of high energy demand, rather than increasing overall mitochondrial activity, may help minimize ROS production. When MARDO is disrupted, mitochondria are dispersed

throughout the cytoplasm. Consequently, the spindle assembly process cannot be powered by locally accumulated active mitochondria as in wild-type oocytes. Gene set enrichment analysis (GSEA) of the RNA-seq results from *Zar1* knockout oocytes reveals that the electron transport chain pathway is significantly up-regulated when MARDO is disrupted (Fig. S9). The up-regulation of overall mitochondrial activity may be a compensatory mechanism to meet ATP demand.

Polysomes are excluded from MARDO, which means that mRNAs sequestered in MARDO are translationally silenced. Our data suggest that MARDO balances mRNA storage and translation. MARDO is a dynamic structure whose components are exchanging with the cytosol. When mRNAs are recruited to MARDO, they are stored safely, but sequestered away from the translational machinery. When they are released from MARDO, they become available for translation again, but are also at risk of degradation. The cycling between MARDO and the cytosol maintains mRNA stability, and also ensures proper translation of stored mRNAs. MARDO is gradually formed during oocyte growth, becomes most prominent in SN oocyte, and is dispersed during meiosis. Changes in MARDO quantity imply a shift in the balance between mRNA storage and translation.

MARDO dissolution depends on proteasome-mediated degradation of ZAR1. This is reminiscent of a recent discovery: the disassembly of stress granule requires ubiquitination of G3BP1, the central protein within the RNA-protein network of stress granule[94]. Ubiquitinated G3BP1 is extracted by the segregase p97/VCP (valosin-containing protein) through the VCP adapter FAF2, and is then targeted to proteasome for degradation[94]. The VCP-FAF2 complex also disassembles RNPs by promoting the extraction of ubiquitinated RNA-binding protein HuR/ELAVL1 from mRNA[95]. Notably, yeast Ubx2, the mammalian homolog of FAF2, is dynamically localized to ER, mitochondria and lipid droplets[96]. FAF2 is also involved in the degradation of mitochondrial outer membrane proteins MFN1 and MFN2 under *Toxoplasma* infection-induced stress[97]. Moreover, an AP-MS (affinity purification-mass spectrometry) assay showed that the *Xenopus* Zar1 interacts with VCP[72]. Together, it is reasonable to hypothesize that MARDO dissolution also requires FAF2-VCP-mediated extraction of ubiquitinated ZAR1 for proteasomal degradation.

MARDOs co-localize with mitochondria, and are therefore distinct from P bodies, stress granules, P granules and polar granules. MARDO and the Balbiani body are both mitochondrial clusters, and may both favor active mitochondria. The balbiani body is thought to be involved in the selection of active/healthy mitochondria[22,98,99]. MARDO formation depends on the increase of mitochondrial membrane potential during oocyte growth. However, they differ in three aspects. 1) They appear at different stages of oocyte development. Balbiani body is formed in primary oocyte, whereas MARDO is formed at later stage of oocyte growth. 2) They have different material properties. Balbiani body is held together by an amyloid-like matrix[16,17], while MARDO is hydrogel-like, and still exchanges with the cytosol. 3) They have different compositions. Balbiani

body contains Golgi apparatus, whereas MARDO does not interact with Golgi. MARDO in oocyte and intermitochondrial cement (IMC) in spermatocyte are both associated with mitochondria and disassembled at later stage of meiosis, although IMC only appears between mitochondria, while MARDO assembles around mitochondria[43-45]. IMC is involved in piRNA biogenesis and piRNA-mediated RNA degradation. Notably, ZAR1, the central protein of MARDO, is expressed in oocyte but not in spermatocyte. Loss of ZAR1 impairs degradation of a subset of maternal transcripts. This raises an intriguing question as to whether MARDO plays a similar role in oocyte as IMC does in spermatocyte.

Materials and methods

Preparation and culture of mouse oocytes and follicles

All mice were maintained in a specific pathogen-free environment according to animal ethics guidelines of the Animal Facility of the Max Planck Institute for Multidisciplinary Sciences. *Zar1* knockout mouse with C57BL/6N background was generated through CRISPR/Cas9-mediated genome engineering[100] by Cyagen Biosciences Inc. The gRNA (gRNA1, matches forward strand of gene, GCCGCCTATTTAACGCAGCGTGG; gRNA2, matches reverse strand of gene, CCACACAAGTCTTGCCGATGGGG) to mouse *Zar1* gene, and *Cas9* mRNA were co-injected into fertilized mouse eggs to generate targeted knockout offspring. F0 founder animals were identified by PCR followed by sequence analysis, which were bred to wild-type mice to test germline transmission and F1 animal generation. 3782 bp of *Zar1* gene was removed, which caused complete removal of exon 1, 2, 3 and partial removal of exon 4. For both gRNA targeting sequences, five potential off-target sites have been identified by PCR and sequence analysis, and the result indicated that no unwanted modifications occur on these sites.

For most experiments, oocytes were isolated from ovaries of 8- to 12-week-old CD1 or C57BL/6N female mice. The localization of RNA-binding proteins and mRNAs is identical in CD1 and C57BL/6N oocytes, although mitochondrial clustering is a little bit more pronounced in C57BL/6N oocytes. CD1 mice were used in Fig. 1, 2, 3, Fig. 5H, J, Fig. 6A, D, M, Fig. S1,3,4,5,6,7 and Fig. S11G, H. C57BL/6J × CBA F1 female mice were used for follicle culture and RNAi in Fig. S8B. C57BL/6N mice were used in all other mouse experiments. Fully grown oocytes with a centered GV were maintained at prophase arrest in homemade phenol red-free M2 medium supplemented with 250 μM dibutyryl cyclic AMP (dbcAMP) under paraffin oil (NidaCon #NO-400K) at 37°C. To collect oocytes at all growing stages, ovaries form 4-week-old female mice were washed in PBS and then dissected into pieces in 2 ml TrypLE Express Enzym (1×) (Thermo Fisher Scientific #12604013) supplemented with 2 mg/ml collagenase IV (Thermo Fisher Scientific #17104019) and 250 μM dbcAMP. 2 ml M2-dbcAMP medium

was added after 20 minutes' incubation at 37°C. Oocytes were released by gentle pipetting. Released oocytes were transferred to M2-dbcAMP medium, and recovered for 30 min at 37°C before use. Day 14, 16, 18 and 21 oocytes were isolated from ovaries of 14-, 16-, 18- or 21-day-old female mice, and oocytes covered with loose granulosa cells were cleaned and collected. Culture of follicles was performed as previously described[101].

Preparation of bovine and porcine oocytes

All porcine and bovine ovaries were obtained from local slaughterhouses. Bovine ovaries were transported to the laboratory within 3 hours of retrieval in a thermo-flask. Porcine ovaries were transported to the laboratory within 1 hour of retrieval in a portable 37°C incubator in M2 medium supplemented with 1 mM dbcAMP. Cumulus-oocyte complexes (COCs) were recovered by aspiration of antral follicles with an 18-gauge needle mounted on a 1-ml syringe. 140 ml of 5000 IU/ml heparin (Merck Millipore #375095-100KU) was added to every 20 ml of aspirates. COCs were allowed to sediment and then washed extensively with pre-warmed HEPES-buffered medium 199 (for bovine oocytes) or M2 medium (for porcine oocytes) supplemented with 1mM dbcAMP. Only fully grown oocytes with a homogeneous cytoplasm and several layers of compact cumulus cells were selected for experiments. Bovine and porcine oocytes were maintained in prophase arrest in dbcAMP-containing medium at 39° and 37°C, respectively. Surrounding cumulus cells of bovine and porcine oocytes were removed by vortex and with 30 nM hyaluronidase (Sigma-Aldrich # H4272-30MG), respectively.

Source of human oocytes

The use of immature unfertilized human oocytes in this study has been approved by the UK's National Research Ethics Service under the REC reference 11/EE/0346 (IRAS Project ID 84952) and the Ärztekammer Niedersachsen (Ethics Committee of Lower Saxony) under the reference 15/2016. Oocytes were sourced from women undergoing assisted reproduction treatments at Bourn Hall Clinic (Cambridge, UK). Only oocytes that were immature and hence unsuitable for intracytoplasmic sperm injection (ICSI) were used. All patients gave informed consent for their surplus oocyte(s) to be used in this study.

Immunofluorescence

To obtain mouse metaphase I and metaphase II oocytes, oocytes were incubated at 37°C for around 7 and 15 hours, respectively, upon release into dbcAMP-free medium. Oocytes from different sources were all fixed with 4% methanol-free formaldehyde in

phosphate-buffered saline (PBS) for 1 hour at room temperature. Fixed oocytes were washed and extracted with PBT buffer (0.5% Triton X-100 in PBS) for 1 hour at room temperature or overnight at 4°C. Permeabilized oocytes were blocked with PBT-BSA buffer (PBS containing 3% BSA and 0.1% Triton X-100) for 1 hour at room temperature or overnight at 4°C. Lipid droplets in bovine and porcine oocytes were cleared with 4000 U/ml lipase from Candida rugose (Sigma-Aldrich #L8525) in lipase buffer (50 mM Tris pH 7.2, 400 mM NaCl, 5 mM CaCl2, and 0.2% sodium taurocholate supplemented with complete, EDTA-free Protease Inhibitor Cocktail (Roche #11873580001)) for 1 hour at 37°C. Cleared oocytes were washed with PBT-BSA and proceeded for antibody incubation. Oocytes were incubated with primary antibodies in PBT-BSA for 1.5 hours at room temperature. After three times of washing with PBT-BSA, oocytes were incubated with secondary antibodies and Hoechst 33342 (Thermo Fisher Scientific #H3570) for 1.5 hours at room temperature. Oocytes were then washed for three times again and mounted for imaging.

Primary antibodies used were goat anti-ZAR1 (Santa Cruz Biotechnology #sc-55994), mouse anti-cytochrome c (Santa Cruz Biotechnology #sc-13561), rabbit anti-YBX2 (Abcam #ab33164), rabbit anti-DDX6 (Abcam #ab174277), mouse anti-DDX6 (Sigma-Aldrich #SAB4200837), rabbit anti-LSM14B (Thermo Fisher Scientific #PA5-66371), rabbit anti-4E-T (Thermo Fisher Scientific #PA5-51680), mouse anti-PABPC1L (Santa Cruz Biotechnology #sc-515476), mouse anti-KDEL (Enzo Life Sciences #ADI-SPA-827), mouse anti-GM130 (BD Biosciences #610822), rabbit anti-RAB11A (Thermo Fisher Scientific #71-5300), rat anti-LAMP1 (Thermo Fisher Scientific #14-1071-82), mouse anti-TOMM20 (Novus Biologicals #H00009804-M01), rabbit anti-FIS1(Sigma-Aldrich #HPA017430), rabbit anti-COX17 (Sigma-Aldrich #HPA042226), rabbit anti-RPL24 (Thermo Fisher Scientific #PA5-30157), mouse anti-phospho-RPS6 (Cell Signaling Technology #62016), rabbit anti-WDR37 (Proteintech #20916-1-AP), rabbit anti-ELOVL7 (Sigma-Aldrich #AV49908), rabbit anti-TEX19.1 (Abcam #ab129726), rabbit anti-EPSTI1 (Proteintech #11627-1-AP), mouse anti-phospho-ERK1/2 (Cell Signaling Technology #9106), guinea pig anti-non-phosphorylated-ZAR1 (made by Cambridge Research Biochemicals). All primary antibodies were diluted at 1:100 except for rabbit anti-YBX2 (Abcam #ab33164) that was diluted at 1:500. Secondary antibodies used were Alexa Fluor 488-, 568-, or 647-conjugated anti-goat IgG, rabbit IgG, mouse IgG, rat IgG or guinea pig IgG highly cross-adsorbed secondary antibodies (Thermo Fisher Scientific). All of them were raised in donkey or goat.

mRNA fluorescence in situ hybridization (FISH)

Oocytes were fixed with 4% methanol-free formaldehyde in PBS for 30 minutes at room temperature, and then permeabilized with fresh 70% ethanol for 20 minutes at room temperature. Permeabilized oocytes were rehydrated with Wash Buffer A (Biosearch Technologies #SMF-WA1-60) containing 10% formamide, and then incubated with 200

nM Cy5-conjugated oligo (dT)30 (Integrated DNA Technologies) in Hybridization Buffer (Biosearch Technologies #SMF-HB1-10) supplemented with 10% formamide for 16 hours at 37°C. After probe incubation, oocytes were washed with Wash Buffer A for 30 minutes at 37°C, and stained with Hoechst in Wash Buffer A for another 30 minutes at 37°C. After sequential washing with Wash Buffer A and Wash Buffer B (Biosearch Technologies #SMF-WB1-20) for 30 minutes each at 37°C and room temperature respectively, oocytes were mounted for imaging or immunofluorescence.

Single-molecule fluorescence in situ hybridization (smFISH)

The ViewRNA Cell Plus Assay-Kit (Thermo Fisher Scientific #88-19000-99) was used for smFISH. The assay was performed as previously described with some optimizations[76]. Oocytes expressing ZAR1-mClover3 were fixed with 4% methanol-free formaldehyde in PBS for 20 minutes at room temperature. After extensive washing with the Homemade Wash Buffer (1% Polyvinylpyrrolidon (Sigma-Aldrich #P0930), 0.1% Triton X-100 and 1× RNase Inhibitor (provided in the kit) in PBS), the oocytes were permeabilized with the Homemade Permeabilization Solution (PBS containing 1% Triton X-100 and 1× RNase inhibitor) for 30 minutes at room temperature. The oocytes were then washed with the Homemade Wash Buffer again and treated with 1:8000 diluted Protease QS (Thermo Fisher Scientific #QVC0001) for 5 minutes at room temperature. Probe Sets of mRNAs of interest (Tcstv1 #VB6-3203791-VCP, Wdr37 #VB6-3215318-VCP, or Elovl7 #VB6-3209719-VCP) and control Probe Set (Actb #VB1-10350-VCP) were mixed and diluted 1:100 with pre-warmed Probe Set Diluent supplemented with 0.1% Triton X-100. After protease treatment, oocytes were washed with the Homemade Wash Buffer, and were then incubated with the diluted Probe Sets for 3 hours at 40 °C. Hybridization and all the following steps were performed in the Agtech 6-well dish (Agtech #3926909910). After Probe Set hybridization, oocytes were washed five times with the ViewRNA Cell Plus RNA Wash Buffer Solution supplemented with 0.5% BSA, and then subjected to sequential hybridization with PreAmplifier Mix, Amplifier Mix and Label Probe Mix, all of which were diluted 1:25 with pre-warmed provided diluent supplemented with 0.1% Triton X-100. Hybridizations with PreAmplifier, Amplifier and Label Probe were performed at 40 °C for 1 hour. Oocytes were washed five times with the ViewRNA Cell Plus RNA Wash Buffer Solution containing 0.5% BSA between every hybridization step. At last, oocytes were stained with Hoechst 33342 in PBT-BSA solution (PBS containing 0.1% Triton X-100 and 3% BSA) for 1.5 hours at room temperature to label DNA.

Proximity ligation assay (PLA)

The Proximity Ligation Assay (PLA) was performed with the Duolink In Situ Red Starter Kit Mouse/Rabbit (Sigma-Aldrich #DUO92101). Oocytes with or without ZAR1-mClover3 were fixed with 4% methanol-free formaldehyde in PBS for 1 hour at room temperature. Fixed oocytes were washed and extracted with PBT buffer (1% Triton X-100 in PBS) for 1 hour at room temperature and then blocked with PBT-BSA (0.1% Triton X-100 and 3% BSA in PBS) overnight at 4°C. All the following steps, including primary antibody incubation, PLA probe incubation, ligation, amplification and final washes, were performed according to the protocol provided with the kit except that primary antibodies were diluted 1:50 or 1:100 with PBT-BSA. Oocytes can be further stained with other antibodies and/or Hoechst 33342 before imaging.

Primary antibody pairs used include goat anti-ZAR1(Santa Cruz Biotechnology #sc-55994) & mouse anti-TOMM20 (Novus Biologicals #H00009804-M01), rabbit anti-RAB11A (Thermo Fisher Scientific #71-5300), or normal rabbit IgG (Merck Millipore #12-370), mouse anti-TOMM20 & rabbit anti-DDX6 (Abcam #ab174277) or normal rabbit IgG, rabbit anti-RPL24 (Thermo Fisher Scientific #PA5-30157) & mouse anti-phosphor-RPS6 (Cell Signaling Technology #62016). Corresponding PLA probes were all purchased from Sigma-Aldrich.

Expression constructs, mRNA synthesis, protein expression, and purification

To generate constructs for mRNA synthesis, pGEMHE-mClover3-N1, pGEMHE-mScarlet-N1, pGEMHE-mClover3-C1 and pGEMHE-mScarlet-C1 were built first for subcloning of other constructs. To generate pGEMHE-mClover3-N1 and pGEMHE-mScarlet-N1, published coding sequences of mClover3[102] and mScarlet[103] were amplified using primers P1/P2, and were then ligated into pGEMHE through BamHI/XbaI. To build pGEMHE-mClover3-C1 and pGEMHE-mScarlet-C1, mClover3 and mScarlet were amplified using primers P3/P4, and were then ligated into pGEMHE through NheI/XhoI. To construct pGEMHE-Mito-EGFP, MitoTimer (Addgene #52659)[104] was first subcloned into pGEMHE through NheI/NotI to get pGEMHE-MitoTimer. EGFP(L221K) was amplified using primers P5/P6, and was used to replace Timer to get pGEMHE-Mito-EGFP. To generate pGEMHE-ZAR1-mScarlet and pGEMHE-ZAR1-mClover3, ZAR1 was amplified from a mouse cDNA library using primers P7/P8, and was assembled with linearized pGEMHE-mScarlet-N1(NheI/NcoI) and pGEMHE-mClover3-N1(NheI/NcoI) through Gibson Assembly (NEB #E2621S). To build pGEMHE-mScarlet-YBX2, YBX2 was amplified from a mouse cDNA library using primers P9/P10, and was then assembled with linearized pGEMHE-mScarlet-C1(XhoI/BamHI) through Gibson Assembly. To build pGEMHE-LSM14B-mScarlet, pGEMHE-DDX6-mScarlet and pGEMHE-4E-T-mScarlet, LSM14B, DDX6 and 4E-T were amplified from mouse cDNA libraries using primers P11/P12, P13/P14 and P15/P16, respectively, and were then assembled with linearized pGEMHE-mScarlet-N1(NheI/NcoI) through Gibson

Assembly. To generate pGEMHE-ZAR1(1-263)-mScarlet and pGEMHE-ZAR1(1-143)-mScarlet, site-directed mutagenesis[105] on pGEMHE-ZAR1-mScarlet was performed using primers P17/P18 and P19/P20 respectively. To build pGEMHE-ZAR1(53-143)-mScarlet, site-directed mutagenesis on pGEMHE-ZAR1(1-143)-mScarlet was performed using primers P21/P22. To construct pGEMHE-ZAR1(53-74)-mScarlet, ZAR1(53-74) was synthesized (Integrated DNA Technologies), and assembled with linearized pGEMHE-mScarlet-N1(NheI/NcoI) through Gibson Assembly. To generate pGEMHE-ZAR1(252-361)-mScarlet, site-directed mutagenesis on pGEMHE-ZAR1-mScarlet was performed using primers P23/P24. To build pGEMHE-mClover3-*2×PP7*, *2×PP7* was amplified from pHAGE-CMV-CFP-*24×PP7* (Addgene #40652)[79] using primers P25/P26, and was then assembled with linearized pGEMHE-mClover3-N1(XbaI) through Gibson Assembly. To build pGEMHE-tdPCP and pGEMHE-tdPCP-ZAR1, pGEMHE-tdPCP-mscarlet was generated first. TdPCP was amplified from pHAGE-UBC-NLS-HA-tdPCP-GFP (Addgene #40650)[79] using primers P27/P28, and was ligated into pGEMHE-mScarlet-N1 through XhoI/NcoI. To generate pGEMHE-tdPCP, site-directed mutagenesis on pGEMHE-tdPCP-mScarlet was performed using primers P29/P30. To construct pGEMHE-tdPCP-ZAR1, ZAR1 with a linker[72] was amplified from pGEMHE-ZAR1-mScarlet using primers P31/P32, and was then assembled with linearized pGEMHE-tdPCP by digesting pGEMHE-tdPCP-mScarlet with NcoI/XbaI. To generate pGEMHE-FLAG-ZAR1(1-263), pGEMHE-FLAG-ZAR1 was built first. FLAG-ZAR1 was amplified from pGEMHE-ZAR1-mScarlet using primers P33/P34, and was ligated into pGEMHE through NheI/XbaI. To build pGEMHE-FLAG-ZAR1(1-263), site-directed mutagenesis on pGEMHE-FLAG-ZAR1 was performed using primers P17/P18. To generate pGEMHE-FLAG-ZAR1(1-263)(T154A) and pGEMHE-FLAG-ZAR1(1-263)(S161A), site-directed mutagenesis on pGEMHE-FLAG-ZAR1(1-263) was performed using primers P35/P36 and P37/P38 respectively. To generate pGEMHE-FLAG-ZAR1(1-263)(T154A, S161A), site-directed mutagenesis on pGEMHE-FLAG-ZAR1(1-263)(T154A) was performed using primers P37/P38. To construct pGEMHE-FLAG-ZAR1(1-263)(S124A, S161A) and pGEMHE-FLAG-ZAR1(1-263)(S161A, S244A), site-directed mutagenesis on pGEMHE-FLAG-ZAR1(1-263)(S161A) was performed using primers P39/P40 and P41/P42 respectively. To build pGEMHE-ZAR1(T154D)-mScarlet and pGEMHE-ZAR1(S161D)-mScarlet, site-directed mutagenesis on pGEMHE-ZAR1-mScarlet was performed using primers P43/P44 and P45/P46 respectively. To generate pGEMHE-ZAR1(T154D, S161D)-mScarlet, site-directed mutagenesis on pGEMHE-mZAR1(S161D)-mScarlet was performed using primers P43/P44. To build pGEMHE-tdPCP-ZAR1(T154D, S161D), ZAR1(T154D, S161D) was amplified from pGEMHE-ZAR1(T154D, S161D)-mScarlet using primers P31/P32, and was then assembled with linearized pGEMHE-tdPCP by digesting pGEMHE-tdPCP-mScarlet with NcoI/XbaI. Constructs pGEMHE-mClover3-MAP4-MTBD, pGEMHE-H2B-miRFP670 and pGEMHE-TRIM21 were generated in previous study[106]. All mRNAs were synthesized

using the HiScribe T7 ARCA mRNA Kit (with tailing) (NEB #E2060S), and then were purified with the RNeasy Mini Kit (Qiagen #74104).

To generate constructs for protein expression, codon optimization (Integrated DNA Technologies) was performed on all genes for better expression in *E. coli*. To generate pET-21c(+)-6xHis-SMT3, 6xHis-SMT3 was synthesized and ligated into pET-21c(+) through NdeI/BamHI. To build pET-21c(+)-6xHis-SMT3-sfGFP, sfGFP was synthesized and ligated into pET-21c(+)-6xHis-SMT3 through BamHI/HindIII. To generate pET-21c(+)-6xHIS-SMT3-ZAR1(1-263), ZAR1(1-263) was amplified from synthesized ZAR1 using primers P47/P48, and was then ligated into pET-21c(+)-6xHis-SMT3 through BamHI/HindIII. All constructs were expressed in BL21(DE3) Competent *E. coli* (NEB #C2527H). Proteins were purified first using Ni-NTA resin (Qiagen #30210), followed by size-exclusion chromatography on HiLoad 16/600 Superdex 200 pg column (Sigma-Aldrich # GE28-9893-35) performed with ÄKTA pure 25 system (Cytiva). SMT3 tag was removed by cutting with SUMO protease (Thermo Fisher Scientific #12588018) when necessary.

Primers used for plasmid construction

Primer name	Primer number	Sequence
mClover3/mScarlet S1	P1	GC **GGATCC** *GCCACC* ATG GTGAGCAAGGGCGAG
mClover3/mScarlet AS1	P2	GC **TCTAGA** TTA CTTGTACAGCTCGTCCATGC
mClover3/mScarlet S2	P3	GC **GCTAGC** *GCCACC* ATG GTGAGCAAGGGCGAG
mClover3/mScarlet AS2	P4	GC **CTCGAG** CTTGTACAGCTCGTCCATGC
EGFP S	P5	CG **GGATCC** ACCGGTC *GCCACC* ATG GTGAGCAA
EGFP AS	P6	CG **GCGGCCGC** TTA TTA CTTGTACAGCTCGTCCATGCCGAGA
ZAR1 S	P7	CAGATCAATTCCCCGGT *GCCACC* ATG TTCCCGGCGAGCACG
ZAR1 AS	P8	CTCGCCCTTGCTCACCAT gctaccgctgccgctacc AATGATGTATTTGAAGCTGAAGGTGCTGTCG
YBX2 S	P9	CATGGACGAGCTGTACAAG ggtagcggcagcggtagc ATG AGCGAGGCGGAGGC
YBX2 AS	P10	GCCGCTTTACTTGTACAGGATCC TCA CTCCAGTATGGTGGTGGG
LSM14B S	P11	CAGATCAATTCCCCGGT *GCCACC* ATG AGCGGCTCGTCCGG
LSM14B AS	P12	CTCGCCCTTGCTCACCAT gctaccgctgccgctacc TACCCGGCCAGTCCCAGC
DDX6 S	P13	CAGATCAATTCCCCGGT *GCCACC* ATG AGCACGGCCAGAACAGAG
DDX6 AS	P14	CTCGCCCTTGCTCACCAT gctaccgctgccgctacc CGGTTTCTCGTCTTCTGCAGGC
4E-T S	P15	CAGATCAATTCCCCGGT *GCCACC* ATG GAGAAAAGTGTGGCTGAAACAG
4E-T AS	P16	CTCGCCCTTGCTCACCAT gctaccgctgccgctacc CTGTCTATATTCCAGTTCATCTACACTGATGAC
ZAR1(1-263) S	P17	GAGCAGAAG ggtagcggcagcggtagc
ZAR1(1-263) AS	P18	ctgccgctacc CTTCTGCTCTAAGAACTGGAAACGCAGGC
ZAR1(1-143) S	P19	CTCTCC ggtagcggcagcggtagc
ZAR1(1-143) AS	P20	ctgccgctacc GGAGAGGCCACAGAAGGTCACG
ZAR1(53-143) S	P21	GT *GCCACC* ATG AGCCACCAGCGGGCACAG
ZAR1(53-143) AS	P22	CTGGTGGCT CAT *GGTGGC* ACCGGGGAATTGATCT
ZAR1(252-361) S	P23	*GCCACC* ATG AAGGAGCGCCTGCGTTTCCAG
ZAR1(252-361) AS	P24	CGCTCCTT CAT *GGTGGC* ACCGGGGAATTG
2×PP7 S	P25	TGGACGAGCTGTACAAG TAA AAGGTACCTAATTGCCTAGAAAGGAGCAGAC
2×PP7 AS	P26	ACCAGATCAAGCTATCATTTA AGGATCTAATGAACCCGGGAATACTGCAG
tdPCP-(mScarlet) S	P27	GC **CTCGAG** *GCCACC* ATG CTAGCCTCCAAAACCATCGTTC
tdPCP-(mScarlet) AS	P28	GC **CCATGG** CGGTGGCGACCGGTGG
tdPCP S	P29	GGTCGCCACCTAAATGATAG CTTGATCTGGTTACCACTAAACCAGC
tdPCP AS	P30	CTATCATTTAGGTGGCGACC GGTGGACG
(tdPCP)-ZAR1 S	P31	CCACCGGTCGCCACC ggaggtggtgggtctggtggaggcgggagcggaggcggagggtcc ATG TTCCCGGCGAGCACGTTC
(tdPCP)-ZAR1 AS	P32	ACCAGATCAAGCTATCATTTAT CTA AATGATGTATTTGAAGCTGAAGGTGCTGTCGC
FLAG-ZAR1 S	P33	GC **GCTAGC** *GCCACC* ATG GACTACAAAGACGATGACGACAAG ATG TTCCCGGCGAGCACG

FLAG-ZAR1 AS	P34	GC **TCTAGA** CTA AATGATGTATTTGAAGCTGAAGGTGCTGTC
ZAR1(T154A) S	P35	CAGGCAG ***GCA*** CCCACGAAGGGAGAGGG
ZAR1(T154A) AS	P36	GTGGG ***TGC*** CTGCCTGCCTCCCGCAAC
ZAR1(S161A) S	P37	GG ***GCA*** CCGGCATCCTCGGG
ZAR1(S161A) AS	P38	GGATGCCGG ***TGC*** CCCCTCTCCCTTCGTGGG
ZAR1(S124A) S	P39	GGGAGA ***GCT*** CCGCGATCCTGGCAGACCG
ZAR1(S124A) AS	P40	ATCGCGG ***AGC*** TCTCCCGGCGCCGGC
ZAR1(S244A) S	P41	AGGCC ***GCC*** CCGCAAAGCACGGAGC
ZAR1(S244A) AS	P42	TGCGG ***GGC*** GGCCTGGTCTCGAGGGGC
ZAR1(T154D) S	P43	CAGGCAG ***GAT*** CCCACGAAGGGAGAGGG
ZAR1(T154D) AS	P44	GTGGG ***ATC*** CTGCCTGCCTCCCGC
ZAR1(S161D) S	P45	GG ***GAC*** CCGGCATCCTCGGG
ZAR1(S161D) AS	P46	GGATGCCGG ***GTC*** CCCCTCTCCCTTCGTGGG
optZAR1(1-263) S	P47	GC **GGATCC** ATG TTCCCTGCGTCTACGTTC
optZAR1(1-263) AS	P48	GC **AAGCTT** TTA CTTCTGTTCCAAAAATTGGAAGCG

Restriction enzyme sites are shown in bold. Kozak sequences are show in italics. Linkers are shown in lower case. Mutation sites are shown in bold italics.

Short-interfering RNAs

All short interfering RNAs (siRNAs) were purchased from Qiagen. For knockdown of *Zar1* by RNAi, a mix of siRNAs targeting the following sequences were used: 5′-CACCAGTAAGGTGTACTTCAA-3′, 5′-CCGAGTGTGTGAGAAATCCTA-3′, 5′-CAGCTTCAAATACATCATTTA-3′, and 5′-TTCCAAATTCTTCATGACAGA-3′. AllStars Negative Control (Qiagen #1027281) was used as a control.

Microinjection of mouse oocytes

Mouse oocytes were microinjected with 6 pl of mRNAs as previously described[107,108]. For overexpression of ZAR1, YBX2, LSM14B, DDX6, 4E-T and their truncations and mutations, mRNAs were injected at a needle concentration of 0.5 μM. To minimize the effect of ZAR1 on MARDO dissolution when following MARDO dynamics, mRNAs were injected at 0.05 μM. *Mito-EGFP* was injected at 0.2 μM. In the tdPCP-PP7 tethering assay, *mClover3-2×PP7* and *mScarlet* were injected at 0.2 μM and 0.1 μM respectively, while *tdPCP* and *tdPCP-Zar1* were overexpressed and injected at 0.5 μM. In the RNase injection assay, 6 pl 10% RNase Cocktail Enzyme Mix (Thermo Fisher Scientific #AM2286) in PBS was injected into each oocyte. Mouse follicles were microinjected with 6 pl of siRNAs at a needle concentration of 2 μM as previously described[101].

Confocal microscopy

For confocal imaging, oocytes were imaged in 3 to 5 μl of M2 medium (for live mouse oocytes) or PBS with 10% fetal bovine serum (Gibco #16000-044) or 5 mg/ml UltraPure BSA (Thermo Fisher Scientific #AM2616) (for fixed oocytes) under paraffin oil in a 35-

mm dish with a #1.0 coverslip. Images were acquired with LSM 880 confocal laser scanning microscopes (Zeiss) equipped with an environmental incubator box and a 40× C-Apochromat 1.2 NA water-immersion objective. Airyscan images were acquired using the Airyscan module on LSM880 confocal laser scanning microscopes (Zeiss) and processed in ZEN (Zeiss) after acquisition. Images of the control and experimental groups were acquired under identical imaging conditions on the same microscope. Care was taken that the imaging conditions (laser power, pixel-dwell time, and detector gain) did not cause phototoxicity (for live imaging), photobleaching, or saturation.

Electron microscopy and immuno-gold labeling

Mouse oocytes with or without ZAR1-mClover3 overexpression were fixed in 100 mM HEPES (pH 7.0, titrated with KOH), 50 mM EGTA (pH 7.0, titrated with KOH), 10 mM MgSO4, 3% EM-grade glutaraldehyde and 0.5% methanol-free formaldehyde at 37°C for 1 h. All following processing steps were performed in a microwave (Ted Pella) and oocytes were washed three times with water for 40 s at 250 W in between every staining step. Oocytes were first stained with 2% osmium tetroxide in water for 12 minutes at 100 W (microwave cycling between on-off every 2 minutes). Oocytes were then stained with 1% uranyl acetate in water for 12 minutes at 100 W (microwave cycling between on-off every 2 minutes). Oocytes were subsequently dehydrated in a graded ethanol series (10, 30, 50, 75, 90, 100 and 100%) for 40 s at 250 W and infiltrated in a graded series (25, 50, 75, 90, 100 and 100%) of Epon resin in ethanol for 3 minutes at 250 W. Samples were then cured overnight at 60°C. Ultra-thin sections (50 – 70 nm) were cut using a diamond knife (Diatome) on an EM UC7 ultramicrotome (Leica) and placed on copper grids.

For immuno-gold labeling, grids were incubated with 1% BSA in PBS (PBS-BSA) for 5 minutes followed by 10 µg/ml goat anti-GFP (Rockland Immunochemicals #600-101-215) in PBS-BSA for 30 minutes. Grids were then washed with PBS and incubated with 10 nm gold-conjugated donkey anti-goat (Aurion #810.333) in PBS-BSA at 1:20 dilution for 30 minutes. Grids were further washed with PBS, contrast-enhanced using UranylLess (Electron Microscopy Sciences #22400) and air-dried. Grids were visualized on a LEO 912 transmission electron microscope (Zeiss) operated at 120 kV.

In vitro phase separation assay

To investigate phase separation of SMT3-ZAR1(1-263), proteins and negative controls dissolved in buffer containing 50 mM HEPES pH 7.4, 300 mM NaCl and 2 mM DTT were diluted with 50 mM HEPES pH 7.4, 2 mM DTT to reach different protein concentrations and different salt conditions. Protein dilution was performed on collagen IV-coated µ-Slide 18 well slide (Ibidi #81822), and the samples were kept in a humidifying chamber for 30 minutes before imaging. To check phase separation of SMT3-ZAR1(1-263) and

ZAR1(1-263) at physiological salt concentration, proteins were diluted to 40 μM in a buffer containing 50 mM HEPES pH 7.4, 150 mM NaCl, 2mM DTT, and 10% Ficoll 400, and were then imaged immediately. To perform FRAP assay in condensates of SMT3-ZAR1(1-263) and ZAR1(1-263) at physiological salt concentration, proteins were dialyzed with 50 mM HEPES pH 7.4, 300 mM NaCl and 0.5 mM TCEP to remove DTT, and were then conjugated with Alexa Fluor 488 C_5 Maleimide (Thermo Fisher Scientific #A10254). Excess dyes were removed by passing through the NAP-5 desalting column (Sigma-Aldrich #GE17-0853-01). 98% non-labeled proteins and 2% labeled proteins were mixed and diluted as above.

Fluorescence recovery after photobleaching (FRAP)

Oocytes expressing ZAR1-mScarlet or condensates labeled by Alexa Fluor 488 were used to perform FRAP assay. Rectangular or circular regions of interest (ROIs) were marked and photobleached using the corresponding excitation laser line at the maximum power after the third time point. Images were captured every 4 s (in vivo) or 1 s (in vitro), and mean intensities of ROIs over time were recorded. Intensities are normalized by subtracting the remaining signal after photobleaching and then normalized to the average intensity of the first three time points before photobleaching.

tdPCP-PP7 tethering assay

0.2 μM reporter mRNA *mClover3-2×PP7* and 0.1 μM injection control *mScarlet* were co-injected with either 0.5 μM *tdPCP* (tandem dimer of PCP) or 0.5 μM *tdPCP-Zar1* mRNA into GV oocytes or oocytes that had just undergo GVBD. Reporter mRNA contains an oligo(A) tail followed by oligo(C) ($A_{34}C_{17}$), and all the other mRNAs contain ~150 bp poly(A) tail. The expression of reporter mRNA was assessed by the signal ratio of mClover3 to mScarlet at 8 h after mRNA injection.

Vital stain labeling and drug treatment

The fluorescence intensity ratio of TMRM to MitoTracker Green (MTG) was used to monitor mitochondrial membrane potential. TMRM was diluted in anhydrous DMSO (Thermo Fisher Scientific #D12345) to make a 25 μM stock. MitoTracker Green and SiR-DNA were diluted in DMSO to make 1 mM stocks. Culture medium containing 400 nM MitoTracker Green, 25 nM TMRM and 2 μM SiR-DNA was prepared freshly, and prewarmed for 30 minutes at 37°C. Oocytes were stained for 30 minutes at 37°C, and were then washed with culture medium without dyes. Oocytes were imaged as quickly as possible after labeling. Antimycin A (Sigma-Aldrich #A8674) was diluted in ethanol to make a 10 mg/ml stock. FCCP (Sigma-Aldrich #C2920) and oligomycin A (Sigma-

Aldrich #75351) were diluted in DMSO to make 10 mM stock and 5 mM stock respectively. Antimycin A was used at the final concentration of 5 μg/ml in culture medium. FCCP and oligomycin A were used at 5 μM. Oocytes were treated for 1 h at 37°C before fixation. To do drug treatment simultaneously with TMRM/MTG staining, oocytes were incubated with 200 nM MitoTracker Green, 12.5 nM TMRM and the drug, and were imaged as quickly as possible after 1 h treatment at 37°C. RO-3306 (Sigma-Aldrich #SML0569), MG-132(Selleckchem #S2619) and nocodazole (Sigma-Aldrich #M1404) were diluted in DMSO to make 10 mM stocks, and were added to treat oocytes at the final concentration of 10 μM. U0126 (Calbiochem #662005) was diluted in DMSO to make a 50 mM stock, and was used at 20 μM. 10% 1,6-hexanediol (Sigma-Aldrich #240117) in culture medium was prepared freshly, and diluted to 3% and 5% for use. Oocytes were treated for 5 minutes at 37°C before fixation.

ZAR1 Trim-Away in mouse oocytes

An anti-ZAR1 antibody was raised in guinea pig against a synthetic peptide corresponding to amino acids 152-168 of mouse ZAR1, and was further purified by affinity purification (Cambridge Research Biochemicals). Ultrafiltration (Merck Millipore #UFC510024) was performed to change the buffer of the anti-ZAR1 antibody and control IgG (Merck Millipore #12-370) to PBS. 2 pl of 0.3 μM *Trim* mRNA and 4 pl of 1.2 mg/ml antibody containing 0.1% NP-40 were microinjected as previously described[109]. Oocytes were fixed at 16 h post injection.

RNA sequencing and data analysis

GV oocytes were collected from three *Zar1*$^{+/+}$ and three *Zar1*$^{-/-}$ mice. 10 oocytes collected from the same mouse were combined to prepare RNA-seq library using the QIAseq FX Single Cell RNA Library Kit (Qiagen #180733). Libraries were prepared according to the handbook of the kit with the following changes. The zona pellucida of oocyte was removed in Acidic Tyrode's Solution (Merck Millipore #MR-004-D) before cell lysis. The adapters in the kit were replaced with xGen UDI-UMI Adapters (Integrated DNA Technologies #10006914). Sequencing of multiplexed libraries with paired-end reads (PE75) was carried out using a NextSeq 550 system (Illumina) at an average sequencing depth of 50 million reads per library. Adapters were trimmed with cutadapt 2.8[110] using the "-q 20 -m 35 -j 15" parameters. Reads were mapped against the Gencode GRCm39 reference genome with the STAR 2.7.8a[111] aligner using the default settings. Counting of reads mapping to features in the Gencode vM26 annotation file was performed with HTSeq 0.13.5[112]. Differentially expressed genes (DEGs, adjusted p-value < 0.05, average log2 fold change $\geqslant$ 0.5) were identified with the DESeq2 v1.32.0[113] package in R. Down-regulated or up-regulated phenotype-

associated pathways were identified with gene set enrichment analysis (GSEA) using the fgsea v1.18.0[114] package in R and the MSigDB[115,116] C5 (ontology) gene set. To find out mRNAs that are translationally activated during meiosis, TMM-normalized CPM values from the RiboTag/RNA-seq experiments of GEO accession number GSE135525[80] were re-analyzed with the Bioconductor packages edgeR v3.34.1[117] and Limma v3.48.3[118].

RT-qPCR

GV oocytes were collected from three *Zar1*$^{+/+}$ and three *Zar1*$^{-/-}$ mice. 10 oocytes collected from the same mouse were combined to do reverse transcription and whole transcriptome amplification using the REPLI-g WTA Single Cell Kit (Qiagen #180733). The cDNA was diluted 1:100, and 5 µl was used for a 25 µl reaction. qPCR was performed on the Rotor-Gene Q (Qiagen) system using the PowerUp SYBR Green Master Mix (Thermo Fisher Scientific #A25742). Endogenous *Actin* (*Actb*) was used as internal control to calculate relative transcript levels in *Zar1*$^{-/-}$ versus *Zar1*$^{+/+}$ oocytes. Three cDNA libraries were built for each genotype. Each library had three technical repeats.

To quantify transcript levels with or without ZAR1 overexpression, 3 amol *mScarlet* or *Zar1-mScarlet* mRNA was injected into GV oocytes. Three hours later, half oocytes were transferred to dbcAMP-free medium for in vitro maturation. After 17 hours, in vitro matured MII oocytes and the remaining GV oocytes were used to prepare cDNA libraries. RT-qPCR was performed using the same method as above. Six cDNA libraries each containing 5 oocytes were built for each experimental condition (*mScarlet* GV, *mScarlet* MII, *Zar1-mScarlet* GV, *Zar1-mScarlet* MII). Each library had three technical repeats.

Primers used for qPCR

Primer name	Primer number	Sequence
Tcstv1 S	P49	GAGGTCTTCCAGAGTGAGAGT
Tcstv1 AS	P50	GTTGGTCTGGCTTCTCTGTATC
Wdr37 S	P51	TGTACGTGTGGCTAAGGATATG
Wdr37 AS	P52	TGGACACTCCAGCACATAATAG
Elovl7 S	P53	GAGAGAGTATTGTGCTGGATGAG
Elovl7 AS	P54	ACCTATGCTGTGCTGTTTGA
Appl1 S	P55	CAGGTTGGCCTAGATCACATAC
Appl1 AS	P56	ACGTAACTGAAGCTGGTTACTC
Slx4ip S	P57	AGCACTTGGTGCTGGAATAG
Slx4ip AS	P58	CTGCACATGCACAACTTCAC
Tex19.1 S	P59	ACCTGCTACCTGTGGAATAAAG

Tex19.1 AS	P60	GTGATAAACAGCCTCTCTCCTG
Epsti1 S	P61	GAAAGCAATCCAGAGGGAGAAG
Epsti1 AS	P62	GGACTGATGATGCTCTCGAAAT
Cox17 S	P63	CTGCCCGGAAACCAAGAA
Cox17 AS	P64	CTTAAATCCCAGTGCCCTCAT
Tle6 S	P65	CACAGCACTCTGGCAATTAGA
Tle6 AS	P66	GCTCACAGCTACCACCAATAG
Rps13 S	P67	GCACCTTGAGAGGAACAGAA
Rps13 AS	P68	GAGCACCCGCTTAGTCTTATAG
Ybx2 S	P69	TTCTTCTATCGAAGGCGGTTTG
Ybx2 AS	P70	TGCTGTCTCCTTGGGTTCTA
Zp2 S	P71	CAGGAAGGATGAGTACCCTCTA
Zp2 AS	P72	GTTGCCCAGCAGTCATCTAA
Actb S	P73	CCGTAAAGACCTCTATGCCAAC
Actb AS	P74	AGGAGCCAGAGCAGTAATCT

Immunoblotting

Oocytes were quickly washed in PBS, resuspended in 10 µl PBS, and immediately snap-frozen in liquid nitrogen. 10 µl of 2×NuPAGE LDS Sample Buffer (Thermo Fisher Scientific #NP0007) with 100 mM DTT was then added followed by heating at 95°C for 10 minutes. Samples were resolved on a 10-well NuPAGE 10% Bis-Tris protein gel of 1.0 mm thickness (Thermo Fisher Scientific #NP0301BOX) with NuPAGE MOPS SDS Running Buffer (Thermo Fisher Scientific #NP0001). Proteins were then transferred onto a 0.45 µm PVDF membrane (Thermo Fisher Scientific #LC2005) with NuPAGE Transfer Buffer (Thermo Fisher Scientific #NP0006). Blocking and antibody incubations were performed in PBS with 5% skim milk and 0.1% tween-20. Primary antibodies used were goat anti-ZAR1 diluted at 1:200 (Santa Cruz Biotechnology #sc-55994), guinea pig anti-non-phosphorylated-ZAR1 diluted at 1:200 (made by Cambridge Research Biochemicals), mouse anti-FLAG diluted at 1:200 (Sigma-Aldrich #F3165), rabbit anti-TEX19.1 diluted at 1:200 (Abcam #ab129726), rabbit anti-EPSTI1 diluted at 1:200 (Proteintech #11627-1-AP), and rabbit anti-DDB1 diluted at 1:4000 (Abcam #ab109027). Secondary antibodies used were HRP-conjugated anti-goat (Santa Cruz Biotechnology #sc-2020), anti-guinea pig (Thermo Fisher Scientific #A18775), anti-mouse (Dako # P0260) and anti-rabbit (Abcam #ab205718). All of them were diluted 1:1000 for use. Blots were developed with SuperSignal West Femto Maximum Sensitivity Substrate (Thermo Fisher Scientific #34095) and documented with Amersham Imager 600 (Cytiva). Care was taken that the exposure time did not cause saturation.

In vitro phosphorylation assay

8 µl 80 µM HIS-SMT3-mZAR1(1-263) in 50 mM HEPES 7.4, 300 mM NaCl, 2 mM DTT was mixed with 2 µl 30 mM MgCl2, 6 mM ATP, 1 µl 100 mM DTT and 1 µl 0.255 mg/ml CDK1-CCNB1 (Enzo Life Sciences #BML-SE295-0010). The reaction mixture was kept at 25°C for 1.5 hours.

Mass spectrometry analysis

Protein samples were processed as previously[119]. The resulting peptides were enriched by TiO2 before loading to nano HPLC coupled with QExactive HF Mass spectrometer (Thermo Fisher Scientific). The peptides were separated with a linear gradient of 5-40% buffer B (80% acetonitrile and 0.1% formic acid) at flow rate of 300 nl/min over 48 minutes total gradient time. The MS data was acquired by scanning the precursors in mass range from 350 to 1600 m/z at a resolution of 60,000 at m/z 200. Top 20 precursor ion were chosen for MS2 by using data-dependent acquisition (DDA) mode at a resolution of 15,000 at m/z 200 with maximum IT of 50 ms. Data analysis and search was performed using Maxquant Software (1.6.17.0) with Uniprot mouse database from April 2016 with 79254 entries.

Image analysis and quantification

Images except for smFISH were all analyzed in ImageJ. The exported data were further processed in Excel and Graphpad Prism 9. Signals from areas without cells were taken as background, and were subtracted before analysis.

Quantification of signals on mitochondrial and in cytosol was performed as below. The channel that labels mitochondria was duplicated, and then processed with Bandpass Filter (filter_large = 40, filter_small = 1, suppress = None, tolerance = 5, autoscale, saturate). Mitochondria were segmented by setting AutoThreshold (Li dark). In rare cases, the threshold value was slightly adjusted for better segmentation. Particles in the range of 0.10 μm^2 – Infinity were added to ROI manager. All non-specific particles outside of the cell were removed. Multi Measure of all channels was applied, and data were saved for further analysis. Mitochondria were then removed to measure fluorescence intensity in cytosol. All the particles were selected (Create Selection) and enlarged for 0.2 – 0.4 µm depending on the size of the particles. After switching to the channel of interest, all signals in the selected region were depleted. The remaining cytosol region was then segmented by setting AutoThreshold (Default). In rare cases, the threshold value was adjusted slightly for better segmentation. The cytosol region was then selected and measured. Average fluorescence intensity on mitochondria was measured by dividing the total intensity by the total area of all objects larger than 0.10 μm^2. The ratio of average intensities between two channels (TMRM/MTG) or between

mitochondria and cytosol was then calculated and normalized. The number of objects (larger than 0.10 μm^2) is also the number (N) of mitochondrial clusters. 1/N was applied as the mitochondrial clustering index, and was normalized to assess mitochondrial clustering.

To quantify total fluorescence intensity change of ZAR1-mScarler or LSM14B-mScarlert over time, Z projection (Sum Slices) was performed first, and then all time points were measured by applying Measure Stack. Except for this experiment, all other fluorescence intensity measurements refer to measurement of the average fluorescence intensity. To measure average fluorescence intensity in oocyte, oocytes were segmented by applying a suitable threshold, or were manually outlined if there is no marker labeling the entire oocyte. To quantify the number of PLA spots, Watershed was applied to separate connected spots after proper thresholding.

Z stacks of smFISH were analyzed with Imaris (Bitplane). Images were processed with "Normalize Layers" before analysis. MARDO labeled by ZAR1-mClover3 was segmented using the "Surface" function of Imaris (Surfaces Detail: 0.165, Background Subtraction: 0.62). Automatic threshold was selected. Surfaces were further filtered with "Number of Voxels Img=1" above 1000. Spots of mRNA were detected with an estimated diameter of 1.2 μm in XY and 2.4 μm in Z, and with "Background Subtraction". A suitable threshold was selected to detect mRNA spots as accurately as possible. Falsely detected spots were removed manually. "Distance transformation" was then performed to calculate the shortest distance of each spot to the surface (MARDO). If the distance is 0, it means that the mRNA spot is inside of MARDO. If the distance is more than 0 but less than 0.6 μm, it means that the mRNA spot is attached to MARDO.

Statistical analysis

The standard deviation (SD) was used as y axis error bars for bar charts and curves plotted from the mean value of the data. Statistical significance based on unpaired, two-tailed Student's t test (for comparison of two groups) was calculated in Excel. Statistical significance based on one-way ANOVA followed by Tukey's *post-hoc* test (for comparison of three or more groups) was calculated in Graphpad Prism 9. All data are from at least two independent experiments. P values are designated as $****P < 0.0001$, $***P < 0.001$, $**P < 0.01$, $*P < 0.05$. Nonsignificant values are indicated as N.S.

References

1 Stitzel, M. L. & Seydoux, G. Regulation of the oocyte-to-zygote transition. *Science* **316**, 407-408, doi:10.1126/science.1138236 (2007).

2 Li, L., Zheng, P. & Dean, J. Maternal control of early mouse development. *Development* **137**, 859-870, doi:10.1242/dev.039487 (2010).

3 Reader, K. L., Stanton, J. L. & Juengel, J. L. The Role of Oocyte Organelles in Determining Developmental Competence. *Biology (Basel)* **6**, doi:10.3390/biology6030035 (2017).

4 Moore, G. P., Lintern-Moore, S., Peters, H. & Faber, M. RNA synthesis in the mouse oocyte. *J Cell Biol* **60**, 416-422, doi:10.1083/jcb.60.2.416 (1974).

5 Dumdie, J. N. *et al.* Chromatin Modification and Global Transcriptional Silencing in the Oocyte Mediated by the mRNA Decay Activator ZFP36L2. *Dev Cell* **44**, 392-402 e397, doi:10.1016/j.devcel.2018.01.006 (2018).

6 Lin, Y., Protter, D. S., Rosen, M. K. & Parker, R. Formation and Maturation of Phase-Separated Liquid Droplets by RNA-Binding Proteins. *Mol Cell* **60**, 208-219, doi:10.1016/j.molcel.2015.08.018 (2015).

7 Feric, M. *et al.* Coexisting Liquid Phases Underlie Nucleolar Subcompartments. *Cell* **165**, 1686-1697, doi:10.1016/j.cell.2016.04.047 (2016).

8 Youn, J. Y. *et al.* Properties of Stress Granule and P-Body Proteomes. *Mol Cell* **76**, 286-294, doi:10.1016/j.molcel.2019.09.014 (2019).

9 Seydoux, G. The P Granules of C. elegans: A Genetic Model for the Study of RNA-Protein Condensates. *J Mol Biol* **430**, 4702-4710, doi:10.1016/j.jmb.2018.08.007 (2018).

10 Trcek, T. & Lehmann, R. Germ granules in Drosophila. *Traffic* **20**, 650-660, doi:10.1111/tra.12674 (2019).

11 Jamieson-Lucy, A. & Mullins, M. C. The vertebrate Balbiani body, germ plasm, and oocyte polarity. *Curr Top Dev Biol* **135**, 1-34, doi:10.1016/bs.ctdb.2019.04.003 (2019).

12 Brangwynne, C. P. *et al.* Germline P granules are liquid droplets that localize by controlled dissolution/condensation. *Science* **324**, 1729-1732, doi:10.1126/science.1172046 (2009).

13 Marnik, E. A. & Updike, D. L. Membraneless organelles: P granules in Caenorhabditis elegans. *Traffic* **20**, 373-379, doi:10.1111/tra.12644 (2019).

14 Kistler, K. E. *et al.* Phase transitioned nuclear Oskar promotes cell division of Drosophila primordial germ cells. *Elife* **7**, doi:10.7554/eLife.37949 (2018).

15 Kloc, M., Bilinski, S. & Etkin, L. D. The Balbiani body and germ cell determinants: 150 years later. *Curr Top Dev Biol* **59**, 1-36, doi:10.1016/S0070-2153(04)59001-4 (2004).

16 Boke, E. *et al.* Amyloid-like Self-Assembly of a Cellular Compartment. *Cell* **166**, 637-650, doi:10.1016/j.cell.2016.06.051 (2016).

17 Roovers, E. F. *et al.* Tdrd6a Regulates the Aggregation of Buc into Functional Subcellular Compartments that Drive Germ Cell Specification. *Dev Cell* **46**, 285-301 e289, doi:10.1016/j.devcel.2018.07.009 (2018).

18 (!!! INVALID CITATION !!! (11, 18)).

19 Hertig, A. T. & Adams, E. C. Studies on the human oocyte and its follicle. I. Ultrastructural and histochemical observations on the primordial follicle stage. *J Cell Biol* **34**, 647-675, doi:10.1083/jcb.34.2.647 (1967).

20 Hertig, A. T. The primary human oocyte: some observations on the fine structure of Balbiani's vitelline body and the origin of the annulate lamellae. *Am J Anat* **122**, 107-137, doi:10.1002/aja.1001220107 (1968).

21 Pepling, M. E., Wilhelm, J. E., O'Hara, A. L., Gephardt, G. W. & Spradling, A. C. Mouse oocytes within germ cell cysts and primordial follicles contain a Balbiani body. *Proc Natl Acad Sci U S A* **104**, 187-192, doi:10.1073/pnas.0609923104 (2007).

22 Lei, L. & Spradling, A. C. Mouse oocytes differentiate through organelle enrichment from sister cyst germ cells. *Science* **352**, 95-99, doi:10.1126/science.aad2156 (2016).

23 Dhandapani, L. *et al.* Comparative analysis of vertebrates reveals that mouse primordial oocytes do not contain a Balbiani body. *J Cell Sci* **135**, doi:10.1242/jcs.259394 (2022).

24 Flemr, M., Ma, J., Schultz, R. M. & Svoboda, P. P-Body Loss Is Concomitant with Formation of a Messenger RNA Storage Domain in Mouse Oocytes. *Biol Reprod* **82**, 1008-1017, doi:10.1095/biolreprod.109.082057 (2010).

25 Schier, A. F. The maternal-zygotic transition: death and birth of RNAs. *Science* **316**, 406-407, doi:10.1126/science.1140693 (2007).

26 Yartseva, V. & Giraldez, A. J. The Maternal-to-Zygotic Transition During Vertebrate Development: A Model for Reprogramming. *Curr Top Dev Biol* **113**, 191-232, doi:10.1016/bs.ctdb.2015.07.020 (2015).

27 Vastenhouw, N. L., Cao, W. X. & Lipshitz, H. D. The maternal-to-zygotic transition revisited. *Development* **146**, doi:10.1242/dev.161471 (2019).

28 Ma, J., Flemr, M., Strnad, H., Svoboda, P. & Schultz, R. M. Maternally Recruited DCP1A and DCP2 Contribute to Messenger RNA Degradation During Oocyte Maturation and Genome Activation in Mouse. *Biol Reprod* **88**, doi:ARTN 11

10.1095/biolreprod.112.105312 (2013).

29 Ma, J., Fukuda, Y. & Schultz, R. M. Mobilization of Dormant Cnot7 mRNA Promotes Deadenylation of Maternal Transcripts During Mouse Oocyte Maturation. *Biol Reprod* **93**, 48, doi:10.1095/biolreprod.115.130344 (2015).

30 Pasternak, M., Pfender, S., Santhanam, B. & Schuh, M. The BTG4 and CAF1 complex prevents the spontaneous activation of eggs by deadenylating maternal mRNAs. *Open Biol* **6**, doi:ARTN 160184

10.1098/rsob.160184 (2016).

31 Yu, C. *et al.* BTG4 is a meiotic cell cycle-coupled maternal-zygotic transition licensing factor in oocytes. *Nat Struct Mol Biol* **23**, 387-394, doi:10.1038/nsmb.3204 (2016).

32 Sha, Q. Q. *et al.* CNOT6L couples the selective degradation of maternal transcripts to meiotic cell cycle progression in mouse oocyte. *EMBO J* **37**, doi:10.15252/embj.201899333 (2018).

33 Zhao, L. W. *et al.* PABPN1L mediates cytoplasmic mRNA decay as a placeholder during the maternal-to-zygotic transition. *Embo Rep* **21**, doi:ARTN e49956

10.15252/embr.201949956 (2020).

34 Harvey, A. J. Mitochondria in early development: linking the microenvironment, metabolism and the epigenome. *Reproduction* **157**, R159-R179, doi:10.1530/REP-18-0431 (2019).

35 Anderson, S. *et al.* Sequence and organization of the human mitochondrial genome. *Nature* **290**, 457-465, doi:10.1038/290457a0 (1981).

36 Shoubridge, E. A. & Wai, T. Mitochondrial DNA and the mammalian oocyte. *Curr Top Dev Biol* **77**, 87-111, doi:10.1016/S0070-2153(06)77004-1 (2007).

37 May-Panloup, P., Chretien, M. F., Malthiery, Y. & Reynier, P. Mitochondrial DNA in the oocyte and the developing embryo. *Curr Top Dev Biol* **77**, 51-83, doi:10.1016/S0070-2153(06)77003-X (2007).

38 Kirillova, A., Smitz, J. E. J., Sukhikh, G. T. & Mazunin, I. The Role of Mitochondria in Oocyte Maturation. *Cells* **10**, doi:10.3390/cells10092484 (2021).

39 Sasaki, H. *et al.* Impact of Oxidative Stress on Age-Associated Decline in Oocyte Developmental Competence. *Front Endocrinol (Lausanne)* **10**, 811, doi:10.3389/fendo.2019.00811 (2019).

40 Zhao, Y. G. & Zhang, H. Phase Separation in Membrane Biology: The Interplay between Membrane-Bound Organelles and Membraneless Condensates. *Dev Cell* **55**, 30-44, doi:10.1016/j.devcel.2020.06.033 (2020).

41 Ma, W. R. & Mayr, C. A Membraneless Organelle Associated with the Endoplasmic Reticulum Enables 3 ' UTR-Mediated Protein-Protein Interactions. *Cell* **175**, 1492-+, doi:10.1016/j.cell.2018.10.007 (2018).

42 Liao, Y. C. *et al.* RNA Granules Hitchhike on Lysosomes for Long-Distance Transport, Using Annexin A11 as a Molecular Tether. *Cell* **179**, 147-+, doi:10.1016/j.cell.2019.08.050 (2019).

43 Nguyen-Chi, M. & Morello, D. RNA-binding proteins, RNA granules, and gametes: is unity strength? *Reproduction* **142**, 803-817, doi:10.1530/REP-11-0257 (2011).

44 Lehtiniemi, T. & Kotaja, N. Germ granule-mediated RNA regulation in male germ cells. *Reproduction* **155**, R77-R91, doi:10.1530/REP-17-0356 (2018).

45 Wang, X., Lv, C., Guo, Y. & Yuan, S. Mitochondria Associated Germinal Structures in Spermatogenesis: piRNA Pathway Regulation and Beyond. *Cells* **9**, doi:10.3390/cells9020399 (2020).

46 Zacharogianni, M., Gomez, A. A., Veenendaal, T., Smout, J. & Rabouille, C. A stress assembly that confers cell viability by preserving ERES components during amino-acid starvation. *Elife* **3**, doi:ARTN e04132

10.7554/eLife.04132 (2014).

47 Fujioka, Y. *et al.* Phase separation organizes the site of autophagosome formation. *Nature* **578**, 301-+, doi:10.1038/s41586-020-1977-6 (2020).

48 Lee, J. E., Cathey, P. I., Wu, H. X., Parker, R. & Voeltz, G. K. Endoplasmic reticulum contact sites regulate the dynamics of membraneless organelles. *Science* **367**, 527-+, doi:ARTN eaay7108

10.1126/science.aay7108 (2020).

49 Zhang, G. M., Wang, Z., Du, Z. & Zhang, H. mTOR Regulates Phase Separation of PGL Granules to Modulate Their Autophagic Degradation. *Cell* **174**, 1492-+, doi:10.1016/j.cell.2018.08.006 (2018).

50 Milovanovic, D., Wu, Y. M., Bian, X. & De Camilli, P. A liquid phase of synapsin and lipid vesicles. *Science* **361**, 604-+, doi:10.1126/science.aat5671 (2018).

51 Yu, X. *et al.* The STING phase-separator suppresses innate immune signalling. *Nat Cell Biol* **23**, 330-340, doi:10.1038/s41556-021-00659-0 (2021).

52 So, C., Cheng, S. & Schuh, M. Phase Separation during Germline Development. *Trends Cell Biol* **31**, 254-268, doi:10.1016/j.tcb.2020.12.004 (2021).

53 Yamamoto, T. M. *et al.* Zar1 represses translation in Xenopus oocytes and binds to the TCS in maternal mRNAs with different characteristics than Zar2. *Biochim Biophys Acta* **1829**, 1034-1046, doi:10.1016/j.bbagrm.2013.06.001 (2013).

54 Miao, L. *et al.* Translation repression by maternal RNA binding protein Zar1 is essential for early oogenesis in zebrafish. *Development* **144**, 128-138, doi:10.1242/dev.144642 (2017).

55 Rong, Y. *et al.* ZAR1 and ZAR2 are required for oocyte meiotic maturation by regulating the maternal transcriptome and mRNA translational activation. *Nucleic Acids Res* **47**, 11387-11402, doi:10.1093/nar/gkz863 (2019).

56 Deutschmeyer, V. E. & Richter, A. M. The ZAR1 protein in cancer; from epigenetic silencing to functional characterisation and epigenetic therapy of tumour suppressors. *Biochim Biophys Acta Rev Cancer* **1874**, 188417, doi:10.1016/j.bbcan.2020.188417 (2020).

57 Bouvet, P. & Wolffe, A. P. A Role for Transcription and Frgy2 in Masking Maternal Messenger-Rna within Xenopus-Oocytes. *Cell* **77**, 931-941, doi:Doi 10.1016/0092-8674(94)90141-4 (1994).

58 Yu, J. Y., Hecht, N. B. & Schultz, R. M. Expression of MSY2 in mouse oocytes and preimplantation embryos. *Biol Reprod* **65**, 1260-1270, doi:DOI 10.1095/biolreprod65.4.1260 (2001).

59 Yu, J. Y., Hecht, N. B. & Schultz, R. M. RNA-binding properties and translation repression in vitro by germ cell-specific MSY2 protein. *Biol Reprod* **67**, 1093-1098, doi:10.1095/biolreprod67.4.1093 (2002).

60 Medvedev, S., Pan, H. & Schultz, R. M. Absence of MSY2 in Mouse Oocytes Perturbs Oocyte Growth and Maturation, RNA Stability, and the Transcriptome. *Biol Reprod* **85**, 575-583, doi:10.1095/biolreprod.111.091710 (2011).

61 Zhang, T. *et al.* RNA-associated protein LSM family member 14 controls oocyte meiotic maturation through regulating mRNA pools. *J Reprod Develop* **63**, 383-388 (2017).

62 Kato, Y. *et al.* ELAVL2-directed RNA regulatory network drives the formation of quiescent primordial follicles. *Embo Rep* **20**, doi:ARTN e48251

10.15252/embr.201948251 (2019).

63 Rasch, F., Weber, R., Izaurralde, E. & Igreja, C. 4E-T-bound mRNAs are stored in a silenced and deadenylated form. *Gene Dev* **34**, 847-860, doi:10.1101/gad.336073.119 (2020).

64 Seli, E. *et al.* An embryonic poly(A)-binding protein (ePAB) is expressed in mouse oocytes and early preimplantation embryos. *P Natl Acad Sci USA* **102**, 367-372, doi:10.1073/pnas.0408378102 (2005).

65 Guzeloglu-Kayisli, O. *et al.* Embryonic poly(A)-binding protein (EPAB) is required for oocyte maturation and female fertility in mice. *Biochem J* **446**, 47-58, doi:10.1042/Bj20120467 (2012).

66 Creed, S. & McKenzie, M. Measurement of Mitochondrial Membrane Potential with the Fluorescent Dye Tetramethylrhodamine Methyl Ester (TMRM). *Methods Mol Biol* **1928**, 69-76, doi:10.1007/978-1-4939-9027-6_5 (2019).

67 Al-Zubaidi, U. *et al.* The spatio-temporal dynamics of mitochondrial membrane potential during oocyte maturation. *Mol Hum Reprod* **25**, 695-705, doi:10.1093/molehr/gaz055 (2019).

68 Yang, H. *et al.* Dynamic Modeling of Mitochondrial Membrane Potential Upon Exposure to Mitochondrial Inhibitors. *Front Pharmacol* **12**, doi:10.3389/fphar.2021.679407 (2021).

69 Csordas, G., Weaver, D. & Hajnoczky, G. Endoplasmic Reticulum-Mitochondrial Contactology: Structure and Signaling Functions. *Trends in Cell Biology* **28**, 523-540, doi:10.1016/j.tcb.2018.02.009 (2018).

70 Maharana, S. *et al.* RNA buffers the phase separation behavior of prion-like RNA binding proteins. *Science* **360**, 918-921, doi:10.1126/science.aar7366 (2018).

71 Brandmann, T. *et al.* Molecular architecture of LSM14 interactions involved in the assembly of mRNA silencing complexes. *EMBO J* **37**, doi:10.15252/embj.201797869 (2018).

72 Cook, J. M. *Zygote arrest (Zar) protein-mediated translational control in Xenopus laevis development: Requirement for the poly(A) tail and protein interactions*, University of Colorado at Denver, (2015).

73 Wu, X. M. *et al.* Zygote arrest 1 (Zar1) is a novel maternal-effect gene critical for the oocyte-to-embryo transition. *Nat Genet* **33**, 187-191, doi:10.1038/ng1079 (2003).

74 Bai, D. D. *et al.* Genome transfer for the prevention of female infertility caused by maternal gene mutation. *J Genet Genomics* **47**, 311-319, doi:10.1016/j.jgg.2020.06.002 (2020).

75 Clift, D. *et al.* A Method for the Acute and Rapid Degradation of Endogenous Proteins. *Cell* **171**, 1692-1706 e1618, doi:10.1016/j.cell.2017.10.033 (2017).

76 Xie, F., Timme, K. A. & Wood, J. R. Using Single Molecule mRNA Fluorescent in Situ Hybridization (RNA-FISH) to Quantify mRNAs in Individual Murine Oocytes and Embryos. *Sci Rep-Uk* **8**, doi:ARTN 7930

10.1038/s41598-018-26345-0 (2018).

77 Jansova, D., Tetkova, A., Koncicka, M., Kubelka, M. & Susor, A. Localization of RNA and translation in the mammalian oocyte and embryo. *Plos One* **13**, doi:ARTN e0192544

10.1371/journal.pone.0192544 (2018).

78 Lim, F., Downey, T. P. & Peabody, D. S. Translational repression and specific RNA binding by the coat protein of the Pseudomonas phage PP7. *J Biol Chem* **276**, 22507-22513, doi:10.1074/jbc.M102411200 (2001).

79 Wu, B., Chao, J. A. & Singer, R. H. Fluorescence Fluctuation Spectroscopy Enables Quantitative Imaging of Single mRNAs in Living Cells. *Biophys J* **102**, 2936-2944, doi:10.1016/j.bpj.2012.05.017 (2012).

80 Luong, X. G., Daldello, E. M., Rajkovic, G., Yang, C. R. & Conti, M. Genome-wide analysis reveals a switch in the translational program upon oocyte meiotic resumption. *Nucleic Acids Research* **48**, 3257-3276, doi:10.1093/nar/gkaa010 (2020).

81 Medvedev, S., Yang, J., Hecht, N. B. & Schultz, R. M. CDC2A (CDK1)-mediated phosphorylation of MSY2 triggers maternal mRNA degradation during mouse oocyte maturation. *Dev Biol* **321**, 205-215, doi:10.1016/j.ydbio.2008.06.016 (2008).

82 Wu, Y., Li, M. & Yang, M. Post-Translational Modifications in Oocyte Maturation and Embryo Development. *Front Cell Dev Biol* **9**, 645318, doi:10.3389/fcell.2021.645318 (2021).

83 Holt, J. E., Lane, S. I. & Jones, K. T. The control of meiotic maturation in mammalian oocytes. *Curr Top Dev Biol* **102**, 207-226, doi:10.1016/B978-0-12-416024-8.00007-6 (2013).

84 Holt, L. J. *et al.* Global Analysis of Cdk1 Substrate Phosphorylation Sites Provides Insights into Evolution. *Science* **325**, 1682-1686, doi:10.1126/science.1172867 (2009).

85 Josefsberg, L. B. Y., Galiani, D., Dantes, A., Amsterdam, A. & Dekel, N. The proteasome is involved in the first metaphase-to-anaphase transition of meiosis in rat oocytes. *Biol Reprod* **62**, 1270-1277, doi:DOI 10.1095/biolreprod62.5.1270 (2000).

86 Bouniol-Baly, C. *et al.* Differential transcriptional activity associated with chromatin configuration in fully grown mouse germinal vesicle oocytes. *Biol Reprod* **60**, 580-587, doi:10.1095/biolreprod60.3.580 (1999).

87 Jankowsky, E. RNA helicases at work: binding and rearranging. *Trends Biochem Sci* **36**, 19-29, doi:DOI 10.1016/j.tibs.2010.07.008 (2011).

88 Hondele, M. *et al.* DEAD-box ATPases are global regulators of phase-separated organelles. *Nature* **573**, 144-+, doi:10.1038/s41586-019-1502-y (2019).

89 Astrom, J., Astrom, A. & Virtanen, A. Properties of a Hela Cell-3' Exonuclease Specific for Degrading Poly(a) Tails of Mammalian Messenger-Rna. *Journal of Biological Chemistry* **267**, 18154-18159 (1992).

90 Gout, E., Rebeille, F., Douce, R. & Bligny, R. Interplay of Mg2+, ADP, and ATP in the cytosol and mitochondria: unravelling the role of Mg2+ in cell respiration. *Proc Natl Acad Sci U S A* **111**, E4560-4567, doi:10.1073/pnas.1406251111 (2014).

91 Zhang, Q. L. *et al.* Structural basis for inhibition of the deadenylase activity of human CNOT6L. *Febs Lett* **590**, 1270-1279, doi:10.1002/1873-3468.12160 (2016).

92 Yu, Y., Dumollard, R., Rossbach, A., Lai, F. A. & Swann, K. Redistribution of mitochondria leads to bursts of ATP production during spontaneous mouse oocyte maturation. *J Cell Physiol* **224**, 672-680, doi:10.1002/jcp.22171 (2010).

93 Dalton, C. M. & Carroll, J. Biased inheritance of mitochondria during asymmetric cell division in the mouse oocyte. *J Cell Sci* **126**, 2955-2964, doi:10.1242/jcs.128744 (2013).

94 Gwon, Y. *et al.* Ubiquitination of G3BP1 mediates stress granule disassembly in a context-specific manner. *Science* **372**, 1410-+, doi:ARTN eabf6548

10.1126/science.abf6548 (2021).

95 Zhou, H. L., Geng, C., Luo, G. & Lou, H. The p97-UBXD8 complex destabilizes mRNA by promoting release of ubiquitinated HuR from mRNP. *Genes Dev* **27**, 1046-1058, doi:10.1101/gad.215681.113 (2013).

96 Wang, C. W. & Lee, S. C. The ubiquitin-like (UBX)-domain-containing protein Ubx2/Ubxd8 regulates lipid droplet homeostasis. *J Cell Sci* **125**, 2930-2939, doi:10.1242/jcs.100230 (2012).

97 Li, X. *et al.* Mitochondria shed their outer membrane in response to infection-induced stress. *Science* **375**, eabi4343, doi:10.1126/science.abi4343 (2022).

98 Tworzydlo, W., Sekula, M. & Bilinski, S. M. Transmission of Functional, Wild-Type Mitochondria and the Fittest mtDNA to the Next Generation: Bottleneck Phenomenon, Balbiani Body, and Mitophagy. *Genes (Basel)* **11**, doi:10.3390/genes11010104 (2020).

99 Colnaghi, M., Pomiankowski, A. & Lane, N. The need for high-quality oocyte mitochondria at extreme ploidy dictates mammalian germline development. *Elife* **10**, doi:ARTN e69344

10.7554/eLife.69344 (2021).

100 Shen, B. *et al.* Generation of gene-modified mice via Cas9/RNA-mediated gene targeting. *Cell Res* **23**, 720-723, doi:10.1038/cr.2013.46 (2013).

101 Pfender, S. *et al.* Live imaging RNAi screen reveals genes essential for meiosis in mammalian oocytes. *Nature* **524**, 239-242, doi:10.1038/nature14568 (2015).

102 Bajar, B. T. *et al.* Improving brightness and photostability of green and red fluorescent proteins for live cell imaging and FRET reporting. *Sci Rep* **6**, 20889, doi:10.1038/srep20889 (2016).

103 Bindels, D. S. *et al.* mScarlet: a bright monomeric red fluorescent protein for cellular imaging. *Nat Methods* **14**, 53-56, doi:10.1038/nmeth.4074 (2017).

104 Laker, R. C. *et al.* A novel MitoTimer reporter gene for mitochondrial content, structure, stress, and damage in vivo. *J Biol Chem* **289**, 12005-12015, doi:10.1074/jbc.M113.530527 (2014).

105 Liu, H. & Naismith, J. H. An efficient one-step site-directed deletion, insertion, single and multiple-site plasmid mutagenesis protocol. *BMC Biotechnol* **8**, 91, doi:10.1186/1472-6750-8-91 (2008).

106 So, C. *et al.* A liquid-like spindle domain promotes acentrosomal spindle assembly in mammalian oocytes. *Science* **364**, doi:10.1126/science.aat9557 (2019).

107 Jaffe, L. A. & Terasaki, M. Quantitative microinjection of oocytes, eggs, and embryos. *Methods Cell Biol* **74**, 219-242, doi:10.1016/s0091-679x(04)74010-8 (2004).

108 Schuh, M. & Ellenberg, J. Self-organization of MTOCs replaces centrosome function during acentrosomal spindle assembly in live mouse oocytes. *Cell* **130**, 484-498, doi:10.1016/j.cell.2007.06.025 (2007).

109 Clift, D., So, C., McEwan, W. A., James, L. C. & Schuh, M. Acute and rapid degradation of endogenous proteins by Trim-Away (vol 13, pg 2149, 2018). *Nat Protoc* **14**, 2596-2596, doi:10.1038/s41596-018-0092-8 (2019).

110 Martin, M. Cutadapt removes adapter sequences from high-throughput sequencing reads. *2011* **17**, 3, doi:10.14806/ej.17.1.200 (2011).

111 Dobin, A. *et al.* STAR: ultrafast universal RNA-seq aligner. *Bioinformatics* **29**, 15-21, doi:10.1093/bioinformatics/bts635 (2013).

112 Anders, S., Pyl, P. T. & Huber, W. HTSeq-a Python framework to work with high-throughput sequencing data. *Bioinformatics* **31**, 166-169, doi:10.1093/bioinformatics/btu638 (2015).

113 Love, M. I., Huber, W. & Anders, S. Moderated estimation of fold change and dispersion for RNA-seq data with DESeq2. *Genome Biol* **15**, 550, doi:10.1186/s13059-014-0550-8 (2014).

114 Korotkevich, G. *et al.* Fast gene set enrichment analysis. *bioRxiv*, 060012, doi:10.1101/060012 (2021).

115 Subramanian, A. *et al.* Gene set enrichment analysis: a knowledge-based approach for interpreting genome-wide expression profiles. *Proc Natl Acad Sci U S A* **102**, 15545-15550, doi:10.1073/pnas.0506580102 (2005).

116 Liberzon, A. *et al.* Molecular signatures database (MSigDB) 3.0. *Bioinformatics* **27**, 1739-1740, doi:10.1093/bioinformatics/btr260 (2011).

117 Robinson, M. D., McCarthy, D. J. & Smyth, G. K. edgeR: a Bioconductor package for differential expression analysis of digital gene expression data. *Bioinformatics* **26**, 139-140, doi:10.1093/bioinformatics/btp616 (2010).

118 Ritchie, M. E. *et al.* limma powers differential expression analyses for RNA-sequencing and microarray studies. *Nucleic Acids Res* **43**, e47, doi:10.1093/nar/gkv007 (2015).

119 Shevchenko, A., Wilm, M., Vorm, O. & Mann, M. Mass spectrometric sequencing of proteins silver-stained polyacrylamide gels. *Anal Chem* **68**, 850-858, doi:10.1021/ac950914h (1996).

Acknowledgments

We are grateful to the staff from the Animal Facility, Proteomics Facility, and Live-Cell Imaging Facility of the Max Planck Institute for Multidisciplinary Sciences for technical assistance. We thank the patients who participated in this study; K. Maier for help with RNA sequencing; M. Daniel and L. Wartosch for coordination of animal experiments and license application; K. Rentsch and L. Timm for genotyping; M. Boiani for antibody; P. Lénárt, A. Politi, and E. Mönnich for advices on image analysis and Life Science Editors for critical comments on the manuscript.

Funding

The research leading to these results received financial support from financial support from the Max Planck Society and Deutsche Forschungsgemeinschaft (DFG, German Research Foundation) under Germany's Excellence Strategy (EXC 2067/1-390729940) and a DFG Leibniz Prize (SCHU 3047/1-1) to M.S. S.C. was further supported by an EMBO long-term postdoctoral fellowship.

Author contributions

S.C. and M.S. conceived the study. S.C. and M.S. designed experiments, and methods for data analysis. S.C. and G.A. performed all experiments and analyzed the data with the following exceptions: C.S. performed electron microscopy experiments with T.R.; L.W. performed mass spectrometry experiments; S.M.P. analyzed the RNA-seq data. K. M. collected and fixed human oocytes; K. H. collected mouse oocytes for mass spectrometry analysis in Fig. S1M. H.U. supervised the mass spectrometry experiments. W.M. supervised the electron microscopy experiments. S.C. and M.S. wrote the manuscript and prepared the figures with input from all authors. M.S. supervised the study.

Competing interests

The other authors declare no competing interests.

Data and materials availability

Plasmids are available from M.S. under a material transfer agreement with the Max Planck Society. All data needed to evaluate the conclusions in the paper are present in the main text or the supplementary materials.

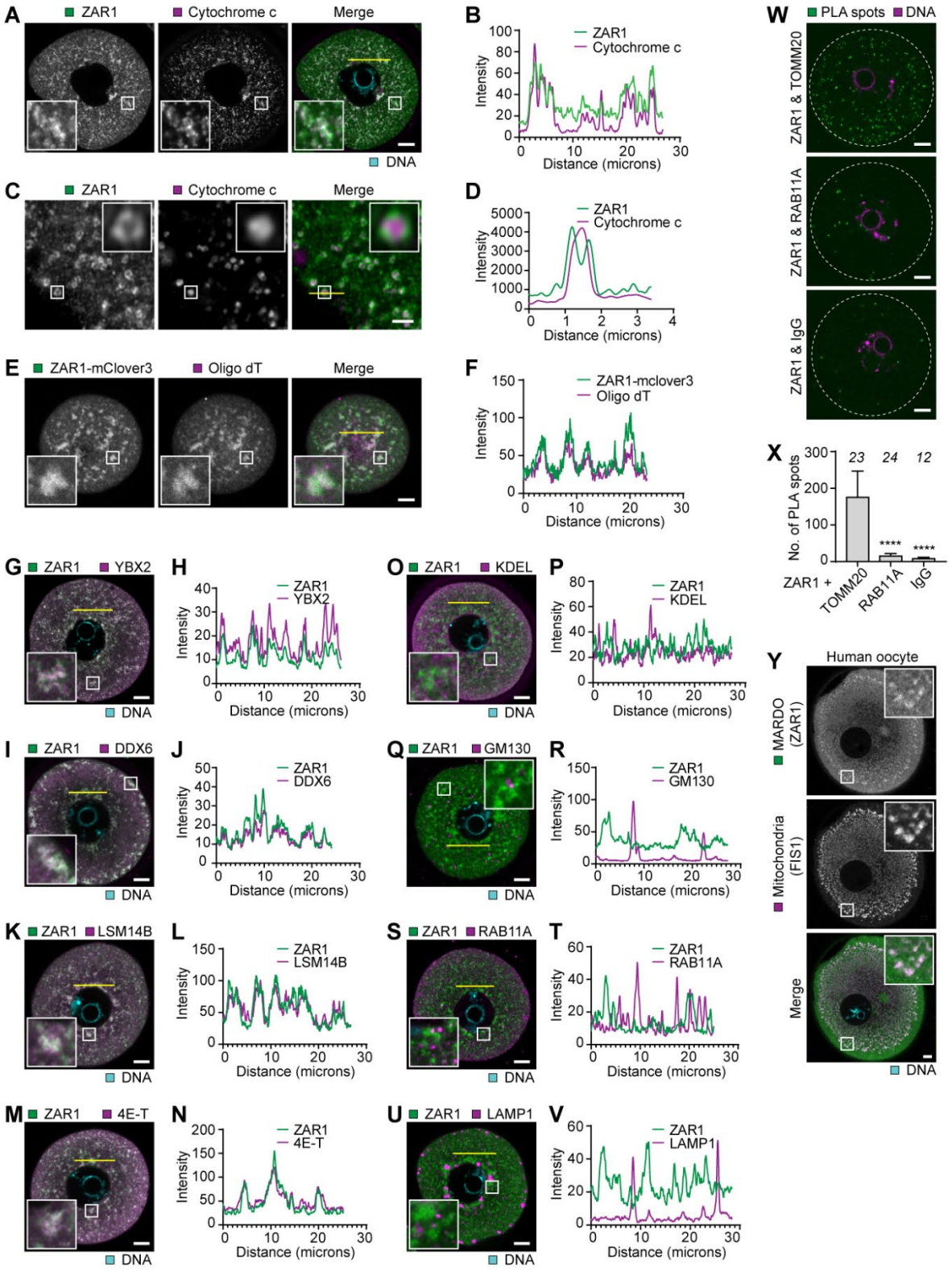
A
ZAR1
Cytochrome c
Merge
DNA
B
ZAR1
Cytochrome c
Intensity
Distance (microns)
C
ZAR1
Cytochrome c
Merge
D
ZAR1
Cytochrome c
Intensity
Distance (microns)
E
ZAR1-mClover3
Oligo dT
Merge
F
ZAR1-mclover3
Oligo dT
Intensity
Distance (microns)
W
PLA spots
DNA
ZAR1 & TOMM20
ZAR1 & RAB11A
ZAR1 & IgG
X
No. of PLA spots
23
24
12
****
****
ZAR1 +
TOMM20
RAB11A
IgG
G
ZAR1
YBX2
DNA
H
ZAR1
YBX2
Intensity
Distance (microns)
O
ZAR1
KDEL
DNA
P
ZAR1
KDEL
Intensity
Distance (microns)
I
ZAR1
DDX6
DNA
J
ZAR1
DDX6
Intensity
Distance (microns)
Q
ZAR1
GM130
DNA
R
ZAR1
GM130
Intensity
Distance (microns)
K
ZAR1
LSM14B
DNA
L
ZAR1
LSM14B
Intensity
Distance (microns)
S
ZAR1
RAB11A
DNA
T
ZAR1
RAB11A
Intensity
Distance (microns)
M
ZAR1
4E-T
DNA
N
ZAR1
4E-T
Intensity
Distance (microns)
U
ZAR1
LAMP1
DNA
V
ZAR1
LAMP1
Intensity
Distance (microns)
Y
Human oocyte
MARDO (ZAR1)
Mitochondria (FIS1)
Merge
DNA

Figure 1

Fig. 1 Identification of a previously unknown mitochondria-associated RNA storage compartment in mammalian oocytes.

(A) Representative immunofluorescence images of mouse GV (germinal vesicle) oocytes. Green, ZAR1; magenta, cytochrome c (mitochondria); blue, DNA. Insets are magnifications of outlined regions.

(B) Intensity profiles of ZAR1 and cytochrome c along the yellow line in (A).

(C) Representative immunofluorescence Airyscan images of mouse GV oocytes. Green, ZAR1; magenta, cytochrome c (mitochondria). Insets are magnifications of outlined regions. Scale bar, 2 μm.

(D) Intensity profiles of ZAR1 and cytochrome c along the yellow line in (C).

(E) Representative RNA fluorescence in situ hybridization (FISH) images of mouse GV oocytes. Green, ZAR1-mClover3; magenta, Cy5-conjugated oligo dT (mRNA). Insets are magnifications of outlined regions.

(F) Intensity profiles of ZAR1-mClover3 and Cy5-conjugated oligo dT along the yellow line in (E).

(G-N) Representative immunofluorescence images of mouse GV oocytes (G, I, K, M). Green, ZAR1; magenta, YBX2 (G), DDX6 (I), LSM14B (K), 4E-T (M); blue, DNA. Insets are magnifications of outlined regions. Intensity profiles along the yellow lines are shown in (H, J, L, N) respectively.

(O-V) Representative immunofluorescence images of mouse GV oocytes (O, Q, S, U). Green, ZAR1; magenta, KDEL (ER) (O), GM130 (Golgi apparatus) (Q), RAB11A (recycling endosomes) (S), LAMP1 (lysosomes) (U); blue, DNA. Insets are magnifications of outlined regions. Intensity profiles along the yellow lines are shown in (P, R, T, V) respectively.

(W) Representative images of in situ proximity ligation assay (PLA) performed with antibody pairs anti-ZAR1 & anti-TOMM20, anti-ZAR1 & anti-RAB11A, or anti-ZAR1 & IgG (immunoglobulin G) control in mouse GV oocytes. Green, PLA spots; magenta, DNA. Dashed lines demarcate the oocytes.

(X) Quantification of the number of PLA spots in (W).

(Y) Representative immunofluorescence images of human GV oocytes. Green, MARDO (ZAR1); magenta, mitochondria (FIS1); blue, DNA. Insets are magnifications of outlined regions.

The number of analyzed oocytes is specified in italics in (X). Data are shown as mean ± SD. *P* values were calculated using one-way ANOVA with Tukey's *post-hoc* test. Scale bars, 10 μm unless otherwise specified.

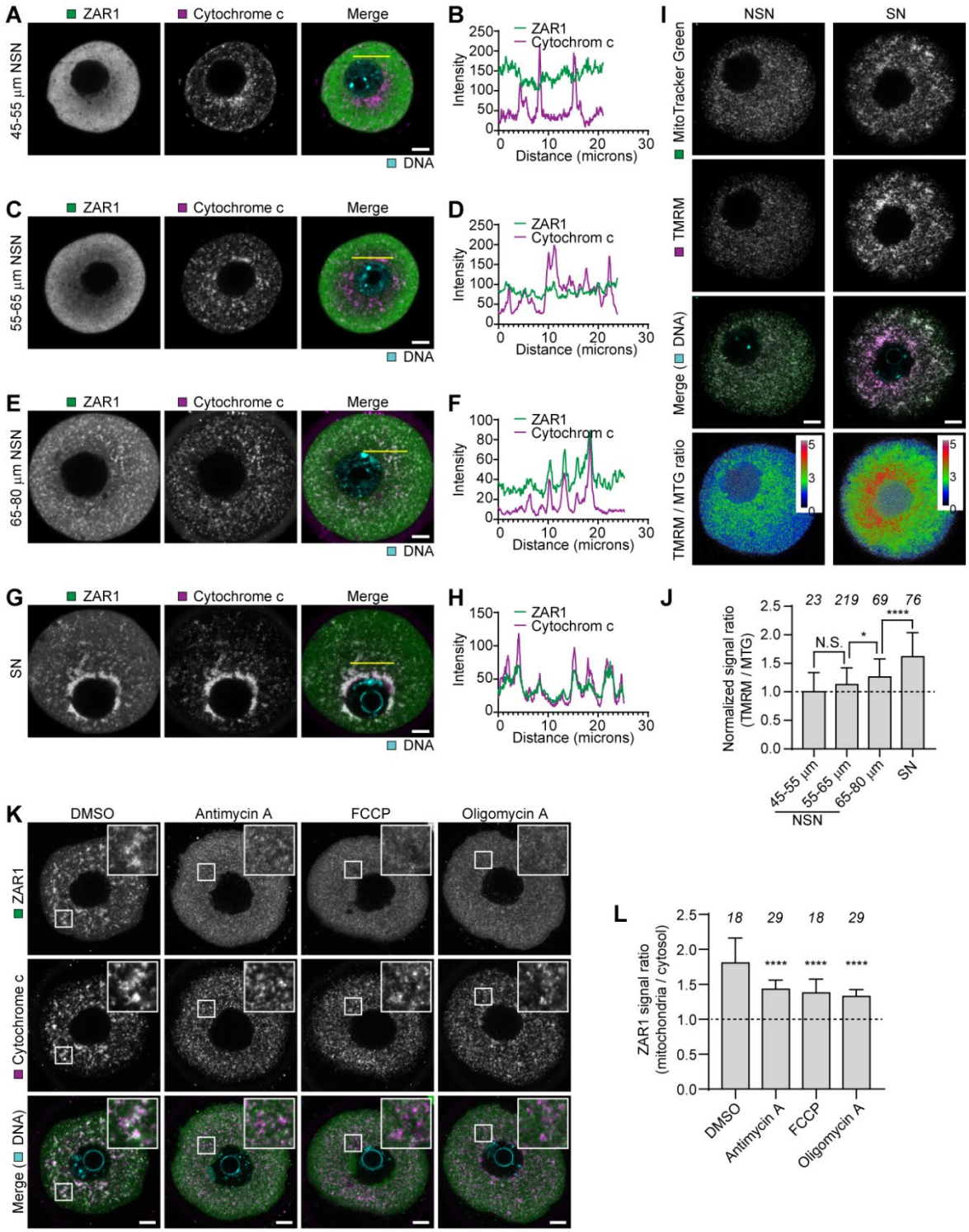
A
ZAR1
Cytochrome c
Merge
45-55 µm NSN
DNA
B
ZAR1
Cytochrom c
Intensity
Distance (microns)
C
55-65 µm NSN
D
E
65-80 µm NSN
F
G
SN
H
I
NSN
SN
MitoTracker Green
TMRM
Merge (DNA)
TMRM / MTG ratio
J
Normalized signal ratio (TMRM / MTG)
23 219 69 76
N.S.
*
****
45-55 µm
55-65 µm
65-80 µm
SN
NSN
K
DMSO
Antimycin A
FCCP
Oligomycin A
ZAR1
Cytochrome c
Merge (DNA)
L
ZAR1 signal ratio (mitochondria / cytosol)
18 29 18 29
****

Figure 2

Fig. 2 Increased mitochondrial membrane potential is essential for MARDO formation during oocyte growth.

(A-H) Representative immunofluorescence images of mouse oocytes at different growing stages. A representative non-surrounded nucleolus (NSN) oocyte with a diameter between 45-55 μm is shown in (A). A representative NSN oocyte with a diameter between 55-65 μm is shown in (C). A representative NSN oocyte with a diameter between 65-80 μm is shown in (E). A representative surrounded nucleolus (SN) oocyte is shown in (G). Green, ZAR1; magenta, cytochrome c (mitochondria); blue, DNA. Intensity profiles along the yellow lines are shown in (B, D, F, H) respectively.

(I) Representative fluorescence images of fully-grown NSN and SN mouse oocytes stained with MitoTracker Geen (green), TMRM (magenta), and SiR-DNA (blue). Fluorescence intensity ratios of TMRM to MitoTracker Green are shown with Rainbow RGB pseudo-colors.

(J) Quantification of the fluorescence intensity ratio of TMRM to MitoTracker Green on mitochondria in mouse oocytes at different growing stages.

(K) Representative immunofluorescence images of mouse GV oocytes treated with DMSO, 5 μg/ml Antimycin A, 5 μM FCCP or 5 μg/ml Oligomycin A. Green, ZAR1; magenta, cytochrome c (mitochondria); blue, DNA. Insets are magnifications of outlined regions.

(L) Quantification of the ratio of average ZAR1 intensities on mitochondria to in cytosol under different treatments (K).

The number of analyzed oocytes is specified in italics. Data are shown as mean ± SD. *P* values were calculated using one-way ANOVA with Tukey's *post-hoc* test. Scale bars, 10 μm.

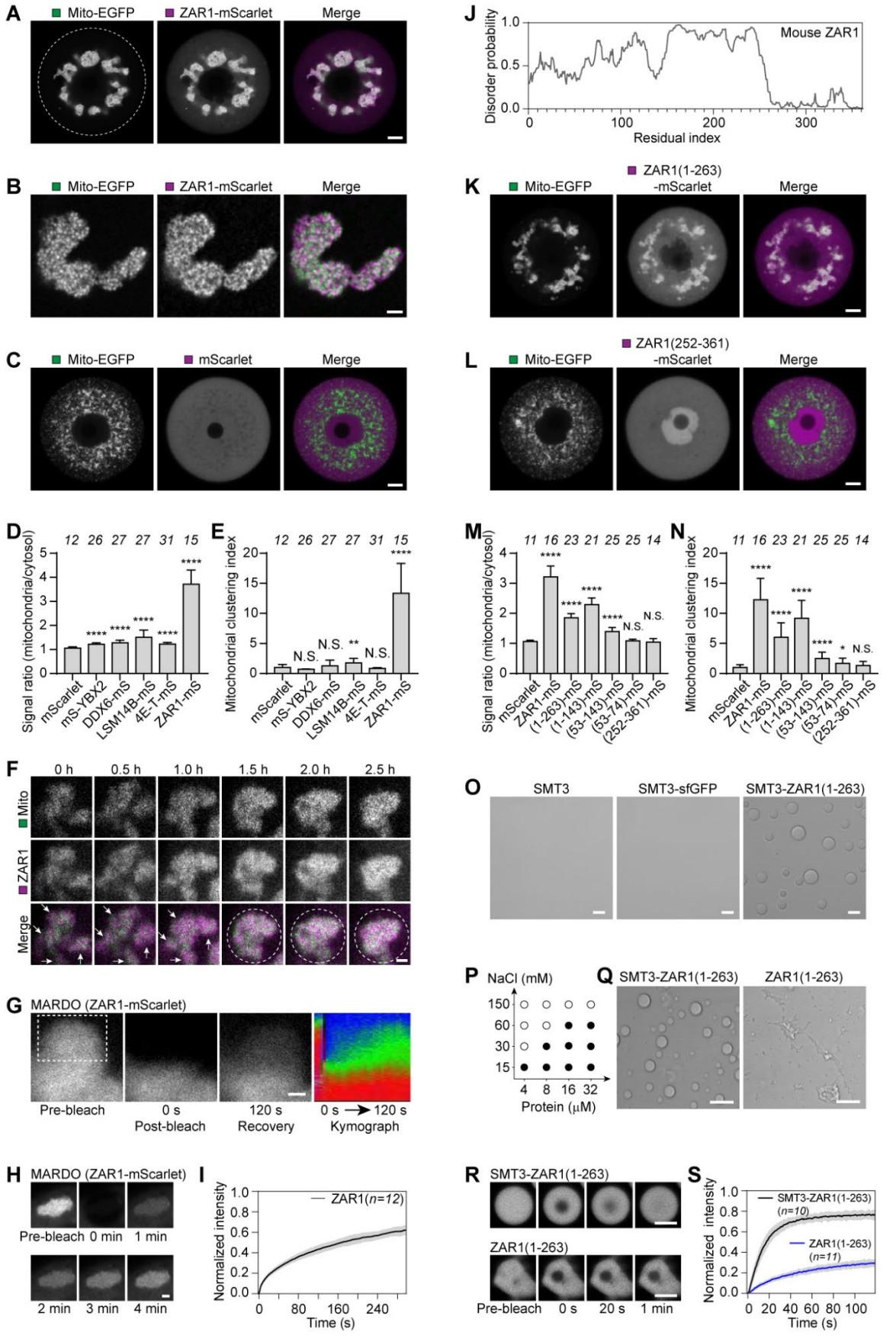
A
Mito-EGFP
ZAR1-mScarlet
Merge
B
Mito-EGFP
ZAR1-mScarlet
Merge
C
Mito-EGFP
mScarlet
Merge
D
Signal ratio (mitochondria/cytosol)
12 26 27 27 31 15
mScarlet
mS-YBX2
DDX6-mS
LSM14B-mS
4E-T-mS
ZAR1-mS
E
Mitochondrial clustering index
12 26 27 27 31 15
N.S.
F
0 h
0.5 h
1.0 h
1.5 h
2.0 h
2.5 h
Mito
ZAR1
Merge
G
MARDO (ZAR1-mScarlet)
Pre-bleach
0 s
Post-bleach
120 s
Recovery
0 s → 120 s
Kymograph
H
MARDO (ZAR1-mScarlet)
Pre-bleach 0 min 1 min
2 min 3 min 4 min
I
Normalized intensity
ZAR1(n=12)
Time (s)
J
Disorder probability
Mouse ZAR1
Residual index
K
Mito-EGFP
ZAR1(1-263)
-mScarlet
Merge
L
Mito-EGFP
ZAR1(252-361)
-mScarlet
Merge
M
Signal ratio (mitochondria/cytosol)
11 16 23 21 25 25 14
mScarlet
ZAR1-mS
(1-263)-mS
(1-143)-mS
(53-143)-mS
(53-74)-mS
(252-361)-mS
N
Mitochondrial clustering index
11 16 23 21 25 25 14
O
SMT3
SMT3-sfGFP
SMT3-ZAR1(1-263)
P
NaCl (mM)
150
60
30
15
4 8 16 32
Protein (μM)
Q
SMT3-ZAR1(1-263)
ZAR1(1-263)
R
SMT3-ZAR1(1-263)
ZAR1(1-263)
Pre-bleach 0 s 20 s 1 min
S
Normalized intensity
SMT3-ZAR1(1-263) (n=10)
ZAR1(1-263) (n=11)
Time (s)

Figure 3

Fig. 3 Phase separation of ZAR1 promotes MARDO formation and mitochondrial clustering

(A) Representative fluorescence images of mouse GV oocytes expressing Mito-EGFP (mitochondria, green) and ZAR1-mScarlet (magenta). Dashed line demarcates the oocyte.

(B) Representative Airyscan fluorescence images of mouse GV oocytes expressing Mito-EGFP (mitochondria, green) and ZAR1-mScarlet (magenta).

(C) Representative fluorescence images of mouse GV oocytes expressing Mito-EGFP (mitochondria, green) and mScarlet (magenta).

(D) Quantification of the signal ratio of indicated proteins on mitochondria (Mito-EGFP) to in cytosol.

(E) Quantification of the mitochondrial (Mito-EGFP) clustering index when the indicated proteins are overexpressed in mouse GV oocytes.

(F) Representative stills from time-lapse movies of mouse GV oocytes expressing Mito-EGFP (mitochondria, green) and ZAR1-mScarlet (magenta). Arrows highlight fusing MARDO-mitochondria clusters. Dashed lines highlight fused MARDO-mitochondria clusters. Scale bar, 2 μm.

(G) Partial bleaching of ZAR1-mScarlet in MARDO in mouse GV oocytes. The bleached area is outlined by the dashed box. Scale bar, 2 μm.

(H) FRAP analysis of ZAR1-mScarlet in MARDO. Scale bar, 2 μm.

(I) Quantification of the FRAP experiment in (H).

(J) Domain organization of mouse ZAR1 showing the disordered region predicted by IUPred2.

(K) Representative fluorescence images of mouse GV oocytes expressing Mito-EGFP (mitochondria, green) and ZAR1(1-263)-mScarlet (magenta).

(L) Representative fluorescence images of mouse GV oocytes expressing Mito-EGFP (mitochondria, green) and ZAR1(252-361)-mScarlet (magenta).

(M) Quantification of the signal ratio of indicated proteins on mitochondria (Mito-EGFP) to in cytosol.

(N) Quantification of the mitochondrial (Mito-EGFP) clustering index when the indicated proteins are overexpressed in mouse GV oocytes.

(O) Representative bright-field images of SMT3 or SMT3-sfGFP solutions and SMT3-ZAR1(1-263) droplets formed by phase separation in vitro. The protein concentrations of SMT3 and SMT3-sfGFP are both 32 μM. The protein concentration of SMT3-

ZAR1(1-263) is 8 μM. The buffer is 50 mM HEPES pH 7.4, containing 30 mM NaCl and 2mM DTT. Scale bar, 2 μm.

(P) Phase separation of SMT3-ZAR1(1-263) at different protein concentrations and under different salt conditions. Solid dot represents phase separation. Hollow dot represents no phase separation. The buffer contains 50 mM HEPES pH 7.4 and 2mM DTT.

(Q) Representative bright-field images of SMT3-ZAR1(1-263) droplets and ZAR1(1-263) hydrogels. The non-spherical morphology of ZAR1(1-263) condensate is due to incomplete fusion. The protein concentrations are both 40 μM. The buffer is 50 mM HEPES pH 7.4 containing 150 mM NaCl, 2mM DTT, and 10% Ficoll 400. Scale bar, 2 μm.

(R) FRAP analysis of SMT3-ZAR1(1-263) droplets and ZAR1(1-263) hydrogels. The protein concentrations are both 40 μM with 2% proteins conjugated by Alexa Fluor 488. The buffer is 50 mM HEPES pH 7.4 containing 150 mM NaCl, 2mM DTT, and 10% Ficoll 400. Scale bar, 2 μm.

(S) Quantification of the FRAP experiment in (R).

The number of analyzed oocytes (D, E, M, N) or FRAP experiments (I, S) is specified in italics. Data are shown as mean ± SD. *P* values were calculated using one-way ANOVA with Tukey's *post-hoc* test. Scale bars, 10 μm unless otherwise specified.

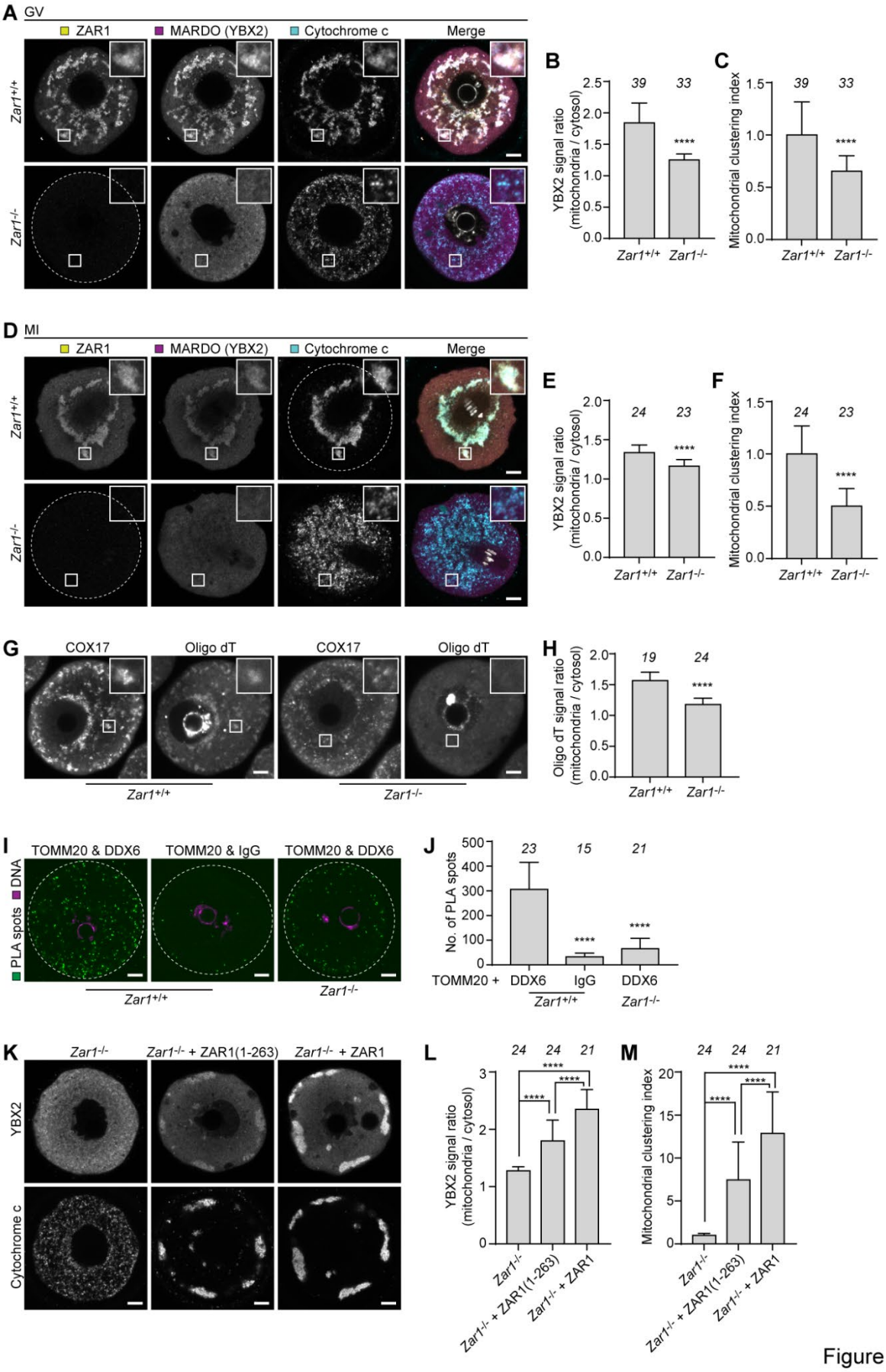
A GV
ZAR1
MARDO (YBX2)
Cytochrome c
Merge
Zar1+/+
Zar1-/-
B
YBX2 signal ratio (mitochondria / cytosol)
39
33
****
Zar1+/+
Zar1-/-
C
Mitochondrial clustering index
39
33
****
Zar1+/+
Zar1-/-
D MI
ZAR1
MARDO (YBX2)
Cytochrome c
Merge
Zar1+/+
Zar1-/-
E
YBX2 signal ratio (mitochondria / cytosol)
24
23
****
Zar1+/+
Zar1-/-
F
Mitochondrial clustering index
24
23
****
Zar1+/+
Zar1-/-
G
COX17
Oligo dT
COX17
Oligo dT
Zar1+/+
Zar1-/-
H
Oligo dT signal ratio (mitochondria / cytosol)
19
24
****
Zar1+/+
Zar1-/-
I
TOMM20 & DDX6
TOMM20 & IgG
TOMM20 & DDX6
DNA
PLA spots
Zar1+/+
Zar1-/-
J
No. of PLA spots
23
15
21
****
****
TOMM20 +
DDX6
IgG
DDX6
Zar1+/+
Zar1-/-
K
Zar1-/-
Zar1-/- + ZAR1(1-263)
Zar1-/- + ZAR1
YBX2
Cytochrome c
L
24
24
21
****
****
****
YBX2 signal ratio (mitochondria / cytosol)
Zar1-/-
Zar1-/- + ZAR1(1-263)
Zar1-/- + ZAR1
M
24
24
21
****
****
****
Mitochondrial clustering index
Zar1-/-
Zar1-/- + ZAR1(1-263)
Zar1-/- + ZAR1

Figure 4

Fig. 4 Knocking out *Zar1* disrupts MARDO and impairs mitochondrial clustering

(A) Representative immunofluorescence images of GV oocytes collected from *Zar1*$^{+/+}$ and *Zar1*$^{-/-}$ mice. Yellow, ZAR1; magenta, YBX2 (MARDO); blue, cytochrome c (mitochondria). Insets are magnifications of outlined regions. Dashed line demarcates the oocyte.

(B) Quantification of the ratio of average YBX2 intensities on mitochondria to in cytosol (A).

(C) Quantification of the mitochondrial clustering index (A).

(D) Representative immunofluorescence images of metaphase I (MI) oocytes collected from *Zar1*$^{+/+}$ and *Zar1*$^{-/-}$ mice. Yellow, ZAR1; magenta, YBX2 (MARDO); blue, cytochrome c (mitochondria). Insets are magnifications of outlined regions. Dashed line demarcates the oocyte.

(E) Quantification of the ratio of average YBX2 intensities on mitochondria to in cytosol (D).

(F) Quantification of the mitochondrial clustering index (D).

(G) Representative RNA FISH images of GV oocytes collected from *Zar1*$^{+/+}$ and *Zar1*$^{-/-}$ mice. Oocytes were further stained with anti-COX17 antibody post FISH. COX17 labels mitochondria. Cy5-conjugated oligo dT labels mRNA. Insets are magnifications of outlined regions.

(H) Quantification of the ratio of average Oligo dT intensities on mitochondria to in cytosol (G).

(I) Representative images of in situ PLA performed with antibody pairs anti-TOMM20 & anti-DDX6 or anti-TOMM20 & IgG control in GV oocytes collected from *Zar1*$^{+/+}$ and *Zar1*$^{-/-}$ mice. Green, PLA spots; magenta, DNA. Dashed lines demarcate the oocytes.

(J) Quantification of the number of PLA spots in (I).

(K) Representative immunofluorescence images of *Zar1*$^{-/-}$ GV oocytes stained with anti-YBX2 and anti-cytochrome c antibodies. Either ZAR1(1-263) or ZAR1 was overexpressed in oocytes before fixation. Non-injected oocytes are fixed directly and used as control.

(L) Quantification of the ratio of average YBX2 intensities on mitochondria to in cytosol (K).

(M) Quantification of the mitochondrial clustering index (K).

The number of analyzed oocytes is specified in italics. Data are shown as mean ± SD. *P* values were calculated using unpaired two-tailed Student's *t* test (B, C, E, F, H) or one-way ANOVA with Tukey's *post-hoc* test (J, L, M). Scale bars, 10 µm.

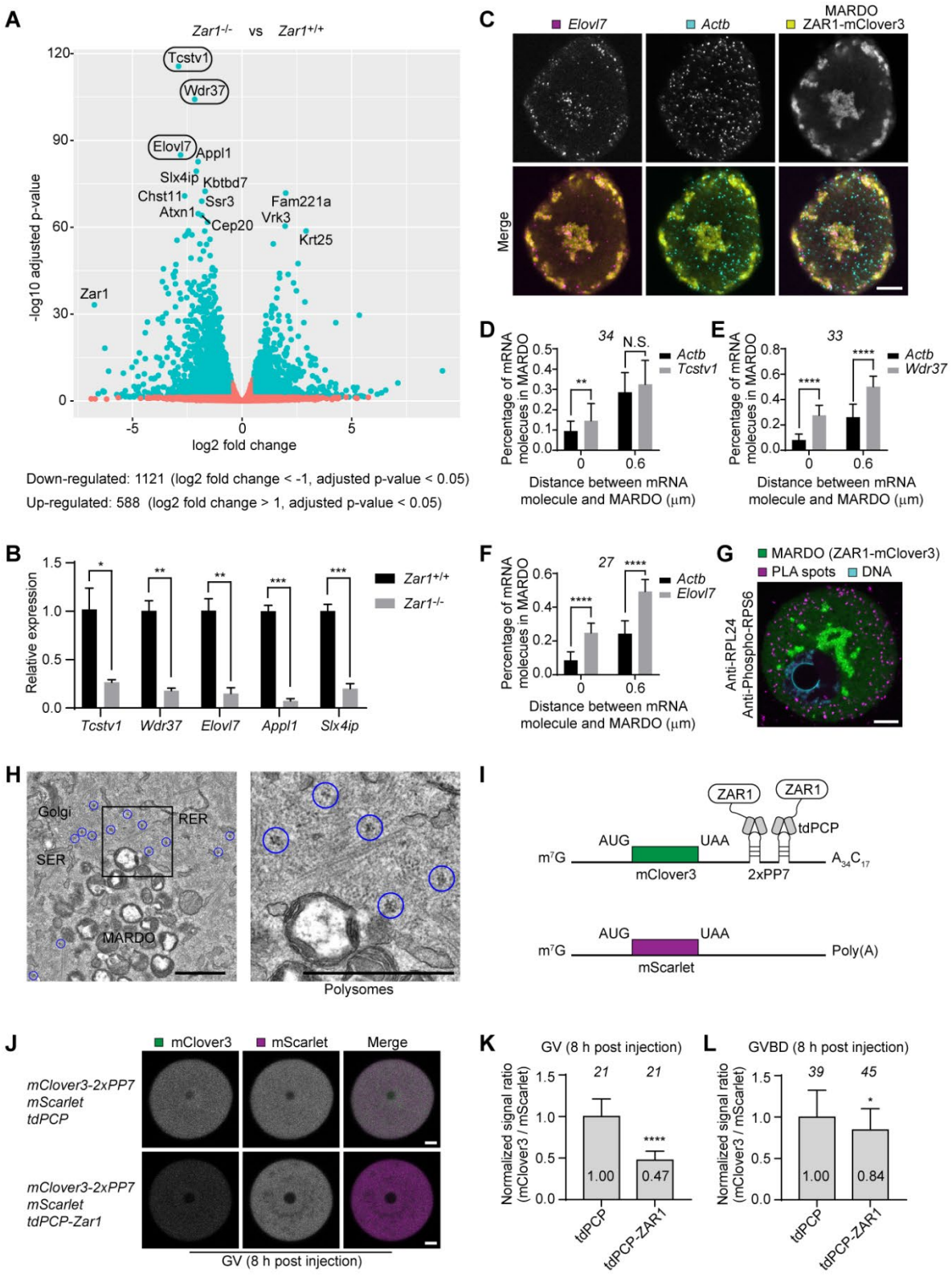
A
Zar1-/- vs Zar1+/+
Tcstv1
Wdr37
Elovl7
Appl1
Slx4ip
Kbtbd7
Chst11
Ssr3
Atxn1
Cep20
Fam221a
Vrk3
Krt25
Zar1
-log10 adjusted p-value
log2 fold change
Down-regulated: 1121 (log2 fold change < -1, adjusted p-value < 0.05)
Up-regulated: 588 (log2 fold change > 1, adjusted p-value < 0.05)
B
Relative expression
Zar1+/+
Zar1-/-
Tcstv1
Wdr37
Elovl7
Appl1
Slx4ip
C
Elovl7
Actb
MARDO
ZAR1-mClover3
Merge
D
Percentage of mRNA molecues in MARDO
Actb
Tcstv1
N.S.
Distance between mRNA molecule and MARDO (μm)
E
Actb
Wdr37
F
Actb
Elovl7
G
MARDO (ZAR1-mClover3)
PLA spots
DNA
Anti-RPL24
Anti-Phospho-RPS6
H
Golgi
RER
SER
MARDO
Polysomes
I
ZAR1
tdPCP
AUG
UAA
m7G
mClover3
2xPP7
A34C17
mScarlet
Poly(A)
J
mClover3
mScarlet
Merge
mClover3-2xPP7
mScarlet
tdPCP
mClover3-2xPP7
mScarlet
tdPCP-Zar1
GV (8 h post injection)
K
GV (8 h post injection)
Normalized signal ratio (mClover3 / mScarlet)
1.00
0.47
tdPCP
tdPCP-ZAR1
L
GVBD (8 h post injection)
1.00
0.84

Figure 5

Fig. 5 MARDO balances mRNA storage and translation

(A) The RNA sequencing analyses reveal differentially expressed genes (DEGs, adjusted p-value < 0.05, average log2 fold change ⩾ 0.5, cyan dots in the volcano plot) in *Zar1*$^{-/-}$ oocytes versus *Zar1*$^{+/+}$ oocytes.

(B) Quantitative reverse transcription PCR (RT-qPCR) results showing expression of five genes (*Tcstv1*, *Wdr37*, *Elovl7*, *Appl1*, and *Slx4ip*) in *Zar1*$^{+/+}$ and *Zar1*$^{-/-}$ oocytes.

(C) Representative single molecule RNA FISH (smFISH) images of mouse GV oocytes expressing ZAR1-mClover3. Yellow, ZAR1-mClover3 (MARDO); magenta, Alexa Fluor 647-conjugated *Elovl7* mRNA probes; blue, Alexa Fluor 546-conjugated *Actb* mRNA probes.

(D-F) Quantification of the percentage of indicated mRNA molecules in MARDO. If the distance between mRNA molecule and MARDO is 0 μm, it means that the mRNA molecule is inside of MARDO. If the distance between mRNA molecule and MARDO is less than 0.6 μm, it means that the mRNA molecule is either inside of MARDO or connected to MARDO.

(G) Representative image of in situ PLA performed with antibody pair anti-RPL24 & anti-Phospho-RPS6 in mouse GV oocytes expressing ZAR1-mClover3. Green, ZAR1-mClover3 (MARDO); magenta, PLA spots; blue, DNA.

(H) Representative transmission electron microscopy (TEM) image of mouse GV oocytes expressing ZAR1-mClover3 showing that polysomes are excluded from MARDO. Outlined regions are magnified on the right. Scale bar, 1 μm.

(I) Cartoon of *mclove3-2xPP7* reporter mRNA and *mScarlet* control mRNA. The signal ratio of mClover3 to mScarlet can be used to assess whether tdPCP fusion proteins regulate translation of tethered reporter mRNA.

(J) Representative fluorescence images of mouse GV oocytes expressing *mclove3-2xPP7*, *mScarlet*, and *tdPCP* or *tdPCP-Zar1* at 8 h post mRNA injection. Green, mClover3; magenta, mScarlet.

(K) Quantification of the fluorescence intensity ratio of mClover3 to mScarlet in mouse GV oocytes expressing *mclove3-2xPP7*, *mScarlet*, and *tdPCP* or *tdPCP-Zar1* at 8 h post mRNA injection.

(L) Quantification of the fluorescence intensity ratio of mClover3 to mScarlet in mouse oocytes expressing *mclove3-2xPP7*, *mScarlet*, and *tdPCP* or *tdPCP-Zar1* at 8 h post mRNA injection. Oocytes that have just undergone GVBD (germinal vesicle breakdown) were used for mRNA injection.

The number of analyzed oocytes is specified in italics. Data are shown as mean ± SD. *P* values were calculated using unpaired two-tailed Student's *t* test. Scale bars, 10 µm unless otherwise specified.

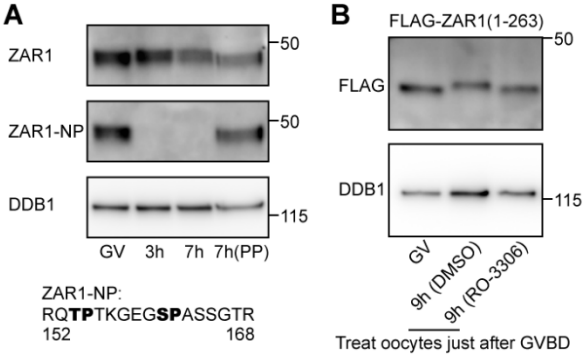

C Phosphorylation sites of ZAR1 by CDK1-Cyclin B1 *(in vitro)*

Phospho (STY) Probabilities	Residuals	PEP	Score
TLQPAGCRAS(1)PDAR	S105	2.59E-43	205.45
GHAGAGRS(1)PR	S124	3.46E-14	164.90
QT(1)PTKGEGSPASSGTR	T154	1.13E-56	213.51
GEGS(1)PASSGTREPEPR	S161	1.91E-140	306.96
DQAS(1)PQSTEQDKER	S244	5.29E-116	285.98

D Phosphorylation sites of ZAR1 *(in vivo)*

Phospho (STY) Probabilities	Residuals	Normalized Phospho-Proteome Intensity (GV)	Normalized Phospho-Proteome Intensity (MI)
TLQPAGCRAS(1)PDAR	S105	1.84	2.54
QT(1)PT(0.002)KGEGS(0.959)PAS(0.031)S(0.007)GT(0.001)REPEPR	T154	NaN	2.63
GEGS(0.999)PAS(0.843)S(0.137)GT(0.021)REPEPR	S161	-0.77	2.63

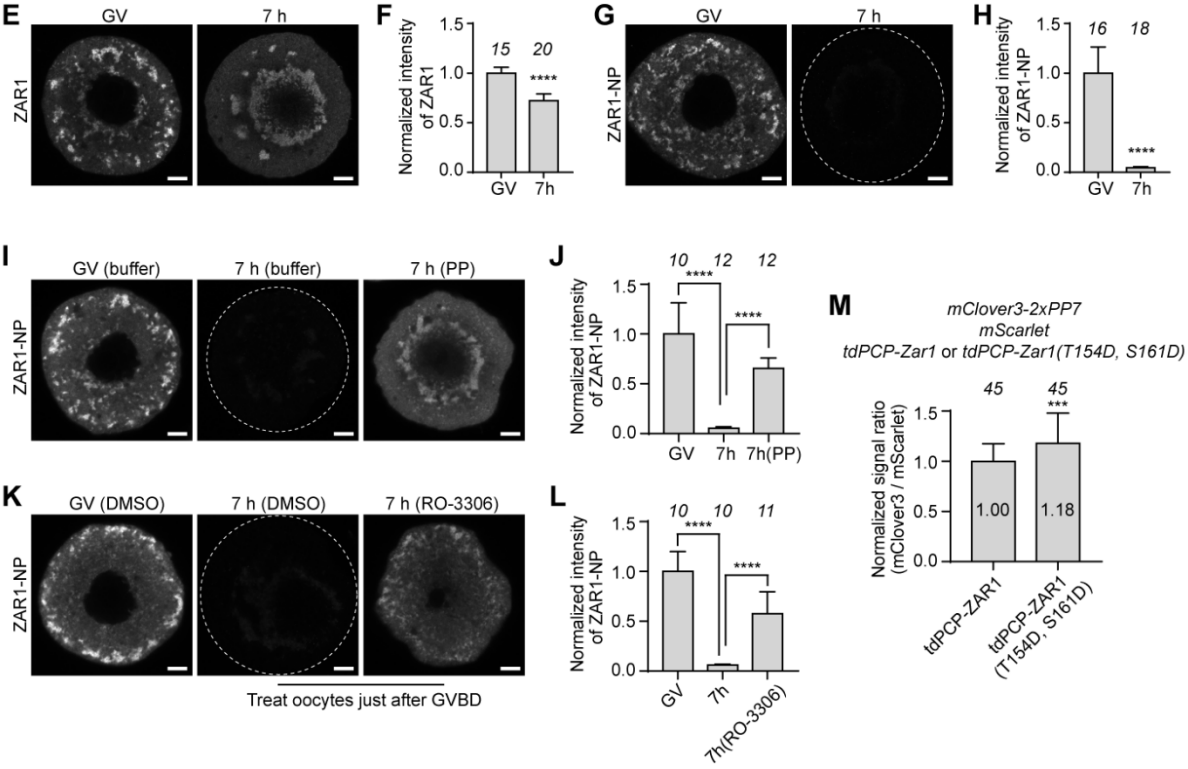

Figure 6

Fig. 6 CDK1-mediated ZAR1 phosphorylation partially relieves translational repression

(A) Western blot analyses showing the expression of ZAR1 and the non-phosphorylated ZAR1 (ZAR1-NP) in mouse oocytes. Oocytes were lysed at different times after dbcAMP washout. Lambda protein phosphatase (PP) treatment on cell lysate was performed before loading. DDB1 was used as a loading control. The antigen used to raise the "non-phosphorylated ZAR1"-specific antibody is shown below.

(B) Western blot analyses showing the expression of overexpressed FLAG-ZAR1(1-263) in mouse oocytes. Oocytes were lysed at different times after dbcAMP washout. DMSO or 10 μM RO-3306 were used to treat oocytes after GVBD. DDB1 was used as a loading control.

(C) Phosphorylation sites of ZAR1 by CDK1-cyclin B1. Phospho (STY) Probabilities: sequence representation of the peptide including PTM positioning probabilities ([0..1], where 1 is best match) for 'Phospho (STY)'. Residuals: the amino acid position of the phosphorylated residue within the protein. PEP: Posterior Error Probability of the identification. This value essentially operates as a p-value, where smaller is more significant. Score: Andromeda score for the best associated MS/MS spectrum.

(D) Phosphorylation sites of ZAR1 in vivo. Intensity: summed up eXtracted Ion Current (XIC) of all isotopic clusters associated with the identified amino acid sequence. Intensities were log2 transformed and median-normalized.

(E) Representative immunofluorescence images of mouse oocytes stained with ZAR1 antibody that recognizes all ZAR1 proteins. Oocytes were kept for 7 hours with dbcAMP (GV) or kept for 7 hours after dbcAMP washout (7 h) before fixation.

(F) Quantification of the fluorescence intensity of ZAR1 in (E).

(G) Representative immunofluorescence images of mouse oocytes stained with anti-ZAR1-NP antibody. Oocytes were kept for 7 hours with dbcAMP (GV) or kept for 7 hours after dbcAMP washout (7 h) before fixation. Dashed line demarcates the oocyte.

(H) Quantification of the fluorescence intensity of non-phosphorylated ZAR1 in (G).

(I) Representative immunofluorescence images of mouse oocytes stained with anti-ZAR1-NP antibody. Oocytes were kept for 7 hours with dbcAMP (GV) or kept for 7 hours after dbcAMP washout (7 h) before fixation. Permeabilized oocytes were treated with Lambda protein phosphatase (PP) or PP buffer before staining. Dashed line demarcates the oocyte.

(J) Quantification of the fluorescence intensity of non-phosphorylated ZAR1 in (I).

(K) Representative immunofluorescence images of mouse oocytes stained with anti-ZAR1-NP antibody. Oocytes were kept for 7 hours with dbcAMP (GV) or kept for 7 hours after dbcAMP washout (7 h) before fixation. GV oocytes were treated with DMSO. 7 h oocytes were treated with either DMSO or 10 μM RO-3306 after GVBD. Dashed line demarcates the oocyte.

(L) Quantification of the fluorescence intensity of non-phosphorylated ZAR1 in (K).

(M) Quantification of the fluorescence intensity ratio of mClover3 to mScarlet in mouse oocytes expressing *mclove3-2xPP7*, *mScarlet*, and *tdPCP-Zar1* or *tdPCP-Zar1(T154D, S161D)* at 8 h post mRNA injection. Oocytes that have just undergone GVBD were used for mRNA injection.

The number of analyzed oocytes is specified in italics. Data are shown as mean ± SD. *P* values were calculated using unpaired two-tailed Student's *t* test (F, H, M) or one-way ANOVA with Tukey's *post-hoc* test (J, L). Scale bars, 10 μm.

Figure 7

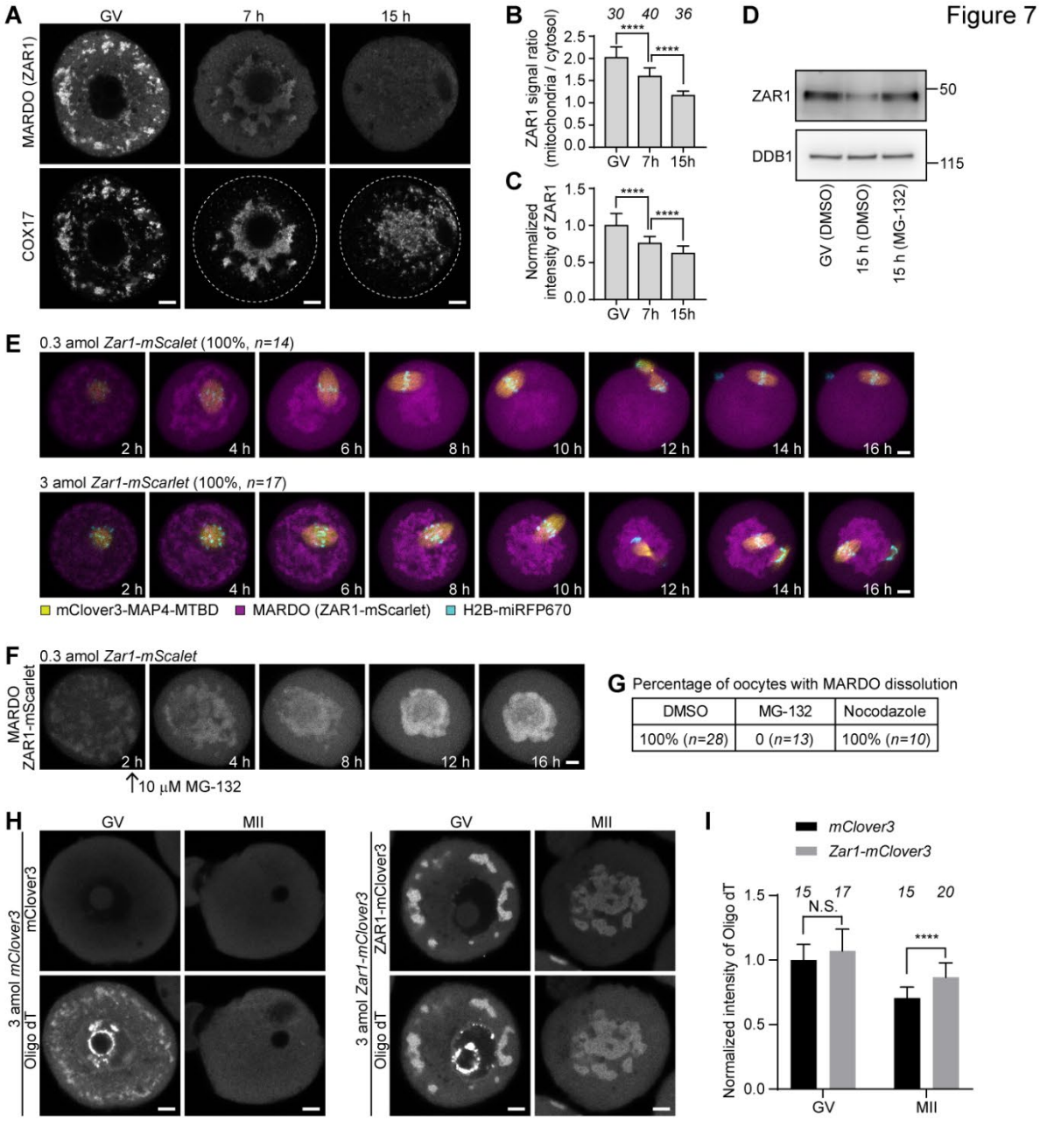
A
GV
7 h
15 h
MARDO (ZAR1)
COX17
B
30 40 36
ZAR1 signal ratio (mitochondria / cytosol)
GV 7h 15h
C
Normalized intensity of ZAR1
GV 7h 15h
D
ZAR1
DDB1
50
115
GV (DMSO)
15 h (DMSO)
15 h (MG-132)
E
0.3 amol Zar1-mScalet (100%, n=14)
3 amol Zar1-mScarlet (100%, n=17)
2 h 4 h 6 h 8 h 10 h 12 h 14 h 16 h
mClover3-MAP4-MTBD
MARDO (ZAR1-mScarlet)
H2B-miRFP670
F
0.3 amol Zar1-mScalet
MARDO ZAR1-mScarlet
2 h 4 h 8 h 12 h 16 h
10 μM MG-132
G
Percentage of oocytes with MARDO dissolution
DMSO | MG-132 | Nocodazole
100% (n=28) | 0 (n=13) | 100% (n=10)
H
GV MII
3 amol mClover3
mClover3
Oligo dT
3 amol Zar1-mClover3
ZAR1-mClover3
I
mClover3
Zar1-mClover3
15 17 15 20
N.S.
Normalized intensity of Oligo dT
GV MII
J
GV
MARDO formed by ZAR1 phase separation sequesters mRNAs and buffers translation
NEBD to MI
CDK1-mediated ZAR1 phosphorylation partially relieves translational repression
MI to MII
Proteasomal degradation of ZAR1 promotes MARDO dissolution and mRNA decay
High ΔΨm
ATP
DDX6 4E-T
LSM14B
ZAR1
YBX2
5'cap
4E-T DDX6
CDK1
CCNB1
PAB

Fig. 7 Proteasome-mediated ZAR1 degradation is required for MARDO dissolution and mRNA decay in MII oocytes.

(A) Representative immunofluorescence images of mouse oocytes at different stages of meiosis. ZAR1 labels MARDO. COX17 labels mitochondria. Dashed lines demarcate the oocytes.

(B) Quantification of the ratio of average ZAR1 intensities on mitochondria to in cytosol (A).

(C) Quantification of the mitochondrial clustering index (A).

(D) Western blot analyses showing the expression of ZAR1 at different stages of meiosis. GV (DMSO): oocytes were kept with dbcAMP and DMSO for 15h. 15 h (DMSO): oocytes were treated with DMSO for 15 h after dbcAMP washout. 15 h (MG-132): oocytes were treated with 10 μM MG-132 for 15 h after dbcAMP washout. DDB1 was used as a loading control.

(E) Representative stills from time-lapse movies of mouse oocytes with 0.3 amol or 3 amol *Zar1-mScarlet* mRNA injected. Yellow, mClover3-MAP4-MTBD (microtubules); magenta, ZAR1-mScarlet (MARDO); blue, H2B-miRFP670 (chromosomes). Time is given as hours after dbcAMP washout. The percentage of oocytes with representative pattern is shown in brackets. "n" indicates the number of analyzed oocytes. Z projections, 11 sections every 6 μm.

(F) Representative stills from time-lapse movies of mouse oocytes with 0.3 amol *ZAR1-mScarlet* mRNA injected. MG-132 or other chemicals were added to the culture medium 2 hours after dbcAMP washout. Time is given as hours after dbcAMP washout. Z projections, 11 sections every 6 μm.

(G) Percentage of oocytes with MARDO dissolution treated with DMSO, 10 μM MG-132, or 10 μM nocodazole. Chemicals were added to the culture medium 2 hours after dbcAMP washout.

(H) Representative RNA FISH images of mouse GV oocytes and metaphase II (MII) oocytes expressing mClover3 or ZAR1-mClover3. 3 amol *mClover3* or *Zar1-mClover3* mRNA was injected into GV oocytes. After 4 hours of expression, half oocytes were transferred to dbcAMP-free medium for in vitro maturation. 17 hours later, in vitro matured MII oocytes and the remaining GV oocytes were fixed and processed for RNA FISH. Cy5-conjugated oligo dT labels mRNA.

(I) Quantification of the fluorescence intensity of oligo dT in (H).

(J) Model showing the mechanism of MARDO formation and dissolution, and how maternal mRNA storage, translation and decay are coupled to meiotic progression. The gradient green indicates MARDO around mitochondria. ΔΨm, the mitochondrial

membrane potential; 4E, EIF4E; 4G, EIF4G; PAB, Poly(A)-binding protein; P, phosphate group; U, ubiquitin; the empty square, unidentified protein that may mediate the interaction of ZAR1 and DDX6-LSM14B-4E-T complex.

The number of analyzed oocytes is specified in italics. Data are shown as mean ± SD. *P* values were calculated using unpaired two-tailed Student's *t* test (I) or one-way ANOVA with Tukey's *post-hoc* test (B, C). Scale bars, 10 μm.

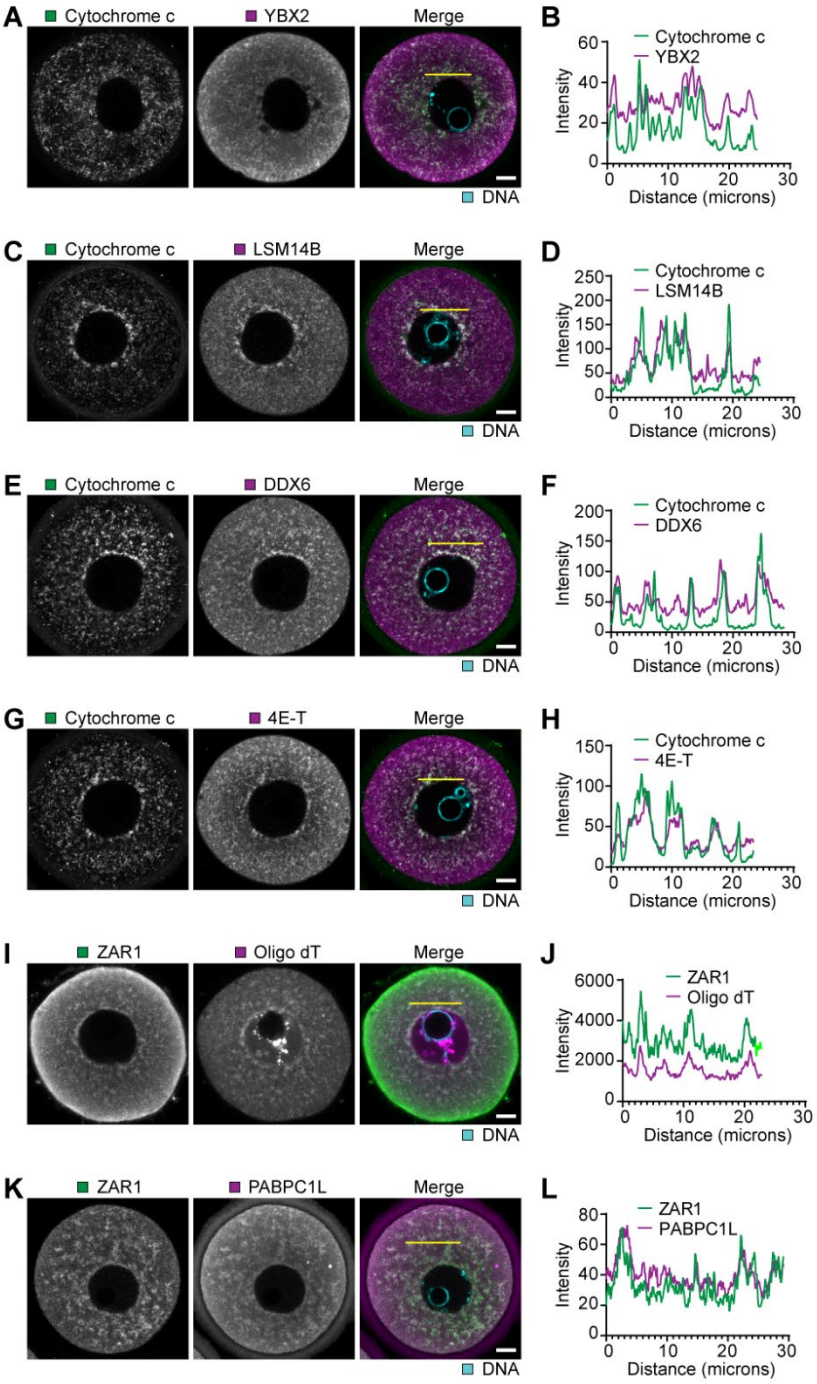

M Highly expressed RNA-binding proteins in mouse oocytes

Rank_1000oo_rep1	Rank_1000oo_rep2	Protein names	MARDO localization
23	23	YBX2	Yes
93	87	DDX19A, DDX19B	Not analyzed
94	86	PABPC1L	Yes
128	123	DDX6	Yes
139	153	4E-T	Yes
156	100	LSM14B	Yes
186	206	ZAR1	Yes

Figure S1

Fig. S1 Accumulation of RNA-binding proteins and mRNA around mitochondria.

(A-H) Representative immunofluorescence images of mouse GV oocytes (A, C, E, G). Green, cytochrome c (mitochondria); magenta, YBX2 (A), LSM14B (C), DDX6 (E), 4E-T (G); blue, DNA. Intensity profiles along the yellow lines are shown in (B, D, F, H) respectively.

(I) Representative RNA FISH images of mouse GV oocytes. Oocytes were further stained with anti-ZAR1 antibody post FISH. Green, ZAR1 (MARDO); magenta, Cy5-conjugated oligo dT (mRNA); blue, DNA.

(J) Intensity profiles of ZAR1 and Cy5-conjugated oligo dT along the yellow line in (I).

(K) Representative immunofluorescence images of mouse GV oocytes. Green, ZAR1 (MARDO); magenta, PABPC1L (Poly(A) Binding Protein Cytoplasmic 1 Like); blue, DNA.

(L) Intensity profiles of ZAR1 and PABPC1L along the yellow line in (K).

(M) Ranking of highly expressed RNA-binding proteins among all identified proteins in mouse oocytes. Proteins are ranked according to the LFQ (label-free quantitation) intensities. Two independent experiments with approximately 1000 oocytes each were performed.

Scale bars, 10 μm.

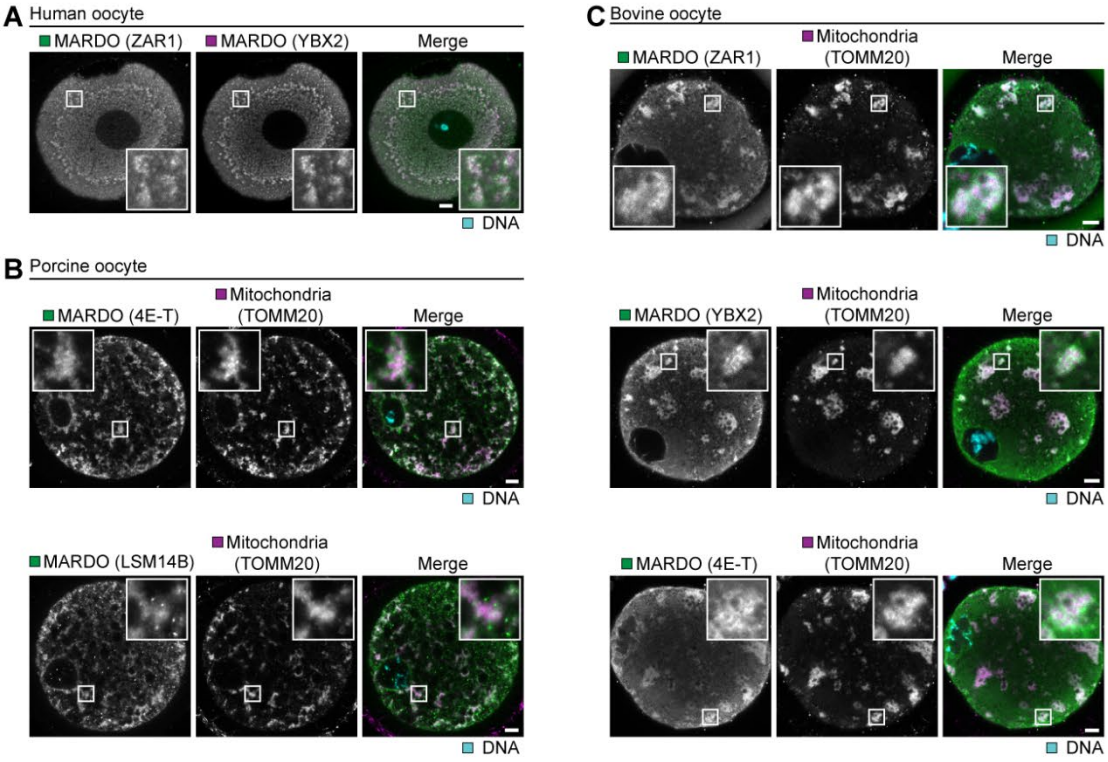
A Human oocyte
MARDO (ZAR1)
MARDO (YBX2)
Merge
DNA
B Porcine oocyte
MARDO (4E-T)
Mitochondria (TOMM20)
Merge
DNA
MARDO (LSM14B)
Mitochondria (TOMM20)
Merge
DNA
C Bovine oocyte
MARDO (ZAR1)
Mitochondria (TOMM20)
Merge
DNA
MARDO (YBX2)
Mitochondria (TOMM20)
Merge
DNA
MARDO (4E-T)
Mitochondria (TOMM20)
Merge
DNA

Figure S2

Fig. S2 MARDO in human, porcine and bovine oocytes.

(A) Representative immunofluorescence images of human GV oocytes. Green, ZAR1 (MARDO); magenta, YBX2 (MARDO); blue, DNA. Insets are magnifications of outlined regions.

(B) Representative immunofluorescence images of porcine GV oocytes. Green, 4E-T or LSM14B (MARDO); magenta, TOMM20 (mitochondria); blue, DNA. Insets are magnifications of outlined regions.

(C) Representative immunofluorescence images of bovine GV oocytes. Green, ZAR1, YBX2 or 4E-T (MARDO); magenta, TOMM20 (mitochondria); blue, DNA. Insets are magnifications of outlined regions.

Scale bars, 10 μm.

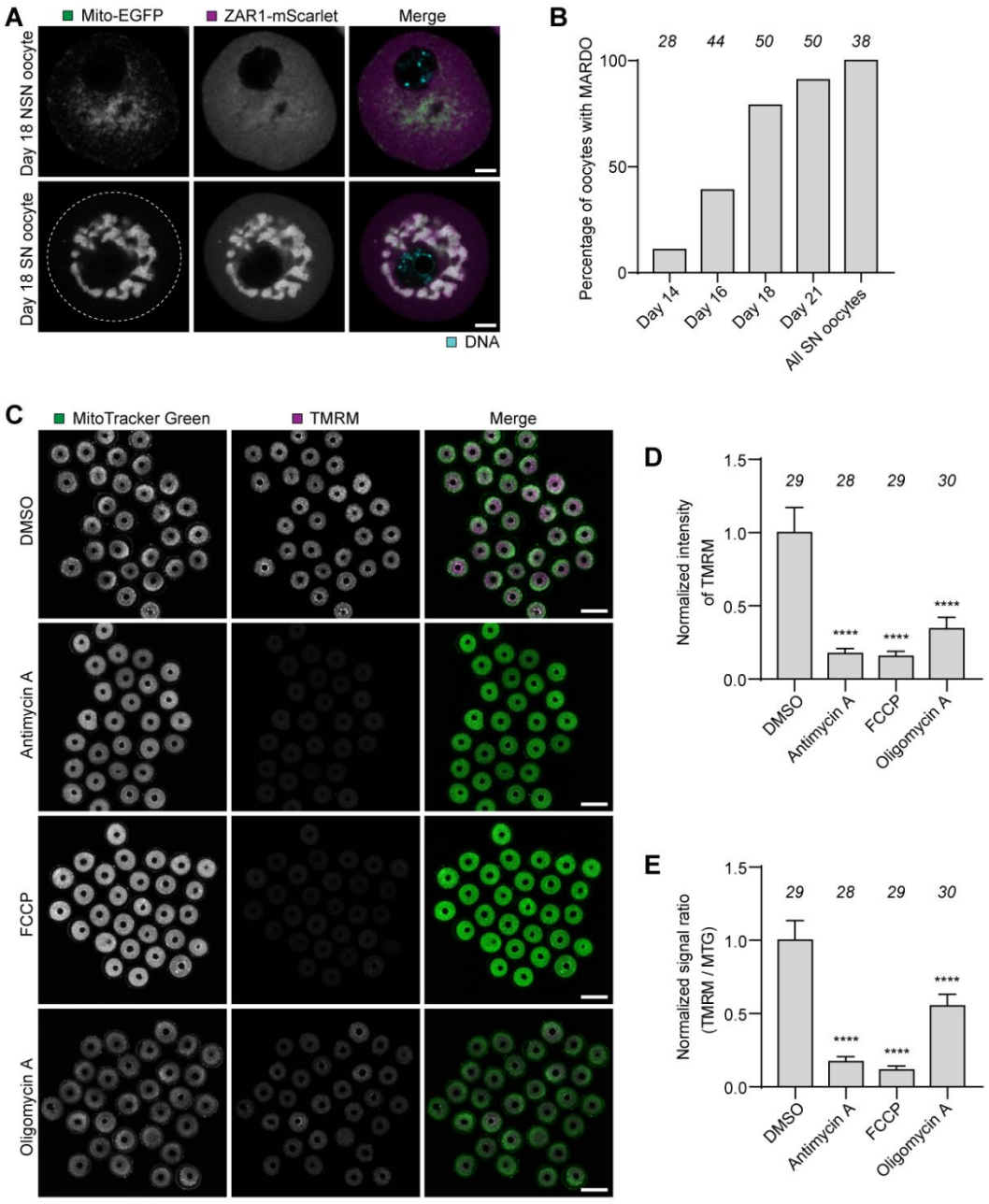
A
Mito-EGFP
ZAR1-mScarlet
Merge
Day 18 NSN oocyte
Day 18 SN oocyte
DNA
B
28
44
50
50
38
Percentage of oocytes with MARDO
100
50
0
Day 14
Day 16
Day 18
Day 21
All SN oocytes
C
MitoTracker Green
TMRM
Merge
DMSO
Antimycin A
FCCP
Oligomycin A
D
Normalized intensity of TMRM
29
28
29
30
****
DMSO
Antimycin A
FCCP
Oligomycin A
E
Normalized signal ratio (TMRM / MTG)
29
28
29
30
****
DMSO
Antimycin A
FCCP
Oligomycin A

Figure S3

Fig. S3 MARDO formation during oocyte growth.

(A) Representative fluorescence images of NSN and SN mouse oocytes expressing Mito-EGFP (mitochondria, green) and ZAR1-mScarlet (MARDO, magenta), and stained with SiR-DNA (DNA, blue). Oocytes were collected from 18 days old mice. Dashed line demarcates the oocyte.

(B) Quantification of the percentage of oocytes with MARDO labeled by ZAR-mScarlet. Oocytes were collected from mice of different ages.

(C) Representative fluorescence images of mouse GV oocytes stained with MitoTracker Geen (green) and TMRM (magenta). Oocytes were treated with DMSO, 5 μg/ml Antimycin A, 5 μM FCCP, or 5 μg/ml Oligomycin A for 1 h at 37℃ during staining.

(D) Quantification of the fluorescence intensity of TMRM in (C).

(E) Quantification of the fluorescence intensity ratio of TMRM to MitoTracker Green in (C).

The number of analyzed oocytes is specified in italics. Data are shown as mean ± SD (D, E). *P* values were calculated using one-way ANOVA with Tukey's *post-hoc* test. Scale bars, 10 μm.

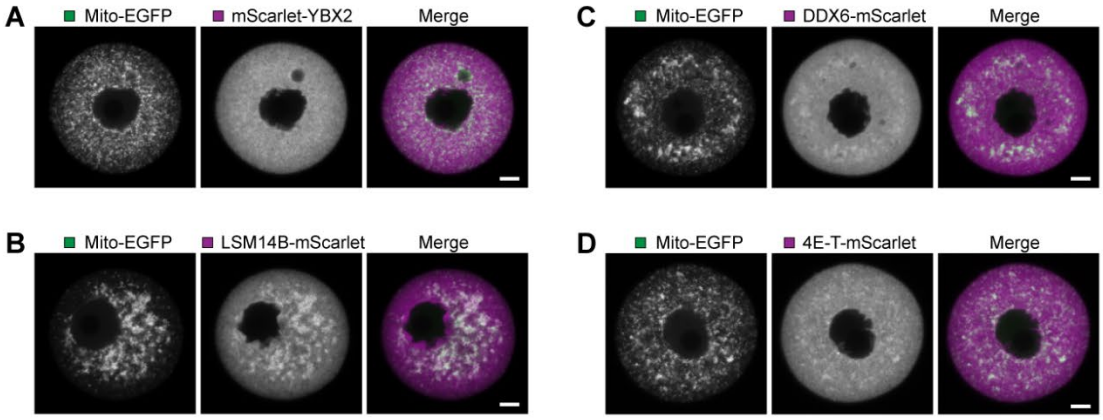
A
Mito-EGFP
mScarlet-YBX2
Merge
B
Mito-EGFP
LSM14B-mScarlet
Merge
C
Mito-EGFP
DDX6-mScarlet
Merge
D
Mito-EGFP
4E-T-mScarlet
Merge

Figure S4

Fig. S4 Overexpression of YBX2, LSM14B, DDX6 or 4E-T has little effect on mitochondrial clustering

(A-D) Representative fluorescence images of mouse GV oocytes. Green, Mito-EGFP (mitochondria); magenta, mScarlet-YBX2 (A), LSM14B-mScarlet (B), DDX6-mScarlet (C), 4E-T-mScarlet (D). Scale bars, 10 μm.

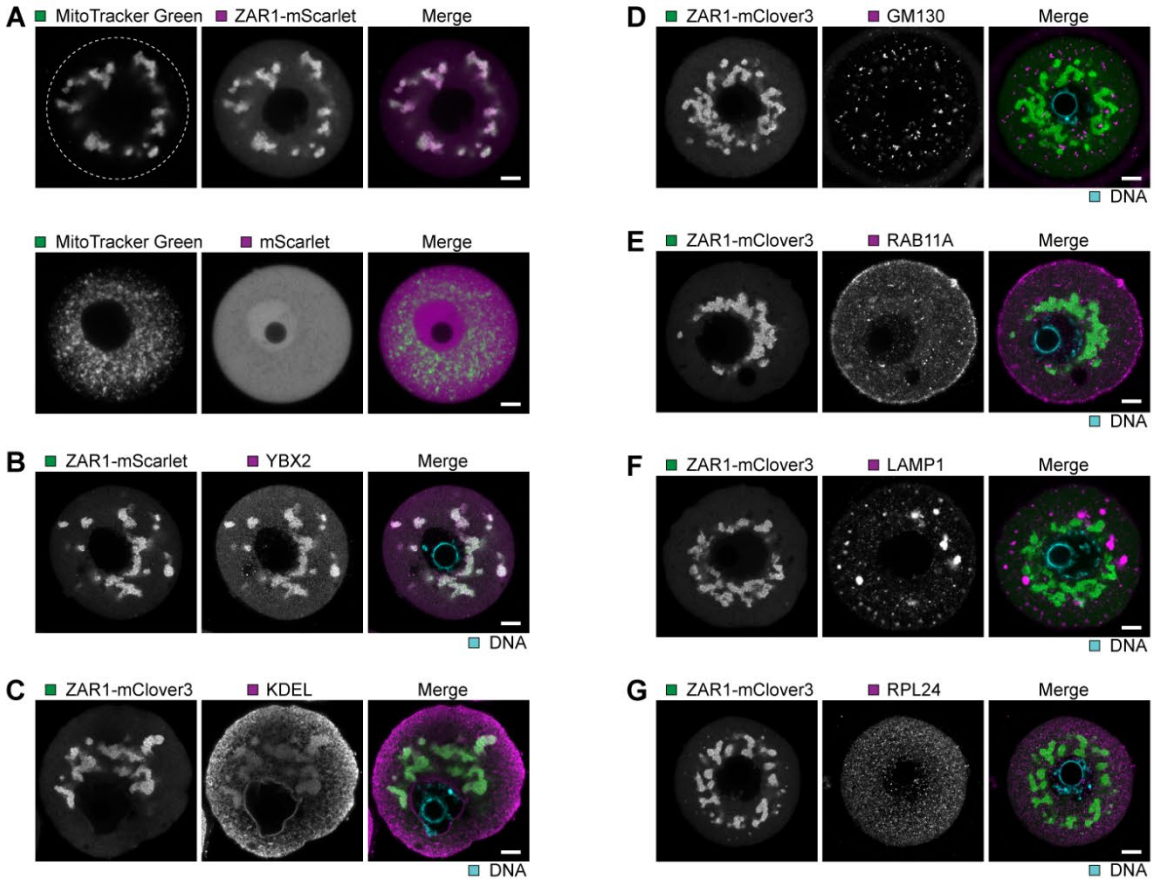
A
MitoTracker Green
ZAR1-mScarlet
Merge
MitoTracker Green
mScarlet
Merge
B
ZAR1-mScarlet
YBX2
Merge
DNA
C
ZAR1-mClover3
KDEL
Merge
DNA
D
ZAR1-mClover3
GM130
Merge
DNA
E
ZAR1-mClover3
RAB11A
Merge
DNA
F
ZAR1-mClover3
LAMP1
Merge
DNA
G
ZAR1-mClover3
RPL24
Merge
DNA

Figure S5

Fig. S5 MARDO is exclusively associated with mitochondria.

(A) Representative fluorescence images of mouse GV oocytes overexpressing ZAR1-mScarlet or mScarlet (magenta). Oocytes were further stained with MitoTracker Green (mitochondria, green). Dashed line demarcates the oocyte.

(B) Representative fluorescence images of mouse GV oocytes overexpressing ZAR1-mScarlet (MARDO, green). Oocytes were further stained with anti-YBX2 antibody (magenta).

(C-G) Representative fluorescence images of mouse GV oocytes overexpressing ZAR1-mClover3 (MARDO, green). Oocytes were further stained with anti-KDEL (C), anti-GM130 (D), anti-RAB11A (E), anti-LAMP1 (F), or anti-RPL24 (G) antibody (magenta).

Scale bars, 10 μm.

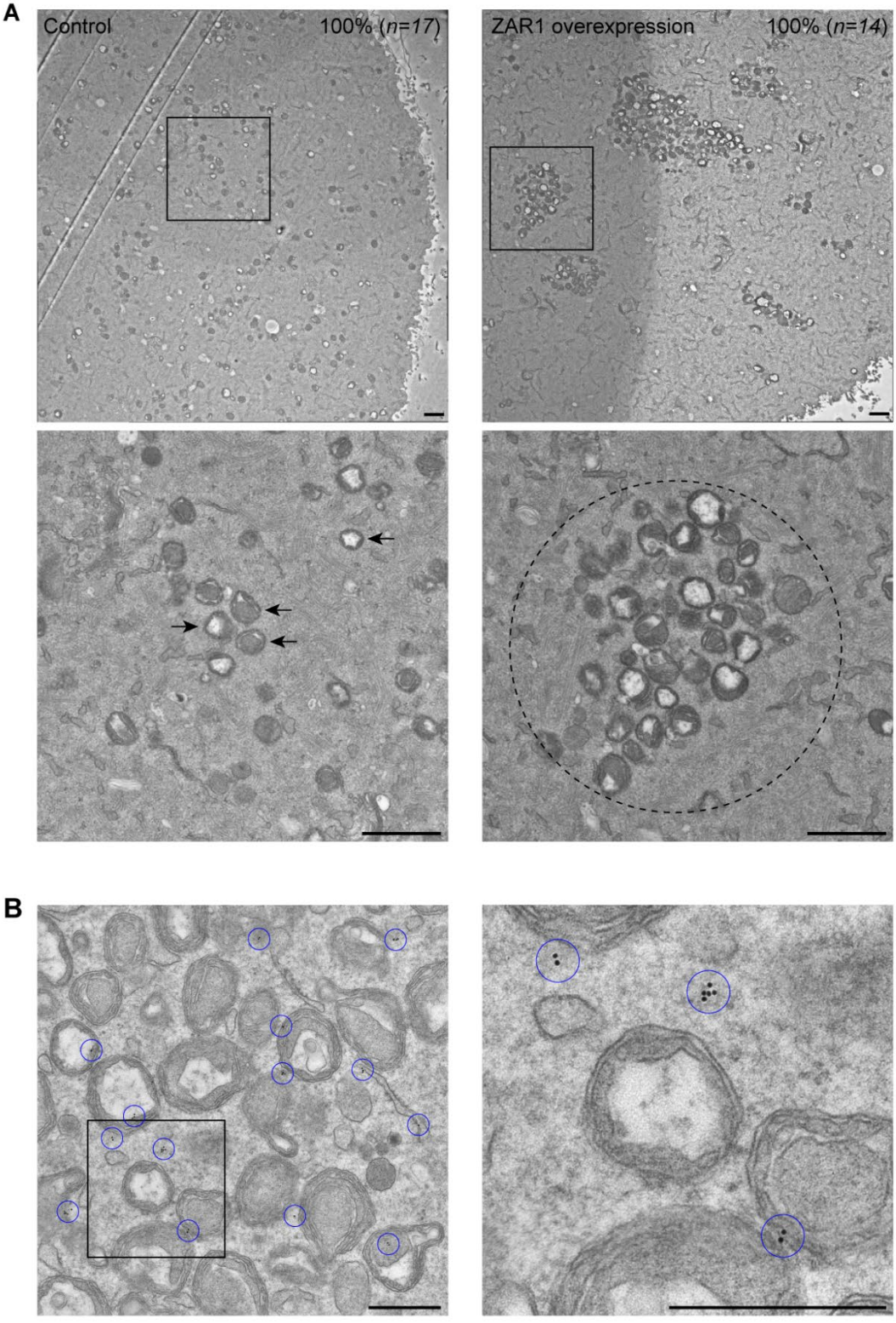

Figure S6

Fig. S6 ZAR1 overexpression promotes mitochondrial clustering.

(A) Representative transmission electron microscopy (TEM) images showing the distribution of mitochondria in mouse GV oocytes with or without ZAR1 overexpression. Outlined regions are magnified at the bottom. Arrows point to individual mitochondrion or mitochondria in small cluster. Dashed line circles a large mitochondrial cluster. The percentage of TEM sections with representative pattern is shown. “n” indicates the number of analyzed oocytes. Scale bar, 1 μm.

(B) Representative immunoelectron microscopy images showing that ZAR1 was localized in the interspace of mitochondrial cluster. Outlined regions are magnified on the right. Scale bar, 0.5 μm.

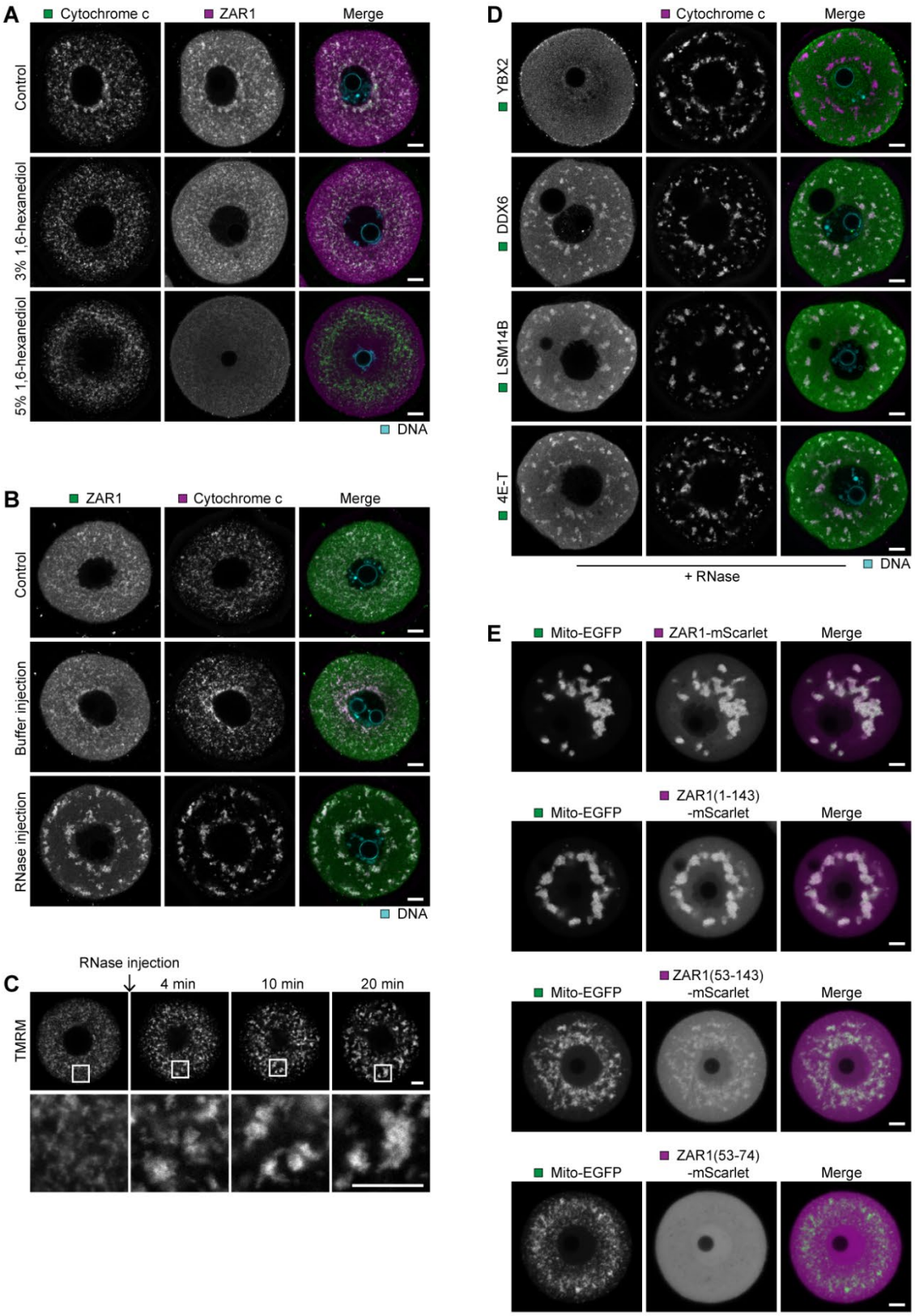
A
Cytochrome c
ZAR1
Merge
Control
3% 1,6-hexanediol
5% 1,6-hexanediol
DNA
B
ZAR1
Cytochrome c
Merge
Control
Buffer injection
RNase injection
DNA
C
RNase injection
4 min
10 min
20 min
TMRM
D
Cytochrome c
Merge
YBX2
DDX6
LSM14B
4E-T
+ RNase
DNA
E
Mito-EGFP
ZAR1-mScarlet
Merge
ZAR1(1-143)
-mScarlet
ZAR1(53-143)
-mScarlet
ZAR1(53-74)
-mScarlet

Figure S7

Fig. S7 RNA buffers MARDO formation and mitochondrial clustering.

(A) Representative immunofluorescence images of mouse GV oocytes kept in culture medium (control) or treated with 3% or 5% 1,6-hexanediol in culture medium for 5 minutes at 37℃ before fixation. Green, cytochrome c (mitochondria); magenta, ZAR1 (MARDO); blue, DNA. 5% but not 3% 1,6-hexanediol completely disrupted MARDO.

(B) Representative immunofluorescence images of mouse GV oocytes injected with buffer or RNase. Oocytes were fixed half an hour after injection. Non-injected oocytes were used as control. Green, ZAR1 (MARDO); magenta, cytochrome c (mitochondria); blue, DNA. There is no significant difference between non-injected control and buffer-injected oocytes.

(C) Representative stills from time-lapse movies of mouse GV oocytes stained with TMRM. Oocytes were injected with RNase and imaged immediately after injection. Time is given as minutes after RNase injection. Outlined regions are magnified at the bottom.

(D) Representative immunofluorescence images of mouse GV oocytes injected with RNase. Oocytes were fixed half an hour after injection. Non-injected oocytes were used as control. Green, YBX2, DDX6, LSM14B or 4E-T; magenta, cytochrome c (mitochondria); blue, DNA.

(E) Representative fluorescence images of mouse GV oocytes expressing Mito-EGFP (mitochondria, green) and ZAR1-mScarlet, ZAR1(1-143)-mScarlet, ZAR1(53-143)-mScarlet, or ZAR1(53-74)-mScarlet (magenta).

Scale bars, 10 μm.

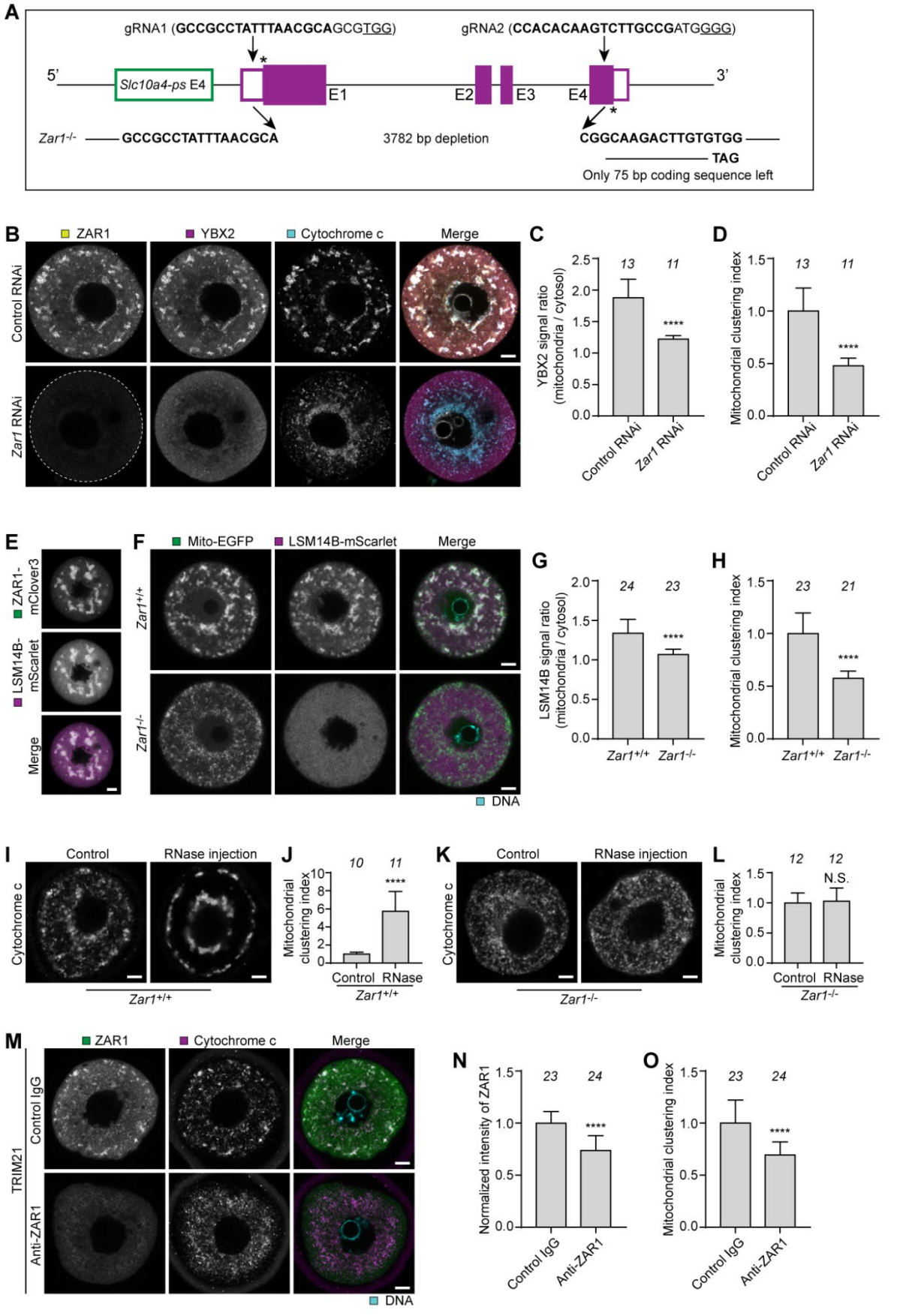
A
gRNA1 (GCCGCCTATTTAACGCAGCGTGG)
gRNA2 (CCACACAAGTCTTGCCGATGGGG)
5'
Slc10a4-ps E4
E1
E2
E3
E4
3'
Zar1-/-
GCCGCCTATTTAACGCA
3782 bp depletion
CGGCAAGACTTGTGTGG
TAG
Only 75 bp coding sequence left
B
ZAR1
YBX2
Cytochrome c
Merge
Control RNAi
Zar1 RNAi
C
YBX2 signal ratio (mitochondria / cytosol)
13
11
****
Control RNAi
Zar1 RNAi
D
Mitochondrial clustering index
13
11
****
Control RNAi
Zar1 RNAi
E
ZAR1-mClover3
LSM14B-mScarlet
Merge
F
Mito-EGFP
LSM14B-mScarlet
Merge
Zar1+/+
Zar1-/-
DNA
G
LSM14B signal ratio (mitochondria / cytosol)
24
23
****
Zar1+/+
Zar1-/-
H
Mitochondrial clustering index
23
21
****
Zar1+/+
Zar1-/-
I
Control
RNase injection
Cytochrome c
Zar1+/+
J
Mitochondrial clustering index
10
11
****
Control
RNase
Zar1+/+
K
Control
RNase injection
Cytochrome c
Zar1-/-
L
Mitochondrial clustering index
12
12
N.S.
Control
RNase
Zar1-/-
M
ZAR1
Cytochrome c
Merge
TRIM21
Control IgG
Anti-ZAR1
DNA
N
Normalized intensity of ZAR1
23
24
****
Control IgG
Anti-ZAR1
O
Mitochondrial clustering index
23
24
****
Control IgG
Anti-ZAR1

Figure S8

Fig. S8 *Zar1* down-regulation impairs MARDO formation and mitochondrial clustering.

(A) Cartoon showing the gene targeting strategy for *Zar1* knockout. Solid magenta bars represent four exons (E1, E2, E3, and E4) of *Zar1*. Hollow magenta bars represent 5′ and 3′ UTR. DNA sequence of *Zar1* knockout mouse and the corresponding sequences in gRNAs were show in bold. gRNA, guide RNA; *, start or stop codon.

(B) Representative immunofluorescence images of control RNAi and *Zar1* RNAi mouse GV oocytes. Yellow, ZAR1; magenta, YBX2 (MARDO); blue, cytochrome c (mitochondria). Dashed line demarcates the oocyte.

(C) Quantification of the ratio of average YBX2 intensities on mitochondria to in cytosol (A).

(D) Quantification of the mitochondrial clustering index (A).

(E) Representative fluorescence images of mouse GV oocytes expressing ZAR1-mClover3 (green) and LSM14B-mScarlet (magenta).

(F) Representative fluorescence images of GV oocytes expressing Mito-EGFP (green) and LSM14B-mScarlet collected from *Zar1*$^{+/+}$ and *Zar1*$^{-/-}$ mice.

(G) Quantification of the ratio of average LSM14B intensities on mitochondria to in cytosol (E).

(H) Quantification of the mitochondrial clustering index (E).

(I) Representative immunofluorescence images of *Zar1*$^{+/+}$ GV oocytes with or without RNase injection. Oocytes were fixed half an hour after injection and then stained with anti-cytochrome c antibody.

(J) Quantification of the mitochondrial clustering index (H).

(K) Representative immunofluorescence images of *Zar1*$^{-/-}$ GV oocytes with or without RNase injection. Oocytes were fixed half an hour after injection and then stained with anti-cytochrome c antibody.

(L) Quantification of the mitochondrial clustering index (J).

(M) Representative immunofluorescence images of control and ZAR1-depleted mouse GV oocytes by Trim-Away. Green, ZAR1; magenta, cytochrome c (mitochondria); blue, DNA.

(N) Quantification of the fluorescence intensity of ZAR1 in (L).

(O) Quantification of the mitochondrial clustering index (L).

The number of analyzed oocytes is specified in italics. Data are shown as mean ± SD. *P* values were calculated using unpaired two-tailed Student's *t* test. Scale bars, 10 μm.

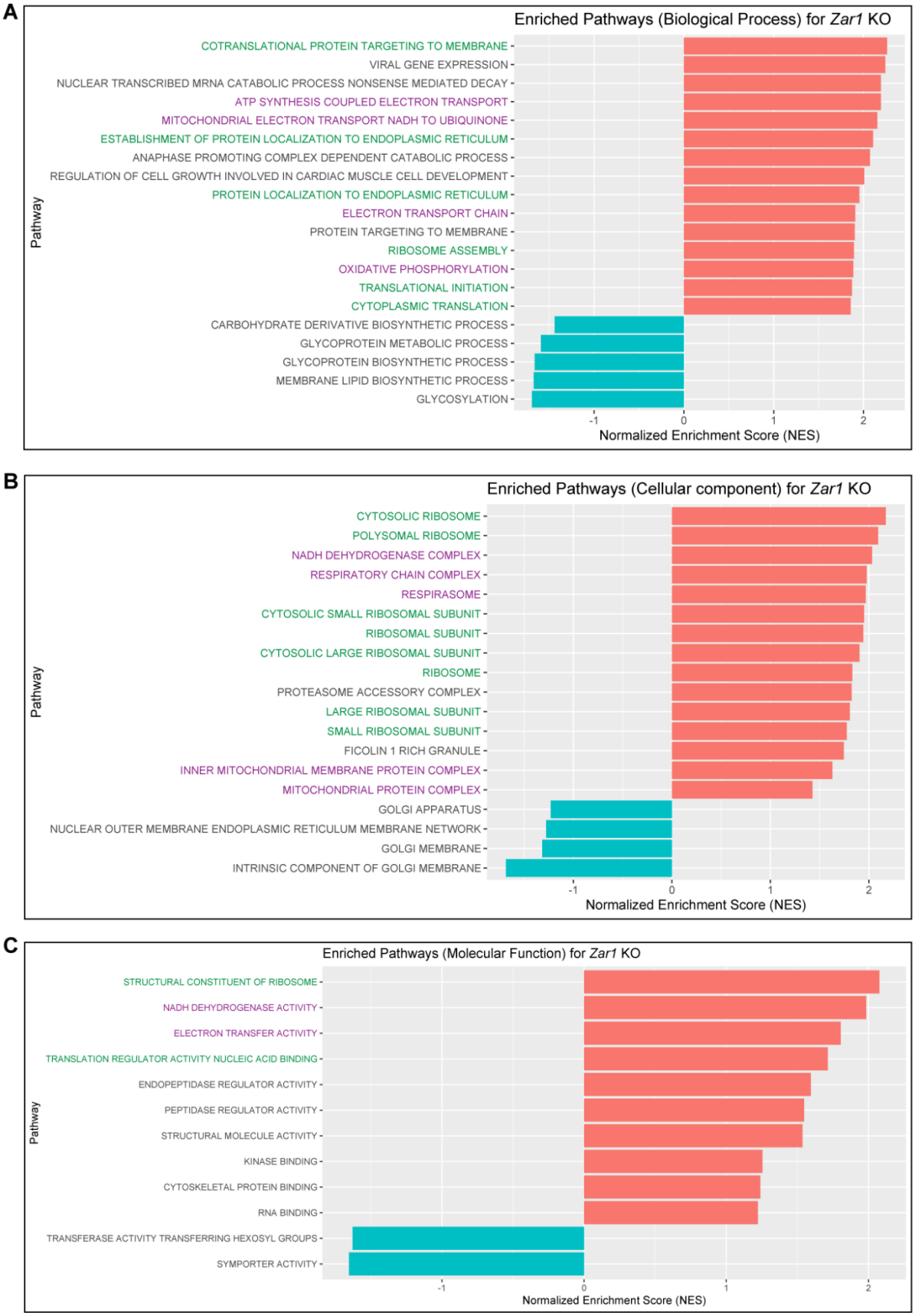
A
Enriched Pathways (Biological Process) for Zar1 KO
COTRANSLATIONAL PROTEIN TARGETING TO MEMBRANE
VIRAL GENE EXPRESSION
NUCLEAR TRANSCRIBED MRNA CATABOLIC PROCESS NONSENSE MEDIATED DECAY
ATP SYNTHESIS COUPLED ELECTRON TRANSPORT
MITOCHONDRIAL ELECTRON TRANSPORT NADH TO UBIQUINONE
ESTABLISHMENT OF PROTEIN LOCALIZATION TO ENDOPLASMIC RETICULUM
ANAPHASE PROMOTING COMPLEX DEPENDENT CATABOLIC PROCESS
REGULATION OF CELL GROWTH INVOLVED IN CARDIAC MUSCLE CELL DEVELOPMENT
PROTEIN LOCALIZATION TO ENDOPLASMIC RETICULUM
ELECTRON TRANSPORT CHAIN
PROTEIN TARGETING TO MEMBRANE
RIBOSOME ASSEMBLY
OXIDATIVE PHOSPHORYLATION
TRANSLATIONAL INITIATION
CYTOPLASMIC TRANSLATION
CARBOHYDRATE DERIVATIVE BIOSYNTHETIC PROCESS
GLYCOPROTEIN METABOLIC PROCESS
GLYCOPROTEIN BIOSYNTHETIC PROCESS
MEMBRANE LIPID BIOSYNTHETIC PROCESS
GLYCOSYLATION
Pathway
-1
0
1
2
Normalized Enrichment Score (NES)
B
Enriched Pathways (Cellular component) for Zar1 KO
CYTOSOLIC RIBOSOME
POLYSOMAL RIBOSOME
NADH DEHYDROGENASE COMPLEX
RESPIRATORY CHAIN COMPLEX
RESPIRASOME
CYTOSOLIC SMALL RIBOSOMAL SUBUNIT
RIBOSOMAL SUBUNIT
CYTOSOLIC LARGE RIBOSOMAL SUBUNIT
RIBOSOME
PROTEASOME ACCESSORY COMPLEX
LARGE RIBOSOMAL SUBUNIT
SMALL RIBOSOMAL SUBUNIT
FICOLIN 1 RICH GRANULE
INNER MITOCHONDRIAL MEMBRANE PROTEIN COMPLEX
MITOCHONDRIAL PROTEIN COMPLEX
GOLGI APPARATUS
NUCLEAR OUTER MEMBRANE ENDOPLASMIC RETICULUM MEMBRANE NETWORK
GOLGI MEMBRANE
INTRINSIC COMPONENT OF GOLGI MEMBRANE
Pathway
-1
0
1
2
Normalized Enrichment Score (NES)
C
Enriched Pathways (Molecular Function) for Zar1 KO
STRUCTURAL CONSTITUENT OF RIBOSOME
NADH DEHYDROGENASE ACTIVITY
ELECTRON TRANSFER ACTIVITY
TRANSLATION REGULATOR ACTIVITY NUCLEIC ACID BINDING
ENDOPEPTIDASE REGULATOR ACTIVITY
PEPTIDASE REGULATOR ACTIVITY
STRUCTURAL MOLECULE ACTIVITY
KINASE BINDING
CYTOSKELETAL PROTEIN BINDING
RNA BINDING
TRANSFERASE ACTIVITY TRANSFERRING HEXOSYL GROUPS
SYMPORTER ACTIVITY
Pathway
-1
0
1
2
Normalized Enrichment Score (NES)

Figure S9

Fig. S9 Gene set enrichment analysis (GSEA) on RNA-seq data of *Zar1*$^{+/+}$ and *Zar1*$^{-/-}$ oocytes.

(A-C) Up-regulated (orange bars) and down-regulated (cyan bars) pathways (biological process (A), cellular component (B), molecular function (C)) in *Zar1*$^{-/-}$ oocytes versus *Zar1*$^{+/+}$ oocytes. Green terms are translation-related pathways. Magenta terms are mitochondrial activity related pathways.

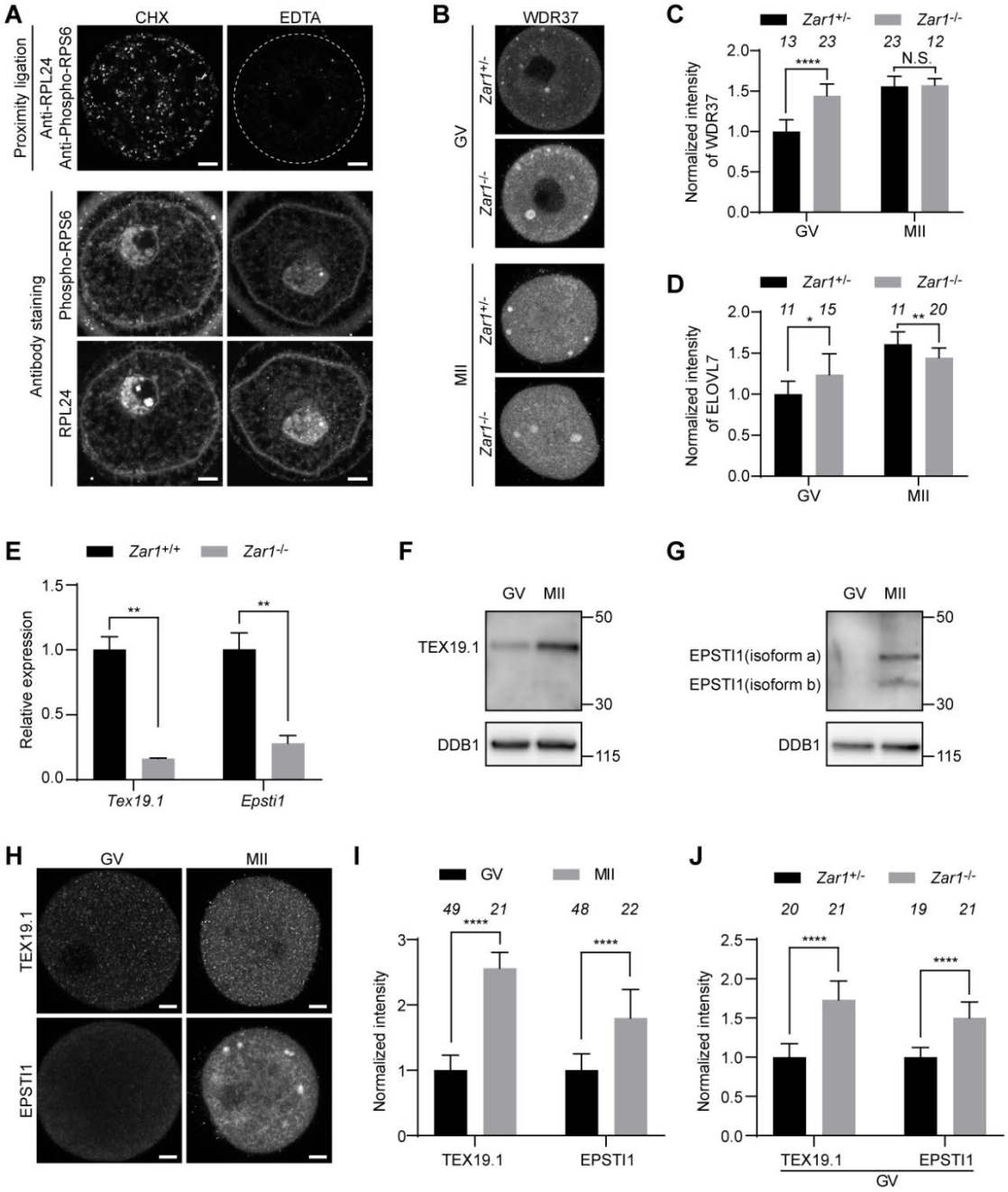
A
CHX
EDTA
Proximity ligation
Anti-RPL24
Anti-Phospho-RPS6
Antibody staining
Phospho-RPS6
RPL24
B
WDR37
GV
MII
Zar1+/-
Zar1-/-
C
Zar1+/-
Zar1-/-
13 23
23 12
****
N.S.
Normalized intensity of WDR37
GV
MII
D
11 15
11 20
*
**
Normalized intensity of ELOVL7
E
Zar1+/+
Zar1-/-
Relative expression
**
Tex19.1
Epsti1
F
GV MII
TEX19.1
DDB1
50
30
115
G
EPSTI1(isoform a)
EPSTI1(isoform b)
H
TEX19.1
EPSTI1
I
49 21
48 22
Normalized intensity
J
20 21
19 21

Figure S10

Fig. S10 MARDO disruption causes premature translation of stored mRNAs.

(A) Representative images of in situ PLA performed with antibody pair anti-RPL24 & anti-Phospho-RPS6 in mouse GV oocytes (top panel). Representative immunofluorescence images of mouse GV oocytes stained with anti-RPL24 and anti-Phospho-RPS6 antibodies (bottom panel). Oocytes were permeabilized and treated with cycloheximide (CHX) or EDTA before fixation.

(B) Representative immunofluorescence images of oocytes collected from *Zar1*$^{+/-}$ and *Zar1*$^{-/-}$ mice. Oocytes were either fixed at GV stage or cultured to MII stage before fixation.

(C) Quantification of the fluorescence intensity of WDR37 in GV oocytes and in vitro matured MII oocytes collected from *Zar1*$^{+/-}$ and *Zar1*$^{-/-}$ mice.

(D) Quantification of the fluorescence intensity of ELOVL7 in GV oocytes and in vitro matured MII oocytes collected from *Zar1*$^{+/-}$ and *Zar1*$^{-/-}$ mice.

(E) RT-qPCR results showing expression of *Tex19.1* and *Epsti1* in *Zar1*$^{+/+}$ and *Zar1*$^{-/-}$ oocytes.

(F-G) Western blot analyses showing the expression of TEX19.1 (F) and EPSTI1 (G) in GV and in vitro matured MII oocytes. DDB1 was used as a loading control.

(H) Representative immunofluorescence images of GV and in vitro matured MII oocytes stained with anti-TEX19.1 or anti-EPSTI1 antibody.

(I) Quantification of the fluorescence intensity of TEX19.1 and EPSTI1 in GV oocytes and in vitro matured MII oocytes

(J) Quantification of the fluorescence intensity of TEX19.1 and EPSTI1 in GV oocytes collected from *Zar1*$^{+/-}$ and *Zar1*$^{-/-}$ mice.

The number of analyzed oocytes is specified in italics. Data are shown as mean ± SD. *P* values were calculated using unpaired two-tailed Student's *t* test. Scale bars, 10 μm.

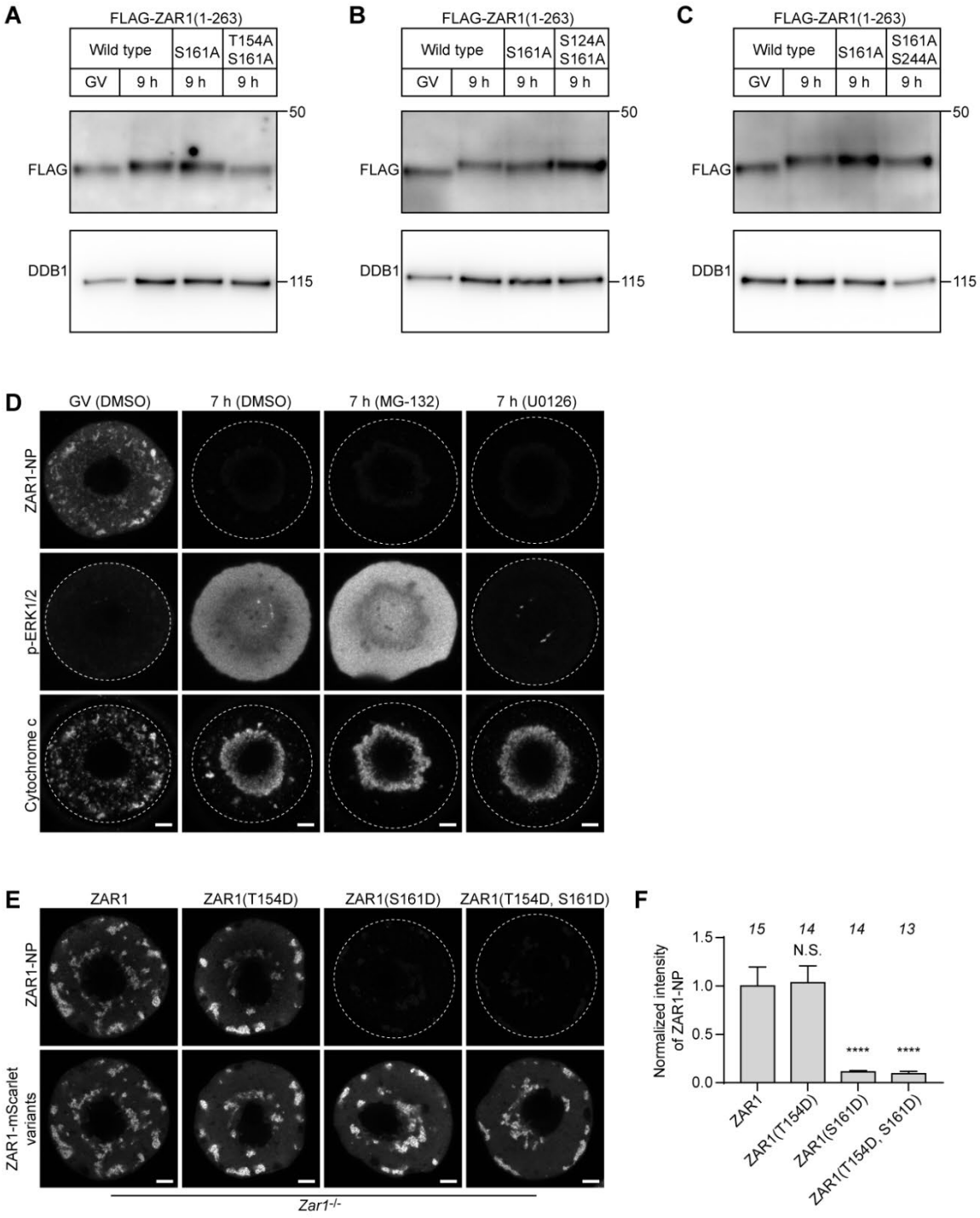
A
FLAG-ZAR1(1-263)
Wild type
S161A
T154A S161A
GV
9 h
9 h
9 h
50
FLAG
DDB1
115
B
FLAG-ZAR1(1-263)
Wild type
S161A
S124A S161A
GV
9 h
9 h
9 h
50
FLAG
DDB1
115
C
FLAG-ZAR1(1-263)
Wild type
S161A
S161A S244A
GV
9 h
9 h
9 h
50
FLAG
DDB1
115
D
GV (DMSO)
7 h (DMSO)
7 h (MG-132)
7 h (U0126)
ZAR1-NP
p-ERK1/2
Cytochrome c
E
ZAR1
ZAR1(T154D)
ZAR1(S161D)
ZAR1(T154D, S161D)
ZAR1-NP
ZAR1-mScarlet variants
Zar1-/-
F
15
14
14
13
N.S.
****
****
Normalized intensity of ZAR1-NP
1.5
1.0
0.5
0.0
ZAR1
ZAR1(T154D)
ZAR1(S161D)
ZAR1(T154D, S161D)
G
Mito-EGFP
ZAR1-mScarlet
Merge
H
Mito-EGFP
ZAR1(T154D, S161D)-mScarlet
Merge

Figure S11

Fig. S11 Identification of ZAR1 phosphorylation sites by CDK1.

(A-C) Western blot analyses showing the expression of overexpressed FLAG-ZAR1(1-263) variants in mouse oocytes. Oocytes were lysed at different times after dbcAMP washout. DDB1 was used as a loading control.

(D) Representative immunofluorescence images of mouse oocytes stained with anti-ZAR1-NP, anti-phospho-ERK1/2 and anti-cytochrome c antibodies. Oocytes were kept for 7 hours with dbcAMP (GV) or kept for 7 hours after dbcAMP washout (7 h) before fixation. GV oocytes were treated with DMSO. 7 h oocytes were treated with DMSO, 10 μM MG-132 or 20 μM U-0126 after dbcAMP washout. Dashed lines demarcate the oocyte.

(E) Representative immunofluorescence images of *Zar1*$^{-/-}$ oocytes stained with anti-ZAR1-NP antibody. Wild-type ZAR1 or ZAR1 variants was overexpressed in oocytes before fixation.

(F) Quantification of the fluorescence intensity of ZAR1-NP in (E).

(G-H) Representative fluorescence images of mouse GV oocytes expressing mito-EGFP (green) and ZAR1-mScarlet or ZAR1(T154D, S161D)-mScarlet (magenta).

The number of analyzed oocytes is specified in italics. Data are shown as mean ± SD. *P* values were calculated using one-way ANOVA with Tukey's *post-hoc* test. Scale bars, 10 μm.

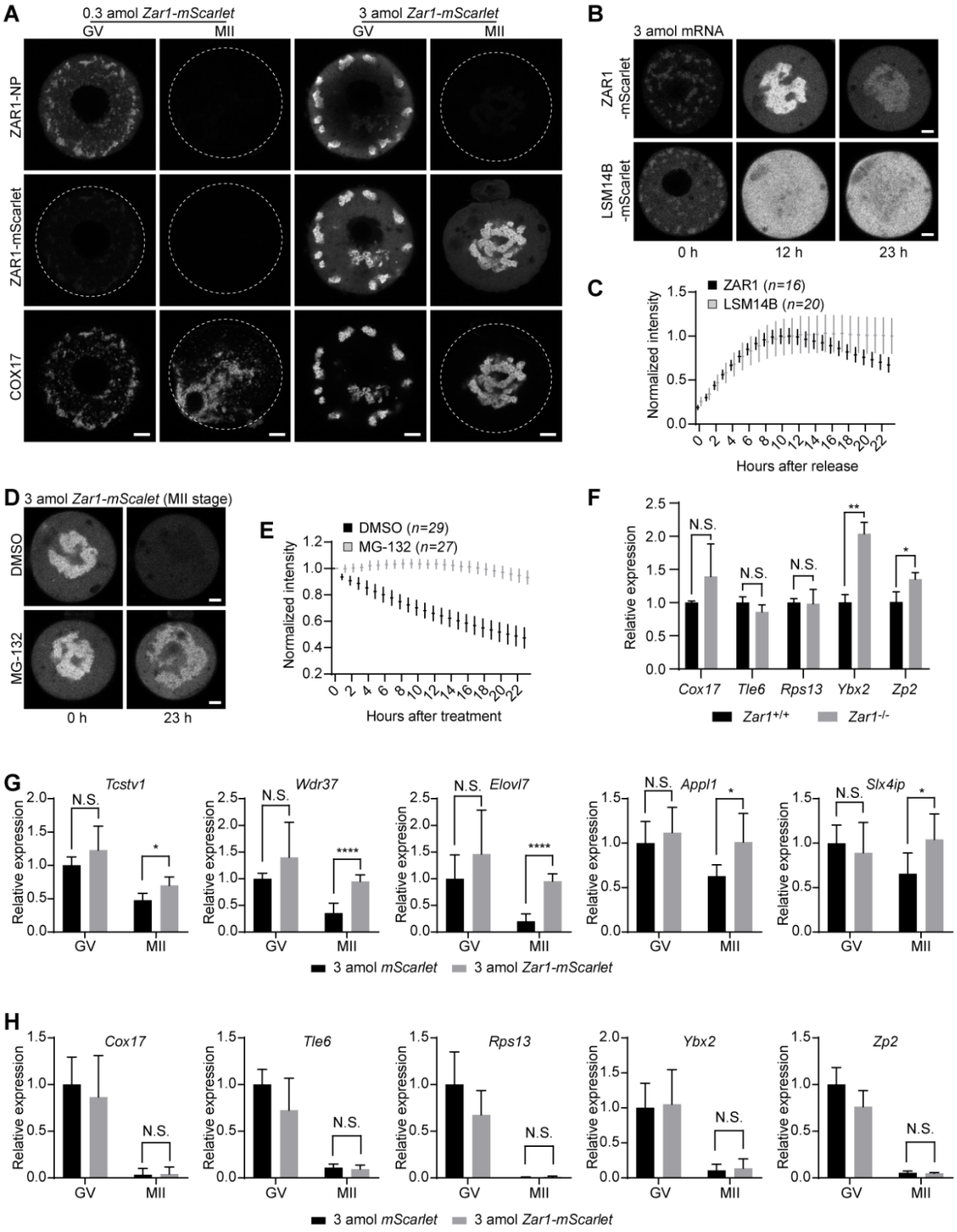
A
0.3 amol Zar1-mScarlet
3 amol Zar1-mScarlet
GV
MII
ZAR1-NP
ZAR1-mScarlet
COX17
B
3 amol mRNA
ZAR1 -mScarlet
LSM14B -mScarlet
0 h
12 h
23 h
C
ZAR1 (n=16)
LSM14B (n=20)
Normalized intensity
Hours after release
D
3 amol Zar1-mScalet (MII stage)
DMSO
MG-132
0 h
23 h
E
DMSO (n=29)
MG-132 (n=27)
Normalized intensity
Hours after treatment
F
Relative expression
N.S.
**
*
Cox17
Tle6
Rps13
Ybx2
Zp2
Zar1+/+
Zar1-/-
G
Tcstv1
Wdr37
Elovl7
Appl1
Slx4ip
Relative expression
N.S.
*
****
GV
MII
3 amol mScarlet
3 amol Zar1-mScarlet
H
Cox17
Tle6
Rps13
Ybx2
Zp2
Relative expression
N.S.
GV
MII
3 amol mScarlet
3 amol Zar1-mScarlet

Figure S12

Fig. S12 Proteasomal degradation of ZAR1 is essential for MARDO dissolution and timely mRNA decay

(A) Representative immunofluorescence images of mouse GV oocytes and MII oocytes stained with anti-ZAR1-NP and anti-COX17 antibodies. 0.3 or 3 amol *Zar1-mScarlet* mRNA was injected into GV oocytes. Oocytes were either kept at GV stage or transferred to dbcAMP-free medium to get in vitro matured MII oocytes. Dashed lines demarcate the oocyte.

(B) Representative stills (mid-section) from time-lapse movies of mouse oocytes with 3 amol *Zar1-mScarlet* or *Lsm14b-mScarlet* mRNA injected. Time is given as hours after dbcAMP washout.

(C) Quantification of the total fluorescence intensity (21 sections every 3 μm) of ZAR1 and LSM14B in (B).

(D) Representative stills (mid-section) from time-lapse movies of mouse MII oocytes expressing ZAR1-mScarlet. 3 amol *Zar1-mScarlet* mRNA was injected into GV oocytes. After 3 hours of expression, oocytes were transferred to dbcAMP-free medium for in vitro maturation. 15 hours later, in vitro matured MII oocytes were either treated with DMSO or 10 μM MG-132 for live cell imaging. Time is given as hours after drug treatment.

(E) Quantification of the total fluorescence intensity (25 sections every 3 μm) of ZAR1 in (D).

(F) RT-qPCR results showing expression of five genes (*Cox17*, *Tle6*, *Rps13*, *Ybx2*, and *Zp2*) in *Zar1*$^{+/+}$ and *Zar1*$^{-/-}$ oocytes.

(G-H) RT-qPCR results showing expression of two groups of genes in GV oocytes and MII oocytes with or without ZAR1 overexpression. 3 amol *mScarlet* or *Zar1-mScarlet* mRNA was injected into GV oocytes. After 3 hours of expression, half oocytes were transferred to dbcAMP-free medium for in vitro maturation. 17 hours later, in vitro matured MII oocytes and the remaining GV were used to prepare cDNA libraries for RT-qPCR analyses.

The number of analyzed oocytes is specified in italics (C, E). Data are shown as mean ± SD. *P* values were calculated using unpaired two-tailed Student's *t* test (G, H). Scale bars, 10 μm.

ZAR1 regulates the lipid metabolism and mitochondrial activity in mouse oocytes by the stabilization of *Hig2* mRNA

Shiya Cheng, Gerrit Altmeppen, Melina Schuh

Abstract

Zygote arrest 1 (Zar1), an mRNA binding protein in mouse oocytes, was reported to regulate the translation of maternal mRNAs. However, the mechanisms of Zar1's regulation of translation were not clear. In this study, single molecule RNA *in situ* hybridization (smRNA-FISH) was used to identify Zar1's role in the regulation of *hypoxia-inducible gene 2 (Hig2) / hypoxia inducible lipid droplet associated (Hilpda)* mRNA. HIG2 is an endogenous inhibitor of Adipose TriGlyceride Lipase (ATGL), which is a lipase that is located on lipid droplets. In combination with immunofluorescence microscopy and live cell imaging, we here show that ZAR1 binds and stabilizes *Hig2* mRNA. *Zar1*$^{-/-}$ oocytes exhibited decreased levels of *Hig2* mRNA that correlated with the *de facto* loss of lipid droplets and mitochondrial hyperpolarization. Our experiments revealed that the metabolic changes in *Zar1*$^{-/-}$ oocytes induced oxidative stress. We therefore conclude that oxidative damage is a factor that contributes to the decrease of developmental competence observed in *Zar1*$^{-/-}$ oocytes.

Introduction

When female mammals age, the quality of their oocytes and ovarian reserve (quantity) decreases[1]. Together, both effects cause the decline of female fertility which is referred to as maternal age effect[2,3]. At an advanced age, female mammals experience increased numbers of miscarriages[4]. Successful pregnancies of elder females often result in genetic disorders of the offspring, e.g. trisomy 21 (Down's syndrome) in humans[5]. Oocytes differentiate from progenitor cells during embryogenesis[6]. After birth, oocytes do not develop further[7]. The main challenge for mammalian oocytes is to maintain the cellular integrity over a long period that can reach up to decades in humans.

One factor that contributes to the decline of the oocyte's quality is the accumulation of reactive oxygen species (ROS)[8]. Oxidative stress is correlated with increased DNA damage that leads to a decreased oocyte competence[9]. The main source of ROS are mitochondria[10,11]. Thus, the regulation, selection and transmission of intact mitochondria to the next generation is important to maintain low ROS levels.

In human and mouse oocytes, at least two different subpopulations of mitochondria are known that differ in their mitochondria membrane potential. Highly

active mitochondria tend to localize cortically / close to the plasma membrane while inactive mitochondria are dispersed in the inner regions of the cytoplasm[12–19].

In oocytes of *Xenopus laevis*, the spatial sorting of mitochondria is assumed to be partly conducted by a structure called the Balbiani body[20,21]. The Balbiani body was found in fish, insects and vertebrates[22–26]. However, whether a related structure exists in mouse oocyte is controversial[27]. Besides mitochondria, the Balbiani body's main component is maternal mRNA[28–32]. In vertebrates like *Xenopus laevis*, the Balbiani body is stable until late oogenesis[33]. In mouse and humans, the Balbiani body disappears during early oogenesis[34]. How fully grown mouse oocytes regulate the mitochondrial activity and translation of maternal mRNAs before the onset of meiosis is so far not understood.

Moreover, in 2010, Jędrzejowska and Janusz found that the yolk nucleus, a structure in spider oocytes that is similar to the Balbiani body, is the initial site of synthesis for lipid droplets[35]. In mammals, the canonical catabolism of intracellular lipids is initiated at the site of the lipid droplets. Lipid droplets are spherical organelles with a single layer of phospholipids. The lipids inside are stored in the form of triacyglycerols[36]. The export in form of fatty acids is controlled by an initial hydrolysis step which is mediated by the enzyme adipose triglyceride lipase (ATGL)[37,38]. Lipid droplets can interact with mitochondria and form contact sites for the transfer of fatty acids. The interaction between lipid droplets and mitochondria is mediated by perlipins[36,39,40]. The energy of the fatty acids is converted into a proton gradient by the fatty acid **β**-oxidation (FAO) and electron transport chain. The proton gradient provides energy for the phosphorylation of ADP to ATP[41–43]. Due to the electrical charge of protons, the gradient along the inner mitochondrial membrane forms an electrical potential that can be visualized by dyes such as JC-1 and tetramethylrhodamine, methyl ester (TMRM)[44–46]. Mammalian oocytes contain a large number of lipid droplets. It was found that the oocyte requires lipid droplets as energy depot between ovulation and implantation of the fertilized egg into the uterus because no external energy supply is provided during this arrest[47]. Hence, the stable maintenance of lipid droplets throughout the growth and maturation of an oocyte is important for the survival of the early embryo. Herein, we propose that maternal mRNAs regulate the stability of lipid droplets in immature oocytes. Maternal mRNAs are prone to degradation. However, binding to proteins can prevent mRNA degradation. Many mRNA-binding proteins determine the fate of the bound mRNA by the interaction with other proteins or modifications of the poly(A)-tail[48–52]. For the *Drosophila* proteins of Smaug, Nanos and ME31B, it was shown that mRNA binding proteins repress translation and reduce stability in different manifestations for different mRNAs[53–58].

Zygote arrest 1 (Zar1) is one of the earliest discovered mRNA-binding proteins that was shown to be essential for early embryogenesis because its absence in knockout mice leads to female infertility[59]. Further, it was shown that ZAR1 and its functional homolog ZAR2 regulate the stability of maternal mRNAs and that both

homologs are required for the integrity of meiosis. The knockout of both genes leads to the delayed onset and progression of meiosis and causes higher aneuploidy rates[60].

In this study, we describe a novel pathway that links the mRNA-binding protein ZAR1 to the export of fatty acids from lipid droplets and to mitochondrial membrane potential. In addition, we propose that maternal mRNAs regulate the stability of lipid droplets in immature oocytes. We used Zar1-deficient mouse oocytes to show the loss of certain mRNAs. HIG2 is a protein that inhibits the activity of the ATGL and reduces the export of fatty acids from the lipid droplets. Because fatty acids are converted into energy by the FAO, HIG2 therefore partly regulates the mitochondrial activity. This study shows that ZAR1 stabilizes *Hig2* mRNA in wild type oocytes and concludes that stable mRNA and protein levels are required to maintain a low mitochondrial activity during the germinal vesicle (GV) stage of oocytes.

Results

ZAR1 is necessary to maintain lipid droplets in mouse oocytes

Zar1$^{-/-}$ mice were generated and analyzed before by Wu *et al.* and Rong *et al*. who reported impaired development during the zygote stage and the maturation of the oocytes[59,60]. In this study, we investigated the effects of the loss of ZAR1 in GV oocytes. We observed that *Zar1*$^{-/-}$ oocytes lack granules which are visible in wildtype (WT) oocytes of various mouse lines (i.e. C57BL/6N, C57BL/6J, CD1) (Fig. 1A)[61–63]. Based on observations made by comparison of different bovine oocytes and their respective lipid droplet content, we proposed that the absent granules in *Zar1*$^{-/-}$ oocytes were lipid droplets[64]. Further, we concluded that ZAR1 is necessary to maintain the number and size of lipid droplets in WT oocytes. Nile red was used to stain lipid droplets in *Zar1*$^{-/-}$ and *Zar1*$^{+/+}$ oocytes and a reduction of fluorescence signal in *Zar1*$^{-/-}$ oocytes was observed by us. Because Nile red stains multivesicular aggregates, too, LipidSpot was tested next, which is a dye that was reported to be specific for lipid droplet (Fig. 1 A)[65]. Staining of *Zar1*$^{-/-}$ and *Zar1*$^{+/+}$ oocytes with LipidSpot confirmed our previous findings on NileRed staining. The LipidSpot signal in *Zar1*$^{-/-}$ oocytes was similar to the background signal, indicating that lipid droplets are almost absent in *Zar1*$^{-/-}$ oocytes (Fig. 1A). To investigate the affected pathway of lipid metabolism, the initial step was the inhibition of the uppermost reaction of neutral lipid degradation. The first hydrolysis step of triacyglycerides is catalyzed by the enzyme adipose triglyceride lipase (ATGL)[37,38]. When ATGL was inhibited by ATGListatin, we observed a rescue the WT phenotype (Fig. 1B). The inhibition of ATGL resulted in even larger lipid droplets and lipid droplet aggregates compared to WT oocytes (Fig. 1B).

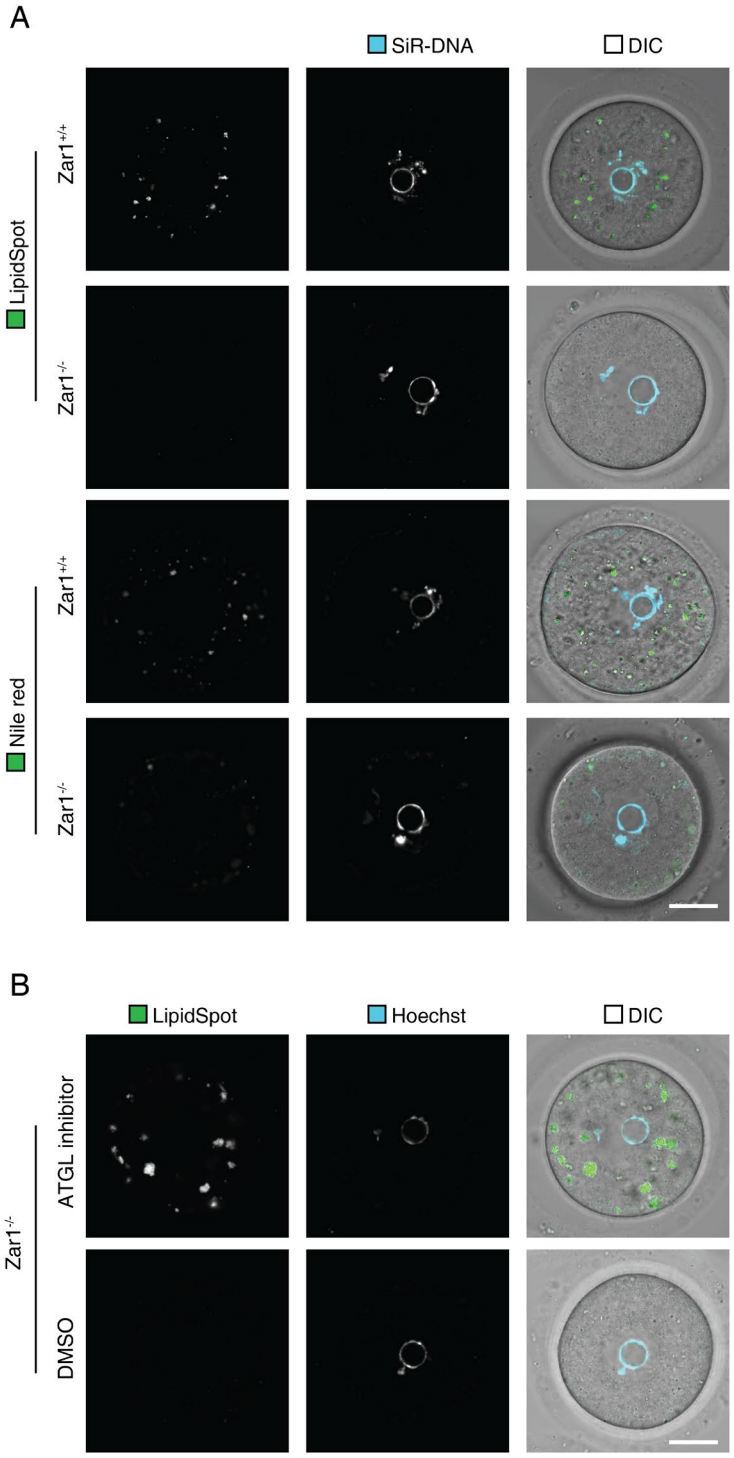

Fig. 1 Lipid droplets are lost in *Zar1*$^{-/-}$ oocytes. (A) Confocal live cell microscopy images of *Zar1*$^{-/-}$ and *Zar1*$^{+/+}$ oocytes staining with SiR-DNA and two lipid droplet specific dyes. Upper panel shows staining with LipidSpot 488, lower panel shows staining with Nile red. (B) Images of *Zar1*$^{-/-}$ and *Zar1*$^{+/+}$ oocytes after fixation and staining with Hoechst (DNA) and LipidSpot 488 (lipid droplets). Oocytes were incubated with Atglistatin, a specific ATGL inhibitor. Control oocytes were incubated in medium supplied with an equivalent amount of DMSO. Scale bars 20 µm.

ZAR1 is needed for the inhibition of ATGL

Concluded from the reduced number of lipid droplets in *Zar1*$^{-/-}$ oocytes, the protein level of the ATGL was assumed to be reduced in *Zar1*$^{-/-}$ oocytes. To analyze the protein level of ATGL, an anti-ATGL antibody was used. Staining of *Zar1*$^{-/-}$ oocytes with an anti-ATGL antibody revealed that lipid droplets were reduced in size and homogenously dispersed in contrast to WT oocytes (Fig. 2A). The signal intensity of the anti-ATGL antibody staining was quantified and compared with anti-ZAR1 antibody signal and RNA polymerase II as negative control. The comparison did not indicate any difference between the signal intensity of ATGL protein of *Zar1*$^{-/-}$ and *Zar1*$^{+/+}$ oocytes (Fig. 2B). Therefore, the protein level of ATGL remained unaffected by the absence of Zar1. No co-localization between ATGL and ZAR1 in WT oocytes was observed (Fig. S1). A previous study performed RNAseq on *Zar1/Zar2*-knockout (KO) oocytes but not on oocytes that only lack ZAR1[60]. To further investigate why the morphology of lipid droplets dispersal was changed in *Zar1*$^{-/-}$ oocytes, RNAseq analysis on *Zar1*-KO oocytes was performed. Both datasets were compared and screened for potential candidates that are involved in lipid metabolism. *Hig2* (also known as *Hilpda*) was particularly reduced in both datasets. HIG2 is a known inhibitor of the ATGL[66]. Compared to gapdh in GV oocytes, *Hig2* showed a 5-fold higher FPKM in *Zar1*$^{+/+}$ to FPKM in *Zar1*$^{-/-}$ ratio in the *Zar1/Zar2*-KO dataset and an 8-fold higher FPKM ratio in our *Zar1*-KO dataset (Fig. 2E). The reduction of *Hig2* mRNA should cause increased ATGL activity. Yet, no assay is published to date that allows the measurement of the ATGL activity to validate the assumption of increased ATGL activity in the absence of HIG2 protein. To validate the RNAseq results, single molecule RNA-fluorescence *in situ* hybridization (smRNA-FISH) was performed to visualize single *Hig2* transcripts in fixed oocytes. A reduction of *Hig2* mRNAs was observed in *Zar1*$^{-/-}$ oocytes compared to *Zar1*$^{+/+}$ when the data is normalized to the internal standard *Actin b* (Fig. 2C). Therefore, the quantification of our results indicated a significant reduction of *Hig2* mRNA (Fig. 2D).

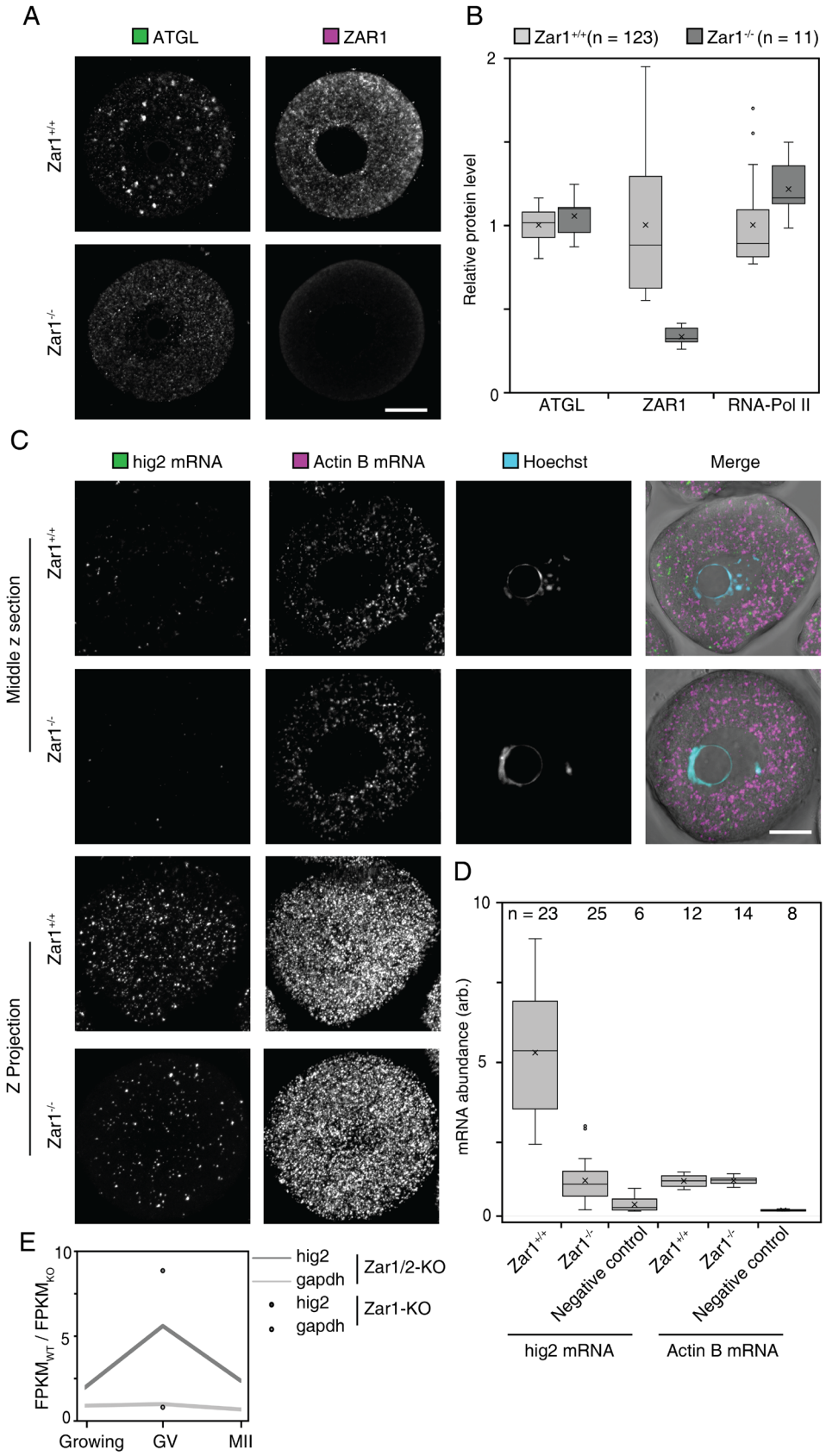

Fig. 2 Loss of *Hig2* causes the ATGL to be hyperactive. (A) Confical microscopy images of *Zar1*$^{-/-}$ and *Zar1*$^{+/+}$ oocytes after fixation and staining with α-ATGL and α-ZAR1 antibodies. The ATGL signal co-localized with dark granules that are visible in DIC images (not shown). *Zar1*$^{-/-}$ oocytes show unspecific signal (background signal) when stained with anti-ZAR1 antibody. The full figure including all individual channels are shown in Fig. S1. (B) Quantification of the fluorescence signal in oocytes from (A). n numbers

are given above. The fluorescence signal was measured for the whole oocyte and normalized to the average signal of *Zar1*$^{+/+}$ oocytes, resulting in mean values of 1 for *Zar1*$^{+/+}$ oocytes. ZAR1 was used as positive control and RNA-Polymerase II as negative control. (C) Confocal microscopy images of *Zar1*$^{-/-}$ and *Zar1*$^{+/+}$ oocytes after fixation and application of the smRNA-FISH protocol to visualize single transcripts based on gene-specific probes. *Actin b* was used as control. Confocal microscopy images were acquired as z stacks and full 3D oocytes were used for quantification of smRNA-FISH spots. For better visualization of the total amount of mRNAs in the respective oocytes, z projections are shown in the lower panel. (D) Quantification of oocytes that were stained with the smRNA-FISH protocol. n numbers are given above. For both Hig2 mRNA and *Actin b* mRNA, the total number of smRNA-FISH spots was normalized to the background number in negative control oocytes. Negative control oocytes were incubated in the absence of specific probes but with all subsequent staining solutions. (E) Analysis of RNAseq data regarding Hig2 mRNA levels. Values are given as the ratio of *Hig2* FPKM in *Zar1*$^{-/-}$ to *Hig2* FPKM in *Zar1*$^{+/+}$ values. The lines show the results of the RNAseq data from Rong *et al.* for *Zar1/Zar2* knockout oocytes at different stages[60]. RNAseq was performed on *Zar1*$^{-/-}$ oocytes at GV stage. The respective values are indicated by dots. Results for gapdh mRNA are shown as control. Scale bars 20 µm.

Global translation rate is reduced in *Zar1*$^{-/-}$ oocytes

Several anti-HIG2 antibodies were tested for Western blot and immunofluorescence analysis but were not classified as sufficiently reliable and specific for HIG2 in mouse oocytes. To compensate for the lack of information about the HIG2 protein level in *Zar1*$^{-/-}$ oocytes, the global translation level in both *Zar1*$^{-/-}$ and *Zar1*$^{+/+}$ oocytes was analyzed by us. Rong *et al.* performed a similar assay and used methionine analog L-homopropargylglycine to visualize the amount of newly synthesized protein within a fixed incubation period[60]. For *Zar1/Zar2*-KO oocytes, Rong *et al.* observed a sharp increase of the translation level from non-surrounded nucleolus (NSN) oocytes to surrounded nucleolus (SN) oocytes and germinal vesicle breakdown (GVBD)[60]. In our study, the translation level was found to decrease while oocyte mature from NSN oocytes to SN oocytes and to GVBD oocytes. The decline was observed in both *Zar1*$^{-/-}$ and *Zar1*$^{+/+}$ oocytes, however, the total translation level was lower in *Zar1*$^{-/-}$ oocytes. The signal intensity of *Zar1*$^{+/+}$ GVBD oocytes was similar to the intensity of *Zar1*$^{-/-}$ NSN oocytes (Fig. 3A). The results were quantified and normalized to the background signal of the negative control that was not incubated for HPG but treated with the Click-reaction mix. While the decreasing trend was observed in all oocytes, the variation of HPG signal in NSN oocytes was very high (Fig. 3B). Due to our observation that the translation levels in *Zar1*$^{-/-}$ oocytes were reduced for all developmental stages before GVBD, we propose that low levels of *Hig2* mRNA in *Zar1*$^{-/-}$ oocytes result in low protein levels of HIG2.

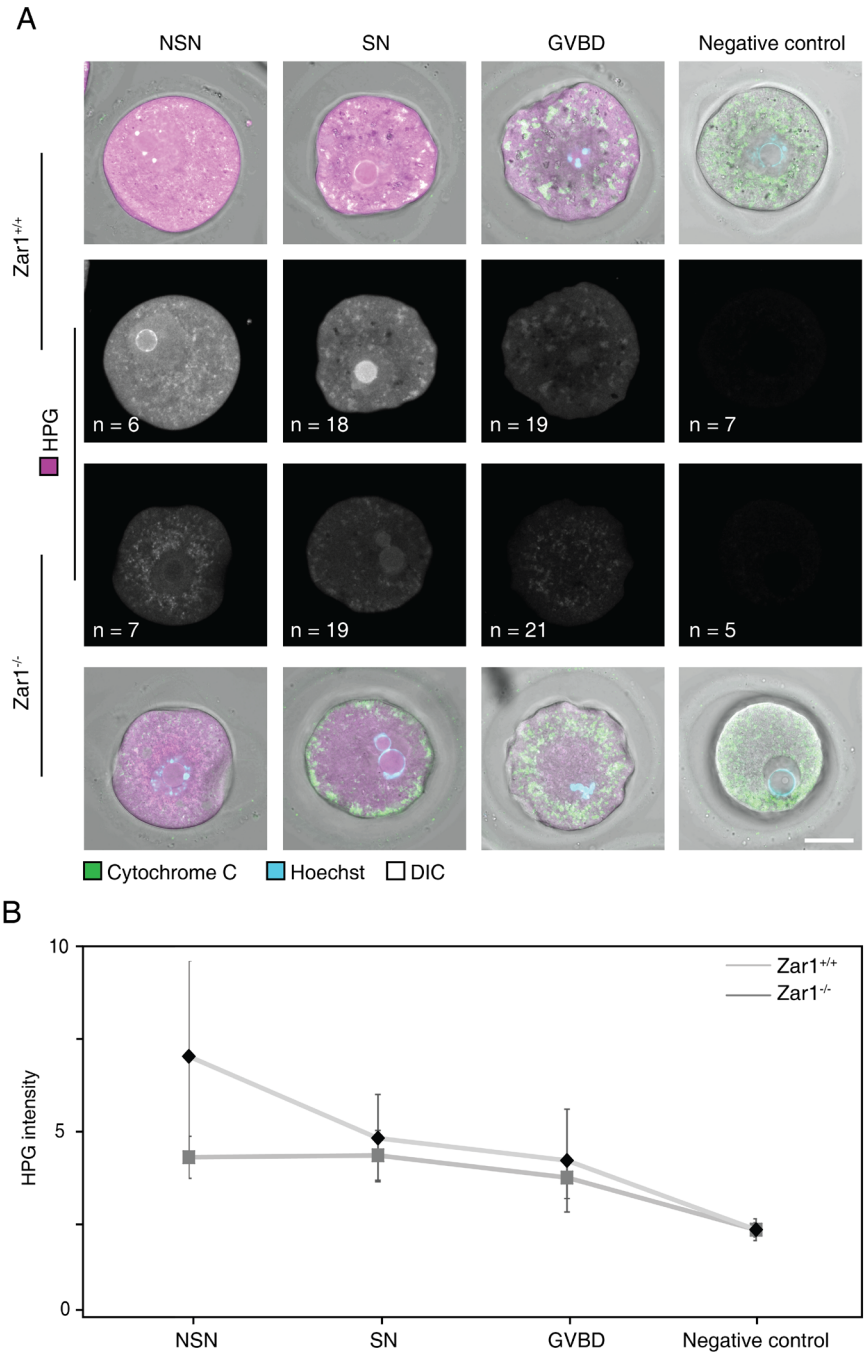

Fig. 3 The global translation level decreases while oocytes mature independent of the presence of Zar1. (A) Microscopy images of *Zar1*$^{-/-}$ and *Zar1*$^{+/+}$ oocytes after fixation and staining with AlexaFluor 488-azide (HPG), α-Cytochrome C antibody (mitochondria) and Hoechst (DNA). Before fixation, oocytes were incubated with the methionine analogue HPG that was compatible for click-reactions with azide groups. For the negative control, no HPG was added to the medium but the click reaction was performed as for the experimental group. n numbers are given in the HPG panels. The full figure including all individual channels are shown in Fig. S2. (B) Quantification of the HPG fluorescence intensity. All values were normalized to the background signal in the respective negative controls. Error bars show the standard deviation. SN and NSN oocytes were discriminated based on the Hoechst signal. Scale bar 40 µm.

Hig2 mRNA is localized to a distinct structure formed by ZAR1 aggregation

ZAR1 is known to bind mRNAs[59]. Because of the mRNA binding capacity of ZAR1, *Hig2* mRNA was expected to co-localize with Zar1. For *Actin b*, it has been shown that the mRNA level is not affected by the loss of ZAR1 and Zar2[60]. Therefore, other mRNAs such as *Actin b* were not expected to co-localize with ZAR1 if their mRNA level was not affected in *Zar1*-KO oocytes based on the RNAseq results (data not shown). The independence of ZAR1 protein suggests that *Actin b* is probably not bound by ZAR1. The overexpression of ZAR1 resulted in the formation of compact aggregates (Fig. 4A). *Actin b* mRNA did not localize to these aggregates and was homogenously distributed in the cytoplasm (Fig. 4A). Based on this finding, the accumulation of *Hig2* mRNAs in ZAR1 aggregates was analyzed. *Hig2* mRNAs were enriched in ZAR1 aggregates compared to *Hig2* mRNAs in the cytoplasm (Fig. 4B). The fraction of smRNA-FISH spots within the aggregates of the total number of smRNA-FISH spots was calculated. Because the optical size of the smRNA-FISH spots was 1.2 µm in the xy-plane, spots within 0.6 µm distance of ZAR1 aggregates were considered as "associated". The fraction of ZAR1 aggregates in the total volume of the oocytes was calculated and all values were compared. A small enrichment of smRNA-FISH spots for *Hig2* inside the ZAR1 aggregates was identified (Fig. 4C). However, 80% of all *Hig2* mRNAs were associated to the ZAR1 aggregates. For a homogenous distribution, fractions between 6.5 and 7.5% were expected. This range equals the fraction of the ZAR1 aggregates in the total oocyte volume. In summary, we showed that the Zar1-positive aggregates was enriched with *Hig2* mRNAs.

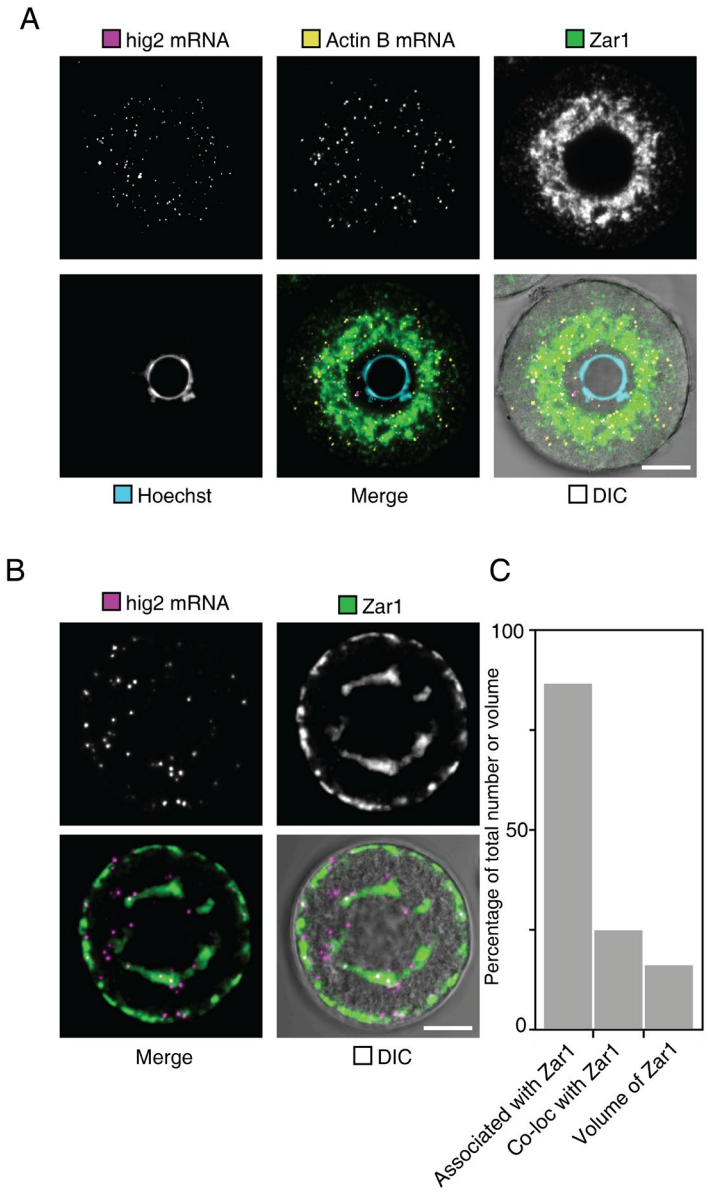

Fig. 4 *Hig2* mRNA locilizes to ZAR1 aggregates. (A) Microscopy images of C57BL/6N wild-type oocytes after fixation and smRNA-FISH staining. The last step included the incubation with an α-ZAR1 antibody. Only single z sections are shown. (B) Confocal microscopy images of C57BL/6N oocytes after fixation and smRNA-FISH staining. Prior to fixation, oocytes were injected with Zar1-mClover3 mRNA and incubated to allow for overexpression. mClover3 remained fluorescent after the smRNA-FISH protocol and the mClover3 signal was used to generate virtual ZAR1 domains during subsequent analysis. (C) Quantification of Zar1-mClover3 overexpressed C57BL/6N oocytes. The modelling of ZAR1 aggregates was used to create a distance transformed channel, and smRNA-FISH spots were quantified based on their distance to the aggregates. Co-localization was defined by distances between 0 µm and 0.001 µm. The optical size in the xy plane for the smRNA-FISH spots was 1.2 µm, ergo the fraction of spots within 0.6 µm distance of ZAR1 aggregates indicates the fraction of smRNA-FISH spots associated with the ZAR1 aggregates. We measured the volume of the ZAR1 aggregates, and the ratio of the ZAR1 aggregates and the total oocyte volume were used to estimate the enrichment of *Hig2* mRNAs on or inside the ZAR1 aggregates. Scale bars 20 µm.

Mitochondrial activity is increased in *Zar1*$^{-/-}$ oocytes

We showed that *Zar1*$^{-/-}$ oocytes have reduced lipid droplet numbers and that in these cells, ATGL is hyperactive. We therefore proposed that downstream processes could be impaired by the excessive export of fatty acids (FAs). FAs are converted into energy by the fatty acid oxidation in mitochondria[41].

We next tested if mitochondrial activity is increased in the absence of ZAR1. Tetramethylrhodamine, methyl ester (TMRM) was used to visualize the mitochondrial membrane potential (MMP, $\Delta\Psi m$) in *Zar1*$^{-/-}$ and *Zar1*$^{+/+}$ oocytes (Fig. 5A). To normalize for the number of mitochondria in oocytes MitoTracker Green was used as a dye that is insensitive to $\Delta\Psi m$[67]. SN oocytes were found to exhibit higher $\Delta\Psi m$ than NSN oocytes, independent of the genotype or mouse strain (Fig. 5A). The ratio of TMRM and MitoTracker Green was calculated. The comparison of *Zar1*$^{-/-}$ and *Zar1*$^{+/+}$ NSN oocytes indicated significantly increased $\Delta\Psi m$ values. In concordance, the $\Delta\Psi m$ values of SN oocytes increased, too.

Because the ZAR1 mouse line used in our study is in C57BL/6N genetic background, in addition to *Zar1*$^{+/+}$, CD1 oocytes were tested to account for potential genetic background effects on $\Delta\Psi m$. The difference of $\Delta\Psi m$ between NSN and SN oocytes was significant for CD1 and *Zar1*$^{+/+}$ oocytes, but not for *Zar1*$^{-/-}$ oocytes (Fig. 5B).

Interestingly, in all WT oocytes investigated the distribution of the TMRM signal was not as homogenous as the MitoTracker Green signal (Fig. S3A). In contrast, *Zar1*$^{-/-}$ oocytes showed a homogenous distribution of TMRM signal. Mitochondrial clusters with low $\Delta\Psi m$ were not identified (Fig. S3A). Therefore, we concluded that mitochondria in *Zar1*$^{-/-}$ oocytes would be hyperpolarized throughout the entire oocyte growth and maturation. Mitochondria with low $\Delta\Psi m$ could be activated by the loss of Zar1. Indeed, we identified mitochondrial hyperpolarization in growing oocytes of *Zar1*$^{-/-}$ females (data not shown), and we hypothesized that the hyperactivity of the ATGL was responsible for the mitochondrial phenotype.

To account for other factors involved in the mitochondrial hyperpolarization in *Zar1*$^{-/-}$ oocytes, we examined the amount of mitochondrial proteins in *Zar1*$^{-/-}$ and *Zar1*$^{+/+}$ oocytes. We performed immunofluorescence experiments to quantify the protein level of mitochondrial proteins. However, no differences were detected (data not shown). As only a fraction of mitochondrial proteins was analyzed, we investigated whether the translation of proteins in the vicinity of mitochondria was affected in *Zar1*$^{-/-}$ oocytes. Yet, no co-localization was observed between mitochondria and cytoplasmic areas with high concentrations of newly synthesized proteins (Fig. S2).

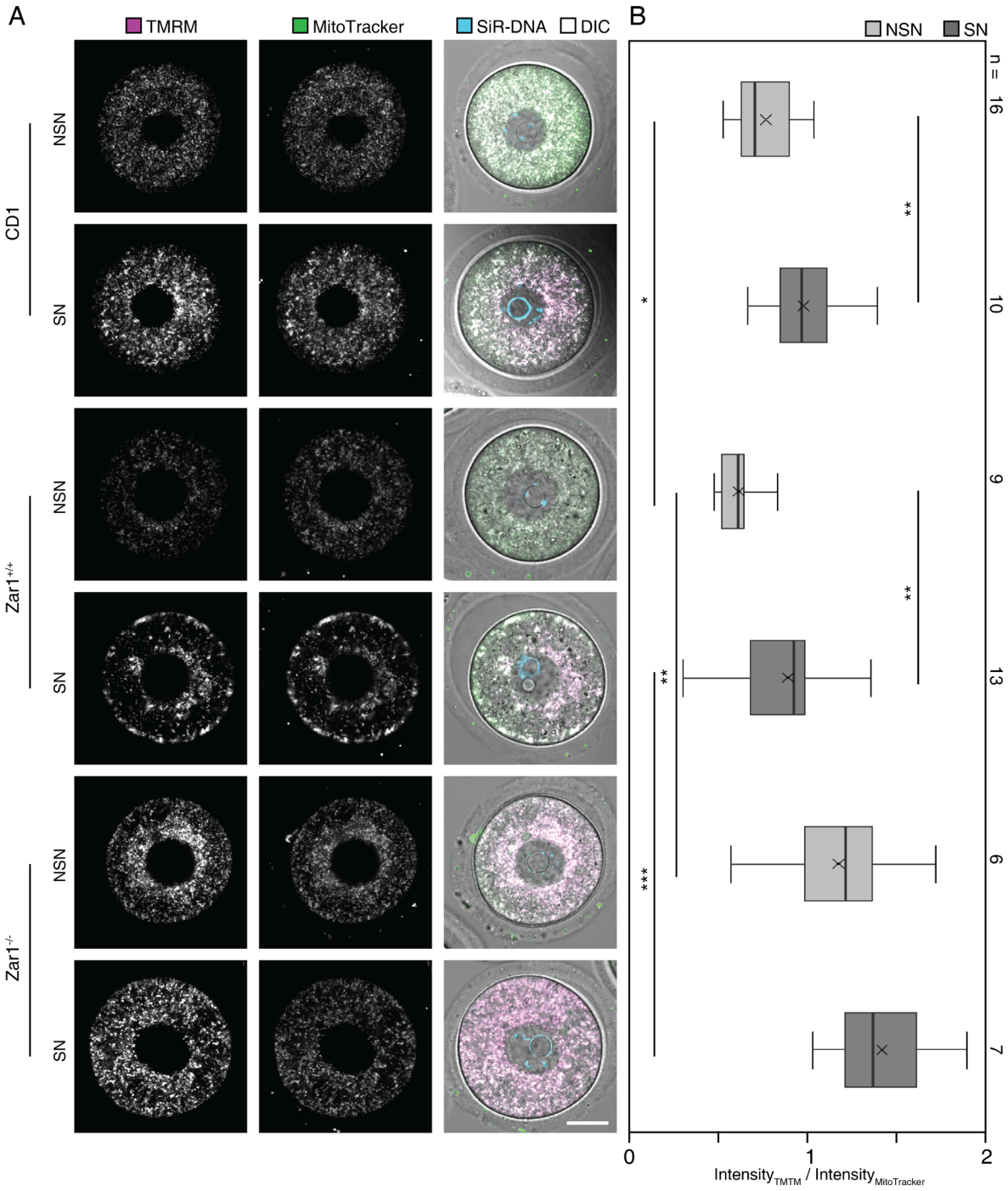

Fig. 5 *Zar1*$^{-/-}$ oocytes exhibit hyperpolarized mitochondria. (A) Confocal live cell microscopy images after staining with TMRM ($\Delta\Psi m$), MitoTracker Green (mitochondria) and SiR-DNA (DNA). Oocytes were incubated in medium supplied with the dyes, washed and imaged. CD1 wild-type oocytes were used to account for genetic background effects. Oocytes of all genotypes were discriminated into either SN or NSN groups based on the SiR-DNA signal. The full figure including all individual channels is shown in Fig. S3. (B) Quantification of TMRM and MitoTracker Green signal. To reduce the influence of the background signal, only mitochondria clusters were used for quantification. Mitochondria clusters were identified based on the MitoTracker Green channel. Statistical significance thresholds: * : p-value < 0.05, ** : p-value < 0.01, *** : p-value < 0.001, **** : p-value < 0.0001. Scale bar 20 µm

Entire gene sets for the lipid metabolism and mitochondrial activity are either enriched in *Zar1*$^{-/-}$ oocytes or *Zar1*$^{+/+}$ oocytes

As no specific mitochondrial proteins were found to be enriched in *Zar1*$^{-/-}$ oocytes, Gene Set Enrichment Analysis (GSEA) on our RNAseq data was performed. We tested if pathways that were related to either lipid metabolism or mitochondrial activity were enriched or lost upon loss of Zar1. In fact, we found that several fatty acid oxidation related pathways were enriched in *Zar1*$^{-/-}$ oocytes. In particular, pathways related to the electron transport chain showed normalized enrichment scores of 1.5 - 2.5. Pathways involved in lipid metabolism were downregulated in terms of mRNA levels in *Zar1*$^{-/-}$ oocytes. Especially anabolic processes were impaired in the absence of ZAR1 and showed normalized enrichment scores of -1.5 - -2 (Fig. 6). Our results indicate that the loss of lipid droplets and mitochondrial hyperpolarization do not solely arise from decreased HIG2 protein levels but that both phenotypes are probably the outcome of multiple affected pathways.

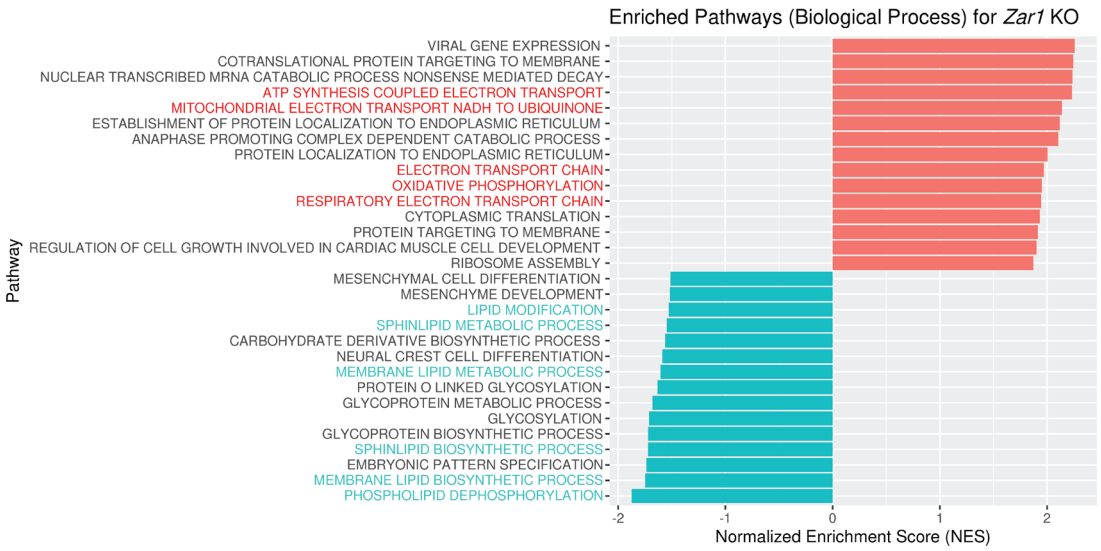

Fig. 6 Mitochondrial respiratory pathways and lipid synthesis are affected by the loss of Zar1. Gene set enrichment analysis (GSEA) on *Zar1*$^{-/-}$ RNAseq dataset for biological processes and restricted to protein-coding genes. Enriched gene sets (upregulated) are presented with red bars and positive enrichment scores. Reduced gene sets (downregulated) are presented with blue bars and negative enrichment scores. The values indicate the ratio of *Zar1*$^{-/-}$ oocytes compared to *Zar1*$^{+/+}$ oocytes. Mitochondrial respiratory pathways are highlighted in red, lipid synthesis pathways are highlighted in blue.

Zar1$^{-/-}$ oocytes experience increased oxidative stress

After showing that the mitochondria are hyperpolarized in *Zar1*$^{-/-}$ oocytes, we tested for higher ATP levels compared to *Zar1*$^{+/+}$ oocytes. To visualize the ATP levels and distribution, we used the live cell reporter AT1.03[68]. We injected the reporter mRNA, and imaged the oocytes after expression. No differences between *Zar1*$^{-/-}$ and *Zar1*$^{+/+}$ oocytes were observed (Fig. S5C and S5D). Further, we hypothesized side products of the fatty acid oxidation to accumulate in *Zar1*$^{-/-}$ oocytes. Reactive oxygen species (ROS) are potential candidates because they are side products of the fatty acid oxidation[69]. ROS have been reported to have severe effects on the developmental competence of oocytes[11,70]. One marker was 4-hydroxynonenal (4-HNE), a peroxidized lipid that is generated under high oxidative stress[71]. By immunofluorescence and an ati-4HNE antibody, we observed increased concentrations in *Zar1*$^{-/-}$ oocytes (Fig. 7A). Another effect of oxidative stress is DNA damage[72]. In previous studies, γ-H2AX was used as marker for DNA damage in the nucleus and 8-oxoguanine (8-oxoG) to visualize cytoplasmic damage on nucleic acids[73,74]. We tested γ-H2AX and 8-oxoG in *Zar1*$^{-/-}$ and *Zar1*$^{+/+}$ oocytes and found for both markers an accumulation in *Zar1*$^{-/-}$ oocytes (Fig. 7A). Quantification of these markers revealed highly significant differences and an up to 2-fold higher signal in the absence of ZAR1 (Fig. 7B). p66SHC was used to measure oxidative stress. As a reaction to higher ROS concentrations, p66SHC is phosphorylated. Thus the ratio of phospho-SHC / SHC is capable to reflect the oxidative stress level in oocytes[75,76]. We observed a mild yet significant increase in the phospho-SHC / SHC ratio in *Zar1*$^{-/-}$ oocytes (Fig. 7C). All oocytes were co-stained with mitochondrial markers to analyze the co-localization of oxidative stress markers and mitochondria, but no correlation was observed (Fig. S5). Commercially available kits work with substances that are oxidized by ROS in situ, which is different from the endogenous markers that accumulate over time. In contrast to the established ROS markers γ-H2AX, 8-oxoG and 4-HNE, commercially available kits kits like CellROX or luminescence-based lipid peroxidation assays did not detect any changes in oxidative stress in *Zar1*$^{-/-}$ oocytes (Fig. 7C and S4A). To put the changes of the ROS markers in relation to the changes in Cytochrome C, we compared the increase of the signal of ROS markers to the increase of the signal of Cytochrome C in immunofluorescence experiments. Cytochrome C is mildly enriched in *Zar1*$^{-/-}$ oocytes (Fig. S4B). Compared to the differences in Cytochrome C basic levels, all tested oxidative stress markers showed only a lower increase in *Zar1*$^{-/-}$ oocytes. γ-H2AX showed the largest difference (Fig. S4B). Therefore, we conclude increased DNA damage in *Zar1*$^{-/-}$ oocytes.

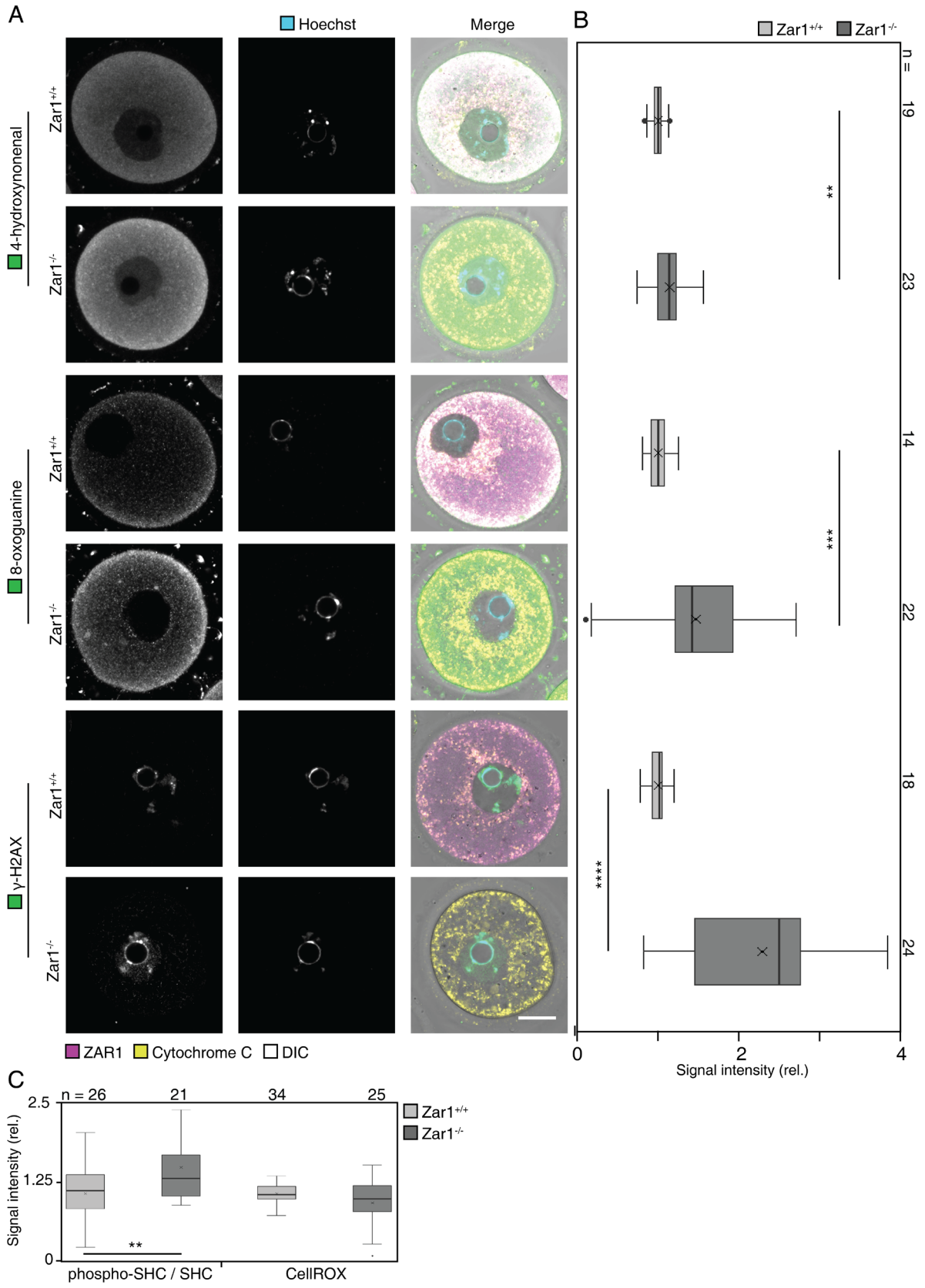

Fig. 7 *Zar1*$^{-/-}$ oocytes experience oxidative stress. (A) Confocal microscopy images of *Zar1*$^{-/-}$ and *Zar1*$^{+/+}$ oocytes after fixation and staining with antibodies of ROS-markers, Zar1, Cytochrome C (mitochondria), and Hoechst (DNA). *Zar1*$^{-/-}$ and *Zar1*$^{+/+}$ oocytes are shown for each of the three ROS markers: 4-hydroxanonenal (4-HNE) as peroxidized lipid, 8-oxoguanine (8-oxoG) as marker for cytoplasmic damage

on nucleic acids and γ-H2AX as marker for nuclear DNA damage. (B) Quantification of the fluorescence signal intensity of the ROS markers in *Zar1*$^{-/-}$ and *Zar1*$^{+/+}$ oocytes. The values were normalized to the respective signal in *Zar1*$^{+/+}$ oocytes. n numbers are shown right. The full figure including all individual channels is shown in Fig. S4. The change in the intensity of ROS markers compared to the change of cytochrome C is shown in Fig. S5B. (C) Quantification of the fluorescence signal intensity of further ROS markers in *Zar1*$^{-/-}$ and *Zar1*$^{+/+}$ oocytes. phospho-p66SHC (phospho-SHC) in relation to its unphosphorylated form represents the oxidative stress level in oocytes. CellROX is a commercial kit visualizing the concentration of ROS in cells. Confocal microscopy images of phospho-SHC / SHC are shown in Fig. S4. Microscopy images of CellROX are shown in Fig. S5A. The values were normalized to the respective signal in *Zar1*$^{+/+}$ oocytes. n numbers are shown right. * : p-value < 0.05, ** : p-value < 0.01, *** : p-value < 0.001, **** : p-value < 0.0001. Scale bar 20 µm

Discussion

In this study, we showed the function of ZAR1 in the regulation of cellular processes far beyond the maternal-to-zygote transition and early embryo development. We demonstrated the link between the stabilization of *Hig2* mRNA, that encodes for the inhibitor of ATGL, and multiple phenotypes in *Zar1*$^{-/-}$ oocytes. Phenotypic effects were the loss of the lipid droplets, mitochondrial hyperpolarization, and increased concentrations of γ-H2AX, 8-oxoG, and 4-HNE.

Lipid droplets in *Zar1*$^{-/-}$ oocytes are lost because the ATGL is hyperactive

In our study we found that lipid droplets were absent in *Zar1*$^{-/-}$ oocytes. It has been previously discovered that different mouse strains exhibit different amounts of lipid droplets. Compared to other species like cows and pigs, mice contain substantially smaller amounts of lipid droplets in their oocytes[77]. However, the lipid droplets that we observed in *Zar1*$^{-/-}$ oocytes were far smaller than in any common wild-type mouse strain. After fertilization, the zygote requires energy for the synthesis of new mRNAs and proteins when it undergoes the first mitotic divisions. At the same time, the zygote is isolated from external energy supply. Lipid droplets are crucial for the survival and subsequent developmental competence of the early embryo[47]. When lipid droplets were stained with Nile red and LipidSpot, large variations of the results and a fast decay of the signal were reported. We observed that these variations were caused by our standard imaging setup. For standard oocyte imaging, the oocytes were placed in medium droplets of less than 1 µL volume that were covered with mineral oil. The volume of oil was 5,000 – 10,000 times larger than the volume of the medium. Nile red and LipidSpot are hydrophilic dyes and were therefore absorbed by the mineral oil. This issue was solved by staining of only small groups of oocytes at once and an immediate acquisition of the images.

Classical dyes like Nile red do not exclusively stain lipid droplets but also other organelles and compartments with high lipid content, low pH or low polarity[78,79]. That

is a problem when only lipid droplets are analyzed. The structures that Nile red stained in *Zar1*$^{-/-}$ oocytes in our experiments were presumably the ER and multivesicular aggregates. To obtain a specific signal for lipid droplets, we used LipidSpot, which only stains lipid droplets and showed barely any signal in *Zar1*$^{-/-}$ oocytes, thereby confirming that lipid droplets are lost in Zar1-depleted oocytes.

Many reasons could have been responsible for the reduction in the amount of lipid droplets. For example, either the synthesis and import of lipids into lipid droplets could have been impaired or the export of lipid from lipid droplets and consumption of lipids could have been increased. It was also possible that the emergence of lipid droplets from the ER membrane was impaired[80]. On the other hand, the lipolysis could have been enhanced. Lipid droplet degradation mostly happens by autophagy and fusion with lysosomes[81]. However, the staining of ATGL revealed unaltered protein levels and did not indicate a specific pattern of lipid droplet or ATGL accumulation at the ER, lysosomes or other organelles. In previous reports, lysosomes showed a specific structure in oocytes that is different from the images that were obtained when we stained ATGL in immunofluorescence experiments[82]. It was therefore unlikely, that the lipid droplet biogenesis or the degradation of lipid droplets were impaired in *Zar1*$^{-/-}$ oocytes.

Another possibility would have been a role of the granulosa cells that surround the oocytes until implantation into the uterus or removal of the granulosa cells during the isolation of the oocytes for our experiments[83]. Granulosa cells supply the oocyte with metabolites including lipids[84]. It can be challenging to investigate impaired energy supply between oocytes and other follicular cells because any kind of isolation and *in vitro* maturation affects the composition of the follicular fluid[85]. However, *Zar1*$^{-/-}$ mice exhibit very clear phenotypes that are limited to infertility and developmental competence of the zygote[59,60]. Moreover, ZAR1 is only low abundant in most cell types other than oocytes[59]. Therefore, we proposed that the loss of lipid droplets in oocytes was most likely caused by oocyte-specific pathways and was not caused by a decreased external supply of lipids.

Inhibition of ATGL in *Zar1*$^{-/-}$ oocytes rescues the wild-type phenotype

The treatment with Atglistatin, a specific inhibitor of ATGL, caused *Zar1*$^{-/-}$ oocytes to exhibit very large lipid droplets compared to *Zar1*$^{+/+}$ oocytes. The uptake of lipids *in vitro* was conclusively not impaired. We also incubated *Zar1*$^{-/-}$ oocytes with different concentrations of linoleic acid and oleic acid when treated with Atglistatin. However, we did not observe a change in the size and number of lipid droplets (data not shown). When incubated in 10% FBS, the size of lipid droplets in *Zar1*$^{-/-}$ oocytes increased. Previous studies propose that the uptake of isolated fatty acids (i.e. not bound to protein carrier or inside protein coated micelles) is not possible[86–91]. The presence of fatty acid binding proteins in the FBS allows the oocyte to import lipid from

the medium[84]. The inhibition of ATGL without external supply of lipids had no effect on the size and number of the lipid droplets, therefore, we proposed that *de novo* synthesis of fatty acids in *Zar1*$^{-/-}$ oocytes was either impaired or in general very slow. Gene set enrichment analysis supported our hypothesis of decreased lipid synthesis efficiency. Taken together, the lipid droplet phenotype in *Zar1*$^{-/-}$ oocytes was multifactorial and a combination of increased fatty acid export from the lipid droplets and reduced fatty acid synthesis.

Hig2 is lost in *Zar1*$^{-/-}$ oocytes

We propose that a key factor in the increase in fatty acid export from lipid droplets upon loss of ZAR1 is the reduced mRNA and protein level of *Hig2*/HIG2. HIG2 acts as inhibitor of the ATGL[66,92]. We found the copy number of *Hig2* mRNAs to be reduced in *Zar1*$^{-/-}$ oocytes. This finding was supported by our RNAseq dataset of *Zar1*-KO oocytes as well as by the *Zar1/Zar2*-KO dataset by Rong *et al.*[60]. Despite optimization by other groups and us, commercial kits were not designed for oocytes, which are non-adherent and operated in small numbers. Therefore, difficulties aroused when performing the smRNA-FISH assay. To account for potential handling mistakes, several negative controls were included, e.g. no addition of the probe, co-staining mRNAs of housekeeping genes and different concentrations of proteases. Compared to the controls, we observed a loss of *Hig2* mRNA in *Zar1*$^{-/-}$ oocytes.

Unfortunately, due to technical difficulties we could not determine the protein levels of HIG2 in *Zar1*$^{-/-}$ and *Zar1*$^{+/+}$ oocytes. Multiple antibodies were tested on both Western blot and immunofluorescence stainings. None of the tested antibodies obtained unequivocal and reproducible results (data not shown). A common alternative to staining endogenous levels of proteins is the generation of transgenic mouse lines that harbor the gene of interest as fusion with a tag or fluorescent protein[93]. Yet the generation of transgenic mouse lines takes considerably long times and no tagged *Hig2* mouse line was available. Therefore, the global translation rate was analyzed instead. The respective assay involved the incubation of oocytes with the methionine analogue L-homopropargylglycine (HPG) that contains an alkyne group. After oocyte fixation, fluorophores that contained an azide group could covalently bind to HPG. This so-called click reaction requires either UV light or copper ions as catalyst. The fluorophores are prone to off-target labeling, therefore, the manufacturer recommended to include negative controls that lacked the incubation HPG. We employed a non-HPG treated control to normalize the acquired data and we found that the global translation in *Zar1*$^{-/-}$ oocytes was reduced. Due to the decreased *Hig2* levels upon absence of ZAR1 in oocytes, we concluded that the protein level of HIG2 is likely to be lower in *Zar1*$^{-/-}$ oocytes. Nevertheless, the average lifetime and turnover rate of HIG2 are not known. Therefore, it could be that HIG2 was maintained even in the absence of its mRNA. In addition, the translation rate of individual genes can be

orders of magnitude higher or lower than the global translation rate. To compensate for this lack of knowledge, we will perform mass spectrometry analysis in the near future. We expect to detect HIG2 in quantifiably amounts. Analysis of the mass spectrometry data will reveal the average HIG2 level in *Zar1*$^{-/-}$ and *Zar1*$^{+/+}$ oocytes.

Remarkably, Rong *et al.* obtained different results when they performed the HPG assay on *Zar1/Zar2*-KO and WT oocytes[60]. While *Zar1/Zar2* deficient oocytes exhibited lower translation rates, too, Rong *et al.* report a peak of global translation during GVBD that is almost 2-fold higher than the translation rate in NSN or MII oocytes. In contrast, we observed a steady decrease of the HPG signal from NSN to GVBD oocytes and further (data not shown) for both *Zar1*$^{-/-}$ and *Zar1*$^{+/+}$ oocytes. A problem in the respective study of Rong *et al.* could have been the small sample size they used[60]. Even though the sample size for our NSN groups was less 10 oocytes and the error for our NSN groups is very high, we obtained consistent data for SN and GVBD oocytes. We think that n numbers below 10 are insufficient when claiming a highly significant phenotype as Rong *et al.* did. Our data indicate that mouse oocytes do not have a peak of global translation during GVBD.

Hig2 mRNA is stabilized by ZAR1

We showed that *Hig2* mRNA localized to ZAR1 aggregates. Immunofluorescence staining of endogenous ZAR1 showed a specific pattern, and overexpression of ZAR1 by the injection of ZAR1 mRNA revealed the formation of aggregates. Previous studies confirmed that ZAR1 binds mRNAs[59,94]. While we will investigate the physical and mechanistical properties of ZAR1 aggregates in forthcoming reports, this study presents a specific example of how the presence of ZAR1 stabilizes mRNAs. ZAR1 is one of the first maternal-effect genes that was reported in mammalian oocytes[59,60]. ZAR1 is an intrinsically disordered protein that contains a zinc finger domain at its C-terminus[59,95]. No consensus sequences or binding preferences are known yet. Hence, no preference of ZAR1 for certain mRNAs was identified so far. Based on the RNAseq datasets, we concluded that some genes are more affected by the loss of ZAR1 than others. A helpful tool to analyze the interaction of specific mRNAs with ZAR1 is smRNA-FISH conjointly with immunofluorescence staining of ZAR1 or expression of fluorescently tagged Zar1. We compared the distribution of *Hig2* mRNA and *Actin b* mRNA and identified increased enrichment of *Hig2* mRNA in ZAR1 aggregates while *Actin b* mRNA was equally distributed. Intensive statistical analysis of sufficient numbers of oocytes are yet to be conducted in further studies. However, the hypothesis of *Hig2* enrichment in ZAR1 aggregates is supported by our smRNA-FISH results. Oocytes that were stained by immunofluorescence had a diffuse cytoplasmic ZAR1 signal. However, for co-localization analysis, the ZAR1 aggregates needed to have distinct boundaries. Our data showed that Zar1-overexpression causes the ZAR1 aggregates to compact (data not shown). In ZAR1 overexpressed oocytes, the signal-

to-noise ratio allows for co-localization analysis. Therefore, we overexpressed Zar1-mClover3 in wild-type oocytes and performed the smRNA-FISH protocol. However, we expected the smRNA-FISH probes to be incapable of penetrating into the ZAR1 aggregates after overexpression because of their size and the fixation step of the smRNA-FISH protocol. Consequently, we expected the number of smRNA-FISH spots that co-localized with ZAR1 aggregates to be lower than the number of mRNA molecules that are physically inside the ZAR1 aggregates. Indeed, only 10% of the total number of transcripts co-localized with Zar1. We tried to facilitate the penetration of the smRNA-FISH probes by protease-treatment. The dilution and incubation time for the protease-treament ranged from 1:4,000 to 1:2,000 and from 5 min to 15 min. Indeed, we observed an increase smRNA-FISH signals inside ZAR1 aggregates after protease-treatment. However, the protease-treatment reduced the overall number of smRNA-FISH spots for yet unknown reasons. Therefore, we focused on the association with the ZAR1 aggregates and not the bare co-localization was that. We defined association of smRNA-FISH spots with ZAR1 aggregates as a maximum distance of 0.6 µm from the nearest ZAR1 aggregate to the respective smRNA-FISH spot. Our results provided indications for an enrichment of *Hig2* mRNA by comparison of the fraction of *Hig2* mRNA that was associated with ZAR1 aggregates and the volume of Zar1. Remarkably, the fraction of *Hig2* mRNAs that interacted with ZAR1 under the refined conditions is 80%. For comparison, the fraction of the ZAR1 aggregates of the total oocyte volume was calculated. The fraction of ZAR1 aggregates was 6.5%. When the expanded volume within 0.6 µm distance was considered, the fraction was 7.5%. We think that compared to the 10% of true co-localization between *Hig2* smRNA FISH spots and Zar1, the associated fraction describes the enrichment of mRNA in the ZAR1 aggregates better than the bare co-localization. Furthermore, the large difference between the associated fraction and the co-localized fraction confirms our hypothesis of impaired penetration of smRNA-FISH probes into dense aggregates.

Hyperactivity of ATGL causes mitochondrial hyperpolarization

Lipid droplets are often adjacent to mitochondria[36,39,40]. Because FAs are converted into energy by the FAO, we expected to observe downstream effects of the ATGL hyperactivity. We expected that the loss of HIG2 and the subsequent export of fatty acids would lead to increased mitochondrial respiration and generation of ROS. Cancer cells often experience hypoxia conditions and are therefore incapable of using mitochondrial respiration for energy supply. To prevent catabolism of fatty acids and the generation of reactive oxygen species, cancer cells upregulate HIG2[66,96]. Initially, we used tetraethylbenzimidazolylcarbocyanine iodide (JC-1) to visualize the mitochondrial membrane potential. JC-1 is excited at 514 nm and emits in the green spectrum as monomer. JC-1 accumulates in the mitochondrial membrane as $\Delta\Psi m$ increases. Notably, high $\Delta\Psi m$ in *Zar1*$^{-/-}$ oocytes indicates the accumulation of protons.

Because of this, we explain the absence of differences between the ATP concentration in *Zar1*$^{-/-}$ and *Zar1*$^{+/+}$ oocytes by an unchanged ATP synthase activity. We hypothesize that in *Zar1*$^{-/-}$ oocytes, the proton gradient is constantly filled whereas the ATP synthase maintains a constant level of ATP.

We think that the steady supply of fatty acids is necessary to maintain *ΔΨm*. *In vitro* incubation for prolonged times, i.e. longer than 4 h, caused *ΔΨm* of *Zar1*$^{-/-}$ oocytes to decline. Therefore, we did not observe any difference between *Zar1*$^{-/-}$ and *Zar1*$^{+/+}$ oocytes after 12 h *in vitro* culture (data not shown). When we supplied the mediium with FBS, *ΔΨm* was maintained at high levels in *Zar1*$^{-/-}$ oocytes. As discussed above, it is not suprising that oocyte exhibit effects during *in vitro* cultures due to the lack of metabolites in the medium.

We hypothesize that ZAR1 aggregates sort mitochondria based on *ΔΨm*. Especially the formation of aggregates reminds us of the phase-separation characteristics of the Balbiani body. In *Xenopus laevis* and *Danio rerio* oocytes, mitochondria with low *ΔΨm* have been shown to be enriched in the Balbiani body. Previous reports hypothesize that mitochondria with low *ΔΨm* are "healthy" as the ROS level is lower and the chance of unwanted mtDNA mutations is lower. The Balbiani body is hence assumed to select mitochondria with high developmental competence[21,97–100]. In mice and humans, the Balbiani body disappears in the early development of the oocytes[34]. We propose that the ZAR1 aggregates might act as sorting domain and separates highly active from inactive mitochondria. In future experiments, we will perform analysis of a potential connection between mitochondria and ZAR1 to further investigate a potential mitochondria-sorting function of Zar1. Overexpression of fluorescently tagged ZAR1 and simultaneous incubation with TMRM will allow the observation whether ZAR1 sequesters mitochondria depends on *ΔΨm*.

Because of mitochondrial hyperpolarization, loss of ZAR1 increases the oxidative stress in mouse oocytes

Based on the mitochondrial hyperpolarization, we hypothesized that loss of ZAR1 further results in higher protein levels of mitochondrial proteins that are involved in the respiratory chain. We visualized multiple mitochondrial proteins in immunofluorescence experiments to analyze whether the loss of ZAR1 causes an increase of the protein level. None of the tested proteins showed higher levels in *Zar1*$^{-/-}$ oocytes (data not shown). Gene set enrichment analysis (GSEA) revealed that mitochondrial pathways were indeed enriched in *Zar1*$^{-/-}$ oocytes. Detailed analysis of the RNAseq data might show potential candidates for further tests. Mitochondrial pathways were some of the most enriched gene sets. Higher GSEA scores correspond to higher numbers of involved proteins Therefore, our conclusions in this study are limited by the indications of a complex and multifactorial network that causes both the lipid droplet and the mitochondria hyperpolarization phenotype.

Rong *et al.* provide data for the developmental success of meiotic steps in *Zar1*$^{-/-}$ and *Zar1/Zar2*-KO oocytes. They report a delayed onset of meiosis and impaired polar body extrusion rates (PBE). Further, their study showed higher incidences of aneuploidies in MII oocytes. While Rong *et al.* suggest a few candidates as potential cause for the developmental phenotypes, none of the tested candidates have been able to explain the whole spectrum of developmental impairment in *Zar1/Zar2*-KO oocytes. Therefore, they think that multiple factors play a role for the developmental phenotypes, too[60]. We hypothesized that a major factor for impaired development is oxidative stress based on mitochondrial hyperpolarization in *Zar1*$^{-/-}$ oocytes. Nucleic acid damage and peroxidized lipids accumulate in oocytes lacking ZAR1. γ-H2AX is recruited to sites of DNA damage in the nucleus. In mammalian cells, prolonged exposure to oxidative stress results in higher levels of γ-H2AX[73]. 8-oxoguanine (8-oxoG) is a direct oxidation product of guanine. While the respective antibody was previously reported to be unable to penetrate the nucleus, the signal in the cytoplasm indicates oxidative damage on cytoplasmic RNAs and mtDNA[74]. In our immunofluorescence experiments, the 8-oxoG pattern correlated with the mitochondrial distribution. We thereby think that areas with high signal intensity of 8-oxoG shows the oxidation of guanine in mitochondria. 4-hydroxynonenal (4-HNE) is a peroxidized lipid and reacts with proteins. Previous studies showed that adducts of 4-HNE have impaired functions and are prone for degradation[101]. Especially in the context of cohesin, 4-HNE is a potential candidate that could explain why *Zar1*$^{-/-}$ oocytes experience higher aneuploidy rates. Adduct formation with cohesin and subsequent degradation of cohesin leads to premature sister chromatid loss, which is one of the main reasons for aneuploidy[102,103]. However, when compared to the increase of the Cytochrome C protein level in *Zar1*$^{-/-}$ oocytes (Fig. S5B), only γ-H2AX showed biological significance. We hypothesize that in young oocytes, such as those used to conduct the experiments, the accumulation of ROS and oxidative damage is still very low. Future experiments will be needed to compare ROS markers in oocytes from older mice. We think that the difference of ROS markers in *Zar1*$^{-/-}$ and *Zar1*$^{+/+}$ oocytes will be larger in aged oocytes.

Taken together, we propose a new model in which ZAR1 binds and stabilizes *Hig2* mRNA in GV oocytes. This stabilization ensures steady translation of *Hig2* mRNA and HIG2 protein prevents the ATGL from hyperactivity. When ZAR1 is lost, *Hig2* mRNA is degraded and the ATGL exports fatty acids into mitochondria. The lipid droplets shrink accordingly. Fatty acids are converted into energy by the fatty acid oxidation and the energy is stored in the proton gradient along the inner mitochondrial membrane. The fatty acid oxidation produces substantial amounts of reactive oxygen species that cause damage on nucleic acids and proteins. Finally, the accumulation of DNA, RNA and protein damage results in decreased developmental competence of *Zar1*$^{-/-}$ oocytes (Fig. 8).

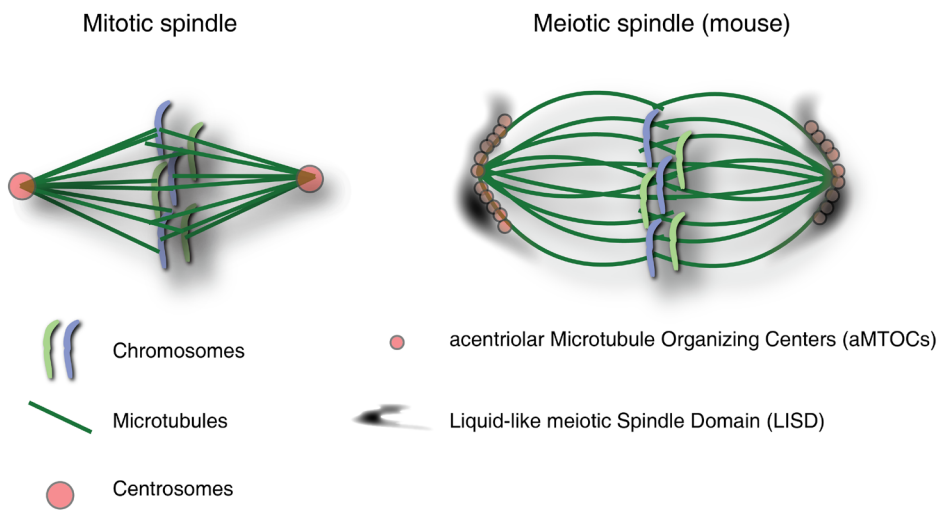

Fig. 8 ZAR1 stabilizes *Hig2* mRNA and thereby regulates the lipid catabolism and mitochondrial activity in mouse oocytes. Schematic figure of the model in *Zar1*$^{+/+}$ (left) and *Zar1*$^{-/-}$ oocytes (right). ZAR1 stabilizes *Hig2* mRNA and ensures steady translation of HIG2 protein. HIG2 protein inhibits the function of ATGL and stabilizes lipid droplets. In *Zar1*$^{-/-}$ oocytes, Hig2 mRNA is degraded, and HIG2 protein is lost. ATGL is hyperactive and the size of lipid droplets is greatly reduced. Fatty acids are exported from lipid droplets and converted into energy in the mitochondria which exhibit a high membrane potential. Reactive oxygen species are generated by the degradation of fatty acids and cause DNA, RNA and protein damage. Accumulation of oxidative damage can lead to impaired oocyte development.

Materials and Methods

Animal handling and isolation of oocytes

All animals were housed in a pathogen-free environment with ad libitum access to water and food, according to the guidelines of the MPI-NAT animal facility and in compliance with the German Law on Animal Welfare. CD1, C57BL/6N and ZAR1 mice were maintained as in-house breeding colonies and non-mated female mice were sacrificed at an age of 7-9 weeks. For the analysis of mitochondrial membrane potential in young mice, mice were sacrificed at either 14, 16, 18 or 21 days postnatal. For the analysis of growing oocytes, mice were sacrificed at 28 days postnatal. The ovaries were taken out and dissected. The oocytes were isolated and kept at 37°C under mineral oil in homemade M2 medium supplemented with 250 µM dbcAMP (Merck; D0627) to maintain the prophase arrest. For the isolation of growing oocytes, the ovaries were briefly dissected in Gibco TrypLE Express Enzym (1x), Phenolred (Thermo Fisher; 10043382) supplied with 40 µL collagenase A (Merck; SCR136) and 250 µM dbcAMP. The ovaries were incubated for 20 min at 37°C in the same medium. The ovaries were fully dissected and all GV oocytes were washed through 4 x 500 µL M2 medium supplied with dbcAMP.
All oocytes were kept in medium for at least 30 min before continuing the experiment to allow the oocytes to recover from the isolation.

Microscopy

All images were acquired on a LSM880 system (Zeiss) based on an Axio Observer Z1 inverted microscope (Zeiss) equipped with an incubation box (Pecon; Zeiss). The oocytes were placed in droplets of less than 1 µL of the respective medium and covered by mineral oil. Imaging was done in #1 35 mm glass bottom dishes (MatTek) at 37°C for live cell experiments and room temperature (ca. 21°C) for fixed cell experiments. Available lasers were 405 nm, 488 nm, 512 nm, 561 nm and 633 nm. The filters were adjusted according to the respective fluorophore. A PMT was used to detect Hoechst signal and another PMT was used for SiR-DNA signal. For all other fluorophores, the 32-channel GaSP detector was used. Imaging was done using a 2.3x digital zoom on a C-Apochromat 40x/1.20 W Corr M27 (Zeiss). Pixel size was adjusted according to the Nyquist criteria. The scan speed was set to 6 for most experiments (corresponds to a pixel dwell of ca. 1.5 – 2 µs). Averaging was set to 2. The laser intensity was limited to 1% for live cell experiments and 5% for fixed cell experiments. The detector gain was limited to 800 V. Laser intensity and detector gain were adjusted to use the dynamic range of the 8-bit histogram. Z stacks for most experiments were imaged by the acquisition of 9 different z planes. Full z stacks, e.g. for the smRNA-FISH experiments, were imaged by the acquisition of 101 z planes in a distance of 0.8 µm. All oocytes within one experiment were imaged using the same parameters.

Injection of mRNA

Zar1-mClover3 and AT1.03 mRNA were prepared using the HiScribe T7 ARCA mRNA Kit (NEB; E2060S) including ARCA-capping and poly(A) tailing. For the injection of oocytes, two different protocols were used. The first protocol uses a homemade chamber as described previously[104]. In brief, a plastic chamber was used on whose outer walls coverslips were mounted and sealed by Baysilon grease (GE Bayer Silicones). On the inner side of one of the coverslips a small piece of double-sided tape was mounted, and a small piece of another coverslip was attached on the other side of the tape, forming a "shelf" with a height of about 100 µm. The chamber was filled with M2 medium supplemented with dbcAMP and placed on a custom-made stage on a Zeiss Axio Vert.A1 inverted microscope using a 20x Air objective. Oocytes were transferred into the "shelf" and an injection needle was prepared.

Glass capillaries with an inner diameter of 1 mm were siliconized to reduce interactions with mRNA. For this, capillaries were dipped into Sigmacote solution (Sigma; SL2) so that a few microliters were taken up by capillary force. Then, the capillaries were inverted multiple times to ensure the complete coating of the inner wall. Excessive solution was removed by paper towels and gentle tapping. Capillaries were dried for at least two weeks before pulling. Homemade injection needles were prepared by pulling glass capillaries with 1 mm inner diameter in a P-97 needle puller

(Sutter instruments) to obtain a ca. 0.5 cm long taper. Then, 1 – 5 µL mercury were filled into the tip by backloading. Needles were attached to a capillary holder (Eppendorf) connected to a CellTram Oil (Eppendorf). The tip of the injection needle was broken by gently moving against the wall of a glass capillary. Excessive air was released, then mineral oil (Sigma; M5310) was taken up to prevent direct contact with the mercury, followed by 10 pL mRNA solution and 3 µL mineral oil to prevent the mixing with medium. The injection needle was moved into the oocytes and the front oil and mRNA solution were injected. Afterwards, oocytes were incubated for 3 – 5 h for proper expression of the construct.

The second protocol uses the FemtoJet 4i system (Eppendorf). The mRNA was injected on an Axio Vert.A1 inverted microscope (Zeiss) using a DIC 40x Air objective (Zeiss). Because of space limitations, a custom made metal frame (25.5 x 75.5 x 2 mm) was used under which a #1 coverslip was mounted and sealed using Baysilon grease (GE Bayer Silicones). Oocytes were kept under mineral oil in homemade M2 medium as described above. For the fixation of oocytes, either commercial holding needles (VacuTip II, Eppendorf) or homemade holding needles were used. Homemade holding needles were prepared by pulling glass capillaries with 1 mm inner diameter in a P-1000 needle puller (Sutter Instruments) to obtain a ca. 1 cm long taper. The taper was cut at an inner diameter of ca. 100 µm using a microforge. After fire-polishing the tip, the holding needle was bent to an angle of ca. 30°. Holding needles were pre-filled with medium and connected to a CellTram Air pump (Eppendorf). For the injection of microspheres, homemade injection needles were prepared. Glass capillaries coated with Sigmacote were used as described above. Needles were bent as described above and back-loaded with the final microsphere solution using GELoader tips (Eppendorf). The injection needle was then connected to a FemtoJet 4i system (Eppendorf) using a capillary holder that was connected to a PiezoXpert system (Eppendorf). Both holding needle and injection needle were mounted on 5MO-202U micromanipulators (Narishige). The tip of the injection needle was broken by pushing the needle against the holding needle. Then, the air in the top of the injection needle was released by applying the highest pressure possible until all air was released. The FemtoJet system was arranged so that a constant flux of solution was ensured. After one or more beads were immobilized in the tip, negative pressure was applied on the CellTram Air pump to capture a single oocyte. Then, the injection needle was moved into focus and moved into the oocyte. Penetration of the membrane was ensured. Ca. 3 pL of 400-500 ng/µL mRNA solution were injected, the injection needle was retracted and the oocyte was release from the holding needle. Afterwards, the oocytes were incubated for 3 – 5 h for proper expression of the construct.

Live cell experiments

The DNA was stained by medium supplied with 2 µM SiR-DNA (SpriroChrome; SC007). For the analysis of lipid droplets, 0.5% LipidSpot 488 (v/v; Biotum; #70065) or 1 µM Nile red (Sigma; N3013) were added to the medium. The oocytes were incubated in 500 µL for 30 min at 37°C in a humidified incubator and then washed 2x in 500 µL medium that contained only SiR-DNA. The washing medium was used for imaging, too. For the ATGL inhibitor experiment, oocytes were first kept for 24 h in medium supplied with 10% FBS (v/v; Thermo Fisher; A4766) and 50 µM Atglistatin (Merck; 530151). The negative control was incubated in medium that contained only FBS. After 24 h, oocytes were washed and stained in medium supplied with SiR-DNA and LipidSpot 488 as described above. For the inhibitor-treated group, the staining and subsequent washing and imaging solutions were supplied with Atglistatin, too.

For the analysis of the mitochondria membrane potential, the oocytes were stained in 500 µL medium latest 60 min after isolation. M2 medium was supplied with dbcAMP, 25 nM TMRM, 400 nM MitoTracker Green and 2 µm SiR-DNA for 30 min at 37°C in a humidified incubator. The oocytes were washed 2 x in 500 µL and imaged in medium supplied with SiR-DNA. For the analysis of mitochondria membrane potential after prolonged in vitro culture, the oocytes were incubated in M2 supplied with dbcAMP for 2, 4 and 24 h. The medium was further supplied with either 10% FBS (v/v) or 3.3 mM oleic acid (Sigma; O1008).

For ATP measurement, 3 pL of 500 ng/µL AT1.03 mRNA were injected with the mercury protocol and oocytes were incubated for 2 h at 37°C. Then, the oocytes were incubated for 30 min in medium supplied with either DMSO, Anhydrous (Thermo Fisher; D12345) or 1 µM FCCP (Merck; SML2959) and imaged in the same medium.

Immunofluorescence

Oocytes were isolated and incubated for recovery. Then, the oocytes were transferred into 500 µLPBS supplied with 2% formaldehyde (Sigma; F8775) and incubated for 3 min at room temperature. The oocytes were transferred into 500 µL PBS supplied with 4% formaldehyde ad incubated for 1 h. Then, the oocytes were washed 3 x 5 min in 500 µL PBS supplied with 1% Triton X-100 (v/v; Sigma; 93443) and incubated for permeabilization and extraction for 1 h in another 500 µL at room temperature. The oocytes were blocked overnight at 4°C in 500 µL PBS supplied with 0.1% triton (v/v) and 3% BSA (m/v; VWR; 9048-46-8). The oocytes were incubated in primary antibody solution for 1.5 h at room temperature. Antibodies were diluted 1:50 – 1:100 in blocking solution. Between primary and secondary antibody incubation, the oocytes were washed 3 x 10 min in 500 µL blocking solution. Secondary antibodies (Thermo Fisher) were diluted 1:100 and Hoechst (Thermo Fisher; H1399) was diluted 1:200. Final washes consisted of 2 x 10 min and 1 x 1 h in 500 µL blocking solution. For imaging, the oocytes

were transferred on an imaging dish in PBS supplied with 10% FBS (v/v) and covered by mineral oil. The sample was kept at 4°C until imaging.

A list of all antibodies that were used can be found in Table S1.

HPG assay

Oocytes were isolated and incubated for recovery. To trigger resumption of meiosis, a subset of oocytes was released into dbcAMP-free medium. GV oocytes were kept in medium containing dbcAMP. The HPG assay is based on the Click-iT HPG Alexa Fluor 488 Protein Synthesis Assay Kit (Thermo Fisher; C10428) and was performed according to the manufacturer's protocol. For the HPG incubation, the oocytes were washed once and incubated in sterile and RPMI medium (Thermo Fisher, 21875034) that was supplied with 1 ‰ Gibco Penicillin-Streptomycin (v/v; Thermo Fisher, 15140148), 1% Fetal Bovine Serum, dialyzed, US origin, One Shot format (v/v; Thermo Fisher; A3382001) and 1 ‰ Click-iT HPG (Homopropargylglycine) reagent (Component A) from the kit. For GV oocytes, RPMI medium was additionally supplied with dbcAMP. The RPMI medium was equilibrated in a CO2 supplied incubator for 1.5 h. Negative control oocytes were incubated in the same medium without the HPG supplement. The oocytes were incubated in 500 µL at 37°C in a humidified CO2 supplied incubator for 30 min before washing in RPMI medium supplied with Penicillin-Streptomycin and dialyzed FBS and fixation for 3 min in 500 µLPBS supplied with 2% formaldehyde (v/v) and 1 h in 500 µLPBS supplied with 4% formaldehyde (v/v). For extraction and permeabilization, the oocytes were washed 3x in 500 µL PBS supplied with 0.2% Triton X-100 (v/v) and 3% BSA (v/v) and incubated in another 500 µL for 1 h. Blocking was done as described for immunofluorescence experiments. Before the Click reaction, the oocytes were washed 2x in 500 µL PBS supplied with 3% BSA (v/v). The Click reaction mix was prepared according to the manufacturer's protocol, and oocytes were immediately transferred into 500 µL of the Click reaction buffer. After incubation for 30 min under dark conditions, the oocytes were washed in 250 µL rinse buffer from the kit for 30 min and 250 µL PBST supplied with 0.11% Triton X-100 (v/v). The oocytes were kept in blocking buffer (see immunofluorescence) overnight at 4°C. Mitochondria were stained by the incubation in blocking buffer with 1:200 dilution of mouse anti-Cytochrome C for 1.5 h at room temperature. Washes and incubation with Hoechst and donkey anti-mouse-Alexa Fluor 647 were done as described for immunofluorescence experiments.

Single molecule RNA Fluorescence In Situ Hybridization

smRNA-FISH was performed in two ways. The first protocol involved overexpression of Zar1-mClover3, the second protocol used immunofluorescence staining to visualize

Zar1. Both protocols used the ViewRNA Cell Plus Assay-Kit (Thermo Fisher; 88-19000-99) and the optimizations made by Xie *et al.*[105].

For overexpression of Zar1-mClover3, 3 pL of 400 ng/µL mRNA solution were injected using the FemtoJet protocol. The oocytes were incubated for 3 h to express the construct. Afterwards, the oocytes were fixed in 500 µL PBS supplied with 4% formaldehyde (v/v) for 20 min at room temperature. All subsequent solutions were maintained RNAse-free and separate sets of pipettes and pipette tips were used. After fixation, the oocytes washed 3x in 15 µL wash buffer. The wash buffer consisted of PBS supplied with 0.1% Polyvinylpyrrolidon (m/v; Sigma; P0930), 0.1% Triton X 100 (m/v) and 1% RNase inhibitor (v/v) from the ViewRNA kit. The oocytes were permeabilized in 500 µL PBS supplied with 1% Triton X-100 (v/v) and 1% RNase inhibitor (v/v). The oocytes were washed in 500 µL wash buffer for 10 min, and in case of protease-treatment, oocytes were kept in 500 µL PBS supplied with 125 ppm Protease QS (v/v; Thermo Fisher, purchased individually upon request). After 5 min, the oocytes were washed for 10 min in 500 µL wash buffer. 100 µL probe set diluent from the ViewRNA kit per experimental group was pre-warmed for 30 min before 0.1% Triton X-100 (v/v), and 1% probe set (v/v) was supplied. The probe sets used were *Hig2* – Type 6 (Alexa Fluor 647; Thermo Fisher; VF6-4295726-VCP) and actb – Type 1 (Alexa Fluor 546; Thermo Fisher; VA1-10351-VT). The probe set solution was transferred into individual wells of a 6 well Dish, Agtech "Solution" (Agtech; 3926909910). The oocytes were transferred immediately and incubated at 40°C for 3 h. The oocytes were washed 5x in wash buffer as given by the manufacturer and explained in the manufacturer's protocol. For the work with oocytes, the wash buffer solution from the kit was supplied with 0.5% BSA (m/v). The oocytes were kept in the last well overnight at 4°C. For the pre-amplification, 100 µL amplifier diluent from the ViewRNA kit per experimental group was pre-warmed for 30 min and supplied with 0.1% Triton X-100 (v/v) and 4% pre-amplifier mix from the ViewRNA kit. The oocytes were transferred immediately and incubated for 1 h at 40°C. 6 washing steps were performed in the wash buffer based on the kit's components as described for the previous step. For the amplification step, amplifier buffer was prepared from amplifier diluent, amplifier mix, and Triton X-100 as described for the previous step. The oocytes were incubated for 1 h at 40°C and washed as for the previous step and additionally washed for 10 min in blocking buffer as described for immunofluorescence. The oocytes that were not overexpressed with Zar1-mClover3 were incubated for 1.5 h in blocking buffer supplied with 1:50 diluted goat anti-ZAR1 antibody at room temperature and washed 3x as described for immunofluorescence. Both overexpressed and antibody-stained oocytes were incubated in blocking buffer supplied with 1:200 dilution of Hoechst as described for immunofluorescence. For antibody-stained oocytes, 1:100 dilution of donkey anti-goat-Alexa Fluor 488 was added to the blocking buffer. After 1.5 h, the oocytes were finally washed as described for immunofluorescence and imaged in PBS supplied with 10% FBS (v/v).

Type 6 probes were excited by the 633 nm laser, type 1 probes by the 561 nm laser and mClover3 or Alexa Fluor 488, respectively, by the 488 nm laser. Hoechst was excited by the 405 nm laser. As described in the microscopy section, full z stacks were acquired for smRNA-FISH experiments besides middle sections at lower scan speeds for higher image quality.

RNA sequencing and Gene Set Enrichment Analysis

60 *Zar1*$^{-/-}$ and *Zar1*$^{+/+}$ oocytes were collected and total RNA was isolated. Isolation, synthesis of cDNA and library preparation were performed as described by Yu *et al.*[106].

Sequencing of multiplexed libraries with paired-end reads (PE75) was carried out using a NextSeq 500/550 (Illumina) at an average sequencing depth of 50 million reads per library. Adapters were trimmed with cutadapt 2.8[107] using the " q 20 -m 35 -j 15" parameters. Reads were mapped against the Gencode GRCm39 reference genome with the STAR 2.7.8a[108] aligner using the default settings. Counting of reads mapping to features in the Gencode vM26 annotation file was performed with HTSeq 0.13.5[109]. Differentially expressed genes (DEGs, adjusted p-value < 0.05, average log2 fold change ≥ 0.5) were identified with the DESeq2 v1.32.0[110] package in R. Downregulated or upregulated phenotype-associated pathways were identified with gene set enrichment analysis (GSEA) using the fgsea v1.18.0[111] package in R and the MSigDB[112,113] C5 (ontology) gene set. Raw sequencing reads from the RNAseq of WT and *Zar1*-KO MII oocytes from Gene Expression Omnibus (GEO) accession number GSE122131 were re-analyzed similarly[114].

TMM-normalized CPM values from the RiboTag/RNAseq experiments of GEO accession number GSE135525[115] were re-analyzed with the Bioconductor packages edgeR v3.34.1[116] and Limma v3.48.3[117] as described in the study.

CellROX assay

Oocytes were isolated and incubated for recovery. Afterwards, the oocytes were transferred into medium that was supplied with 5 µM CellROX Green (Thermo Fisher; C10444) and 2 µM SiR-DNA. After 30 min at 37°C, oocytes were washed 3x and imaged in medium supplied with SiR-DNA.

Lipid peroxidation assay

The lipid peroxidation assay was based on the Click-iT Lipid Peroxidation Imaging Kit - Alexa Fluor 488 (Thermo Fisher; C10446). Oocytes were isolated and incubated for recovery. Then, the LAA (Linoleamide alkyne) from the Click kit was added to the medium to achieve a final concentration of 50 µM, and oocytes were incubated with

LAA for 24 h in a humidified incubator at 37°C. For negative control, a subset of oocytes was incubated in medium without LAA. For positive control, a subset of oocytes was incubated for 2h in medium that contained LAA and cumene hydroxide from the Click kit after the 24 h incubation. Before fixation, all oocytes were washed 2x 1 min in PBS and fixed as described for immunofluorescence. After overnight blocking, the oocytes were washed in PBS that contained 0.1% Triton X-100. The Click reaction mix was prepared according to the manufacturer's protocol, and the oocytes were transferred into 500 µL reaction mix and incubated for 30 min under dark conditions. Afterwards, the oocytes were washed 3x 10 min in blocking buffer from the immunofluorescence protocol. Subsequent immunofluorescence staining with 1:50 rabbit anti-Cox17 and 1:100 guinea pig anti-ZAR1 as primary antibodies and donkey anti-rabbit-Alexa Fluor 647 and goat anti-guinea pig-Alexa Fluor 568 and Hoechst for the incubation with secondary antibodies was performed, and final washes and imaging was done as described for immunofluorescence.

Luminescent ATP assay

The ATP detection assay was based on the Luminescent ATP Detection Assay Kit (abcam; ab113849). A white opaque 96 well plate (Costar) was used. The dilution series of the ATP standard was prepared first. A 100 µM ATP working standard was prepared and diluted down to 0.0001 µM. All standard solutions were diluted 1:10 in M2 medium supplied with dbcAMP for the final dilution series. 100 µL of the medium were filled into wells that were dedicated for oocyte measurement and 3 – 4 *Zar1*$^{-/-}$ or *Zar1*$^{+/+}$ oocytes were added. 50 µL of the kit's detergent were filled in each well, and the plates were shaken for 5 min and 50 µL substrate solution from the kit was added to each well. The plate was shaken for 5 minutes and incubated under dark conditions for 10 min before insertion into a Neo2 plate reader (BioTek). The reading was done from 4 mm distance with 50 s integration time. All values were normalized to the 0 µM ATP standard and Origin (OriginLab) was used to calculate a linear fit. Based on the linear fit, the ATP concentration for each cell was calculated and divided by the number of oocytes in the respective well.

Analysis, ImageJ, Imaris, R

Initial analysis of imaging data as well as image export was done in Zen Blue (Zeiss). Further analysis, and quantification of fluorescence signal intensity was done in ImageJ[118]. The oocytes were selected individually and analyzed using Script S1. For the analysis of TMRM and MitoTracker Green signal, Script S2 was used. Script S2 uses the threshold function to select for mitochondrial clusters and ignore cytoplasmic background. For the calculation of smRNA-FISH spots, Imaris (Bitplane) was used. The

spot tool was used to create spots for the respective channel using background subtraction and a modelled point spread function of 1.2 µm in the xy- and 2.4 µm in the z-dimension. The quality threshold was adjusted according to the image quality, and wrong spots were removed manually. For the calculation of the ZAR1 aggregates volume, the sphere function was used for the respective channel using background subtraction sphere and the 0.165 surface grain size. The background substraction threshold was adjusted according to the image quality, and aggregates smaller than 1000 voxels were removed. To measure the distance of smRNA-FISH spots to the next ZAR1 aggregate surface, distance transformation was applied outside of the ZAR1 spheres (based on MatLab), and the information for all spots were extracted.

Data collection was done in Excel (Microsoft), and statistical analysis was performed in R (Script S3).

Authors' contribution

G.A. performed all experiments if not stated otherwise. S.C. performed the live cell imaging of Nile red and the AT1.03 expression assay for the determination of ATP levels. S.C. established the initial HPG protocol and prepared the RNA and cDNA library for the RNAseq experiment. G.A. wrote the manuscript. The Materials and Methods section for the RNAseq was written by S.C. M.S. supervised the study, provided all materials and proofread the manuscript.

Acknowledgments

The authors thank Sarah Penir for the analysis of the RNAseq dataset and the generation of the GSEA figure and the MPI-NAT animal facility and animal care takers for maintaining the mouse lines used in this study. We also would like to acknowledge Kevin Rentsch and Lion Timm for genotyping of the *Zar1*-KO line and Martina Daniel and Silke Schlott for organizing the purchase of antibodies.

Funding

The study was funded by the Deutsche Forschungsgemeinschaft (DFG, German Research Foundation) under Germany's Excellence Strategy - EXC 2067/1- 390729940, the Max Planck Society, the European Research Council under grant agreement 337415, the Lister Institute for Preventive Medicine and the DFG under a Leibniz Prize to M.S. (SCHU 3047/1-1).

Conflict of interest

The authors declare no conflict of interest.

Supplemental material and methods

Table S1 Table of antibodies used for immunofluorescence

Primary antibodies	Secondary antibodies (1:100)
Guinea pig anti-ZAR1 (custom-made; 1:50)	Goat anti-Mouse IgG (H+L) Cross-Adsorbed Secondary Antibody, Alexa Fluor 488 (Thermo Fisher; A-11001; RRID: AB_2534069)
Goat anti-ZAR1 (Santa cruz; sc-55994; RRID: AB_2218783; 1:50)	Goat anti-Mouse IgG (H+L) Highly Cross-Adsorbed Secondary Antibody, Alexa Fluor 568 (Thermo Fisher; A-11031; RRID: AB_144696)
Mouse anti-Cytochrome C (Santa cruz; sc-13156; RRID: AB_627385; 1:50)	Goat anti-Mouse IgG (H+L) Cross-Adsorbed Secondary Antibody, Alexa Fluor 647 (Thermo Fisher; A-21235; RRID: AB_2535804)
Mouse anti-Cytochrome C (Santa cruz; sc-13561; RRID: AB_627381; 1:200)	Donkey anti-Mouse IgG (H+L) Highly Cross-Adsorbed Secondary Antibody, Alexa Fluor 488 (Thermo Fisher; A-21202; RRID: AB_141607)
Rabbit anti-Cox17 (Sigma; HPA042226; RRID: AB_2677911; 1:100)	Donkey anti-Mouse IgG (H+L) Highly Cross-Adsorbed Secondary Antibody, Alexa Fluor 568 (Thermo Fisher; A10037; RRID: AB_2534013)
Rabbit anti-ATGL (Cell signaling; 2138S; RRID: AB_2167955; 1:50)	Donkey anti-Mouse IgG (H+L) Highly Cross-Adsorbed Secondary Antibody, Alexa Fluor 647 (Thermo Fisher; A-31571; RRID: AB_162542)
Rabbit anti-4-hydroxynonenal (Biotrend; STA-035; 1:50)	Goat anti-Rabbit IgG (H+L) Cross-Adsorbed Secondary Antibody, Alexa
Mouse anti-8-oxoG (Trevigen; 4354-MC-050; RRID: AB_1857195; 1:50)	
Rabbit anti-gamma-H2AX (R&D Systems; 4418-APC-020; 1:50)	
Rabbit anti-phosphp-S36-SHC (abcam; ab267413; 1:100)	
Mouse anti-SHC (BD; 610879; RRID: AB_398196; 1:50)	

Fluor 488 (Thermo Fisher; A-11008; RRID: AB_143165)

Goat anti-Rabbit IgG (H+L) Cross-Adsorbed Secondary Antibody, Alexa Fluor 568 (Thermo Fisher; A-11011; RRID: AB_143157)

Goat anti-Rabbit IgG (H+L) Highly Cross-Adsorbed Secondary Antibody, Alexa Fluor 647 (Thermo Fisher; A-21245; RRID: AB_2535813)

Donkey anti-Rabbit IgG (H+L) Highly Cross-Adsorbed Secondary Antibody, Alexa Fluor 488 (Thermo Fisher; A-21206; RRID: AB_2535792)

Donkey anti-Rabbit IgG (H+L) Highly Cross-Adsorbed Secondary Antibody, Alexa Fluor 568 (Thermo Fisher; A10042; RRID: AB_2534017)

Donkey anti-Rabbit IgG (H+L) Highly Cross-Adsorbed Secondary Antibody, Alexa Fluor 647 (Thermo Fisher; A-31573; RRID: AB_2536183)

Donkey anti-Goat IgG (H+L) Cross-Adsorbed Secondary Antibody, Alexa Fluor 488 (Thermo Fisher; A-11055; RRID: AB_2534102)

Donkey anti-Goat IgG (H+L) Cross-Adsorbed Secondary Antibody, Alexa Fluor 568 (Thermo Fisher; A-11057; RRID: AB_2534104)

Donkey anti-Goat IgG (H+L) Cross-Adsorbed Secondary Antibody, Alexa Fluor 647 (Thermo Fisher; A-21447; RRID: AB_2535864)

	Goat anti-Guinea Pig IgG (H+L) Highly Cross-Adsorbed Secondary Antibody, Alexa Fluor 488 (Thermo Fisher; A-11073; RRID: AB_2534117) Goat anti-Guinea Pig IgG (H+L) Highly Cross-Adsorbed Secondary Antibody, Alexa Fluor 568 (Thermo Fisher; A-11075; RRID: AB_2534119) Goat anti-Guinea Pig IgG (H+L) Highly Cross-Adsorbed Secondary Antibody, Alexa Fluor 647 (Thermo Fisher; A-21450; RRID: AB_2735091)

Script S1 Quantification of fluorescence intensity in microscopy images

```
run("Duplicate...", "duplicate channels=2"); # Change depending on the channel of interest
waitForUser(); #DrawCircle
run("Measure");
```

Script S2 Quantification of TMRM and MitoTracker Green signal in areas of clustered mitochondria

```
Stack.setPosition(1,1,3); # Change depending on the channel of interest
waitForUser(); #DrawCircle run("Enhance Contrast", "saturated=0.35");
run("Bandpass Filter...", "filter_large=40 filter_small=1 suppress=None tolerance=5 autoscale saturate");
setAutoThreshold("Li dark");
run("Analyze Particles...", "size=0.10-Infinity clear add stack");
roiManager("Multi Measure");
saveAs("Results", "...");
```

Script S3 Boxplot generation for quantifies fluorescence intensity data

```
library(tidyverse)
library(dplyr)
library(tidyr)
library(ggplot2)
library(gapminder)
```

```
setwd("...")
DATA <- read.csv("....csv", sep = ";",
                 header = TRUE,
                 dec = ",", na.strings = "NA")
DATA$Treatment <- factor(DATA$Treatment, levels=c("CD1-NSN", "CD1-SN", "WT-
NSN", "WT-SN", "KO-NSN", "KO-SN"))
ggplot(data=DATA, aes(y=Value , x=Treatment, fill=Treatment)) +
  theme_classic()+
  stat_boxplot(geom = "errorbar", width=0.2) +
  geom_boxplot(width=0.4)+
  stat_summary(fun="mean", color="black", shape=4)+
  coord_flip()+
  scale_fill_manual(values=c("#BFBFBF", "#7F7F7F","#BFBFBF", "#7F7F7F", "#BFBFBF",
"#7F7F7F"))
# saved as 1000 height and 450 width
```

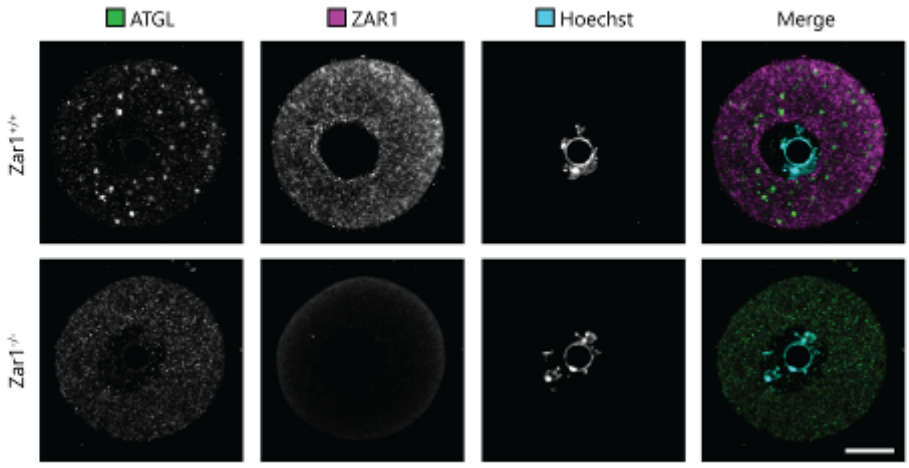

Fig. S1 ZAR1 and ATGL do not co-localize. Confical microscopy images of *Zar1*$^{-/-}$ and *Zar1*$^{+/+}$ oocytes after fixation and staining with α-ATGL and α-ZAR1 antibodies. Scale bar 20 µm

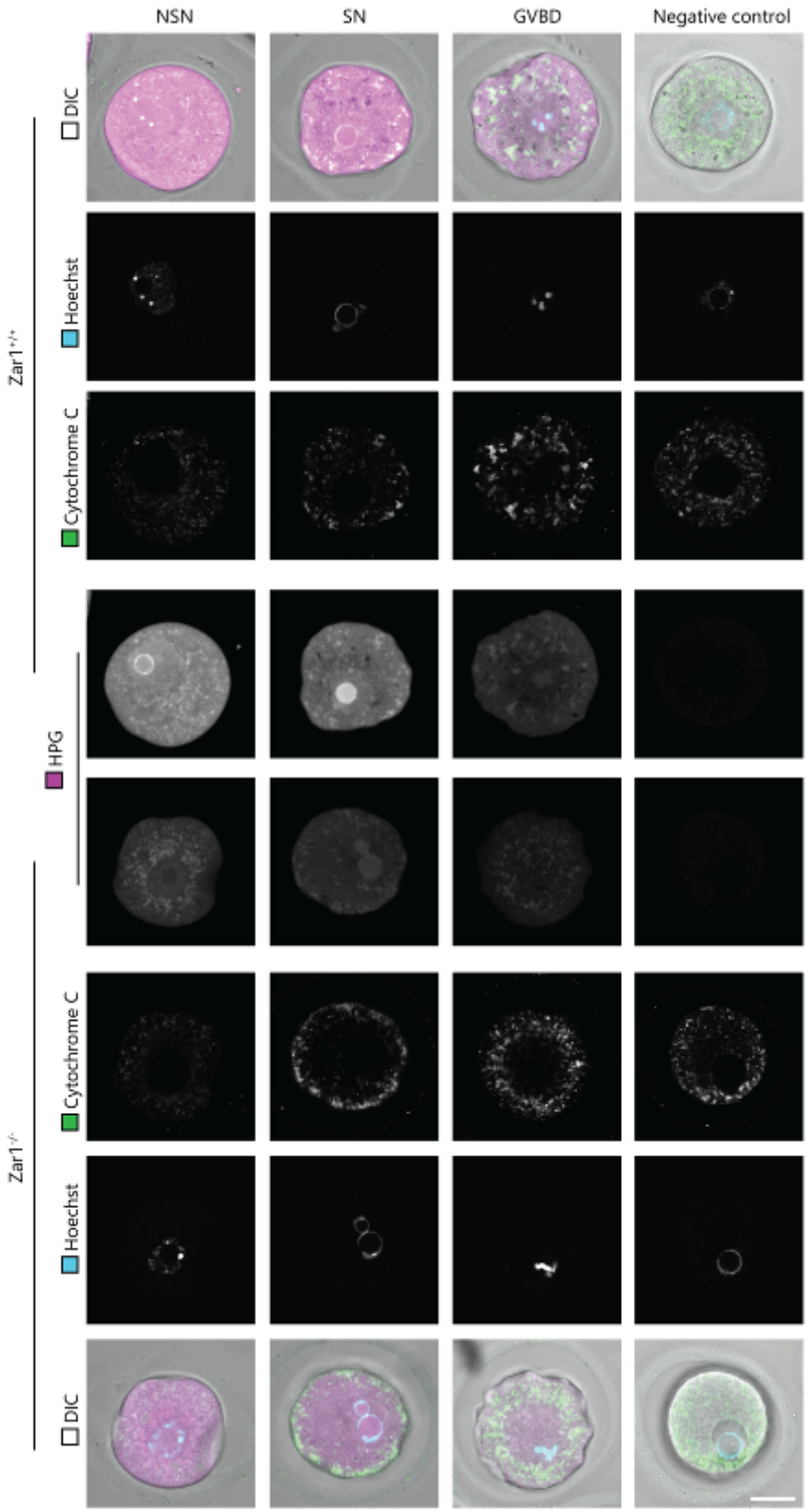

Fig. S2 No enriched translation in the vicinity of mitochondria. Confocal microscopy images of *Zar1*$^{-/-}$ and *Zar1*$^{+/+}$ oocytes after fixation and staining with AlexaFluor 488-azide (HPG), α-Cytochrome C antibody (mitochondria) and Hoechst (DNA). Scale bar 40 µm.

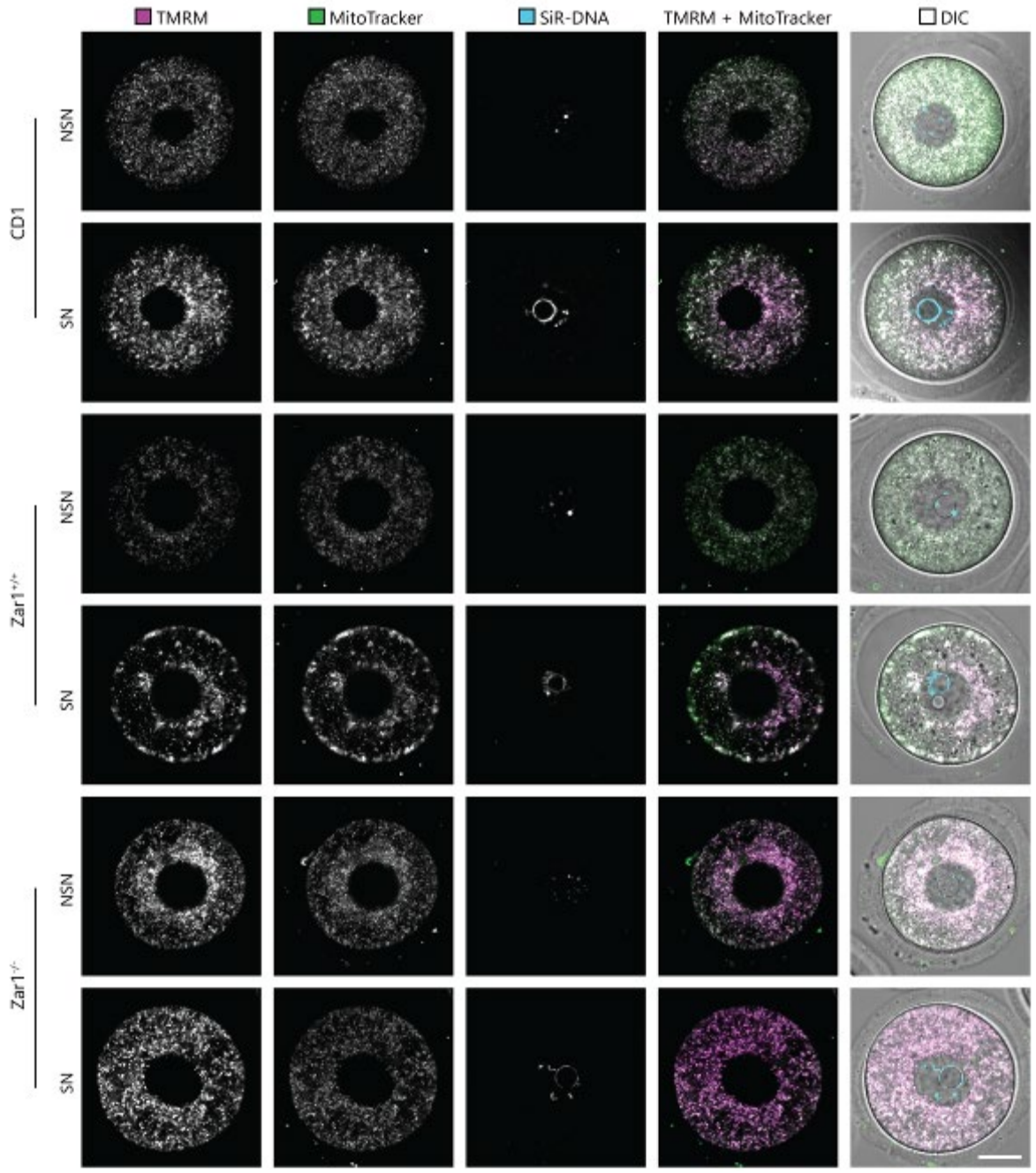

Fig. S3 Mouse oocytes exhibit two populations of mitochondria based on the mitochondria membrane potential (MM). Confocal live cell microscopy images after staining with TMRM, MitoTracker Green and SiR-DNA. The superimposition of TMRM (*ΔΨm)* and MitoTracker Green signal (mitochondria) reveals uneven distribution of mitochondria with high *ΔΨm* and low *ΔΨm*. The effect is stronger in SN oocytes. In *Zar1*$^{-/-}$ oocytes, the distribution is homogenous, indicating that there is only one group of mitochondria. Scale bar 20 µm.

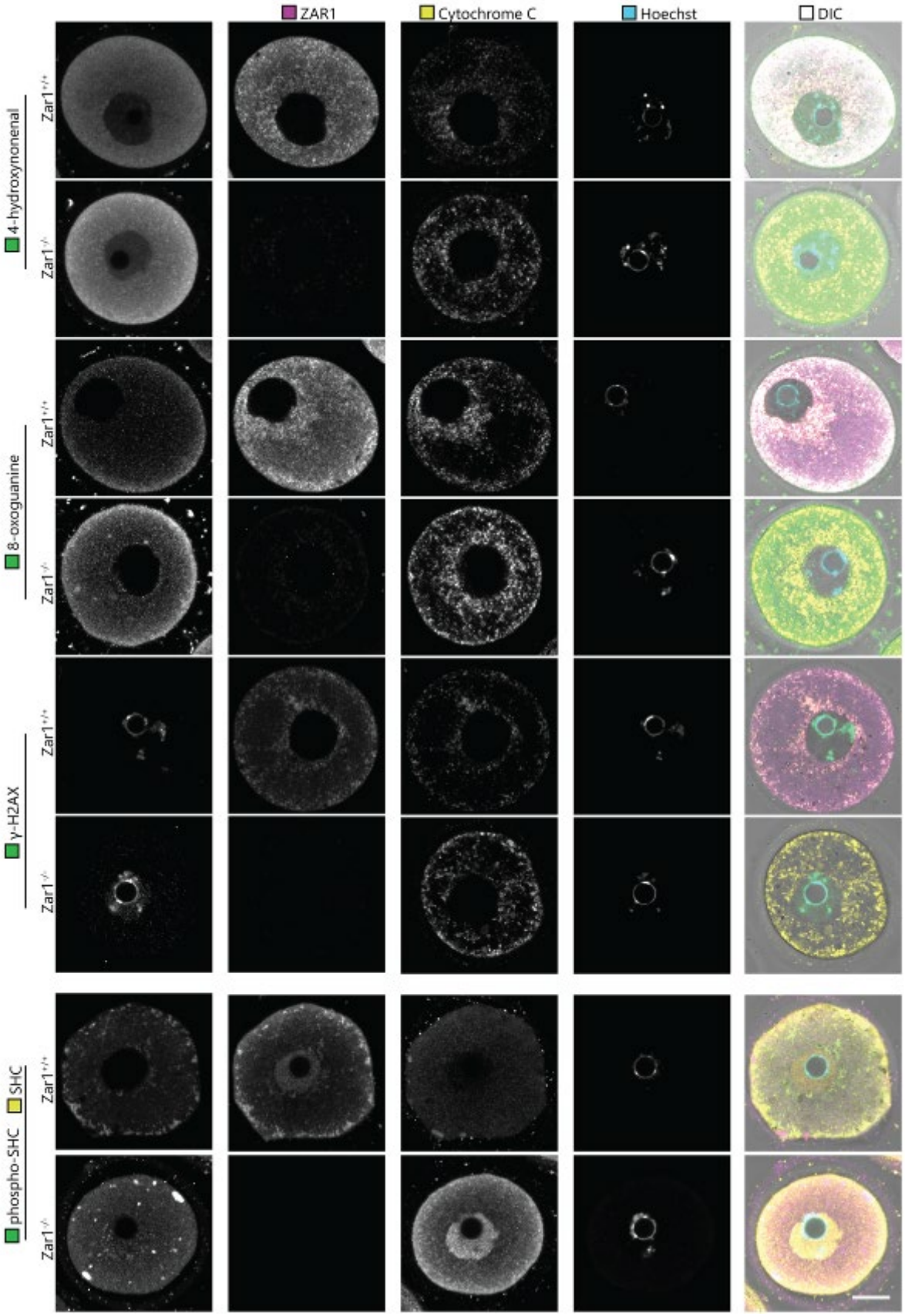

Fig. S4 ROS markers are not enriched in the vicinity of mitochondria. Confocal microscopy images of *Zar1*$^{-/-}$ and *Zar1*$^{+/+}$ oocytes after fixation and staining with antibodies of ROS-markers, Zar1, Cytochrome C (mitochondria) and Hoechst (DNA). For phospho-SHC / SHC, the co-localization with mitochondria was indirectly measured by checking for co-localization with Zar1, as ZAR1 is known to co-localize with

mitochondria (data not shown). For quantification, the ratio of the total phospho-SHC signal and the total SHC signal was used. For both populations of p66SHC, specific antibodies were used. Scale bar 20 µm.

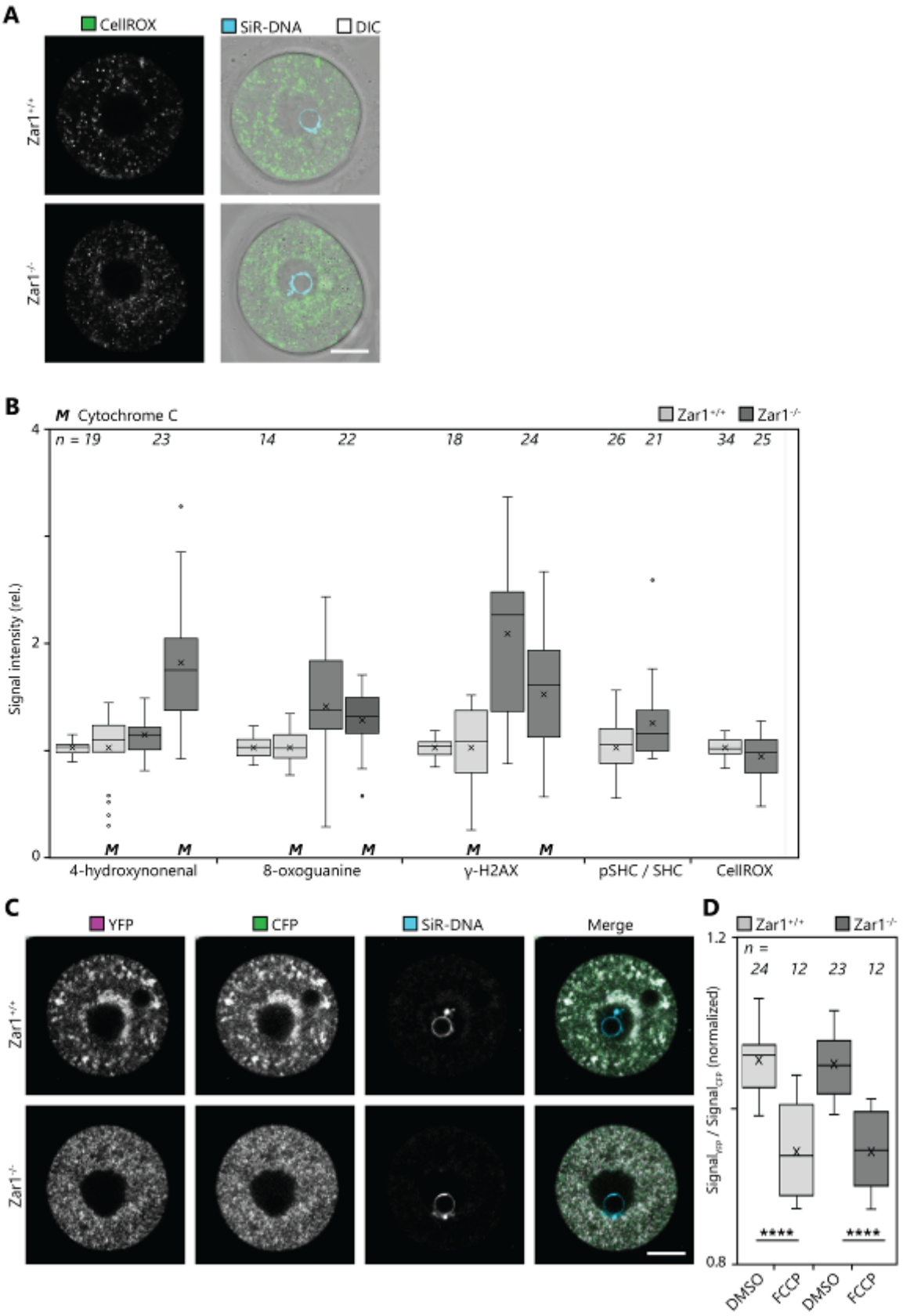

Fig. S5 ROS markers show considerably low increase in *Zar1*$^{-/-}$ oocytes compared to Cytochrome C. (A) Confocal microscopy images of *Zar1*$^{-/-}$ and *Zar1*$^{+/+}$ oocytes after fixation and staining with Hoechst. Oocytes were treated with CellROX dye according to the manufacturer's protocol. (B) Full quantification of the fluorescence signal intensity of all ROS markers and Cytochrome C in fixed oocytes. Cytochrome C was not stained in phospho-SHC (pSHC) / SHC and CellROX experiments. The M indicates the data of Cytochrome C analysis. (C) Live cell microscopy images of *Zar1*$^{-/-}$ and *Zar1*$^{+/+}$ oocytes that were injected with the ATP-sensitive reporter AT1.03 and incubated for 2 h. Oocytes were stained with SiR-DNA for imaging. The ratio of the cp173-mVenus (YFP) and the mseCFP (CFP) reflects the amount of ATP. (D) Quantification of AT1.03 assay. The overall intensity of YFP was divided by the overall intensity of CFP for each oocyte. FCCP uncouples the oxidative phosphorylation (OXPHOS) and reduces the ATP concentration. FFCP treatment was used as negative control. The values for both genotypes were normalized to the mean FCCP intensity for the respective groups. This results in a mean of 1 for both FCCP groups. n numbers are shown above. **** : p-value < 0.0001. Scale bar 20 µm.

References

1. Hassold, T. & Hunt, P. To err (meiotically) is human: the genesis of human aneuploidy. *Nat. Rev. Genet.* **2**, 280–291 (2001).
2. Cimadomo, D. *et al.* Impact of Maternal Age on Oocyte and Embryo Competence. *Front. Endocrinol. (Lausanne).* **9**, (2018).
3. Janny, L. & Menezo, Y. J. R. Maternal age effect on early human embryonic development and blastocyst formation. *Mol. Reprod. Dev.* **45**, 31–37 (1996).
4. Hassold, T. & Chiu, D. Maternal age-specific rates of numerical chromosome abnormalities with special reference to trisomy. *Hum. Genet.* **70**, 11–17 (1985).
5. Nagaoka, S. I., Hassold, T. J. & Hunt, P. A. Human aneuploidy: mechanisms and new insights into an age-old problem. *Nat. Rev. Genet.* **13**, 493–504 (2012).
6. Wallace, W. H. B. & Kelsey, T. W. Human Ovarian Reserve from Conception to the Menopause. *PLoS One* **5**, e8772 (2010).
7. MANDL, A. M. & ZUCKERMAN, S. THE RELATION OF AGE TO NUMBERS OF OOCYTES. *J. Endocrinol.* **7**, 190–193 (1951).
8. Sasaki, H. *et al.* Impact of Oxidative Stress on Age-Associated Decline in Oocyte Developmental Competence. *Front. Endocrinol. (Lausanne).* **10**, 811 (2019).
9. Titus, S., Stobezki, R. & Oktay, K. Impaired DNA Repair as a Mechanism for Oocyte Aging: Is It Epigenetically Determined? *Semin. Reprod. Med.* **33**, 384–388 (2015).
10. Cadenas, E. & Davies, K. J. A. Mitochondrial free radical generation, oxidative stress, and aging. *Free Radic. Biol. Med.* **29**, 222–230 (2000).
11. Banerjee, R., Starkov, A. A., Beal, M. F. & Thomas, B. Mitochondrial dysfunction in the limelight of Parkinson's disease pathogenesis. *Biochim. Biophys. Acta - Mol. Basis Dis.* **1792**, 651–663 (2009).
12. Pasquariello, R. *et al.* Alterations in oocyte mitochondrial number and function are related to spindle defects and occur with maternal aging in mice and humans†. *Biol. Reprod.* **100**, 971–981 (2019).
13. Boudoures, A. L. *et al.* Obesity-exposed oocytes accumulate and transmit damaged mitochondria due to an inability to activate mitophagy. *Dev. Biol.* **426**, 126–138 (2017).
14. Zhao, X.-M. *et al.* Effect of cyclosporine pretreatment on mitochondrial function in vitrified bovine mature oocytes. *Fertil. Steril.* **95**, 2786–2788 (2011).
15. Tatone, C. *et al.* Evidence that carbonyl stress by methylglyoxal exposure induces DNA damage and spindle aberrations, affects mitochondrial integrity in mammalian oocytes and contributes to oocyte ageing. *Hum. Reprod.* **26**, 1843–

1859 (2011).

16. Van Blerkom, J. & Davis, P. Mitochondrial signaling and fertilization. *Mol. Hum. Reprod.* **13**, 759–770 (2007).

17. Van Blerkom, J., Davis, P. & Thalhammer, V. Regulation of mitochondrial polarity in mouse and human oocytes: the influence of cumulus derived nitric oxide. *Mol. Hum. Reprod.* **14**, 431–444 (2008).

18. Van Blerkom, J., Davis, P. & Alexander, S. Differential mitochondrial distribution in human pronuclear embryos leads to disproportionate inheritance between blastomeres: relationship to microtubular organization, ATP content and competence. *Hum. Reprod.* **15**, 2621–2633 (2000).

19. Yan, C.-L. *et al.* Mitochondrial behaviors in the vitrified mouse oocyte and its parthenogenetic embryo: effect of Taxol pretreatment and relationship to competence. *Fertil. Steril.* **93**, 959–966 (2010).

20. TOURTE, M., MIGNOTTE, F. & MOUNOLOU, J.-C. ORGANIZATION AND REPLICATION ACTIVITY OF THE MITOCHONDRIAL MASS OF OOGONIA AND PREVITELLOGENIC OOCYTES IN XENOPUS LAEVIS. *Dev. Growth Differ.* **23**, 9–21 (1981).

21. Tworzydlo, W., Sekula, M. & Bilinski, S. M. Transmission of Functional, Wild-Type Mitochondria and the Fittest mtDNA to the Next Generation: Bottleneck Phenomenon, Balbiani Body, and Mitophagy. *Genes (Basel).* **11**, 104 (2020).

22. Boke, E. *et al.* Amyloid-like Self-Assembly of a Cellular Compartment. *Cell* **166**, 637–650 (2016).

23. Kloc, M., Jedrzejowska, I., Tworzydlo, W. & Bilinski, S. M. Balbiani body, nuage and sponge bodies – The germ plasm pathway players. *Arthropod Struct. Dev.* **43**, 341–348 (2014).

24. Yang, C., Wilson, G. M., Champion, M. M. & Huber, P. W. Remnants of the Balbiani body are required for formation of RNA transport granules in Xenopus oocytes. *bioRxiv* 2020.05.27.119487 (2020) doi:10.1101/2020.05.27.119487.

25. Marlow, F. L. Maternal Control of Development in Vertebrates. *Colloq. Ser. Dev. Biol.* **1**, 1–196 (2010).

26. Zelazowska, M., Kilarski, W., Bilinski, S. M., Podder, D. D. & Kloc, M. Balbiani cytoplasm in oocytes of a primitive fish, the sturgeon Acipenser gueldenstaedtii, and its potential homology to the Balbiani body (mitochondrial cloud) of Xenopus laevis oocytes. *Cell Tissue Res.* **329**, 137–145 (2007).

27. Dhandapani, L. *et al.* Mouse oocytes do not contain a Balbiani body. *bioRxiv* 2021.02.01.429160 (2021) doi:10.1101/2021.02.01.429160.

28. Kloc, M. & Etkin, L. D. Two distinct pathways for the localization of RNAs at the vegetal cortex in Xenopus oocytes. *Development* **121**, 287–297 (1995).

29. Kloc, M., Larabell, C., Chan, A. P.-Y. & Etkin, L. D. Contribution of METRO pathway localized molecules to the organization of the germ cell lineage. *Mech. Dev.* **75**, 81–93 (1998).

30. Kloc, M., Bilinski, S., Pui-Yee Chan, A. & Etkin, L. D. The Targeting of Xcat2 mRNA to the Germinal Granules Depends on a cis-Acting Germinal Granule Localization Element within the 3'UTR. *Dev. Biol.* **217**, 221–229 (2000).

31. Wilk, K., Bilinski, S., Dougherty, M. T. & Kloc, M. Delivery of germinal granules and localized RNAs via the messenger transport organizer pathway to the vegetal cortex of Xenopus oocytes occurs through directional expansion of the mitochondrial cloud. *Int. J. Dev. Biol.* **49**, 17–21 (2005).

32. Owens, D. A. *et al.* High-throughput analysis reveals novel maternal germline RNAs crucial for primordial germ cell preservation and proper migration. *Development* **144**, 292–304 (2017).

33. Cox, R. T. & Spradling, A. C. A Balbiani body and the fusome mediate mitochondrial inheritance during *Drosophila* oogenesis. *Development* **130**, 1579–1590 (2003).

34. Pepling, M. E., Wilhelm, J. E., O'Hara, A. L., Gephardt, G. W. & Spradling, A. C. Mouse oocytes within germ cell cysts and primordial follicles contain a Balbiani body. *Proc. Natl. Acad. Sci.* **104**, 187–192 (2007).

35. Jędrzejowska, I. & Kubrakiewicz, J. Yolk nucleus – The complex assemblage of cytoskeleton and ER is a site of lipid droplet formation in spider oocytes. *Arthropod Struct. Dev.* **39**, 350–359 (2010).

36. Olzmann, J. A. & Carvalho, P. Dynamics and functions of lipid droplets. *Nat. Rev. Mol. Cell Biol.* **20**, 137–155 (2019).

37. Smirnova, E. *et al.* ATGL has a key role in lipid droplet/adiposome degradation in mammalian cells. *EMBO Rep.* **7**, 106–113 (2006).

38. Wagner, P. D. New ideas on limitations to VO2max. *Exerc. Sport Sci. Rev.* **28**, 10–4 (2000).

39. Granneman, J. G., Moore, H.-P. H., Mottillo, E. P., Zhu, Z. & Zhou, L. Interactions of Perilipin-5 (Plin5) with Adipose Triglyceride Lipase. *J. Biol. Chem.* **286**, 5126–5135 (2011).

40. Boutant, M. *et al.* Mfn2 is critical for brown adipose tissue thermogenic function. *EMBO J.* **36**, 1543–1558 (2017).

41. Houten, S. M., Violante, S., Ventura, F. V. & Wanders, R. J. A. The Biochemistry and Physiology of Mitochondrial Fatty Acid β-Oxidation and Its Genetic Disorders. *Annu. Rev. Physiol.* **78**, 23–44 (2016).

42. Adeva-Andany, M. M., Carneiro-Freire, N., Seco-Filgueira, M., Fernández-Fernández, C. & Mouriño-Bayolo, D. Mitochondrial β-oxidation of saturated

fatty acids in humans. *Mitochondrion* **46**, 73–90 (2019).

43. Giordano, A. *et al.* tBid induces alterations of mitochondrial fatty acid oxidation flux by malonyl-CoA-independent inhibition of carnitine palmitoyltransferase-1. *Cell Death Differ.* **12**, 603–613 (2005).

44. Poburko, D., Santo-Domingo, J. & Demaurex, N. Dynamic Regulation of the Mitochondrial Proton Gradient during Cytosolic Calcium Elevations. *J. Biol. Chem.* **286**, 11672–11684 (2011).

45. Sivandzade, F., Bhalerao, A. & Cucullo, L. Analysis of the Mitochondrial Membrane Potential Using the Cationic JC-1 Dye as a Sensitive Fluorescent Probe. *BIO-PROTOCOL* **9**, (2019).

46. Creed, S. & McKenzie, M. Measurement of Mitochondrial Membrane Potential with the Fluorescent Dye Tetramethylrhodamine Methyl Ester (TMRM). in *Methods in Molecular Biology* vol. 1928 69–76 (Humana Press Inc., 2019).

47. Arena, R. *et al.* Lipid droplets in mammalian eggs are utilized during embryonic diapause. *Proc. Natl. Acad. Sci.* **118**, e2018362118 (2021).

48. Herrick, D., Parker, R. & Jacobson, A. Identification and comparison of stable and unstable mRNAs in Saccharomyces cerevisiae. *Mol. Cell. Biol.* **10**, 2269–2284 (1990).

49. Sachs, A. The role of poly(A) in the translation and stability of mRNA. *Curr. Opin. Cell Biol.* **2**, 1092–1098 (1990).

50. Jalkanen, A. L., Coleman, S. J. & Wilusz, J. Determinants and implications of mRNA poly(A) tail size – Does this protein make my tail look big? *Semin. Cell Dev. Biol.* **34**, 24–32 (2014).

51. Ferg, M. *et al.* The TATA-binding protein regulates maternal mRNA degradation and differential zygotic transcription in zebrafish. *EMBO J.* **26**, 3945–3956 (2007).

52. Laver, J. D. *et al.* The RNA-Binding Protein Rasputin/G3BP Enhances the Stability and Translation of Its Target mRNAs. *Cell Rep.* **30**, 3353-3367.e7 (2020).

53. Chen, L. *et al.* Global regulation of mRNA translation and stability in the early Drosophila embryo by the Smaug RNA-binding protein. *Genome Biol.* **15**, R4 (2014).

54. Sysoev, V. O. *et al.* Global changes of the RNA-bound proteome during the maternal-to-zygotic transition in Drosophila. *Nat. Commun.* **7**, 12128 (2016).

55. Cao, W. X., Karaiskakis, A., Lin, S., Angers, S. & Lipshitz, H. D. The F-box protein Bard (CG14317) targets the Smaug RNA-binding protein for destruction during the Drosophila maternal-to-zygotic transition. *Genetics* **220**, (2022).

56. Wang, M. *et al.* ME31B globally represses maternal mRNAs by two distinct

mechanisms during the Drosophila maternal-to-zygotic transition. *Elife* **6**, (2017).

57. Semotok, J. L. *et al.* Drosophila Maternal Hsp83mRNA Destabilization Is Directed by Multiple SMAUG Recognition Elements in the Open Reading Frame. *Mol. Cell. Biol.* **28**, 6757–6772 (2008).

58. Smibert, C. A., Wilson, J. E., Kerr, K. & Macdonald, P. M. smaug protein represses translation of unlocalized nanos mRNA in the Drosophila embryo. *Genes Dev.* **10**, 2600–2609 (1996).

59. Wu, X. *et al.* Zygote arrest 1 (Zar1) is a novel maternal-effect gene critical for the oocyte-to-embryo transition. *Nat. Genet.* **33**, 187–191 (2003).

60. Rong, Y. *et al.* ZAR1 and ZAR2 are required for oocyte meiotic maturation by regulating the maternal transcriptome and mRNA translational activation. *Nucleic Acids Res.* **47**, 11387–11402 (2019).

61. Kim, B., Kan, R., Anguish, L., Nelson, L. M. & Coonrod, S. A. Potential Role for MATER in Cytoplasmic Lattice Formation in Murine Oocytes. *PLoS One* **5**, e12587 (2010).

62. Tatsumi, T. *et al.* Forced lipophagy reveals that lipid droplets are required for early embryonic development in mouse. *Development* **145**, (2018).

63. Aizawa, R. *et al.* Synthesis and maintenance of lipid droplets are essential for mouse preimplantation embryonic development. *Development* **146**, (2019).

64. Ordoñez-Leon, E., Merchant, H., Medrano, A., Kjelland, M. & Romo, S. Lipid Droplet Analysis Using In Vitro Bovine Oocytes and Embryos. *Reprod. Domest. Anim.* **49**, 306–314 (2014).

65. O'Rourke, E. J., Soukas, A. A., Carr, C. E. & Ruvkun, G. C. elegans Major Fats Are Stored in Vesicles Distinct from Lysosome-Related Organelles. *Cell Metab.* **10**, 430–435 (2009).

66. Zhang, D., Keilty, D., Zhang, Z. F. & Chian, R. C. Mitochondria in oocyte aging: current understanding. *Facts, views Vis. ObGyn* **9**, 29–38 (2017).

67. AL-Zubaidi, U. *et al.* The spatio-temporal dynamics of mitochondrial membrane potential during oocyte maturation. *Mol. Hum. Reprod.* **25**, 695–705 (2019).

68. Imamura, H. *et al.* Visualization of ATP levels inside single living cells with fluorescence resonance energy transfer-based genetically encoded indicators. *Proc. Natl. Acad. Sci.* **106**, 15651–15656 (2009).

69. Rosca, M. G. *et al.* Oxidation of fatty acids is the source of increased mitochondrial reactive oxygen species production in kidney cortical tubules in early diabetes. *Diabetes* **61**, 2074–2083 (2012).

70. Soto-Heras, S. & Paramio, M.-T. Impact of oxidative stress on oocyte

competence for in vitro embryo production programs. *Res. Vet. Sci.* **132**, 342–350 (2020).

71. Mihalas, B. P., De Iuliis, G. N., Redgrove, K. A., McLaughlin, E. A. & Nixon, B. The lipid peroxidation product 4-hydroxynonenal contributes to oxidative stress-mediated deterioration of the ageing oocyte. *Sci. Rep.* **7**, 6247 (2017).

72. Cooke, M. S., Evans, M. D., Dizdaroglu, M. & Lunec, J. Oxidative DNA damage: mechanisms, mutation, and disease. *FASEB J.* **17**, 1195–1214 (2003).

73. Mah, L.-J., El-Osta, A. & Karagiannis, T. C. γH2AX: a sensitive molecular marker of DNA damage and repair. *Leukemia* **24**, 679–686 (2010).

74. Leon, J. *et al.* 8-Oxoguanine accumulation in mitochondrial DNA causes mitochondrial dysfunction and impairs neuritogenesis in cultured adult mouse cortical neurons under oxidative conditions. *Sci. Rep.* **6**, 22086 (2016).

75. Edwards, N. A., Watson, A. J. & Betts, D. H. P66Shc, a key regulator of metabolism and mitochondrial ROS production, is dysregulated by mouse embryo culture. *Mol. Hum. Reprod.* **22**, 634–647 (2016).

76. Fernandes, R. *et al.* NLRP5 Mediates Mitochondrial Function in Mouse Oocytes and Embryos1. *Biol. Reprod.* **86**, 1–10 (2012).

77. Ibayashi, M., Aizawa, R., Mitsui, J. & Tsukamoto, S. Homeostatic regulation of lipid droplet content in mammalian oocytes and embryos. *Reproduction* **162**, R99–R109 (2021).

78. Hungerford, G., Castanheira, E. M. S., Baptista, A. L. F., Coutinho, P. J. G. & Oliveira, M. E. C. D. R. Domain Formation in DODAB–Cholesterol Mixed Systems Monitored via Nile Red Anisotropy. *J. Fluoresc.* **15**, 835–840 (2005).

79. Filimonenko, M. *et al.* Functional multivesicular bodies are required for autophagic clearance of protein aggregates associated with neurodegenerative disease. *J. Cell Biol.* **179**, 485–500 (2007).

80. Nguyen, T. B. & Olzmann, J. A. Getting a handle on lipid droplets: Insights into ER–lipid droplet tethering. *J. Cell Biol.* **218**, 1089–1091 (2019).

81. Wang, C.-W. Lipid droplets, lipophagy, and beyond. *Biochim. Biophys. Acta - Mol. Cell Biol. Lipids* **1861**, 793–805 (2016).

82. MCGinnis, L. K., Pelech, S. & Kinsey, W. H. Post-ovulatory aging of oocytes disrupts kinase signaling pathways and lysosome biogenesis. *Mol. Reprod. Dev.* **81**, 928–945 (2014).

83. Alam, M. H. & Miyano, T. Interaction between growing oocytes and granulosa cells in vitro. *Reprod. Med. Biol.* **19**, 13–23 (2020).

84. Sanchez-Lazo, L. *et al.* Fatty Acid Synthesis and Oxidation in Cumulus Cells Support Oocyte Maturation in Bovine. *Mol. Endocrinol.* **28**, 1502–1521 (2014).

85. Dunning, K. R., Russell, D. L. & Robker, R. L. Lipids and oocyte developmental competence: the role of fatty acids and β-oxidation. *REPRODUCTION* **148**, R15–R27 (2014).

86. del Collado, M. *et al.* Influence of bovine serum albumin and fetal bovine serum supplementation during in vitro maturation on lipid and mitochondrial behaviour in oocytes and lipid accumulation in bovine embryos. *Reprod. Fertil. Dev.* **28**, 1721 (2016).

87. del Collado, M. *et al.* Fatty Acid Binding Protein 3 And Transzonal Projections Are Involved In Lipid Accumulation During In Vitro Maturation Of Bovine Oocytes. *Sci. Rep.* **7**, 2645 (2017).

88. Pawlak, P., Malyszka, N., Szczerbal, I. & Kolodziejski, P. Fatty acid induced lipolysis influences embryo development, gene expression and lipid droplet formation in the porcine cumulus cells†. *Biol. Reprod.* **103**, 36–48 (2020).

89. Sanchez-Lazo, L. *et al.* Fatty Acid Synthesis and Oxidation in Cumulus Cells Support Oocyte Maturation in Bovine. *Mol. Endocrinol.* **28**, 1502–1521 (2014).

90. Dubeibe Marin, D. F. *et al.* Influence of l-carnitine on lipid metabolism of buffalo cumulus-oocyte complexes matured in either fetal bovine serum or fatty acid-free bovine serum albumin. *Theriogenology* **158**, 382–390 (2020).

91. Dunning, K. R., Russell, D. L. & Robker, R. L. Lipids and oocyte developmental competence: the role of fatty acids and β-oxidation. *REPRODUCTION* **148**, R15–R27 (2014).

92. DiStefano, M. T. *et al.* The Lipid Droplet Protein Hypoxia-inducible Gene 2 Promotes Hepatic Triglyceride Deposition by Inhibiting Lipolysis. *J. Biol. Chem.* **290**, 15175–15184 (2015).

93. Alberts, B. *et al. Molecular Biology of the Cell*. (W.W. Norton & Company, 2017). doi:10.1201/9781315735368.

94. Wu, Y.-K. & Fan, H.-Y. Revisiting ZAR proteins: the understudied regulator of female fertility and beyond. *Cell. Mol. Life Sci.* **79**, 92 (2022).

95. Jumper, J. *et al.* Highly accurate protein structure prediction with AlphaFold. *Nature* **596**, 583–589 (2021).

96. Povero, D., Johnson, S. M. & Liu, J. Hypoxia, hypoxia-inducible gene 2 (HIG2)/HILPDA, and intracellular lipolysis in cancer. *Cancer Lett.* **493**, 71–79 (2020).

97. Wilding, M. *et al.* Confocal microscopy analysis of the activity of mitochondria contained within the 'mitochondrial cloud' during oogenesis in Xenopus laevis. *Zygote* **9**, 347–352 (2001).

98. Zhang, Y.-Z. *et al.* Mitochondrial behavior during oogenesis in zebrafish: A confocal microscopy analysis. *Dev. Growth Differ.* **50**, 189–201 (2008).

99. Hill, J. H., Chen, Z. & Xu, H. Selective propagation of functional mitochondrial DNA during oogenesis restricts the transmission of a deleterious mitochondrial variant. *Nat. Genet.* **46**, 389–392 (2014).

100. Tworzydlo, W., Kisiel, E., Jankowska, W., Witwicka, A. & Bilinski, S. M. Exclusion of dysfunctional mitochondria from Balbiani body during early oogenesis of Thermobia. *Cell Tissue Res.* **366**, 191–201 (2016).

101. Castro, J. P., Jung, T., Grune, T. & Siems, W. 4-Hydroxynonenal (HNE) modified proteins in metabolic diseases. *Free Radic. Biol. Med.* **111**, 309–315 (2017).

102. Cheng, J.-M. & Liu, Y.-X. Age-Related Loss of Cohesion: Causes and Effects. *Int. J. Mol. Sci.* **18**, 1578 (2017).

103. Webster, A. & Schuh, M. Mechanisms of Aneuploidy in Human Eggs. *Trends in Cell Biology* vol. 27 55–68 (2017).

104. Jaffe, L. A., Norris, R. P., Freudzon, M., Ratzan, W. J. & Mehlmann, L. M. Microinjection of Follicle-Enclosed Mouse Oocytes. in 157–173 (2009). doi:10.1007/978-1-59745-202-1_12.

105. Xie, F., Timme, K. A. & Wood, J. R. Using Single Molecule mRNA Fluorescent in Situ Hybridization (RNA-FISH) to Quantify mRNAs in Individual Murine Oocytes and Embryos. *Sci. Rep.* **8**, 7930 (2018).

106. Yu, C. *et al.* BTG4 is a meiotic cell cycle–coupled maternal-zygotic-transition licensing factor in oocytes. *Nat. Struct. Mol. Biol.* **23**, 387–394 (2016).

107. Martin, M. Cutadapt removes adapter sequences from high-throughput sequencing reads. *EMBnet.journal* **17**, 10 (2011).

108. Dobin, A. *et al.* STAR: ultrafast universal RNA-seq aligner. *Bioinformatics* **29**, 15–21 (2013).

109. Anders, S., Pyl, P. T. & Huber, W. HTSeq--a Python framework to work with high-throughput sequencing data. *Bioinformatics* **31**, 166–169 (2015).

110. Love, M. I., Huber, W. & Anders, S. Moderated estimation of fold change and dispersion for RNA-seq data with DESeq2. *Genome Biol.* **15**, 550 (2014).

111. Korotkevich, G. *et al.* Fast gene set enrichment analysis. *bioRxiv* 60012 (2021) doi:10.1101/060012.

112. Liberzon, A. *et al.* Molecular signatures database (MSigDB) 3.0. *Bioinformatics* **27**, 1739–1740 (2011).

113. Subramanian, A. *et al.* Gene set enrichment analysis: A knowledge-based approach for interpreting genome-wide expression profiles. *Proc. Natl. Acad. Sci.* **102**, 15545–15550 (2005).

114. Bai, D. *et al.* Genome transfer for the prevention of female infertility caused by maternal gene mutation. *J. Genet. Genomics* **47**, 311–319 (2020).

115. Luong, X. G., Daldello, E. M., Rajkovic, G., Yang, C.-R. & Conti, M. Genome-wide analysis reveals a switch in the translational program upon oocyte meiotic resumption. *Nucleic Acids Res.* **48**, 3257–3276 (2020).

116. Robinson, M. D., McCarthy, D. J. & Smyth, G. K. edgeR: a Bioconductor package for differential expression analysis of digital gene expression data. *Bioinformatics* **26**, 139–140 (2010).

117. Ritchie, M. E. *et al.* limma powers differential expression analyses for RNA-sequencing and microarray studies. *Nucleic Acids Res.* **43**, e47–e47 (2015).

118. Schneider, C. A., Rasband, W. S. & Eliceiri, K. W. NIH Image to ImageJ: 25 years of image analysis. *Nat. Methods* **9**, 671–675 (2012).

Magnetic tweezers and biopsy needles are capable of removing single chromosomes from meiotic spindles in mouse oocytes

Gerrit Altmeppen, Alexandre Webster, Melina Schuh

Abstract

When women get older, the quality of oocytes decreases. Aged oocytes exhibit decreased developmental competence due to higher incidences of aneuploidy. Social freezing and the use of donated oocytes from younger women are the favored options for women to conceive children at advanced ages. There is no tool available to repair aneuploidy in oocytes in assisted reproductive techniques. In this study, we aimed to establish a system that allows for the manipulation of single chromosomes within isolated living oocytes. We present two main approaches to manipulate individual chromosomes within meiotic spindles. In the first approach, magnetic tweezers were designed to guide magnetic microspheres to the chromosomes and displace a chromosome once it is bound. Secondly, we designed small glass needles for the use as biopsy needles to aspirate single chromosomes from oocytes, treated with monastrol. Altogether, this study lays the foundation for tools that allow for the precise control of single chromosomes in oocytes.

Introduction

Before an egg and a sperm fuse and form a zygote, the set of chromosomes is halved. In humans and mice, meiosis segregates the chromosomes. If an abnormal number of chromosomes remains in the egg, the state is called aneuploidy. Aneuploidy is common in human eggs and the prevalence increases when women age[1]. Until today, no method is available for fixing the chromosome segregation effects in human and mouse eggs[2]. One potential solution would be to artificially take control of the chromosome segregation.

In a long-term perspective, artificial solutions for the segregation of chromosomes will help to overcome problems of aged oocytes in IVF medicine. Moreover, solid techniques that allow the precise manipulation of chromosomes will facilitate the research on causes and prevention of aneuploidy.

Manipulation techniques for the *in vivo* manipulation of chromosomes require full controllability and real-time feedback. This can only be achieved by a continuous observation of the chromosome localization and movement inside the oocyte. Laser microscopes are a suitable tool to visualize chromosomes and the cellular environment[3].

Previous studies established four different microscope-based approaches to manipulate chromosomes in live cells[4–7]: optical tweezers to trap single chromosomes[4], laser scissors to cut chromosomes and microtubules[5], magnetic tweezers to guide chromosomes over large distances[6] and direct manipulation by glass needles to displace chromosomes inside the spindle or simulating pulling forces[7].

So far, no system has been reported which is compatible with mammalian oocytes and allows the precise maneuver of single chromosomes. Here, we present attempts to build a reliable setup that is capable of removing single chromosomes from an intact mouse oocyte. We tested various drugs to depolymerize cytoskeletal structures and tried to replace the magnetic needles of our previous setup by more robust ones. We also attempted to improve the field strength created by the magnetic needles. In parallel, we designed a microcontrolled system that involves glass capillaries. With this system, we prepared special glass needles which enabled us to successfully aspirate single chromosomes from monastrol-treated mouse metaphase I (MI) oocytes. For all techniques presented here, we were able to displace chromosomes within live cells in at least one experiment.

Results

2.8 µm microspheres moved chromosomes with low efficiency

In previous experiments that we conducted as part of a Mater's thesis, we established a magnetic tweezer system that successfully pulled chromosomes in mouse oocytes after nocodazole treatment (data not published)[8]. In brief, magnetic microspheres were coated with anti-H2B or anti-GFP antibodies to allow for the attachment to chromosomes. The oocytes were uninjected when anti-H2B antibody was used and injected with H2B-GFP when anti-GFP was used. The magnetic microspheres were injected into the oocyte after the coating with the respective antibodies. The oocytes were released from prophase arrest I and resumed meiosis. Metaphase I (MI) oocytes were transferred onto a confocal microscope that was equipped with micromanipulators. The micromanipulators were used to move magnetic needles and thereby displace the magnetic microspheres inside the oocytes. Because nocodazole caused the spindle to collapse, the system did not allow for the accessibility of single chromosomes. Therefore, in this study we aimed to use non-treated oocytes to achieve single chromosome sensitivity. Two technical problems arose during the experiments: first, microspheres with a diameter of 2.8 µm were not able to pass through the spindle and either diverted around the spindle or lost the mobility inside the spindle. Second, there was a low binding affinity between the 2.8 µm microspheres and the chromosomes. In 20% of the total number of experiments that were performed, the 2.8 µm microspheres moved through the spindle and were close to the chromosomes for several minutes but did not attach, as indicated by 2.8 µm microspheres leaving the

spindle empty (Fig. 1A). Yet, in two out of fifty cases, a successful attachment of chromosomes to the 2.8 µm microspheres were observed. When attached, the microspheres with 2.8 µm diameter were able to displace a single chromosome within the spindle (Fig. 1B). The velocity of microspheres during the manipulation was heterogeneous: While some 2.8 µm microspheres moved with constant velocities, the velocity of other 2.8 µm microspheres was characterized by abrupt oscillations. The degree of heterogeneity of velocities increased when the 2.8 µm microspheres were located inside the spindle (Fig. 1C).

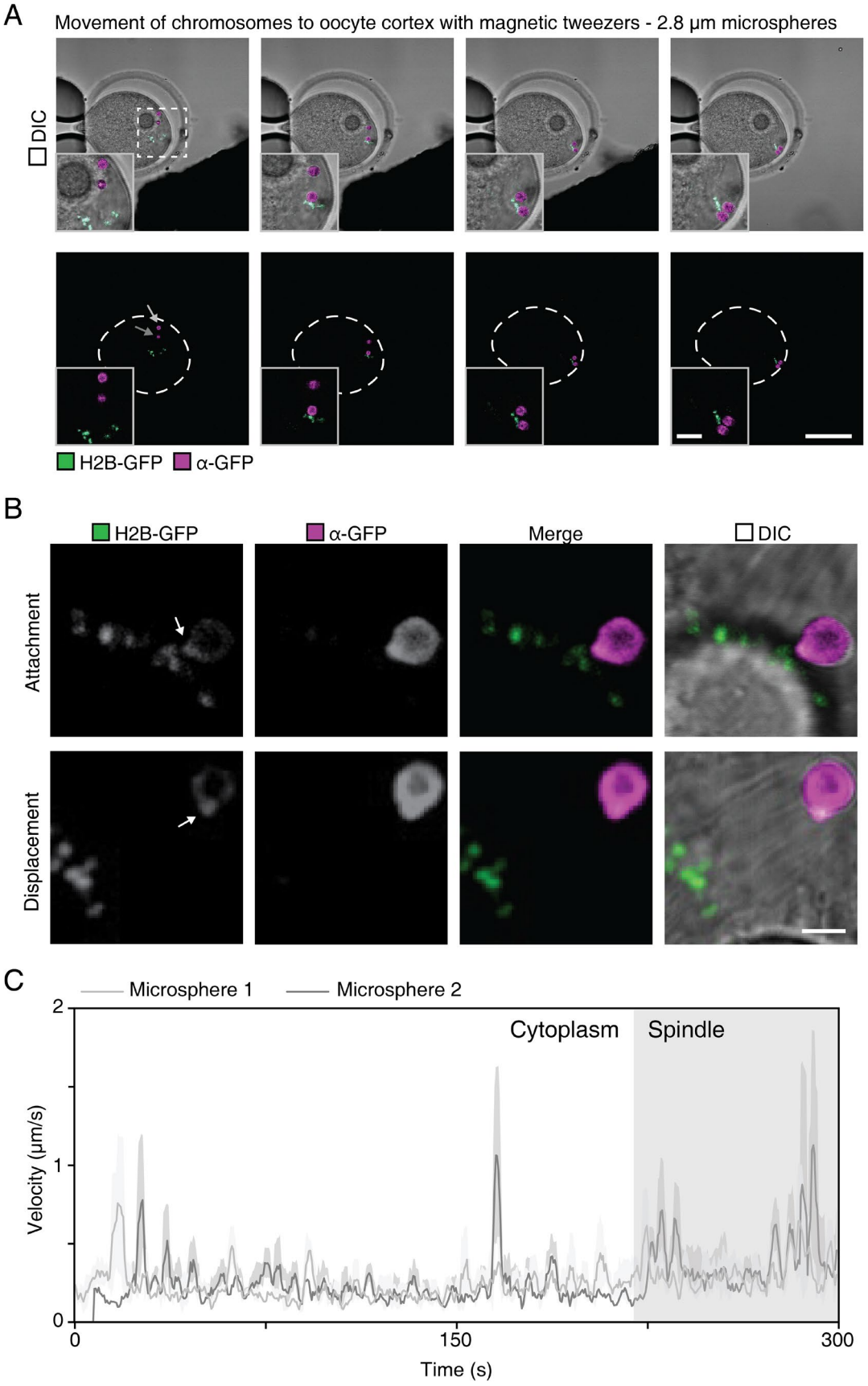

Fig. 1 2.8 µm microspheres are able to bind chromosomes fully intact meiotic spindles. (A) Time series of the displacement of microspheres with a diameter of 2.8 µm that were coated with α-H2B antibody and Alexa Fluor 647. Oocytes were previously injected with mRNA that encoded H2B-GFP which labels

chromosomes. The upper panels show the fluorescence signals (lower panels) merged with the transmitted light images. The dark structure at the bottom edge of the upper panels shows the needle of the magnetic tweezer. The inserts show a magnified image of the position of the microspheres and the chromosomes. Key frames were chosen to represent the time series that was acquired by the microscope. The dashed line represents the outline of the oocyte respective to the plasma membrane. The pale and the dark arrow indicate the two different microspheres that were analyzed for (C). Scale bar in outer panels 50 µm. Scale bar in insert 10 µm. (B) Two time points of the manipulation of a single microsphere that successfully attached to a chromosome. As in (A), the microspheres were coated with α-H2B antibody and Alexa Fluor 648 and the oocyte was previously injected with mRNA that encoded H2B-GFP in order to visualize the chromosomes. Autofluorescence of the microsphere is visible in the H2B-GFP channel. The attachment panel represents the incubation period in which the microsphere attached to the chromosome. The displacement panel represents the arrangement of the spindle, the chromosomes and the microsphere after the microsphere was pulled by the magnetic tweezer. In the DIC panels, the microtubules of the spindle are clearly visible. Scale bar 3 µm. (C) Analysis of the velocity of the two microspheres in (A). The two lines represent the velocity determined for each image of the time series. The dark line corresponds to the movement of the microsphere indicated by the dark arrow in (A) and the pale line represents the movement of the microsphere indicated by the pale arrow in (A). The shadows of both lines represent the standard deviation of the velocity in regard of the previous five time points. The white background represents the movement of both microspheres in the cytoplasm. The dark background represents the movements of the microspheres inside the spindle, indicating the velocity while penetrating the spindle.

1 µm microspheres penetrated the meiotic spindle without attachment to the chromosomes

We expected smaller 1 µm microspheres to penetrate the spindle with higher success rates. Therefore, we replaced the 2.8 µm microspheres that were used previously (data not published)[8] with 1 µm microspheres of identical magnetic properties and with the same coating. For these experiments, we additionally stained spindle microtubules with SiR-Tubulin as we expected that visualizing the spindle would increase the control we had of the tweezer set-up. Microspheres with a diameter of 1 µm successfully penetrated the spindle in 30% of all performed experiments. Although the penetration of the spindle was increased by 26%, the attachment of the microspheres to the chromosomes remained on the same level as for 2.8 µm microspheres (Fig. 2A). We only achieved a successful attachment of the microspheres to the chromosome and the subsequent displacement of the bound chromosome in one out of fifty oocytes. However, the revised tweezer system was unable to remove the chromosomes from the spindle (Fig. 2B). Interestingly, the velocity of the microspheres with a diameter of 1 µm was observed to be more homogenous than 2.8 µm microspheres. Especially when the 1 µm microspheres were located inside the spindle, we found a constant velocity and linear response to the external magnetic field (Fig. 2C).

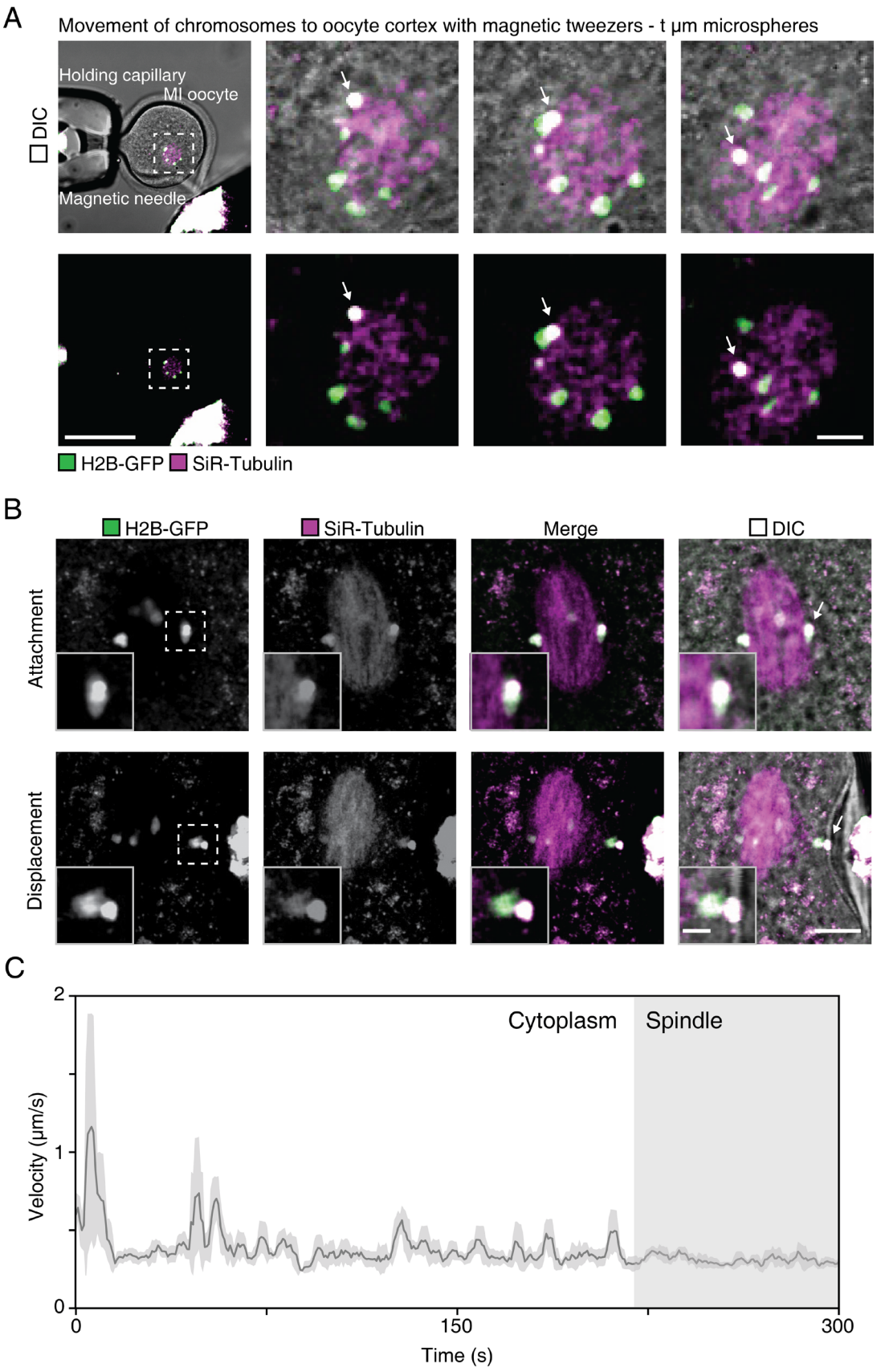

Fig. 2 1 µm microspheres penetrate fully intact meiotic spindles but rarely bind to the chromosomes. (A) Time series of the displacement of microspheres with a diameter of 1 µm that were coated with α-H2B antibody. The oocyte was incubated in medium supplied with SiR-Tubulin to visualize the spindle with the 644 nm laser. The oocyte was previously injected with mRNA that encoded H2B-GFP in order to

visualize the chromosomes. Autofluorescence of the microsphere is visible in both the H2B-GFP and the SiR-Tubulin channel, thus the microsphere appears white. The upper panels show the fluorescence signals (lower panels) merged with the transmitted light images. The dark structure at the bottom edge of the upper-left panel shows the needle of the magnetic tweezer. The corresponding fluorescence panel shows bright white signal. The microsphere is indicated by the white arrow. Scale bar of the left panel 50 µm. Scale bar of the right panel 10 µm. (B) Two time points of the manipulation of a single microsphere that successfully attached to a chromosome. As in (A), the microspheres were coated with α-H2B antibody and the oocyte was previously injected with mRNA that encoded H2B-GFP in order to visualize the chromosomes. Autofluorescence of the microsphere is visible in both the H2B-GFP and the SiR-Tubulin channel, thus the microsphere appears white. The inserts show a magnified image of the position of the microsphere and the chromosome that was displaced. The attachment panel represents the incubation period in which the microsphere attached to the chromosome. The displacement panel represents the arrangement of the spindle, the chromosomes and the microsphere after the microsphere was pulled by the magnetic tweezer. The structure that shows strong signal in both channels is the needle tip of the magnetic tweezer. The plasma membrane between the microsphere and the needle tip is clearly visible in the transmitted light. The microsphere that attached to a chromosome is indicated by the arrow in the last panel. Scale bar in outer panels 20 µm. Scale bar in insert 2 µm. (C) Analysis of the velocity of the microsphere in (A). The line represent the velocity determined for each image of the time series. The microsphere is indicated by an arrow in (A). The shadow represents the standard deviation of the velocity in regard of the previous five time points. The white background represents the movement of the microsphere in the cytoplasm. The dark background represents the movements of the microsphere inside the spindle.

Monastrol treatment does not prevent the collapse of the spindle when nocodazole is added

Because the chromosomes were poorly accessible inside the meiotic spindle, we sought for treatments that made the chromosomes more accessible. We focused on two drugs that alter the shape of the spindle: nocodazole and monastrol. Nocodazole binds tubulin monomers and prevents the polymerization of microtubules. Therefore, nocodazole's net effect is the depolymerization of microtubules[9]. Monastrol inhibits the kinesin Eg5 that maintains bipolarity in the meiotic spindle and therefore causes the spindle to become monopolar[10,11].

We tested monastrol in an attempt to further increase the accessibility of single chromosomes. Monastrol resulted in a monopolar spindle in which the chromosomes were exposed to the cytoplasm. Since the experiments of Fig. 2 indicated strong retraction forces of the microtubules on the chromosomes, we tested a sequential treatment of monastrol and nocodazole. Monastrol treatment alone did not reduce the retraction force of the spindle (data not shown). It was expected that subsequent addition of nocodazole would lead to the dispersion of single chromosomes into the cytoplasm. Yet, the spindle collapsed in the presence of monastrol, similarly to the nocodazole-only treatment (Fig. 3).

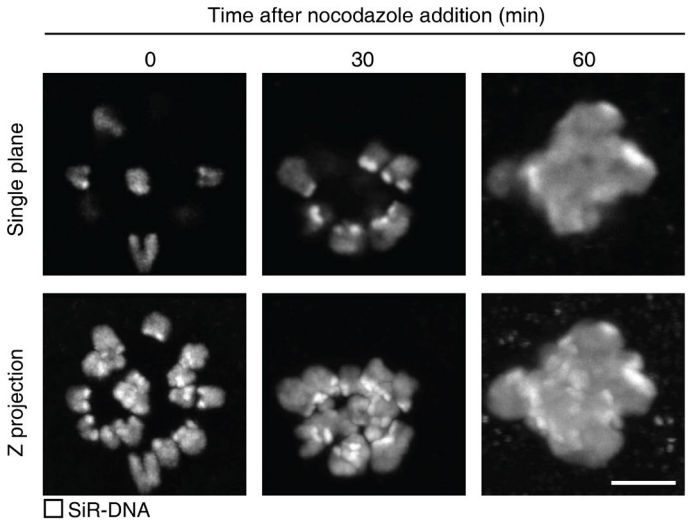

Fig. 3 Nocodazole causes the collapse of the spindle in monastrol-treated oocytes. The oocytes were incubated with SiR-DNA to visualize the chromosomes. 4 h after the release of the oocytes, monastrol was added to the medium for 1 h before a z stack of a spindle was acquired. Then, nocodazole was added and more z stacks were acquired after 30 and 60 min. The bottom panels show the projection along the z axis. Scale bar 5 µm.

Neodymium magnets exert significant forces on microspheres while electromagnetic tweezers do not

To further refine our system, we additionally tested whether solenoid magnets had the capacity to overcome the retraction forces of the spindle. In general, electromagnets, i.e. solenoid magnets, generate a controllable magnetic field that increases linearly with the electric current. Because of the correlation between electric current and magnetic field strength, the maximum magnetic field strength of solenoids is exclusively limited by the heat that is being produced by the electric current. We compared the solenoid system to the neodymium-based magnetic needle used for the experiments in Fig. 1 and Fig. 2. Both systems were compared with regards to the responsiveness of magnetic microspheres in 0.05% agarose droplets to the external magnetic field. Interestingly, the microspheres rearranged in vertically oriented stacks within 0.05% agarose droplets when a magnetic field was applied. The neodymium system was able to turn the stacks of microspheres by up to 90°. However, the neodymium system could not perform the exhaustive reorientation of stacks by 360°. It appeared that the stack flipped back when the magnetic tip was moved over the droplet (Fig. 4A). The solenoid system was not able to move the microspheres at all. We performed a second *in vitro* test to measure the final strength of the magnetic field. The neodymium system was able to magnetize the microspheres and attract the stacks towards the tip. The solenoid system was not able to form stacks or attract microspheres (Fig. 4B). The maximum velocity of microspheres attracted by the neodymium magnet was significantly higher than the maximum velocity of microspheres attracted by the solenoid (Fig. 4C).

Therefore, the solenoid system was not suitable to improve the magnetic tweezer system.

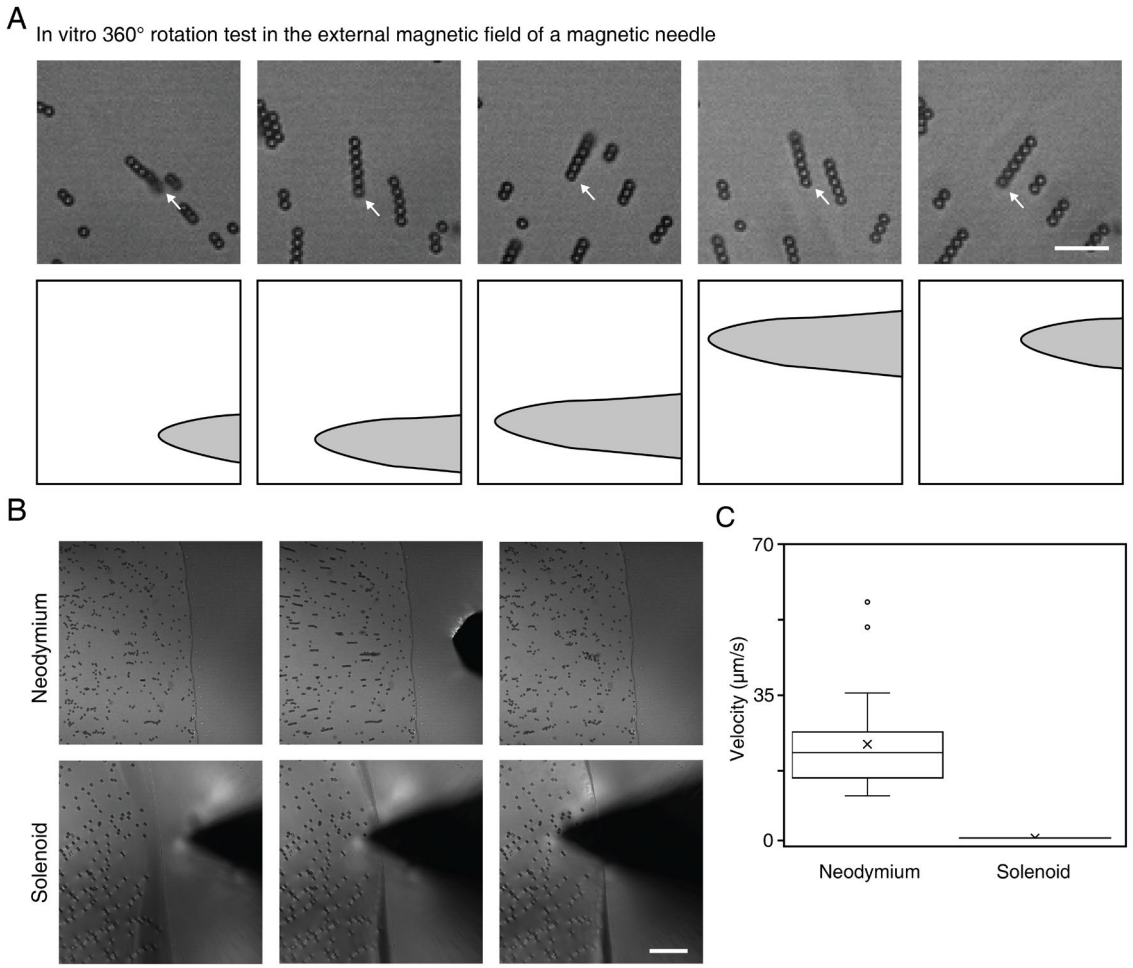

Fig. 4 Magnetic needle lacks full accessibility and electromagnetic tweezers are incapable to displace microspheres. (A) Time series of the *in vitro* test of the response of the microspheres to the magnetic tweezer set-up. The microspheres were dissolved in 0.05% agarose and installed on the magnetic tweezer set-up. In an external magnetic field, the microspheres formed elongated stacks. The upper panels show the position of a representative stack. One end is indicated by an arrow. The lower panels illustrate the position of the magnetic needle. The magnetic needle was moved clockwise in the time series. Scale bar 10 µm. (B) Quantitative *in vitro* test of the response of the microspheres to the magnetic tweezer set-ups. Upper panels show the distribution of the microspheres in 0.05% agarose before the magnetic needle was moved close to the droplet, while the needle is close to the droplet and after the needle was removed. The magnetic needle was attached to neodymium rods. The lower panels show the distribution of the microspheres in 0.05% agarose while the magnetic needle was moved closer to the droplet. The needle was attached to a solenoid powered by 8 A. Scale bar 50 µm. (C) Quantification of the velocity of representative microspheres in (B). The displacement of the microspheres was measured between different time points in which the magnetic needle was moved to the droplet and divided by the temporal difference of both time points. n = 50.

Small magnetic tips can be moved with high precision and do not attract magnetic microspheres

Since none of the tested systems allowed for reproducible control over single chromosomes and the detachment from the spindle, we considered optical tweezers to generate sufficient force to remove single chromosomes from the microtubules. However, optical tweezers are limited to small distances and therefore require the microspheres to be proximal to the chromosomes at the time of manipulation. One possibility to bring the microspheres close to the chromosomes was to inject the microspheres close to the chromosomes. To inject the microspheres in close proximity of the chromosomes, the chromosomes must be fully condensed and accessible in the cytoplasm. Beneficial conditions were hence met when the injection was performed after germinal vesicle breakdown (GVBD). However, injection of microspheres into oocytes that passed germinal vesicle breakdown led to low survival rates of the oocytes. For this reason, we chose to inject microspheres into oocytes in the germinal vesicle (GV) stage for all the experiments shown. The drawback of the injection of microspheres into GV oocytes was the random distribution of the microspheres after GVBD. To counteract the effect, we designed magnetic tips with low magnetic field strength and high controllability to establish a system that reliably mobilizes the microspheres to chromosomes without having to pull the chromosomes. To ensure sufficient control over the movement, we needed a sharp tip that allowed a sensitivity of a few micrometers. The first system consisted of a glass needle with an inner diameter of 10 µm. The needle was filled with ferromagnetic microspheres up to a total length of 50 µm and was then positioned near the oocyte to guide the intracellular microspheres. However, the system was not able to move intracellular microspheres (Fig. 5A). In a second approach to make our own magnetic tips with a low magnetic field, we cut magnetized nickel sheets with a thickness of 10 µm to obtain sharp tips. The magnetized nickel sheets were attached to neodymium rods. While this set-up was able to direct intracellular microspheres, it did not enhance the level of control we had over the motion. The tips of the cut sheets were irregularly shaped and did not show a pointy tip in which the magnetic field was focused (Fig. 5B). A different approach to bring the microspheres in proximity of the chromosomes was to centrifuge the injected oocytes. Based on the knowledge that centrifugation concentrates lipid droplets and vesicles on one side of the oocyte, we proposed that the spindle locates to this side,

too[12,13]. Indeed, the spindle re-located to one side. However, the microspheres were not affected by the centrifugation and remained at their previous position (Fig. 5C).

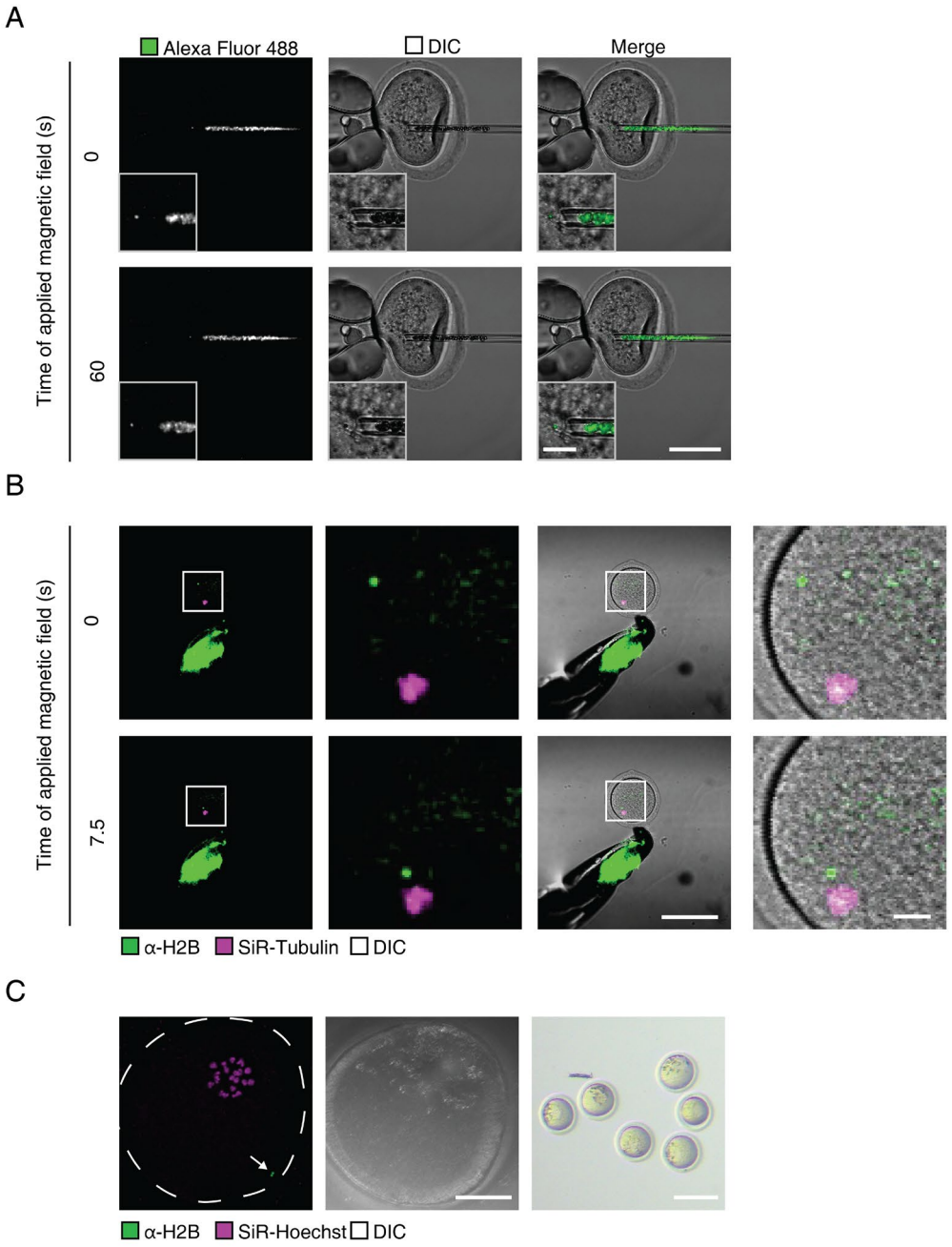

Fig. 5 High precision magnetic tweezer set-ups either lack force or controllability. (A) Two time points of the displacement of a 1 µm intracellular microsphere that had super-paramagnetic characteristics with a micromagnet that consisted of a glass needle that was filled with ferromagnetic microspheres. To visualize the microspheres in laser-scanning microscopy, all microspheres were coated with Alexa Fluor 488 prior to use. The inserts show magnified images of the intracellular microsphere and the needle tip. Scale bar in outer panels 50 µm. Scale bar in insert 5 µm. (B) Two time points of the displacement of a 1 µm intracellular microsphere by a sharp tip of a nickel sheet with a thickness of 10 µm. The left panels show fluorescent signal. The right panels show both fluorescent signal and transmitted light. Microspheres with a diameter of 1 µm were coated with α-H2B antibody and Alexa Fluor 488. The oocyte was incubated in medium supplied with SiR-Tubulin to visualize the spindle with the 644 nm laser. The second and fourth panel (left to right) show magnified versions of the first and third panel. The respective

area is indicated by a white square. The nickel sheet shows strong autofluorescence in the green channel. Scale bar of the first and third panel 100 µm. Scale bar of the second and fourth panel 10 µm. (C) Confocal microscopy images (left and middle) of an oocyte that was injected with a 1 µm microsphere and centrifuged for 5 min during metaphase I. The dashed line indicates the outline of the oocyte in regard to the plasma membrane. The white arrow indicates the position of the microsphere. The 1 µm microsphere was coated with α-H2B antibody and Alexa Fluor 488 prior to injection. The oocyte was stained with SiR-DNA (DNA) prior to image acquisition. Scale bar 20 µm. Wide-field stereoscope image (right) of multiple uninjected oocytes after centrifugation for 5 min. Lipid droplets (dark spots inside the oocytes) are concentrated on one side of each oocyte. Scale bar 100 µm.

Glass capillaries aspirate single chromosomes from monastrol-treated MI mouse oocytes and cause developmental arrest

Since none of the tested systems described in the previous sections was able to guide intracellular microspheres adjacent to the chromosomes, we turned our focus to the use of invasive methods to allow for the successful and reproducible removal of a single chromosome from an oocyte. We adapted the magnetic tweezer set-up as follows: Instead of trying to move microspheres with magnets, we tried to displace them by direct fixation on the tip of a glass needle. Glass needles were designed accordingly with a diameter smaller than the mean diameter of the intracellular microspheres. Upon the application of negative pressure, we were able to fix the microspheres inside the tip of the glass needles. We then positioned the glass needle with the fixed microsphere in proximity of the chromosomes and incubated to allow for attachment of the anti-H2B antibodies on the surface of the microspheres to the respective H2B of the chromosomes. However, the microspheres did not attach to the chromosomes and we could not control the release of the microspheres (Fig. 6A). Next, we hypothesized that direct aspiration of chromosomes would result in a reliable method to remove chromosomes from an oocyte. Because chromatin is fragile and our method aims to produce eggs that are capable to form healthy offspring, we chose a design in which the chromosomes are protected from damage during the removal from the oocyte. In this study, the formation of karyoplasts was investigated as protective agent for the integrity of the chromosomes. Karyoplasts are portions of genetic material inside a plasma membrane-surrounded container of small size and they are generated by an experimenter[14,15]. As a proof-of-principle, we tested the displacement of a whole spindle. It was possible to aspirate the whole spindle from monastrol treated oocytes into a karyoplast. The spindle collapsed inside the glass capillary and aggregated chromosomes were released back into the cytoplasm (Fig. 6B). In subsequent experiments, we were able to remove single chromosomes from monastrol treated oocytes and successfully recovered them as an intact karyoplast while maintaining the integrity of the spindle (Fig. 6B). Oocytes that had undergone the direct removal of a chromosomes did not return to a functional meiosis after the removal of monastrol.

Instead, the oocytes arrested in metaphase I. We additionally observed a continuous cytoplasmic flow in live cell microscopy (Fig. 6C).

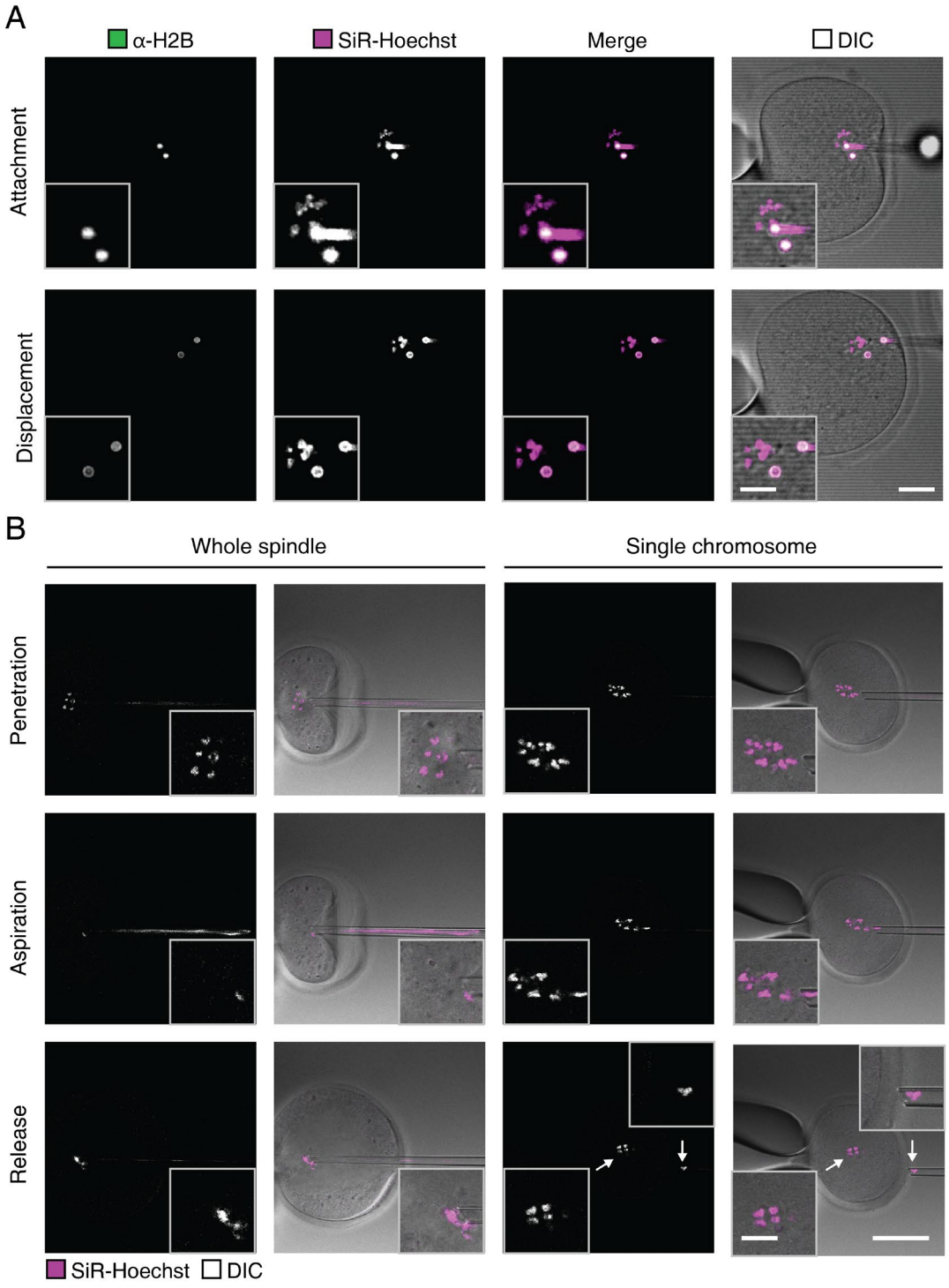
A
α-H2B
SiR-Hoechst
Merge
DIC
Attachment
Displacement
B
Whole spindle
Single chromosome
Penetration
Aspiration
Release
SiR-Hoechst
DIC
C
0 h
7 h

Fig. 6 Aspiration of karyoplasts allows the removal of single chromosomes but impairs oocyte maturation. (A) Two time points of the manipulation of a single microsphere that successfully attached to a chromosome. Microspheres with a diameter of 1 µm that were coated with α-H2B antibody and Alexa Fluor 488. The oocyte was incubated in medium supplied with SiR-Hoechst to visualize the chromosomes with the 644 nm laser. Autofluorescence of the microsphere and the glass needle is visible in the SiR-Hoechst channel. The attachment panel represents the incubation period in which the microsphere attached to the chromosome. The displacement panel represents the arrangement of the spindle, the chromosomes and the microsphere after the microsphere was displaced. The inserts show magnified images of the intracellular microspheres and the needle tip. Scale bar in outer panels 20 µm. Scale bar in insert 5 µm. (B) Three time points of the removal of chromosomes as karyoplasts. The first time point shows the arrangement of the glass needle and the chromosomes after the penetration of the zona pellucida. The second time point shows the uptake of chromosomes inside the needle. The third time point shows the release of the chromosomes. The oocyte was incubated in medium supplied with SiR-Hoechst to visualize the chromosomes with the 644 nm laser. The glass needle shows weak autofluorescence in the fluorescent images. The autofluorescence is distinguishable from the strong signal of the chromosomes (e.g. aspiration of whole spindle). The transmitted light images are merged with the fluorescence images. The inserts show magnified images of the chromosomes and the needle tip. The left panel shows the process of the aspiration of a whole spindle. The right panel shows the process of the aspiration of a single chromosome. The arrows in the bottom panels indicate the single chromosome that was removed (right) and the remaining chromosomes in the spindle (left). Scale bar in outer panels 50 µm. Scale bar in insert 5 µm. (C) Two time points and cytoplasmic flow analysis of an overnight study of oocytes after the removal of a single chromosome. Images were taken immediately after the removal of the chromosome and after 7 hours under physiological conditions. The cytoplasmic flow was analyzed and illustrated by multiple trajectories of cytoplasmic granules. Blue indicates early time points. Red indicates late time points. Scale bar 20 µm.

Discussion

In this study, we aimed to develop a new technique to remove single chromosomes from a mouse oocyte. Neither the magnetic tweezer approaches that we tried nor the aspiration of a single chromosome by a glass capillary worked reliably.

Magnetic tweezers are superior with regards to minimal invasiveness: The only invasive steps is the injection of the microspheres and the aspiration of a single chromosome. Magnetic fields do not harm cells[16]. Optical tweezers are also non-invasive[17]. However, photo-damage and heating have been reported as potential negative side effects when optical tweezers are used in live cell experiments on HeLa cells[18]. Despite the potential damage, successful manipulation of intracellular structures in live cell experiments have been described previously[19]. Optical tweezer applications are limited to a small spatial frame as the objectives used have a high magnification and the maximum deflection of the trapping laser is limited by the galvano elements of the scan unit. It remains a challenging task to increase the field of view for optical tweezer set-ups[20]. In order to be able to use optical tweezers, the microspheres and the chromosomes would have to be in close proximity to each other first. In this study, we built on our experience with magnetic tweezer set-ups and aimed to design a

magnet that allows to move magnetic microspheres precisely to the chromosomes and to subsequently remove the bound chromosomes.

We found that magnetic tweezers do not allow for a sufficient degree of control over the injected microspheres to remove single chromosomes. Our second approach, the aspiration of chromosomes by glass capillaries, seems to be too damaging to the oocyte. As an alternative to our approaches, advanced optical tweezer set-ups could be able to overcome the problems of invasiveness and the lack of control, since optical tweezers can produce higher forces than magnetic tweezers when the trapped objects are displaced[21]. Professionally engineered 3D magnetic tweezers are another alternative that could ensure more control than our inferior attempts.

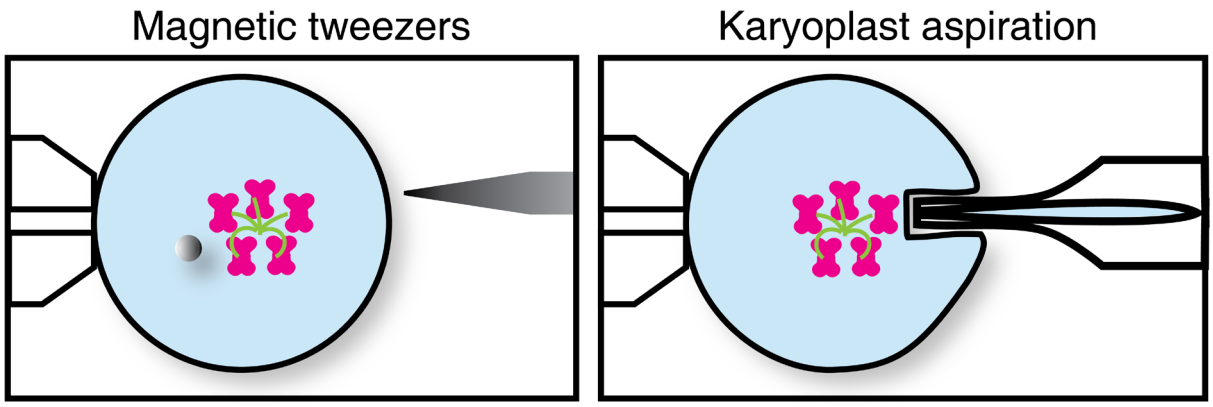

Fig. 7 While magnetic tweezer lack sensitivity to guide microspheres to the chromosomes, glass needles combine unlimited force and sufficient sensitivity to remove single chromosomes. Schematic figure that shows the two categories of manipulation approaches. The first set of experiments was done with magnetic tweezers that consisted of previously injected magnetic microspheres and magnetic tips attached to micromanipulators. The second set of experiments was based on open glass needles that were attached to adjustable pumps to apply positive and negative pressure. The chromosomes and microtubules were stained with live cell compatible dyes and monastrol was added to create a monopolar spindle that facilitated the access to the chromosomes.

Materials and Methods

Animal handling and isolation of oocytes

All animals were housed in a pathogen-free environment with *ad libitum* access to water and food, according to the guidelines of the MPI-bpc animal facility and in compliance with the German Law on Animal Welfare. CD1 mice were maintained as in-house breeding colony and non-mated female mice were sacrificed at an age of 7-10 weeks. The ovaries were removed. The oocytes were isolated and kept at 37°C under mineral oil in homemade M2 medium supplemented with 250 µM dbcAMP (Sigma; D0627) to maintain prophase arrest.

Injection of mRNA

H2B-GFP mRNA was prepared using the HiScribe T7 ARCA mRNA Kit (NEB) including ARCA-capping and poly(A) tailing. For the injection of oocytes, a homemade chamber was used as described previously[22]. In brief, we used a plastic chamber with coverslips mounted and sealed by Baysilon grease (GE Bayer Silicones) on its outer walls. On the inner side of one of the coverslips a small piece of double-sided tape was mounted and a small piece of another coverslip was attached on the other side of the tape, forming a "shelf" with a height of about 100 µm. The chamber was filled with M2 medium supplemented with dbcAMP and placed on a custom-made stage on a Zeiss Axio Vert.A1 inverted microscope using a 20x Air objective. Oocytes were transferred into the "shelf" and an injection needle was prepared.

Glass capillaries with an inner diameter of 1 mm were siliconized to reduce interactions with mRNA. For this, capillaries were dipped into Sigmacote solution (Sigma; SL2) so that a few microliters were taken up by capillary force. Then, the capillaries were inverted multiple times to ensure the complete coating of the inner wall. Excessive solution was removed by paper towels and gentle tapping. Capillaries were dried for at least two weeks before pulling. Homemade injection needles were prepared by pulling glass capillaries with 1 mm inner diameter in a P-97 needle puller (Sutter instruments) to obtain a 0.5 cm long taper. Then, 1 – 5 µL mercury were filled into the tip by backloading. Needles were attached to a capillary holder (Eppendorf) connected to a CellTram Oil (Eppendorf). The tip of the injection needle was broken off by gently moving against the wall of a glass capillary. Excessive air was released, then mineral oil (Sigma; M5310) was taken up to prevent direct contact with the mercury, followed by 10 pL mRNA solution and 3 µL mineral oil to prevent the mRNA solution from mixing with medium. The injection needle was gently moved into the oocytes and the front oil and mRNA solution were injected. Afterwards, oocytes were incubated for 3 – 5 h to allow for expression of the construct.

Preparation of microspheres

For 2.8 µm microspheres, Dynabeads Protein G (Thermo Fisher; 10003D) were used. For 1 µm microspheres, Dynabeads MyOne Streptavidin T1 (Thermo Fisher; 65601) were used. Microsphere slurry was homogenized and 10 µL were transferred into a tube with 500 µL PBS. The tube was inverted multiple times and then placed on a magnetic rack. After 1 min, the supernatant was carefully removed and another 500 µL of PBS was added. The tube was removed and inverted again. Three washing steps were performed, to remove any traces of sodium azide from the microsphere slurry. For *in vivo* displacement experiments, the microspheres were coated with antibodies first. 2.8 µm microspheres were incubated with 10 µL α-H2B antibody solution (Abcam; ab134211) for 1 h at 4°C on a spinning wheel. Microspheres were separated on a magnetic rack and the supernatant of the antibody solution was removed. Antibody

solutions were reused for up to three batches of microspheres. Subsequently, microspheres were washed three times as described above. For 1 µm microspheres, 10 µL α-H2B antibody solution was biotinylated with the Pierce Antibody Biotinylation Kit for IP (Thermo Fisher; 90407) according to the manufacturer's protocol. In brief, 40-fold molar excess of NHS-PEG_4-Biotin was added to the antibody solution and incubated for 30 min at 4°C. Then a Zeba desalting column was equilibrated with equilibration solution provided by the manufacturer and the biotin/antibody-solution was loaded onto the column and centrifuged. The final solution of biotinylated antibody was added to 1 µm microspheres that were washed as described above and incubated for 1 h at 4°C on a spinning wheel. Microspheres were separated on a magnetic rack and the supernatant of the antibody solution was removed. Antibody solutions were re-used for up to three batches. Subsequently, microspheres were washed three times as described above. For experiments that involved the use of SiR-Tubulin or SiR-Hoechst, microspheres were reconstituted after the last wash step. The final reconstitution was done in volumes of 10 – 100 µL depending on the desired concentration. Microspheres were kept in PBS for up to one week at 4°C. Immediately prior to injection, microspheres were sonicated in a SONOREX sonication bath (Bandelin) for 5 min at 4°C and mixed before loaded into the injection needle.

For experiments that did not involve the use of SiR-Tubulin or SiR-Hoechst, microspheres were further functionalized with Alexa Fluor 488. In brief, the Alexa Fluor 488 Antibody Labeling Kit (Thermo Fisher; A20181) was used according to the manufacturer's protocol. The microspheres were then incubated with the Alexa Fluor 488 solution for 1 h on a spinning wheel. The microspheres were washed as described above and reconstituted in PBS. For experiments that involved H2B-GFP expressing oocytes in medium free of any live cell dye, the microspheres were stained with Alexa Fluor 647. The respective Alexa Fluor 647 Antibody Labeling Kit (Thermo Fisher; A20186) was used as described above.

Injection of microspheres

Microspheres were injected on an Axio Vert.A1 inverted microscope (Zeiss) using a DIC 40x Air objective (Zeiss). To facilitate the recognition of cellular structures and microspheres, the microscope was equipped with DIC filters (Zeiss) in the condenser and below the objective. Because of space limitations, a custom made metal frame (25.5 x 75.5 x 2 mm) was used under which a #1 coverslip was mounted and sealed using Baysilon grease (GE Bayer Silicones). Oocytes were kept under mineral oil in homemade M2 medium as described above. For the fixation of oocytes, either commercial holding needles (VacuTip II, Eppendorf) or homemade holding needles were used. Homemade holding needles were prepared by pulling glass capillaries with 1 mm inner diameter in a P-1000 needle puller (Sutter Instruments) to obtain a ca. 1 cm long taper. The taper was cut at an inner diameter of ca. 100 µm using a microforge.

After fire-polishing the tip, the holding needle was bent to an angle of ca. 30°. Holding needles were pre-filled with medium and connected to a CellTram Air pump (Eppendorf). For the injection of microspheres, homemade injection needles were prepared. Glass capillaries with an inner diameter of 1 mm were coated with poly-L-Lysine to prevent the attachment of microspheres to the capillary wall. For this, capillaries were dipped into poly-L-Lysine solution (Sigma; P4707) and coated as described for the coating of injection needles for the injection of mRNA solution above. Injection needles were pulled as described above. However, instrument-specific values were used to obtain a 0.5 cm long taper. Needles were bent as described above and back-loaded with the final microsphere solution using GELoader tips (Eppendorf). The injection needle was then connected to a FemtoJet 4i system (Eppendorf) using a capillary holder that was connected to a PiezoXpert system (Eppendorf). Both holding needle and injection needle were mounted on 5MO-202U micromanipulators (Narishige). The tip of the injection needle was broken by pushing the needle against the holding needle. Then, the air in the top of the injection needle was released by applying the highest pressure possible until all air was released. To obtain larger diameters of the opening, the tapers were moved inside the holding needle and set under tension by moving the injection needle vertically until a large part of the taper broke off. For the injection of microspheres, the diameter was adjusted to fit the average size of the respective microspheres. This was indicated by single microspheres becoming immobilized in the tip. The FemtoJet system was arranged so that a constant flux of solution was ensured. After one or more beads were immobilized in the tip, negative pressure was applied on the CellTram Air pump to capture a single oocyte. Then, the injection needle was moved into focus and pierced into the oocyte. For the release of microspheres, one or a few soft pulses by the PiezoXpert were applied. After the microspheres entered the cytoplasm, the injection needle was retracted and the oocyte was release from the holding needle.
After the injection, oocytes were kept in M2 medium supplemented with dbcAMP for 30-60 min. Then, oocytes were release into dbcAMP-free medium to trigger resumption of meiosis. Oocytes were incubated for 6-7 h to ensure the proper formation of the meiotic spindle and thereby declustering of chromosomes.

Oocyte treatment

If not stated otherwise, the oocytes were incubated in M2 medium supplied with 1 µM SiR-Tubulin (Spirochrome; SC002) or 1 µM SiR-Hoechst (Spirochrome; SC007), respectively, for 1 h prior to the imaging. The oocytes were kept in M2 medium supplied with the respective live cell dye during the imaging to maintain signal intensity. For overnight imaging, oocytes were kept in a #1 35 mm round glass bottom dish (MatTek; P35G-1.5-14-C) in 1 – 2 µL medium covered with mineral oil. For experiments involving monastrol, the oocytes were incubated in M2 supplied with 100

µM monastrol 1 h prior to the imaging. For experiments involving nocodazole, the oocytes were first imaged after monastrol treatement and then transferred into medium supplied with 100 µM monastrol and 1 µM nocodazole. For experiments that involved the centrifugation of oocytes, the oocytes were incubated with monastrol and SiR-Hoechst as described above and centrifuged for 5 min at 1,500 x g

Microscopy

All setups were mounted on a LSM800 system (Zeiss) based on an Axio Observer Z1 inverted microscope (Zeiss) equipped with an incubation box (Pecon; Zeiss) and TransferMan 4r micromanipulators (Eppendorf). To decouple vibrations from the handling of the joysticks, the control units were placed on separate custom-made holders. If not stated otherwise, oocytes were placed in #1 35 mm glass bottom dishes (MatTek) in M2 medium covered with mineral oil. The incubation box was set to 37°C and pre-warmed before the experiment. A 488 nm laser was used to illuminate GFP and Alexa Fluor 488, respectively, and a 647 nm laser was used to visualize SiR-Tubulin and SiR-Hoechst, respectively. Transmitted light was used to identify the outer boundaries of the oocyte as well as the magnetic tips or glass needles. Images were taken at the highest speed and shortest time interval rate possible.

Magnetic tweezer setup

The neodymium tweezer set-up consisted of two TransferMan 4r Micromanipulators. A capillary holder was attached and a holding needle (VacuTip II, Eppendorf) or homemade holding needle was mounted onto the capillary holder. 5 neodymium rods (Supermagnete; S-05-13-N) were aligned to form a long rod and inserted into the other micromanipulator. An iron sewing needle was ground with sandpaper of a grit size of 1000 to obtain a pointy tip. Metal swarf was removed and the needle was glued to the tip of the neodymium rod. The needle was replaced after 3 – 5 experiments as a result of oxidative damage to the tip.

Solenoid magnets were designed and assembled by the in-house electronics workshop. 50 – 500 turns of insulated copper wire with an iron core were prepared and the tip was designed to hold the custom-ground sewing needles. The solenoids were connected to a power supply unit and the maximum electric current was limited to 8 A. The solenoid tweezers were attached to the micromanipulators only before the experiment.

The micromagnet was assembled from a glass needle and ferromagnetic microspheres. The glass needle was pulled and broken as described above. Fluorescent Yellow Carboxyl Ferromagnetic Particles (Spherotech; FCFM-2052-2) were washed as described above and reconstituted in PBS. The microspheres were backloaded in the

glass needle and pushed to the tip by using the FemtoJet until the tip was filled with the microspheres.

For the magnetic sheet tweezer, magnetized nickel sheet (a gift of JFC GmbH) was cut using household scissors or dissection scissors and forceps. The tip was glued to the neodymium rod as described for the sewing needle.

Glass needle setup

For glass needle experiments, a pair of holding needle and injection needle was prepared as described above. The holding needle was pre-filled with M2 medium supplied with dbcAMP. The holding needle was attached to a CellTram Air (Eppendorf), and mounted onto a TransferMan 4r micromanipulator (Eppendorf). The injection needle was pre-filled with 1 µL PBS, either attached to a CellTram Air (Eppendorf) or to a CellTram Oil (Eppendorf) and mounted on a TransferMan 4r micromanipulator. The tip of the injection needle was broken as described above. For small openings, the tip was moved against the holding capillary. For openings larger than 0.5 µm, the injection needle was set under tension. The diameter was adjusted to the respective experiment. For the penetration of the plasma membrane, openings smaller than 1 µm were necessary. Prior to recording of an experiment, oocytes were identified through the eyepieces of the microscope and fixed by the holding needle applying gentle negative pressure via the air pump. Then, the injection needle was moved into focus and the imaging system was switched to confocal mode. The oocytes were fixed by the holding needle and the penetration of the zona pellucida was supported by the PiezoXpert with a series of soft pulses.

In vitro measurement of microspheres

The microspheres were washed as described above and reconstituted in PBS supplied with 0.05% agarose. The solution was immediately transferred onto the custom made metal frame attached to a #1 coverslip, covered with mineral oil and placed on the microscope. Time-lapse imaging was done and magnetic tips of permanent magnets and electromagnets were moved from 1 mm distance to the agarose droplet. The displacement was quantified in ImageJ.

Image analysis

The velocity of the microspheres was measured in Imaris (Bitplane). In brief, microscopy images were imported and virtual spheres were generated for the microspheres. Trajectories were calculated and the corresponding velocities were exported. For the cytoplasmic flow analysis, virtual spheres were generated for the cytoplasmic granules

and trajectories were calculated and mapped when a minimum length of 50% of the entire time series was given.

Authors' contribution

G.A. performed all experiments if not stated otherwise. A.W. injected H2B-GFP mRNA for experiments in which the DNA was not stained by a live cell dye. G.A. performed the analysis and quantification of all experiments. G.A. drafted the figures and the manuscript. A.W. provided critical comments on the study design. M.S. designed and supervised the study and proofread the manuscript.

Acknowledgments

The authors would like to thank Martina Daniel and Silke Schlott for technical support. We acknowledge the animal facility of the MPI-NAT and the animal caretakers for providing the mice and the in-house workshop for technical equipment and help with adaptations that were needed to design the set-ups used in this study. We would like to thank Sarah Köster and Charlotta Lorenz for discussions about the requirements for optical tweezer set-ups.

Funding

The study was funded by the Deutsche Forschungsgemeinschaft (DFG, German Research Foundation) under Germany's Excellence Strategy - EXC 2067/1-390729940, the Max Planck Society, the European Research Council under grant agreement 337415, the Lister Institute for Preventive Medicine and the DFG under a Leibniz Prize to M.S. (SCHU 3047/1-1).

Conflict of interest

The authors declare no conflict of interest.

References

1. Hassold, T. & Hunt, P. To err (meiotically) is human: the genesis of human aneuploidy. *Nat. Rev. Genet.* **2**, 280–291 (2001).
2. Ubaldi, F. M. *et al.* Advanced Maternal Age in IVF: Still a Challenge? The Present and the Future of Its Treatment. *Front. Endocrinol. (Lausanne).* **10**, 94 (2019).
3. Zhou, Y. *et al.* Painting a specific chromosome with CRISPR/Cas9 for live-cell imaging. *Cell Res.* **27**, 298–301 (2017).
4. Liang, H., Wright, W. H., He, W. & Berns, M. W. Micromanipulation of mitotic chromosomes in PTK2 cells using laser-induced optical forces ("optical tweezers"). *Exp. Cell Res.* **197**, 21–35 (1991).
5. Vorobjev, I. A., Liang, H., Wright, W. H. & Berns, M. W. Optical trapping for chromosome manipulation: a wavelength dependence of induced chromosome bridges. *Biophys. J.* **64**, 533–538 (1993).
6. Hong, J., Purwar, P., Cha, M. & Lee, J. Spatial control of chromosomal location in a live cell with functionalized magnetic particles. *Nanoscale* **7**, 19110–19117 (2015).
7. Li, X. & Nicklas, R. B. Mitotic forces control a cell-cycle checkpoint. *Nature* **373**, 630–632 (1995).
8. Altmeppen, G. Development of methods to decrease aneuploidy in mammalian oocytes (Master thesis).
9. Xu, K., Schwarz, P. M. & Ludueña, R. F. Interaction of nocodazole with tubulin isotypes. *Drug Dev. Res.* **55**, 91–96 (2002).
10. Maliga, Z., Kapoor, T. M. & Mitchison, T. J. Evidence that Monastrol Is an Allosteric Inhibitor of the Mitotic Kinesin Eg5. *Chem. Biol.* **9**, 989–996 (2002).
11. Kapoor, T. M., Mayer, T. U., Coughlin, M. L. & Mitchison, T. J. Probing Spindle Assembly Mechanisms with Monastrol, a Small Molecule Inhibitor of the Mitotic Kinesin, Eg5. *J. Cell Biol.* **150**, 975–988 (2000).
12. Cavazza, T. *et al.* Parental genome unification is highly error-prone in mammalian embryos. *Cell* **184**, 2860-2877.e22 (2021).
13. Arena, R. *et al.* Lipid droplets in mammalian eggs are utilized during embryonic diapause. *Proc. Natl. Acad. Sci.* **118**, e2018362118 (2021).
14. Tachibana, M., Sparman, M. & Mitalipov, S. Chromosome transfer in mature oocytes. *Nat. Protoc.* **5**, 1138–1147 (2010).
15. Wallace, D. C. & Chalkia, D. Mitochondrial DNA Genetics and the Heteroplasmy Conundrum in Evolution and Disease. *Cold Spring Harb. Perspect. Biol.* **5**, a021220–a021220 (2013).

16. de Vries, A. H. B., Krenn, B. E., van Driel, R. & Kanger, J. S. Micro Magnetic Tweezers for Nanomanipulation Inside Live Cells. *Biophys. J.* **88**, 2137–2144 (2005).

17. Ketelaar, T., de Ruijter, N. & Niehren, S. Optical Trapping in Plant Cells. in *Methods in Molecular Biology* vol. 1992 231–238 (Humana Press Inc., 2019).

18. Català, F., Marsà, F., Montes-Usategui, M., Farré, A. & Martín-Badosa, E. Influence of experimental parameters on the laser heating of an optical trap. *Sci. Rep.* **7**, 16052 (2017).

19. Ferraro-Gideon, J. *et al.* Measurements of forces produced by the mitotic spindle using optical tweezers. *Mol. Biol. Cell* **24**, 1375–1386 (2013).

20. Pitzek, M., Steiger, R., Thalhammer, G., Bernet, S. & Ritsch-Marte, M. Optical mirror trap with a large field of view. *Opt. Express* **17**, 19414 (2009).

21. Neuman, K. C. & Nagy, A. Single-molecule force spectroscopy: optical tweezers, magnetic tweezers and atomic force microscopy. *Nat. Methods* **5**, 491–505 (2008).

22. Jaffe, L. A., Norris, R. P., Freudzon, M., Ratzan, W. J. & Mehlmann, L. M. Microinjection of Follicle-Enclosed Mouse Oocytes. in 157–173 (2009). doi:10.1007/978-1-59745-202-1_12.

Final discussion

Loss of physical protection of maternal mRNAs impairs oocyte maturation and might cause aneuploidy which could be restored by manipulating the chromosomes of mammalian oocytes

In this thesis, we observed that maternal mRNAs in mouse oocytes are sequestered by a phase-separated structure we named Mitochondria-Associated RNP Domain in Oocytes (MARDO). We classify ZAR1 as the essential protein for the formation of MARDO. Physical sequestration into MARDO acts on both, stabilization of transcripts and translational silencing until MARDO dissolves upon GVBD. *Hig2* mRNA is one of the transcripts sequestered by MARDO. Because HIG2 protein represses fatty acid catabolism, MARDO indirectly stabilizes lipid droplets and reduces the mitochondrial activity[1]. We observed that oxidative damage accumulates in *Zar1*-KO oocytes. Oxidative stress could explain why previous studies have reported increased aneuploidy rates in *Zar1*-KO oocytes[2]. We present approaches to restore euploidy by the manipulation of single chromosomes. The combination of magnetic tweezers with magnetic microspheres enabled the successful removal of single chromosomes by glass capillaries from the meiotic spindle.

Membraneless organelles perform specific functions

Our results highlight that the protein Zygote arrest 1 (ZAR1) undergoes phase-separation in mouse oocytes (part I). To maintain confidentiality, we termed the protein MMSP in the abstract and in previously published texts. We assumed that the ZAR1 condensate performs a distinct function in mouse oocytes during growth and maturation.

In *in vitro* experiments, we observed the formation of droplets and *in vivo* Fluorescence Recovery After Photobleaching (FRAP) assays confirmed a liquid-liquid phase separation behavior (LLPS). Phase separation has been discussed controversially in recent publications and within the scientific community[3]. Yet, novel structures are identified and analyzed for LLPS behavior. The field of developmental biology has created a focus on phase separation recently[4]. Phase separation performs specific functions for within the cell[5]. Phase-separated structures are also called membraneless organelles[6]. For some membraneless organelles, the functions have been well described: besides the involvement in the transcription of ribosomal RNA, the nucleolus serves as site for protein quality control, especially under stress conditions[7]. Centrosomes mediate the nucleation of microtubules[8]. RNA particle (RNP) structures such as the Balbiani body, P granules, germ granules, the P body and stress granules sequester mRNAs under certain conditions and regulate the translation and

degradation[9–11]. For MARDO, we observed similar features of mRNA sequestering and translational control. Because the P body and stress granules have not been identified in mouse oocytes so far, it remains unclear if and how oocytes react to translational stress and if MARDO is involved in the regulation of stress[12]. The recently described liquid-like meiotic spindle domain (LISD) structure is oocyte specific, similar to MARDO. The LISD structure sequesters and regulates spindly assembly factors to stabilize the process of spindle assembly[13]. However, we observed that MARDO dissolved during meiosis. It is therefore unlikely that MARDO interacts with the spindle.

The interaction between membraneless condensates and membrane-bound organelles is yet to be understood

ZAR1 has been observed to bind and regulate maternal mRNAs[14,15]. Our studies confirm that ZAR1 co-localizes with mRNAs in the germinal vesicle (GV) oocyte. Interestingly, injection of RNase caused ZAR1 and mitochondria to form aggregated clusters. Therefore, we conclude that mRNAs buffer the phase-separation of ZAR1. We further confirmed this correlation by overexpression of *Zar1* in mouse oocytes, where we observe that an excess of ZAR1 molecules that are unbound to mRNAs increased aggregation of the condensates. The ratio between ZAR1 and mRNAs determines the thermodynamic properties of the LLPS structure. Nevertheless, most of the published LLPS structures consist of a large number of factors under *in vivo* conditions[16]. The structure formed by ZAR1 is no exception. The mRNA binding protein YBX2 (also called MSY2), the RNA helicase DDX6, parts of the RNA degradation signaling machinery (LSM14B and 4E-T) and especially mitochondria co-localize with the ZAR1 LLPS structures. The MARDO structure contains mitochondria. Therefore, our results imply the connection of membrane-bound organelles with membraneless organelles. Recent studies of phase-separated structures have begun to open a new area in the field of cell biology and have shown the interaction of RNP granules with membrane-bound organelles like mitochondria. A representative example is the interaction between P bodies and mitochondria in HeLa cells[17]. The reason for the interaction between RNP granules and mitochondria or the ER has remained elusive[18]. For some phase-separated condensates, evidence for membrane proteins that mediate the formation, stability, function and decay has been provided. For membrane-bound organelles, previous studies have shown the active transport by cytoskeletal networks[19,20]. Therefore, the interaction between membraneless and membrane-bound organelles has also been suspected to be a way of "hitchhiking" onto the membrane-bound organelles. While our studies report co-localization of ZAR1 with the condensates, no such co-localization was observed with the ER. We did not observe any directed movement of MARDO in living oocytes and therefore, we do not suspect the sequestered mitochondria to be involved in intracellular trafficking.

MARDO does not require excessive amounts of ATP

Our studies reveal the composition of MARDO and the function of the essential component ZAR1 on maternal mRNAs. Yet, our studies do not explain the function of mitochondria within MARDO. The majority of experiments dedicated to shed light onto the role of mitochondria in MARDO gave inconclusive results. Although we observed that *Zar1*$^{-/-}$ oocytes show mitochondrial hyperpolarization, we could not identify the role of the mitochondria that were sequestered by MARDO. Because the mitochondrial membrane potential is a consequence of the respiratory activity, mitochondrial hyperpolarization in oocytes that lack ZAR1 and MARDO suggests a role of ZAR1 and MARDO in the regulation of the mitochondrial respiration[21]. In line with the assumption of mitochondrial regulation, local translation was recently reported to happen on mitochondria[22,23]. In the reported cases, the local translation has been interpreted as regulatory mechanism for the maintenance of mitochondria by renewal of mitochondrial proteins[22]. We developed a model in which MARDO allows the local translation of mitochondrial proteins while the mitochondria are required to provide ATP that is necessary to maintain the translation. In addition to this model, ATP is consumed for the loading of tRNAs during local translation. Hence, we expect to find increased supply of ATP in MARDO. To investigate the localization of ATP inside an oocyte under live cell conditions, we used a live ATP reporter called AT1.03. AT1.03 contains the ε subunit of the bacterial F_oF_1-ATP synthase, and the fluorophores mVenus and mseCFP. Upon binding of ATP to the reporter, the ε subunit undergoes conformational changes and positions both fluorescent proteins in close vicinity, allowing Förster Resonance Energy Transfer (FRET)[24]. We expected the ATP concentration in MARDO to be either significantly higher than in the cytosol (excessive supply) or significantly lower (excessive consumption). We found that while the concentration of ATP inside the mitochondria is higher than in the cytosol, MARDO does not exhibit higher or lower ATP levels than the surrounding cytosol. Furthermore, mitochondria inside MARDO and in the cytoplasm exhibit similar signal intensities in the ATP concentration asasy. Two theoretical options can be described to fit our observations. Firstly, mitochondria could indeed be needed for the supply of ATP inside MARDO. However, either the consumption or the diffusion of ATP might happen so quickly that the reporter in combination with laser scanning microscopes is incapable of visualizing the gradient. Secondly, ATP might not be consumed in excessive amounts and the molecular processes in MARDO might not rely on the supply of ATP from mitochondria within the condensates. After all, no final conclusion can be drawn regarding the role of mitochondria within MARDO as special ATP suppliers.

MARDO does not serve as a structure for local translation on mitochondria

To further verify or falsify the model of local translation within MARDO, the amount of mitochondrial proteins was analyzed for mitochondria within MARDO and

mitochondria in the cytoplasm. We expected to detect differences in the composition of mitochondrial proteins. An extensive screen was performed to analyze the amount of several subunits of the F_oF_1-ATP synthase (ATP5E, ATP5E2, ATP5J, ATP5O, ATPIF5), proteins of the respiratory chain (UQCRQ, COX17, NDUFA3, NDUFA7, NDUFB5), mitochondrial pore proteins (TIMM17, TOMM6), and other mitochondria-associated proteins (PRDX AND FIS1) in mitochondria within MARDO and mitochondria in the cytoplasm. We observed no enrichment of any of these proteins for mitochondria that are located inside MARDO. We explain this lack of a qualitative difference by the continuous degradation of mitochondrial proteins and replacement by newly synthesized proteins from MARDO. To investigate global translational rates in MARDO, we performed two experiments were performed. The first one was discussed in the second part of this thesis, where L-homopropargylglycine (HPG) is incorporated into newly synthesized proteins and allows for the *in situ* visualization of translational sites when the oocytes were pulsed for a short time only ("pulse-chase"). The visualization of HPG shows reduced translation levels in *Zar1*$^{-/-}$ oocytes but co-staining with ZAR1 in WT oocytes does not show increased translation rates within MARDO. The second experiment on local translation was the visualization of polysomes. Polysomes are active sites of translation and characterized by concentrated actively translating ribosomes and the respective vicinity of the small and the large ribosomal subunit[25]. To identify and visualize polysomes, we used an assay called Proximity Ligation assay (PLA)[26]. In this method, the visualization of sites within a cell where many small and large ribosomal subunits are located in proximity of each other using fluorescence microscopy reveals the location of polysomes[27]. Preliminary data suggests no enrichment of polysomes in MARDO. Therefore, we conclude that translation does not take place within MARDO. The discovery of ribosomal exclusion is further discussed below. Also, the results imply that the model assuming that MARDO facilitates the re-loading of tRNA synthetases seems to be wrong. To confirm this further, we co-stained several tRNA synthesases (CARS, RARS, HARS) with ZAR1 in immunofluorescence experiments and we observed no co-localization.

In conclusion, local translation does not take place on mitochondria in MARDO and the protein composition and amount is unchanged for mitochondria sequestered in MARDO. The hyperpolarization of mitochondria could have been explained by the interaction of ZAR1 with respective proteins of the respiratory chain. Therefore, we analyzed the co-localization of ZAR1 with certain mitochondrial proteins to see whether MARDO might regulate the expression and/or function of mitochondrial proteins. To investigate the interaction between ZAR1 and mitochondrial proteins, we used the PLA protocol. We found no enrichment of interaction with ZAR1 in mitochondria inside MARDO compared with mitochondria in the cytoplasm. Furthermore, high resolution imaging reveals that ZAR1 localizes outside of mitochondria. We therefore propose that the sequestering of mitochondria does not

serve mitochondrial integrity but the integrity of MARDO. The hyperpolarization of mitochondria can be explained by the secondary effects of the loss of *Hig2* mRNA and further changes in the composition of the maternal mRNA pool. None of our observation was able to verify the idea that MARDO is a site for local translation. The function of mitochondria in the MARDO structure remains to be investigated. The hyperpolarization observed in *Zar1*$^{-/-}$ oocytes appear to be a downstream effect caused by the loss of maternal mRNAs rather than by the impaired function of mitochondrial proteins.

It remains to be tested whether MARDO might sequester mitochondria to suppress their activity and protect the oocyte from oxidative stress. For the Balbiani body, previous studies have suggested a sequestering function for "healthy" mitochondria with high membrane potential[28]. MARDO could serve the same purpose and additionally silence mitochondrial activity for the prolonged period that oocytes remain arrested for in mice and other mammals, including humans[29]. In that case, the Balbiani body would be a primitive version of MARDO that is stable in oocytes of invertebrates. The Balbiani body would not have to suppress mitochondrial activity and protect the oocyte from oxidative stress because invertebrates have the ability to undergo neo-oogenesis[30]. Because of this and with regards to the fact that invertebrates produce considerably higher numbers of offspring, oxidative damage is less severe in terms of evolutionary advantages for invertebrates.

ZAR1 does not directly interact with proteins of the mRNA decay or mRNA translation machinery

We tested another model in which we hypothesized that ZAR1 induces the mRNAs to fold and thereby to reduce the physical accessibility of the ribosomes. To test the model, we assumed a close proximity of various mRNA binding proteins (YBX2, DDX6 and PABPC1L) to each other. We used the PLA protocol to quantify and localize the interaction sites. No enrichment of interaction sites was observed in MARDO and no differences in the number of interaction sites were detected when comparing *Zar1*$^{-/-}$ and *Zar1*$^{+/+}$ oocytes.

Further models that we tested focused on the role of ZAR1 acting as translational repressor protein[2]. Translation of mRNAs is controlled by the length of the poly(A) tail[31]. Cytoplasmic polyadenylation is catalyzed by the poly(A) polymerase α (PAPOLA)[32]. PAPOLA is recruited by cleavage and polyadenylation specificity factor (CPSF)[33]. The poly(A) tail acts as protection against degradation and initiation of translation by the recruitment of Eukaryotic translation Initiation Factor 4 G (eIF4G) subsequently to the binding of the Poly(A) tail Binding Protein (PABP)[34]. Immunofluorescence co-staining of ZAR1 and any of the poly(A) related proteins did not show co-localization. Moreover, the interaction between the different proteins was

analyzed by the application of the PLA protocol on *Zar1*$^{-/-}$ and *Zar1*$^{+/+}$ oocytes but again, no difference was detected. However, 4E-T, LSM14B, DDX6 co-localized with ZAR1 in wildtype oocytes. All three proteins are involved in translational repression[35,36]. While the PLA experiments did not indicate any close interaction between any of the three proteins with ZAR1, the localization inside MARDO provides an explanation for the translational repression.

In addition to its role in translational repression, ZAR1 is known to stabilize maternal mRNAs. We demonstrated this effect by our smRNA-FISH experiments on various candidates, including Hig2. When MARDO is lost, as is the for *Zar1*$^{-/-}$ oocytes, maternal mRNAs were degraded. Our results are in line with previous reports[2]. The initial signal for mRNA degradation is the shortening of the poly(A)-tail[37]. The deadenylation and further decay of the 3' end is catalyzed by the exonuclease subunit of the carbon catabolite repression 4 (CCR4)-negative on TATA-less (NOT) complex[38]. Upon degradation of the poly(A)-tail, the decapping complex is recruited. The decapping complex consist of DCP1, DCP3, EDC4 and further auxiliary proteins[39,40]. We selected a set of proteins involved in the degradation of mRNAs (ZFP36L2, CNOT1, EDC4 and DCP2) and looked at their localization using immunofluorescence staining. None of the tested proteins involved in the degradation of mRNAs co-localizes or interacts with ZAR1. That finding indicates that ZAR1 is no direct suppressor of mRNA decay. Therefore, we investigated whether MARDO's physical properties stabilize the mRNAs sequestered inside MARDO.

MARDO provides a structure to physically sequester mRNAs from translation and decay

Fluorescence *In Situ* Hybridization (FISH) of Oligo dT probes indicates an enrichment of mRNA in MARDO. Previous reports on the effects of *Zar1*-KO on maternal mRNAs focused on the relative level of mRNAs[2]. The most common techniques for quantitative RNA analysis are quantitative PCR (qPCR) and RNA sequencing (RNAseq). While both techniques provide reliable data on relative quantity, they lack information about the RNAs' location inside the cell. To shed light onto the spatial distribution of various mRNAs in mouse oocytes, we applied the powerful tool that is single molecule RNA-FISH (smRNA-FISH). smRNA-FISH allows for the quantification of absolute numbers of mRNAs. Based on a commercial kit and adapted for the use in oocytes, we further refined the protocol to allow compatibility with immunofluorescence staining of LLPS condensates and visualization of dense aggregates by overexpression of ZAR1. The new protocol maintains the properties of fluorescent proteins and therefore provides a base for the investigation of the localization of mRNAs in relation to MARDO[41]. We observed smRNA-FISH signal within MARDO but the majority of candidate mRNAs is located very close to the condensates. The reason for this observation could be that

the mRNAs inside the aggregated MARDO structure are less readily accessible by the smRNA-FISH probes. Performing a partial protein digestion before did not improve the accessibility. In the group of associated transcripts, candidate mRNAs affected by the loss of ZAR1 were enriched compared to mRNAs that were unaffected by the loss of MARDO and therefore considered to be rather randomly distributed. Moreover, our data suggests that for each specific gene, the enrichment of mRNA is different. *Actin B* is an example for evenly distributed mRNA, whereas *Wdr37* and *Elov7* are up to 50% enriched within MARDO. Yet, no transcript showed stronger enrichment. Therefore, translational repression cannot solely be explained by the sequestration into the condensates. Nevertheless, we observed a reciprocal correlation between the enrichment of gene-specific transcripts and the respective protein level. The model as shown in the first part of this thesis is the physical sequestration from translation. The second factor that contributes to translational repression is the direct binding of ZAR1. Phosphorylation of ZAR1 *in vivo* correlates with the translational activation of candidate mRNAs that are enriched in MARDO. ZAR1 is considered to repress translation partly depending on the phosphorylation state. Further experiments need to be done to support the model of phosphorylation-induced release of the translational repression. Evidence for the model could be provided if the inhibition of ZAR1 phosphorylation during meiosis maintained the translational repression or if expression of a phosphomimic ZAR1 construct in wild-type GV oocytes caused the pre-mature translation of the respective mRNAs.

MARDO likely provides a site for mRNA stabilization and translational repression and relies on further factors to adjust the specific translational level

We propose that MARDO sequesters certain mRNAs at different levels and expect MARDO to be involved in translational repression. However, this model is challenged by the results of the protein level analysis using both Western blot experiments and preliminary mass spectrometry data. Wdr37 and Tex19.1 protein levels are higher in *Zar1*$^{-/-}$ oocytes. At the same time, *Zar1*$^{-/-}$ oocytes have decreased mRNA levels for both candidates. Moreover, *Hig2* is stably translated in *Zar1*$^{-/-}$ GV oocytes even though we observed the localization of *Hig2* mRNA inside MARDO in wildtype oocytes. The model as shown in the first part of this thesis proposes the release of all sequestered mRNAs during meiosis and subsequent translation. If that is the case, growing *Zar1*$^{-/-}$ oocytes were expected to continuously synthesize proteins of mRNAs that are repressed in WT oocytes. While mRNAs have a very short life-time of about two weeks in immature oocytes, some proteins in oocytes are known to be long-lived[42,43]. For example, cohesin remains on the chromosomes for decades[44]. Yet, no data on the average protein lifetime is available for the candidates shown here. *Wdr37* has been shown to have a

half-life of about two weeks in brain tissue[45]. Our group is currently investigating which proteins are long-lived proteins in mouse oocytes (Gorry & Harasimov *et al.*, data not published). Moreover, mass spectrometry analysis is going to be performed on *Zar1*$^{-/-}$ and *Zar1*$^{+/+}$ oocytes that will enable insights into the mRNA-protein relation on mRNAs that are sequestered in MARDO. Based on preliminary data, we observed 50% of genes that we detected to be equally up- or downregulated in both the RNAseq dataset and the mass spectrometry dataset and 50% of genes that have decreased mRNA levels in *Zar1*$^{-/-}$ oocytes to have increased protein levels (data not published). So far, no final conclusions can be drawn in regard to the translation of MARDO-specific mRNAs in *Zar1*$^{-/-}$ oocytes. Nevertheless, the data provided in this thesis propose a complex combination of stabilization effects and translational repression by MARDO. Furthermore, we found the degree of translational repression to be different for different mRNAs. Future analysis of the localization of polysomes in oocytes in relation to MARDO will provide respective evidence. Nevertheless, the mRNA localization is not static and mRNAs can diffuse between the cytoplasm and the condensates. While it is known that mRNAs are found both inside MARDO and in the cytosol, future analysis will be necessary to investigate the dynamics of MARDO-specific mRNAs. For example, FRAP experiments on fluorescently tagged mRNAs would allow the quantification of dynamics and kinetics. We propose that an equilibrium of uptake and release of mRNAs into and out of MARDO is maintained. When the mRNAs are located in the cytosol, they are accessible for the translational apparatus. The fraction of mRNAs in the cytosol determines translational activity. Therefore, we propose that the translation level of MARDO-specific mRNAs is not limited to the phosphorylation state of ZAR1. The concept of individual regulation of mRNA stabilization and translational repression is similar to the function of Smaug in *Drosophila melanogaster* oocytes. Smaug is an mRNA-binding and regulating protein and exhibits differentiated effects on its targets[46]. As an example, *nanos* is translationally repressed by Smaug, whereas *Hsp83* is not repressed but significantly destabilized. Yet, *nanos*' mRNA stability is unaffected by Smaug[47,48]. Translation for both mRNAs occurs at the posterior pole exclusively as another factor called Oskar prevents Smaug from binding *nanos* mRNA whereas *Hsp83* contains a so-called *Hsp83* protection element (HPE) that stabilizes mRNAs at the posterior pole[49]. The major difference between both mRNA is that *Hsp83* contains more Smaug-binding sites[50]. Similar to the assumptions for Smaug's differential effects on its targets, we propose further trans-factors that determine the kinetics for each maternal mRNA in mouse oocytes with regards to the import into and export from MARDO. While other factors are considered to regulate the translation for each transcript in a complex interplay, MARDO is rather interpreted as the structure in which mRNAs are stabilized and sequestered from ribosomes. For the majority of an oocyte's lifetime, multiple factors determine the distinct translational level for each gene and

rely on MARDO as a "sanctuary" for the mRNAs. We have discussed the function of maternal mRNAs in the general introduction. As an oocyte matures, the transcription and therefore the synthesis of mRNAs is silenced[51]. The spatiotemporal translation of maternal mRNAs is tightly orchestrated for each gene[52]. Furthermore, with the onset of meiosis, the complete removal of the entire maternal mRNA pool is necessary to allow the future zygote to be totipotent[53]. MARDO dissolves and allows the mRNAs to be degraded. The involvement of ZAR1 in MARDO formation explains why Zar1-deficient mice produce embryos that arrest in the zygote stage[14]. Therefore, we postulate that MARDO is one of the central organelles in the mouse oocyte for the regulation of maternal mRNA translation. A number of questions still remain: Which co-factors determine the translational activity of mRNAs? Do the co-factors indeed affect the kinetics of mRNAs that are sequestered within MARDO or do they act as activators/repressors themselves? Do the co-factors interact with ZAR1? Is ZAR1 actually bound to mRNAs outside of MARDO? Many questions could be elucidated by the performance of pulldown experiments. For example, WT oocytes could be fixed by a cross-linking agent, i.e. formaldehyde, and ZAR1 could be extracted by a pulldown step. Subsequent mass spectrometry experiments could provide information about associated factors. To assess the proteins that bind to mRNAs in the cytosol, oocytes could be released in the presence of nuclease inhibitors that prevent the degradation of cytosolic mRNAs. Then, cross-linking, pulldown and mass spectrometry could be performed similarly.

While the reasons for aneuploidy are known, no solution is known yet to revert the process

The impact of ATGL activity on mitochondrial activity demonstrates the implications of oxidative stress in oocytes and how the translational control of maternal mRNAs is linked to female meiosis. Maintenance of maternal mRNAs and the respective translation is required to allow the preservation of developmental competence[54]. The third part of this thesis is unrelated to the formation and actions of MARDO at a first glance. We investigated the question of how damage that has already occurred could be repaired. In other words, after the finding of natural control mechanisms for the metabolic stability of the oocyte, what could be done if the control mechanisms of the fail? As female mammals age, the control mechanisms for metabolic stability and oxidative stress reduction fail more often, which leads to increased rates of aneuploidy[55]. The main challenge in this context is to combine biological knowledge with physical expertise and engineering. Simple chromosome displacement experiments using large permanent magnets have been reported already[56] but the purpose of this study was to allow highest sensitivity regarding the forces exerted on the chromosomes and the spatial direction of movement. Moreover, the study was

intended to provide a protocol on the displacement of individual chromosomes. Unfortunately, none of the reported set-ups have given reproducible results yet. The frequency of successful incidences in which a single chromosomes were removed from the spindle was low. Nevertheless, the successful experiments demonstrate the feasibility as a proof-of-concept. Individual chromosomes can be removed from the oocyte. However, is has been reported that in non-treated oocytes, the removal of intact chromosomes from the spindle is hindered by the cellular microenvironment[57]. The next steps will be the improvement of reproducibility and developmental competence after this kind of manipulation. New optical tweezer set-ups have been shown to be able to displace microspheres over the ranges of whole oocytes[58]. With larger working ranges, microspheres would not have to be moved into the vicinity of chromosomes before the actual manipulation. Laser scissors have been shown to enable the removal of chromosomes from intact spindles without the need to exert large forces on the chromosomes or microtubules[59,60].

Further validation of chromosome manipulation tools will require suitable mouse lines and live cell-compatible labelling of specific chromosomes

Further tests of the set-up would include the manipulation of chromosomes in mouse oocytes that harbor genetic disorders. Two particular mouse lines are suitable for testing the technique to repair aneuploidies. Firstly, the mouse line transchromatic 1 (Tc1) which resembles the human trisomy 21, was generated after an almost complete human chromosome 21 was stably inserted into mouse ES cells[61]. Various studies were done that confirmed the karyotype and phenotypes that are similar to humans with Down syndrome[62,63]. Recently, a refined Tc1 mouse line was reported that expresses more than 93% of the genes on the human chromosome[64]. The second chromosome aberration model produces offspring with XO karyotype (Turner syndrome)[65]. While Tc1 oocytes provide a chromosome set in which the removal of the human chromosome causes the rescue of a healthy phenotype, XO oocytes require a chromosome transfer. If the successful recovery of healthy karyotypes were shown in both mouse models, the tool could proof its strength and compatibility with developmental competence of the oocytes. The development of an an upgraded tool can remove single chromosomes from oocytes without harming the oocytes will therefore not be trivial and must consider multiple factors from experimental parameters like temperature, medium, laser exposure and drug treatment, to engineering implications of size, material, costs and notably the user-friendliness. Once a functional set-up for the manipulation of chromosomes is available, further requirements must be assessed. First, the protocol must be validated for the developmental competence and potential damage of the oocytes. Second, a method must be established to identify specific chromosomes under live cell conditions.

While human chromosomes differ in their respective morphology, mouse chromosomes share the same shape and physical size[66–68]. Differentiation of the chromosomes is hard to impossible when the DNA is stained by simple live cell dyes[69]. Except for mouse models like the Tc1 mouse, which allows the easy identification of the extra chromosome based on morphology and size, normal mouse lines and human oocytes require tailored solutions for the identification of the karyotype *in vivo*. Classic approaches to discriminate the different chromosomes are the Giemsa staining in combination with trypsin treatment and the use of FISH-based banding[70,71]. Yet, both approaches are incompatible with live cell applications because they require permeabilization and/or fixation of the cell. While DNA dyes are generally able to visualize bands on chromosomes, too, the quality is insufficient to identify a certain chromosome solely based on dyes[72]. Recent approaches have used Clustered regularly interspaced palindromic repeats and Clustered regularly interspaced palindromic repeats-associated protein 9 (CRISPR/Cas9)-mediated labeling of specific chromosomes. Cas9 lacking nuclease activity (dCas9) is introduced into the cell together with a guide RNA (gRNA) that targets a specific sequence. The sequence must be repetitive and should ideally be concentrated on one chromosome[73]. The limitation is that the concept works better for interphase chromatin, which is relaxed and accessible. Chromosomes in mitosis and meiosis are condensed and the accessibility of many chromatin regions is restricted[74]. A similar but more refined approach is to target a large number of non-repetitive sequences[75]. While the approach works well for condensed chromosomes under live cell conditions, it requires intense preparations and is not suitable for a daily routine protocol. Quantum dots-labelled transcription activator-like effectors (TALEs) were previously observed to enter live cells and visualize single genomic loci[76]. Nevertheless, no such staining is available for condensed chromosomes yet. Other approaches that have successfully visualized specific chromosomes during mitosis require transgenic modifications and are therefore not compatible with applications in human oocytes[77,78]. In summary, no protocol that allows for the identification of specific chromosomes under live cell conditions is available to date. Future projects on *in vivo* chromosome manipulation will have to work on chromosome labeling, too.

MARDO maintains the oocyte's developmental competence and optical tweezers might be able to restore lost developmental competence

In this thesis, we investigated the nature of ZAR1 and the LLPS structure MARDO in regards to their effects on maternal mRNAs. We propose that ZAR1 forms a phase-separated structure together with mitochondria and RNA binding proteins. MARDO sequesters maternal mRNAs which are then physically protected from both ribosomes and decay mediating-enzymes. Therefore, mRNAs located inside of MARDO are both translationally silenced and stabilized. The kinetics of the migration into the condensates and into the cytoplasm are a key parameter that determines the translation of the mRNAs. Further, we propose that additional mRNA binding proteins contribute to the translation rate. Together, MARDO and further factors tightly orchestrate the translation of different genes in GV oocytes. When the oocytes resume meiosis, ZAR1 is phosphorylated and the translation of sequestered mRNAs is increased. After metaphase I, ZAR1 via degraded by proteasome pathways and MARDO dissolves. The maternal mRNAs are translated and degraded, allowing the fertilized egg to replenish its mRNA pool with zygotic mRNAs. Many questions remain to be elucidated. What is the function of mitochondria in MARDO? How similar is MARDO to the Balbiani body? Which other factors determine the translation rate of maternal mRNAs. Can this structure be found in human oocytes, too?

Further, we developed tools to remove single chromosome from the meiotic spindle in mouse oocytes. The tools are not efficient and harm oocytes. However, our designs could be refined and the experimental set-up could be transferred to optical tweezers. If optical tweezers can exert higher forces than our magnetic tweezer set-up, they might be able to completely remove chromosomes from the spindle. Alternatively, one could use laser scissors to disconnect the chromosome from the spindle. Many commercially available optical tweezers are easy to handle and allow the incorporation of confocal microscopy. Confocal microscopy would allow for the visualization of specifically labelled single chromosomes. We expect that optical tweezers-based approached should be able to manipulate the karyotype of oocytes without harming them.

Author's contribution

A mitochondria-associated membraneless compartment governs the fate of maternal mRNAs in mammalian oocytes

Shiya Cheng wrote the manuscript.

Gerrit Altmeppen performed the following experiments:

Experiment	Experimental details
Fig. 1 A + B	Isolation of oocytes, immunofluorescence staining and imaging
Fig. 1 G - N	Isolation of oocytes, immunofluorescence staining and imaging
Fig. 1 W + X	Isolation of oocytes, application of PLA protocol, analysis of the images and quantification
Fig. S1 A - G	Isolation of oocytes, immunofluorescence staining and imaging
Fig. S1 K	Isolation of oocytes, immunofluorescence staining and imaging
Fig. 2 A - H	Isolation of oocytes, immunofluorescence staining, imaging and sorting based on the oocytes' size
Fig. 2 I + J	Isolation of oocytes, live cell staining, imaging and quantification
Fig. 4 I + J	Isolation of oocytes, application of PLA protocol, analysis of the images and quantification
Fig. 5 C - f	Isolation of oocytes, injection and overexpression of ZAR1-mClover3, application of the smRNA-FISH protocol, analysis, quantification of smRNA-FISH spots, identification of localization and statistical analysis
Fig. 5 G	Isolation of oocytes, application of PLA protocol and analysis of the images
Fig. 7 A	Isolation of oocytes, *in vivo* maturation, immunofluorescence staining and imaging
Fig. S10 A	Isolation of oocytes, treatment with CHX or EDTA, application of PLA protocol, analysis of the images and quantification
Fig. S10 B - D	Isolation of oocytes, immunofluorescence staining, imaging and quantification
Fig. S10 F + G	Isolation of oocytes, preparation of cell lysate, application of SDS-PAGE and Western blot protocol and imaging
Fig. S10 H - J	Isolation of oocytes, *in vivo* maturation, immunofluorescence staining, imaging and quantification

ZAR1 regulates the lipid metabolism and mitochondrial activity in mouse oocytes by the stabilization of *Hig2* mRNA

Gerrit Altmeppen wrote the manuscript.

Gerrit Altmeppen performed and analyzed all experiments except for the following ones:

Experiment	Done by
Fig. 1 A	Nile red staining and imaging was done by Shiya Cheng.
Fig. 2 E + Fig. 6	RNAseq library was prepared by Shiya Cheng. RNAseq raw data was analyzed by Sarah Penir. *Zar1/2*-KO data was used from Rong *et al.*[2]. Fig. 6 was prepared by Sarah Penir. Pathways of interest were highlighted by Gerrit Altmeppen based on a discussion with Shiya Cheng.
Fig. S5 C	Injection of AT1.03 mRNA, treatment with FCCP/DMSO and imaging was done by Shiya Cheng.

Magnetic tweezers and biopsy needles are capable of removing single chromosomes from meiotic spindles in mouse oocytes

Gerrit Altmeppen wrote the manuscript.

Gerrit Altmeppen performed and analyzed all experiments. Alexandre Webster injected H2B-GFP mRNA in oocytes for experiments in which no live cell dye was used to stain the DNA.

Acknowledgments

The author thanks Laura Redzich, Tabea Marx, Carsten Placke-Yan, Lena Wartosch and Melina Schuh for critical comments on the manuscripts and chapters.

References

1. Zhang, X. *et al.* Inhibition of intracellular lipolysis promotes human cancer cell adaptation to hypoxia. *Elife* **6**, 1–24 (2017).
2. Rong, Y. *et al.* ZAR1 and ZAR2 are required for oocyte meiotic maturation by regulating the maternal transcriptome and mRNA translational activation. *Nucleic Acids Res.* **47**, 11387–11402 (2019).
3. Leslie, M. Sloppy science or groundbreaking idea? Theory for how cells organize contents divides biologists. *Science (80-.).* (2021) doi:10.1126/science.abg6495.
4. So, C., Cheng, S. & Schuh, M. Phase Separation during Germline Development. *Trends Cell Biol.* **31**, 254–268 (2021).
5. Alberti, S., Gladfelter, A. & Mittag, T. Considerations and Challenges in Studying Liquid-Liquid Phase Separation and Biomolecular Condensates. *Cell* **176**, 419–434 (2019).
6. Boeynaems, S. *et al.* Protein Phase Separation: A New Phase in Cell Biology. *Trends Cell Biol.* **28**, 420–435 (2018).
7. Frottin, F. *et al.* The nucleolus functions as a phase-separated protein quality control compartment. *Science (80-.).* **365**, 342–347 (2019).
8. Raff, J. W. Phase Separation and the Centrosome: A Fait Accompli? *Trends Cell Biol.* **29**, 612–622 (2019).
9. Luo, Y., Na, Z. & Slavoff, S. A. P-Bodies: Composition, Properties, and Functions. *Biochemistry* **57**, 2424–2431 (2018).
10. Maruri-López, I., Figueroa, N. E., Hernández-Sánchez, I. E. & Chodasiewicz, M. Plant Stress Granules: Trends and Beyond. *Front. Plant Sci.* **12**, 1538 (2021).
11. Cabral, S. E. & Mowry, K. L. Organizing the oocyte: RNA localization meets phase separation. in 87–118 (2020). doi:10.1016/bs.ctdb.2020.02.007.
12. Schisa, J. A. Germ Cell Responses to Stress: The Role of RNP Granules. *Front. Cell Dev. Biol.* **7**, 220 (2019).
13. So, C. *et al.* A liquid-like spindle domain promotes acentrosomal spindle assembly in mammalian oocytes. *Science (80-.).* **364**, (2019).
14. Wu, X. *et al.* Zygote arrest 1 (Zar1) is a novel maternal-effect gene critical for the oocyte-to-embryo transition. *Nat. Genet.* **33**, 187–191 (2003).
15. Wu, Y.-K. & Fan, H.-Y. Revisiting ZAR proteins: the understudied regulator of female fertility and beyond. *Cell. Mol. Life Sci.* **79**, 92 (2022).
16. Gao, J. *et al.* Translational regulation in the brain by TDP-43 phase separation. *J. Cell Biol.* **220**, (2021).

17. Huang, L. *et al.* Mitochondria Associate with P-bodies and Modulate MicroRNA-mediated RNA Interference. *J. Biol. Chem.* **286**, 24219–24230 (2011).

18. Koppers, M., Özkan, N. & Farías, G. G. Complex Interactions Between Membrane-Bound Organelles, Biomolecular Condensates and the Cytoskeleton. *Front. Cell Dev. Biol.* **8**, 1661 (2020).

19. Zhang, C. & Rabouille, C. Membrane-Bound Meet Membraneless in Health and Disease. *Cells* **8**, 1000 (2019).

20. Zhao, Y. G. & Zhang, H. Phase Separation in Membrane Biology: The Interplay between Membrane-Bound Organelles and Membraneless Condensates. *Dev. Cell* **55**, 30–44 (2020).

21. Nicholls, D. G. Mitochondrial membrane potential and aging. *Aging Cell* **3**, 35–40 (2004).

22. Cioni, J.-M. *et al.* Late Endosomes Act as mRNA Translation Platforms and Sustain Mitochondria in Axons. *Cell* **176**, 56-72.e15 (2019).

23. Rossoll, W. & Bassell, G. J. Crosstalk of Local Translation and Mitochondria: Powering Plasticity in Axons and Dendrites. *Neuron* **101**, 204–206 (2019).

24. Imamura, H. *et al.* Visualization of ATP levels inside single living cells with fluorescence resonance energy transfer-based genetically encoded indicators. *Proc. Natl. Acad. Sci.* **106**, 15651–15656 (2009).

25. Reboll, M. R. & Nourbakhsh, M. Identification of Actively Translated mRNAs. in *Methods in Molecular Biology* vol. 1182 173–178 (Humana Press Inc., 2014).

26. Tom Dieck, S. *et al.* Direct visualization of newly synthesized target proteins in situ. *Nat. Methods* **12**, 411–414 (2015).

27. Tetkova, A., Jansova, D. & Susor, A. Spatio-temporal expression of ANK2 promotes cytokinesis in oocytes. *Sci. Rep.* **9**, 13121 (2019).

28. Marlow, F. L. Mitochondrial matters: Mitochondrial bottlenecks, self-assembling structures, and entrapment in the female germline. *Stem Cell Res.* **21**, 178–186 (2017).

29. Packer, C., Tatar, M. & Collins, A. Reproductive cessation in female mammals. *Nature* **392**, 807–811 (1998).

30. Elis, S. *et al.* Genes Involved in Drosophila melanogaster Ovarian Function Are Highly Conserved Throughout Evolution. *Genome Biol. Evol.* **10**, 2629–2642 (2018).

31. Eichhorn, S. W. *et al.* mRNA poly(A)-tail changes specified by deadenylation broadly reshape translation in Drosophila oocytes and early embryos. *Elife* **5**, (2016).

32. Komini, C., Theohari, I., Lambrianidou, A., Nakopoulou, L. & Trangas, T. PAPOLA

contributes to cyclin D1 mRNA alternative polyadenylation and promotes breast cancer cell proliferation. *J. Cell Sci.* **134**, (2021).

33. Venkataraman, K., Brown, K. M. & Gilmartin, G. M. Analysis of a noncanonical poly(A) site reveals a tripartite mechanism for vertebrate poly(A) site recognition. *Genes Dev.* **19**, 1315–1327 (2005).

34. Moore, K. S. & von Lindern, M. RNA Binding Proteins and Regulation of mRNA Translation in Erythropoiesis. *Front. Physiol.* **9**, 910 (2018).

35. Kamenska, A. *et al.* The DDX6–4E-T interaction mediates translational repression and P-body assembly. *Nucleic Acids Res.* **44**, 6318–6334 (2016).

36. Brandmann, T. *et al.* Molecular architecture of LSM 14 interactions involved in the assembly of mRNAsilencing complexes. *EMBO J.* **37**, (2018).

37. Jalkanen, A. L., Coleman, S. J. & Wilusz, J. Determinants and implications of mRNA poly(A) tail size – Does this protein make my tail look big? *Semin. Cell Dev. Biol.* **34**, 24–32 (2014).

38. Chalabi Hagkarim, N. & Grand, R. J. The Regulatory Properties of the Ccr4–Not Complex. *Cells* **9**, 2379 (2020).

39. Charenton, C. & Graille, M. mRNA decapping: finding the right structures. *Philos. Trans. R. Soc. B Biol. Sci.* **373**, 20180164 (2018).

40. Mugridge, J. S., Tibble, R. W., Ziemniak, M., Jemielity, J. & Gross, J. D. Structure of the activated Edc1-Dcp1-Dcp2-Edc3 mRNA decapping complex with substrate analog poised for catalysis. *Nat. Commun.* **9**, 1152 (2018).

41. Xie, F., Timme, K. A. & Wood, J. R. Using Single Molecule mRNA Fluorescent in Situ Hybridization (RNA-FISH) to Quantify mRNAs in Individual Murine Oocytes and Embryos. *Sci. Rep.* **8**, 7930 (2018).

42. Brower, P. T., Gizang, E., Boreen, S. M. & Schultz, R. M. Biochemical studies of mammalian oogenesis: Synthesis and stability of various classes of RNA during growth of the mouse oocyte in vitro. *Dev. Biol.* **86**, 373–383 (1981).

43. Jahn, C. L., Baran, M. M. & Bachvarova, R. Stability of RNA synthesized by the mouse oocyte during its major growth phase. *J. Exp. Zool.* **197**, 161–171 (1976).

44. Szydłowska, A., Ladstätter, S . & Tachibana, K. Manipulating Cohesin Levels in Live Mouse Oocytes. in *Methods in Molecular Biology* vol. 1818 113–128 (Humana Press Inc., 2018).

45. Fornasiero, E. F. *et al.* Precisely measured protein lifetimes in the mouse brain reveal differences across tissues and subcellular fractions. *Nat. Commun.* **9**, 4230 (2018).

46. Tadros, W. *et al.* SMAUG Is a Major Regulator of Maternal mRNA Destabilization in Drosophila and Its Translation Is Activated by the PAN GU

Kinase. *Dev. Cell* **12**, 143–155 (2007).

47. Chen, L. *et al.* Global regulation of mRNA translation and stability in the early Drosophila embryo by the Smaug RNA-binding protein. *Genome Biol.* **15**, R4 (2014).

48. Bruzzone, L. A crosstalk between the RNA binding protein Smaug and the Hedgehog pathway links cell signaling to mRNA regulation in drosophila.

49. Farley, B. M. & Ryder, S. P. Regulation of Maternal mRNAs in Early Development. *Crit. Rev. Biochem. Mol. Biol.* **43**, 135–162 (2008).

50. Semotok, J. L. *et al.* Drosophila Maternal Hsp83mRNA Destabilization Is Directed by Multiple SMAUG Recognition Elements in the Open Reading Frame. *Mol. Cell. Biol.* **28**, 6757–6772 (2008).

51. Dumdie, J. N. *et al.* Chromatin Modification and Global Transcriptional Silencing in the Oocyte Mediated by the mRNA Decay Activator ZFP36L2. *Dev. Cell* **44**, 392-402.e7 (2018).

52. Winata, C. L. & Korzh, V. The translational regulation of maternal <scp>mRNA</scp> s in time and space. *FEBS Lett.* **592**, 3007–3023 (2018).

53. Lee, M. T., Bonneau, A. R. & Giraldez, A. J. Zygotic Genome Activation During the Maternal-to-Zygotic Transition. *Annu. Rev. Cell Dev. Biol.* **30**, 581–613 (2014).

54. Barckmann, B. & Simonelig, M. Control of maternal mRNA stability in germ cells and early embryos. *Biochim. Biophys. Acta - Gene Regul. Mech.* **1829**, 714–724 (2013).

55. Nagaoka, S. I., Hassold, T. J. & Hunt, P. A. Human aneuploidy: mechanisms and new insights into an age-old problem. *Nat. Rev. Genet.* **13**, 493–504 (2012).

56. Hong, J., Purwar, P., Cha, M. & Lee, J. Spatial control of chromosomal location in a live cell with functionalized magnetic particles. *Nanoscale* **7**, 19110–19117 (2015).

57. Parsa, S. UC San Diego UC San Diego Electronic Theses and Dissertations Title A double tweezers and laser ablation (scissors) microscope for biological studies. (2010).

58. Melzer, J. E. & McLeod, E. Fundamental Limits of Optical Tweezer Nanoparticle Manipulation Speeds. *ACS Nano* **12**, 2440–2447 (2018).

59. Berns, M. W. Laser Scissors and Tweezers to Study Chromosomes: A Review. *Front. Bioeng. Biotechnol.* **8**, (2020).

60. Ono, M., Preece, D., Duquette, M. L., Forer, A. & Berns, M. W. Mitotic tethers connect sister chromosomes and transmit “cross-polar” force during anaphase A of mitosis in PtK2 cells. *Biomed. Opt. Express* **8**, 4310 (2017).

61. O'Doherty, A. *et al.* An Aneuploid Mouse Strain Carrying Human Chromosome 21 with Down Syndrome Phenotypes. *Science (80-.).* **309**, 2033–2037 (2005).

62. Hall, J. H. *et al.* Tc1 mouse model of trisomy-21 dissociates properties of short- and long-term recognition memory. *Neurobiol. Learn. Mem.* **130**, 118–128 (2016).

63. Morice, E. *et al.* Preservation of long-term memory and synaptic plasticity despite short-term impairments in the Tc1 mouse model of Down syndrome. *Learn. Mem.* **15**, 492–500 (2008).

64. Kazuki, Y. *et al.* A non-mosaic transchromosomic mouse model of Down syndrome carrying the long arm of human chromosome 21. *Elife* **9**, 1–29 (2020).

65. Probst, F. J., Cooper, M. L., Cheung, S. W. & Justice, M. J. Genotype, Phenotype, and Karyotype Correlation in the XO Mouse Model of Turner Syndrome. *J. Hered.* **99**, 512–517 (2008).

66. Al-Aish, M. S. HUMAN CHROMOSOME MORPHOLOGY. I. STUDIES ON NORMAL CHROMOSOME CHARACTERIZATION, CLASSIFICATION AND KARYOTYPING. *Can. J. Genet. Cytol.* **11**, 370–381 (1969).

67. Bachvarova, R., Burns, J. P., Spiegelman, I., Choy, J. & Chaganti, R. S. K. Morphology and transcriptional activity of mouse oocyte chromosomes. *Chromosoma* **86**, 181–196 (1982).

68. Guilly, M. N., Fouchet, P., de Chamisso, P., Schmitz, A. & Dutrillaux, B. Comparative karyotype of rat and mouse using bidirectional chromosome painting. *Chromosome Res.* **7**, 213–21 (1999).

69. Levasseur, M. D., Thomas, C., Davies, O. R., Higgins, J. M. G. & Madgwick, S. Aneuploidy in Oocytes Is Prevented by Sustained CDK1 Activity through Degron Masking in Cyclin B1. *Dev. Cell* **48**, 672-684.e5 (2019).

70. Korf, B. R., Schuh, B. E., Salwen, M. J., Warburton, D. & Miller, O. J. The role of trypsin in the pre-treatment of chromosomes for giemsa banding. *Hum. Genet.* **31**, 27–33 (1976).

71. Liehr, T., Heller, A., Starke, H. & Claussen, U. FISH banding methods: applications in research and diagnostics. *Expert Rev. Mol. Diagn.* **2**, 217–225 (2002).

72. Zink, D., Sadoni, N. & Stelzer, E. Visualizing chromatin and chromosomes in living cells. *Methods* **29**, 42–50 (2003).

73. Qin, P. *et al.* Live cell imaging of low- and non-repetitive chromosome loci using CRISPR-Cas9. *Nat. Commun.* **8**, 14725 (2017).

74. Daer, R. M., Cutts, J. P., Brafman, D. A. & Haynes, K. A. The Impact of Chromatin Dynamics on Cas9-Mediated Genome Editing in Human Cells. *ACS Synth. Biol.* **6**, 428–438 (2017).

75. Zhou, Y. *et al.* Painting a specific chromosome with CRISPR/Cas9 for live-cell imaging. *Cell Res.* **27**, 298–301 (2017).

76. Ma, Y. *et al.* Live cell imaging of single genomic loci with quantum dot-labeled TALEs. *Nat. Commun.* **8**, 15318 (2017).

77. Gerlich, D. *et al.* Global Chromosome Positions Are Transmitted through Mitosis in Mammalian Cells. *Cell* **112**, 751–764 (2003).

78. Mora-Bermúdez, F. & Ellenberg, J. Measuring structural dynamics of chromosomes in living cells by fluorescence microscopy. *Methods* **41**, 158–167 (2007).

List of abbreviations

4-HNE	4-HydroxynoNEnal
8-oxoG	8-oxoguanine
aMTOC	Acentriolar MTOC
APC	Anaphase Promoting Complex
APC/C	Anaphase Promoting Complex/Cyclosome
AREs	AU-Rich Element
ART	Assisted Reproductive Technology
ATGL	Adipose TriGlyceride Lipase
BSA	Bovine Serum Albumin
CCR4-NOT	carbon catabolite repression 4 -negative on TATA-less complex
CHX	CycloHeXidin
CPE	Cytoplasmic Polyadenylation Element
CRISPR/Cas9	Clustered regularly interspaced palindromic repeats-associated protein 9
dCas9	Deactivated Cas9
DIC	Differential Interference Contrast
DSB	Double-Strand Break
FA	Fatty Acid
FAO	Fatta Acid β-Oxidation
FBS	Fetal Bovine Serum
FISH	Fluorescent *In Situ* Hybridization
FRAP	Fluorescence Recovery After Photobleaching
gRNA	Guide RNA
GSEA	Gene Set Enrichment Analysis
GV	Germinal Vesicle
GVBD	Germinal Vesicle BreakDown
H2B	Histone 2B
Hig2	Hypoxia-Inducible Gene 2
Hilpda	Hypoxia Inducible LiPid Droplet Associated
IDP	Intrinsically Disordered Protein
IMS	InterMitochondrial Cement
IVF	*In Vitro* fertilization
JC-1	tetraethylbenzimidazolylcarbocyanine iodide
KO	Knock-Out
LH	Luteinizing Hormone
LISD	Liquid-like meiotic Spindle Domain
LLPS	Liquid-Liquid Phase Separation
MARDO	Mitochondria-Associated RNP Domain in Oocyte
MI	Meiosis I
MII	Meiosis II
MMP / ΔΨm	Mitochondrial Membrane Potential
MMSP	maternal mRNA-Sequestering Protein

MRT	Mitochondria Replacement Therapies
mtDNA	Mitochondrial DNA
MTG	MitoTracker Green
MTOC	MicroTubule Organizing Center
MZT	Maternal-to-Zygotic Transition
NDJ	Non-Disjunction
NEBD	Nuclear Envelope BreakDown
PABP	Poly(A)-Binding proteins
PAP	Poly(A)-Polymerase
PLA	Proximity Ligation Assay
PSSC	Pre-mature Separation of Sister Chromatid
RBP	RNA-Binding Proteins
rDNA	Ribosomal DNA
RNAseq	RNA sequencing
RNPs	RNA Particles / RiboNucleoprotein particles
ROS	Reactive Oxygen Species
SAC	Spindle Assembly Checkpoint
smRNA-FISH	and single molecule RNA-FISH
TAC	TriAcylGlycerol
TALE	Transcription Activator-Like Effectors
TMRM	TetraMethylRhodamine, Methyl ester
UTR	UnTranslated 3' Region
WT	Wild-Type

A Tribute to my PhD

It starts with one
All I know
It's so unreal
Watch you go
I tried so hard and got so far
But in the end, it doesn't even matter
I had to fall to lose it all
But in the end, it doesn't even matter
One thing, I don't know why
It doesn't even matter how hard you try
Keep that in mind, I designed this rhyme
To remind myself of a time when I tried so hard
In spite of the way you were mockin' me
Actin' like I was part of your property
Remembering all the times you fought with me
I'm surprised it got so far
Things aren't the way they were before
You wouldn't even recognize me anymore
Not that you knew me back then
But it all comes back to me in the end
You kept everything inside
And even though I tried, it all fell apart
What it meant to me will eventually
Be a memory of a time when I
I tried so hard and got so far
But in the end, it doesn't even matter
I had to fall to lose it all
But in the end, it doesn't even matter
One thing, I don't know why
It doesn't even matter how hard you try
Keep that in mind
I designed this rhyme to explain in due time
All I know
Time is a valuable thing
Watch it fly by as the pendulum swings
Watch it count down to the end of the day
The clock ticks life away
It's so unreal
You didn't look out below
Watch the time go right out the window
Tryin' to hold on, they didn't even know
I wasted it all just to watch you go
I kept everything inside
And even though I tried, it all fell apart
What it meant to me will eventually be a memory
Of a time when I tried so hard

In the end by Linkin Park